Application and Analysis of Silicon Nitride Films for Surface Passivation of High Efficiency Silicon Solar Cells

Application and Analysis of Silicon Nitride Films for Surface Passivation of High Efficiency Silicon Solar Cells

Toepassing en Analyse van Siliciumnitride Lagen voor Oppervlaktepassivering van Hoog-Rendement Zonnecellen

(met een samenvatting in het Nederlands)

ACADEMISCH PROEFSCHRIFT

ter verkrijging van de graad van doctor
aan de Universiteit van Amsterdam
op gezag van de Rector Magnificus
Prof. Dr. D.C. van den Boom
ten overstaan van een door het college voor promoties
ingestelde commissie,
in het openbaar te verdedigen in de Agnietenkapel
op donderdag 2 april 2015, te 14:00 uur

door

Machteld Willemijn Petronel Elisabeth Lamers

geboren te Lienden

Promotiecommissie:

Promotor:
Prof. dr. W.C. Sinke

Co-promotor:
Dr. A.W. Weeber

Overige leden:
Prof. dr. T. Gregorkiewicz
Prof. dr. A. Polman
Prof. dr. R.E.I. Schropp
Prof. dr. M. Zeman

Faculteit der Natuurwetenschappen, Wiskunde en Informatica

The work described in this thesis was carried out at the

Energy research Centre of the Netherlands
Solar Energy
Westerduinweg 3
1755 LE Petten
The Netherlands

and was carried out in the framework of the Hipersol Project, the CrystalClear Integrated Project and the EOS-ES Starfire Project. The EC and SenterNovem are both acknowledged for the financial support under respective contract numbers MMP3-SL-2009-228513, SES6-CT 2003-502583 and S063024.

Voor Michiel en Ysbrand

Contents

1 Introduction **1**
1.1 Photovoltaic market . . . 1
1.2 Scope of this work . . . 3
1.3 Outline of the thesis . . . 5

I Technological aspects **7**

2 Description of the solar cell fabrication process **9**
2.1 Industrial p-type Si cell process . . . 9
2.2 Light management . . . 11
2.2.1 Texture . . . 11
2.2.2 Anti-Reflection Coating . . . 13
2.3 Emitter formation . . . 16
2.4 a-SiN_x:H deposition . . . 20
2.4.1 Remote-PECVD . . . 20
2.4.2 Tuning the layer characteristics . . . 23
2.5 Contacting . . . 25
2.5.1 Front Side Contacting . . . 25
2.5.2 Rear Side Contacting . . . 26

3 Introduction to surface passivation **29**

4 Experimental Methods **33**
4.1 Characterization Methods . . . 33
4.1.1 Transmission Electron Microscopy . . . 33
4.1.2 Time-of-Flight Secondary Ion Mass Spectroscopy . . . 34
4.1.3 X-ray Photoelectron Spectroscopy . . . 34
4.1.4 Fourier Transform Infrared Spectroscopy . . . 35
4.1.5 Spectroscopic Ellipsometry . . . 36
4.1.6 Combining FTIR and Ellipsometry to extract atomic densities . . . 37
4.1.7 Minority Carrier Lifetime . . . 37
4.1.8 CV-MIS . . . 38
4.2 Modeling Approaches . . . 39
4.2.1 *Ab Initio* Density Functional Theory . . . 39
4.2.2 Force Field Molecular Dynamics . . . 40

II High Efficiency Solar Cells **43**

5 17.9% Metal-wrap-through mc-Si solar cells resulting in world record module efficiency of 17.0% **45**
5.1 Introduction . . . 46
5.2 ECN-MWT cell and module processing . . . 49

5.3 Evolution of ECN-MWT cells 52
5.4 ECN-MWT cell process optimization 52
5.4.1 Laser drilling of the holes 53
5.4.2 Texturing 53
5.4.3 Emitter 54
5.4.4 a-SiN_x:H 56
5.4.5 Emitter contacting 58
5.4.6 Metal wrap-through 58
5.4.7 Rear side aluminum 59
5.4.8 Isolation 61
5.4.9 Front side metalization pattern 61
5.4.10 Integration of optimized steps 63
5.5 17% module efficiency 65
5.6 Losses and gains 67
5.6.1 Transmission of light 67
5.6.2 Emitter recombination 68
5.6.3 Rear side passivation and reflection 68
5.7 Conclusions 68

6 Towards 21% n-Cz IBC solar cells based on screen-printing 71
6.1 Introduction 72
6.2 Solar Cell and Process Description 73
6.3 Solar Cell Optimization 74
6.3.1 Front surface field optimization 74
6.3.2 Emitter fraction and pitch optimization 76
6.4 Best Cell Results 79
6.5 Conclusions 81

III Analysis of the a-SiN_x:H layer and interface with c-Si 83

7 Characterization of the a-SiN_x:H layer: bulk properties, interface with Si and solar cell efficiency 85
7.1 Introduction 86
7.2 Setting the background 86
7.2.1 Sample preparation 86
7.2.2 Optical properties, bond densities and passivation . . 87
7.3 Characterization accuracy 91
7.3.1 Homogeneity in the layer: atomic concentration measured by SIMS and FTIR/ellipsometry 91
7.3.2 Homogeneity in the layer: atomic concentration measured by XPS, TEM and FTIR/ellipsometry . . . 97
7.3.3 Homogeneity in the layer: optical properties as determined by ellipsometry and spectral reflection . . 99
7.4 Passivation 100

7.4.1 Bulk passivation 100
7.4.2 Surface passivation 101
7.5 Solar Cells 104
7.5.1 Light management 105
7.5.2 Bulk passivation: low versus good wafer quality 106
7.5.3 Surface passivation 108
7.6 Conclusions 108

8 Modification of interface properties of a-SiN$_x$:H and Si to improve surface passivation 111
8.1 Introduction 112
8.2 Layer study 113
8.2.1 General a-SiN$_x$:H 113
8.2.2 Nitridation of the Si surface 116
8.3 Solar cell study 116
8.3.1 Solar cell and semi-fabric processing 116
8.3.2 Effect of doping density 119
8.3.3 Relation Q_f and implied V_{OC} 119
8.4 Modeling of the SiN$_x$:H/Si interface 121
8.5 Conclusions 122

9 The interface of a-SiN$_x$:H and Si: Linking the nano-scale structure to passivation quality 125
9.1 Introduction 126
9.2 Results 127
9.2.1 A graded interface 127
9.2.2 Nitridation, Q_f, D_{it} and K-centers 128
9.2.3 Hydrogen and D_{it} 132
9.2.4 Effect on solar cells 136
9.3 Conclusions 136

IV Background: Modeling of the a-SiN$_x$:H layer and interface with c-Si 139

10 Molecular dynamics studies of the bonding properties of amorphous silicon nitride coatings on crystalline silicon 141
10.1 Introduction 142
10.2 Methods 143
10.2.1 Generating a-SiN$_x$:H 143
10.2.2 Generating a-SiN$_x$:H/c-Si interfaces 144
10.3 Results and discussion 145
10.3.1 Bulk a-SiN$_x$:H 145
10.3.2 Clean a-SiN$_x$:H/c-Si interfaces 147
10.3.3 Gradual a-SiN$_x$:H/c-Si interfaces 150
10.4 Conclusions 152

11 Molecular dynamics studies of graded a-SiN_x:H at the interface with Si for improved surface passivation 155
11.1 Introduction 156
11.2 Computational Methods 158
11.3 Results and discussion 159
11.3.1 Fixed charge 159
11.3.2 Trap density 161
11.3.3 Effects of the gradient interface on recombination . . . 161
11.4 Conclusions 165

12 Density functional theory study of the structural and electronic properties of a-Si_3N_{4-x}:H 169
12.1 Introduction 170
12.2 Modeling Setup 171
12.2.1 Compositions, concentrations and densities 171
12.2.2 PAW potentials and technical parameters 175
12.2.3 Large simulation cells, slow annealing 177
12.2.4 Small simulation cells 178
12.3 Structural properties 180
12.3.1 Pair correlation function 181
12.3.2 Angular distribution function 186
12.3.3 Structure factor 186
12.3.4 Clustering or simple percolation 190
12.4 Electronic properties 190
12.4.1 Density of states 190
12.4.2 Inverse participation ratio 193
12.4.3 Optical band-gap 194
12.5 Conclusions 199

13 Density functional theory study of defects and defect healing in a-$Si_3N_{4-x}H_y$ 203
13.1 Introduction 204
13.2 Method 205
13.3 Results 207
13.3.1 Defect classification 207
13.3.2 Energy and defect resolved density of states 209
13.4 Discussion and conclusions 211

Summary 215

Nederlandse Samenvatting 219

Curriculum Vitae 223

List of publications **225**
Publications derived from this work 225
Journals, first author 225
Journals, co-author 225
Conferences, first author 226
Conferences, co-author 227
Other publications 227
Journals, co-author 227
Conferences, first author 228
Conferences, co-author 228

Acknowledgments (Dankwoord) **233**

Bibliography **234**

Chapter 1

Introduction

1.1 Photovoltaic market

The photovoltaic effect was discovered by Edmond Becquerel in 1839 [1], but only in 1954 the first practical solar cell was manufactured at Bell Laboratories [2]. Since, solar cells have become increasingly more efficient with growing production volume at lower costs. This can be seen in the photovoltaic (PV) module price experience curve for different types of solar modules in Figure 1.1. The price experience curve is an empirical law of price reduction and shows that per each doubling of cumulated production the specific price decreases by a nearly stable percentage: the learning rate (LR) [3]. In the PV industry the learning rate is high, as over the last 30 years this is 19.6%, allowing fluctuations for economic circumstances [4]. Recently, due to low-cost cell and module production in emerging economies (China and others) and global overproduction, prices dropped substantially to below the trend line. A high learning rate can be observed for different types of PV technologies, both for the crystalline Silicon (c-Si) modules, divided into multi-crystalline (multi-Si, mc-Si) and mono-crystalline (mono-Si), and for thin film modules. In June 2014, the global prices for all types of modules were similar, around 0.43-0.46 €/Wp [5], but regional differences exist. In the Netherlands, April 2014, c-Si modules could be bought for on average 1.09 €/Wp including taxes [6].

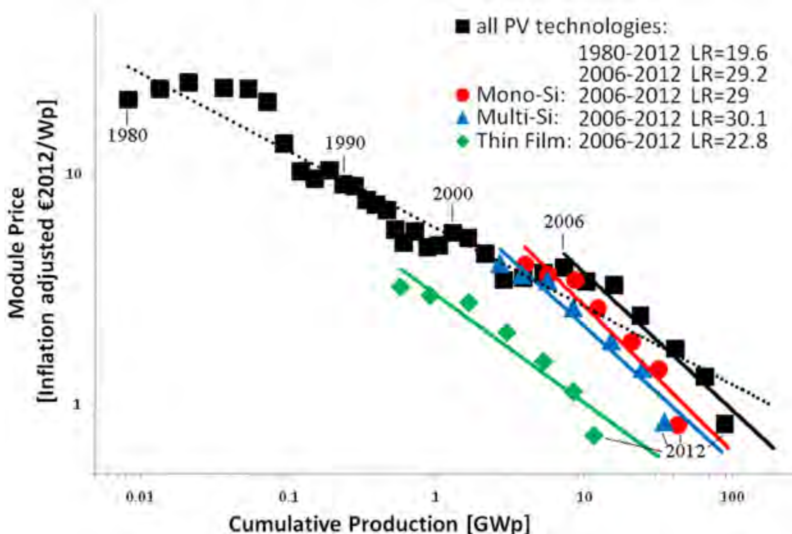

Figure 1.1: PV module price experience curve [7].

Grid parity occurs when PV can generate electricity at a levelized cost of energy (LCOE) that is equal to the price of purchased power from the electricity grid. A distinction is made between residential, commercial and industrial prices. In Figure 1.2 the LCOE of PV generated electricity is shown as it was in 2008-2013 in the Netherlands and is highlighted in grey; the width of the band signifies the range in system price, variations in financing costs of the system and the generated energy yield, which depends on the exact location of the installed system. The figure shows that grid parity, both for residential and commercial electricity prices, has already been reached in the Netherlands in 2011 and 2012, respectively [8].

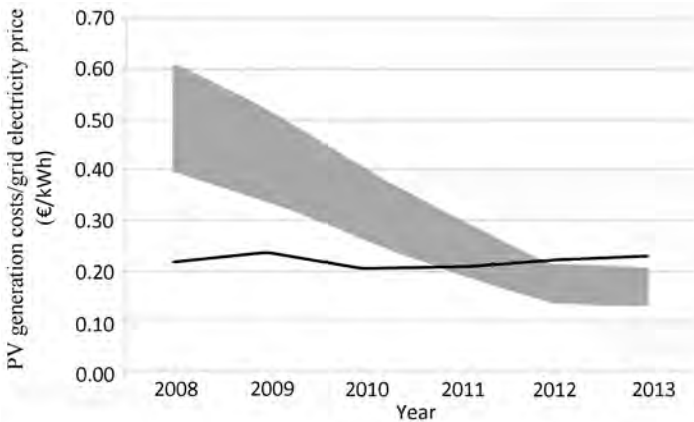

(a)

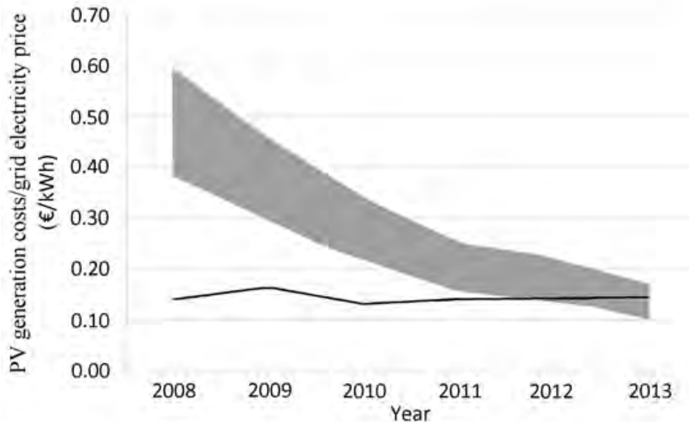

(b)

Figure 1.2: Levelized cost of energy of PV generated electricity (grey band), based on PV system prices, versus the electricity price for a) residential consumers and b) small-scale commercial consumers in the Netherlands [8].

For PV to become competitive in all markets worldwide, PV module costs (€/Wp) need to become even lower. This may either be achieved by lowering production costs per m^2 at fixed efficiency, increasing efficiency at fixed production cost per m^2 or increasing efficiency at lower production costs per m^2.

1.2 Scope of this work

To achieve higher efficiencies, various cell technologies are investigated by the solar cell community. In Figure 1.3 an overview is given of the most researched types of silicon solar cells.

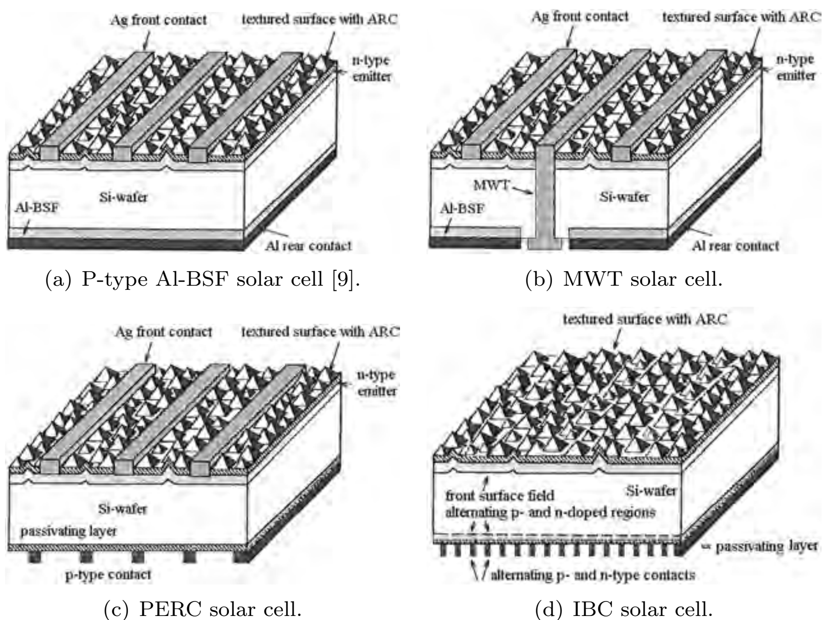

(a) P-type Al-BSF solar cell [9]. (b) MWT solar cell. (c) PERC solar cell. (d) IBC solar cell.

Figure 1.3: Overview of the most researched solar cell technologies.

The most produced solar cell is the p-type Al-BSF solar cell (see Figure 1.3a). The rear side contact of this type of solar cell is made of aluminium (Al). During the short high temperature step to create the contacts, Al and Si form an alloy. During the cool down in this step, the Si is regrown epitaxially on the surface, incorporating Al to form the back surface field (BSF). The cell further consists of a lightly doped p-type (boron) silicon (Si) wafer, which is textured on the front side to reduce reflection. The first few hundred nanometers of the front surface are highly doped with phosphorus, this is the n-type emitter. On the front surface an anti-reflection coating (ARC) is deposited to reduce reflection and to reduce charge carrier recombination at the surface (passivation). The most common layer used to achieve this is

hydrogenated amorphous silicon nitride, a-SiN_x:H. The front side is contacted by silver (Ag) lines which are spread over the surface. Charge carriers are created by the photovoltaic effect and diffuse through the wafer. Separation of charge carriers occurs at the interface between the P-doped region and the lightly doped p-type wafer. More details on the fabrication of this type of solar cell can be found in Chapter 2. The cells are integrated in a module by tabbing the front side of the solar cell to the rear of the next cell.

To improve cell interconnection in the module and reduce the metal coverage and consumption on the front side of the solar cell, holes can be drilled in the cell, through which the front side Ag metal is led to the rear side, thereby effectuating both front and rear metal contacts on the rear side. This technology is called Metal-Wrap-Through (MWT) and is illustrated in Figure 1.3b. In the MWT module, the front and rear side contacts are connected to a conductive foil using a conductive adhesive. This thesis shows how different parts of the cell can be optimized to achieve higher cell efficiencies while maintaining low production costs. Integration of these optimized cells in modules led to world record module efficiencies in 2009 and 2010.

One of the most limiting factors in increasing solar cell efficiency is the charge carrier recombination at the surfaces. To improve the surface passivation at the rear side, the Al-BSF can be replaced by a layer with improved surface passivating properties. This type of solar cell is called PERC (passivated emitter and rear cell) and is shown in Figure 1.3c. Contact to the p-type base can still be made by locally creating an Al-BSF. Variations to this concept exist where the Al-BSF is replaced by a highly doped boron region created by diffusion and this region can be contacted with Al-Ag. Such a cell concept is called PERT (passivated emitter and rear, totally-diffused). The highly doped boron region can also be only locally created underneath the metal lines, this is the PERL cell (passivated emitter, rear locally diffused).

A type of solar cell that focusses not only on improving the rear side surface passivation, but also, and mostly, the front side, is the interdigitated back contact (IBC) solar cell, shown in Figure 1.3d. In this cell design, all contacts are moved to the rear side. The p- and n-doped regions alternate and to these regions locally metal contacts are applied. The front side can be fully optimized to reduce recombination. In this work, this type of cell is also developed. It is shown, by achieving a high short-circuit current (J_{SC}) of 41.5 mA/cm^2 which is close to the maximum possible for Si-wafer based cells (42.5 mA/cm^2) [10, 11], that with low cost technologies high efficiencies are within reach.

To further enhance solar cell efficiency, surface passivation needs to be improved. The most commonly used passivating layer is a-SiN_x:H. Although commonly used, full understanding of the interface of this layer with Si is

still lacking. So far, separate tuning of the interface and bulk properties of the a-SiN_x:H layer is not possible, and usually a compromise is made. This thesis analyzes a-SiN_x:H, more specifically the physical interface, and the nanostructure is linked to the passivation quality. Moreover, it is shown how the physical properties of this interface can be modified to tune the passivation. The analysis of the physical interface and the correlated surface passivation is backed with *ab initio* density functional theory and molecular dynamics modeling studies done by international partners in research: the University of Vienna, Austria and the University of Sheffield, UK.

1.3 Outline of the thesis

This thesis is divided into four parts.

The first part provides more background of some technological aspects. In Chapter 2 the p-type Al-BSF solar cell fabrication process is described. As improvements in surface passivation are crucial to improve solar cell efficiency further, this concept is explained in Chapter 3. The various characterization techniques used in the thesis are described in Chapter 4.

The second part describes the fabrication and results on the processing of two types of high efficiency solar cells: the MWT p-type Si solar cells (Chapter 5) and the IBC n-type Si solar cells (Chapter 6).

The most common surface passivating layer is a-SiN_x:H. In the third part this material is analyzed in detail and understanding of the physical interface with Si is increased. In Chapter 7, the bulk properties of various a-SiN_x:H layers and the effects on solar cells are studied. In Chapters 8 and 9 a method to control the interface and bulk properties independently is described, including the effect on solar cells. Also, the physical interface with Si is characterized and its properties are related to the passivation quality and conditions during deposition.

The understanding of the physical interface and the correlation with passivation quality, as described in the previous part, is reinforced with modeling. In the fourth part, as background, the modeling results on the a-SiN_x:H/Si interface using force field Molecular Dynamics are given in Chapters 10 and 11. For the modeling using *ab initio* Density Functional Theory, Chapter 12 gives the results on layer properties of a-SiN_x:H, while Chapter 13 provides the results on the interface with a-SiN_x:H.

Part I

Technological aspects

Chapter 2

Description of the solar cell fabrication process

This chapter explains the silicon solar cell fabrication process. First the basic steps of the industrial p-type Si solar cell fabrication process are discussed. Several individual steps are subsequently studied in more detail in the remaining part of this chapter.

2.1 Industrial p-type Si cell process

An example of the industrial p-type Si cell process consists of a sequence of several steps and these steps are given in Table 2.1. The standard industrial p-type Si cell is schematically drawn in Figure 2.1.

Table 2.1: Industrial H-pattern solar cell processing on Si wafers.

Process sequence mc-Si cells
Saw damage removal and texturing
Emitter formation
Phosphorus glass removal and cleaning
Front-side a-SiN_x:H deposition
Screen-printing of the Ag front side, Ag rear side and Al rear-side metalization
Contact sintering and Al Back Surface Field formation during a short high temperature step (firing)
Front side laser isolation around the edge

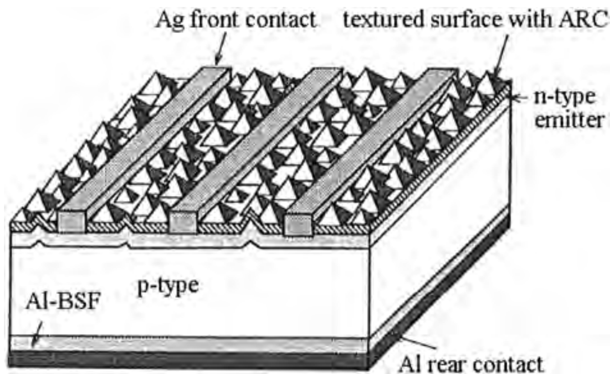

Figure 2.1: Schematic cross-section of an industrial p-type Si cell [9].

The processing begins with a bare Si wafer. The Si wafer is cut from the Si ingot using a wire sawing process. Depending on the growth process of the ingot, the wafer can consist of one (mono) or many (multi) crystals. The size of the crystals in multi-material can vary in size and is usually in the millimeter to centimeter range. During or before the growth process, boron is added, doping the wafer to a resistivity of 1-3 Ω·cm (ca. $1 \cdot 10^{16}$ cm^{-3}). The wafer is commonly cut to a thickness of about 180 µm thick and a size of 156×156 mm^2. The Si wafer surface region has a significant amount of damage due to the wire sawing process and the surface is contaminated with residual slurry used in the cutting process. The damage in the wafer usually extends to the depth of a few µm. To remove the damage and residual slurry and simultaneously texture the surface, the Si wafer is treated in alkaline or acidic baths depending on whether the wafer is respectively mono- or multi-crystalline (mc). Texturing is performed to reduce reflection losses of the solar cell.

With a high temperature diffusion step, an emitter highly doped with phosphorus is created on the front side, effectively creating a p-n junction. During the diffusion step a SiO_2 layer doped with phosphorus (phosphorus silicate glass, PSG layer) is formed on the wafer surface. This is removed by a two minute dip in about 5% HF, followed by two times one minute H_2O cascade rinse and spin drying in N_2.

Subsequently, the front side of the wafer is coated with 70-75 nm of a-SiN_x:H. This layer reduces the front side reflection and, by passivation, reduces recombination at defects at the front side of the wafer. It is also a source of hydrogen, which is released from the layer during the subsequent high temperature step (firing) and which, by passivation, reduces recombination at defects and impurities in the bulk of the wafer.

With screen-printing, silver (Ag) lines are applied to the front side, while aluminum (Al) is printed over the full rear side. On the front and rear side, Ag busbars respectively pads are present that are needed for series connection of the cells in the module. In the firing step, the glass frit in the front side Ag paste melts and etches through the a-SiN_x:H and a contact with the emitter is established. Simultaneously, at the rear side, the Si is doped with Al (6-8 µm with a doping level of $1 \cdot 10^{18}$-$1 \cdot 10^{19}$ atoms/cm^3) with on top a Si-Al layer with eutectic composition (12.5% Si and 87.5% Al). Above this eutectic layer, a thick layer of Al grains (also with eutectic composition) coated with AlO_x is present. The Si doped with Al forms the p^{++} back-surface-field (BSF). The processing is finalized by a front side laser isolation step. A laser groove is made very close to the edge of the wafer, effectively isolating the front side n^{++} emitter from the rear side p^{++}. Alternatively, after the diffusion step a single side chemical etching step is performed in which the parasitic P-doped layer is removed from the rear side, effectively isolating the front side from the rear.

2.2 Light management

In order to maximize light absorption in the Si cell to obtain the highest possible short-circuit current J_{SC}, maximum light transmission from air to the silicon wafer is required. For this, the reflection needs to be low and parasitic absorption by anti-reflection layer(s) must virtually be absent. Reflection is reduced by the formation of a texture and the application of an anti-reflection coating (ARC) on the front side of the solar cell. During the module assembly, an encapsulant, commonly made from EVA (ethylene vinyl acetate), is placed on the cells which is subsequently covered with glass. The gradual change in refraction from air, to glass and EVA, to ARC and finally the Si cell, ensures a low reflection on module level.

2.2.1 Texture

Texturing reduces overall light reflection by directing reflected rays onto a neighboring surface facet, allowing for more incident light from various angles to be transmitted into the Si wafer. This is visualized in Figure 2.2.

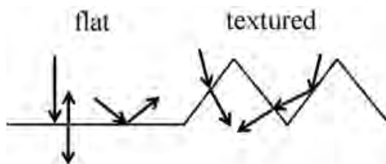

Figure 2.2: Reflection on flat and pyramid textured surface.

Industrial saw damage removal and texturing of mc-Si and mono-Si solar cells occurs in different chemical baths. Saw damage removal and texturing of mc-Si wafers are commonly performed in a single in-line acidic bath, while for mono-Si wafers these are done in two different alkaline baths in batches. The first alkaline bath has a high concentration (e.g. 5-10% KOH or NaOH at 80-90°C) for saw damage removal, while the second has a low concentration (e.g. 2.5% KOH at 97°C) for texturing.

The use of an acidic or alkaline bath is related to the crystal orientation(s) exposed on the surface of the Si wafer. A mono-Si wafer exposes only one crystal orientation, the (100) surface, while a mc-Si exposes various crystal orientations. Alkaline etchants, such as NaOH and KOH, are highly anisotropic, depending on temperature and concentration [12]. This means that the alkaline etch rate in the (100) direction is several times higher than in the (111) direction. The high anisotropy of the etch solution exposes slow etching (111) facets, thereby creating the pyramid structure. Mc-Si wafers exposed to an alkaline etchant would end up with parts of the wafers having pyramids, while other areas would be smooth. This type of etch was used on mc-Si wafers prior to the development of acidic etchants. Acidic

etchants can etch all crystal orientations more homogeneously, hence give a more homogeneous appearance, and total lower reflection. An acidic etchant consists of a mixture of HNO_3, H_2O and HF and smooths or roughens the surface depending on the composition of the mixture [13]. It is also possible to etch defects, exposed to the surface, more strongly. In general, to obtain a good acidic texture the exposed surface must be rough at start. The resultant surfaces of an alkaline etched mono-Si and acidic etched mc-Si wafer are shown in Figure 2.3. The bird eye views of the surfaces are made with Scanning Electron Microscopy (SEM). The resultant total reflection curves, measured using an integrating sphere, of a planar mono-Si, acidic etched mc-Si and alkaline etched mono-Si wafer are given in Figure 2.4.

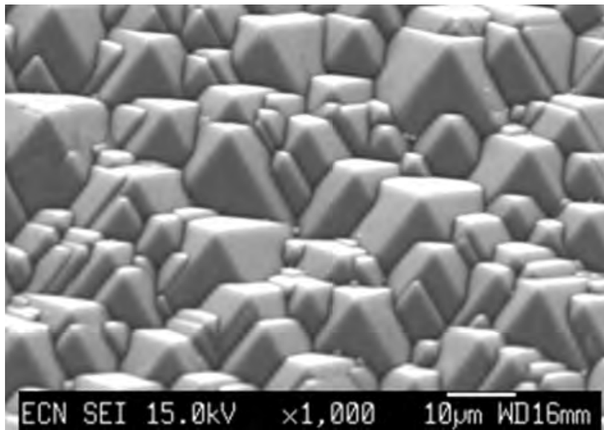

(a) Alkaline etched mono-Si surface [14].

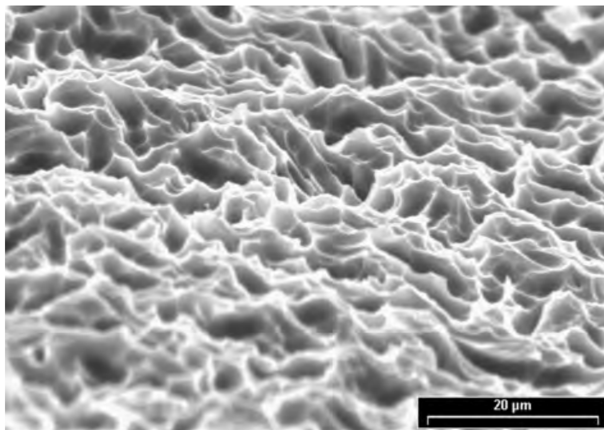

(b) Acidic etched mc-Si surface [15].

Figure 2.3: Bird eye view of etched Si surfaces.

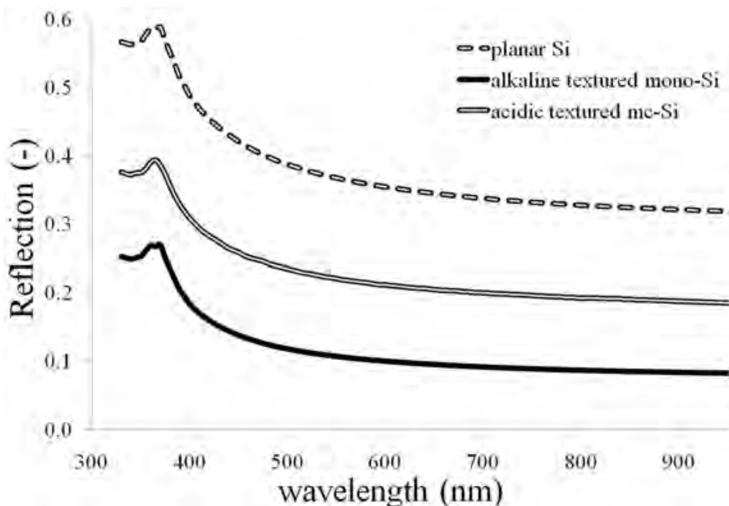

Figure 2.4: Total reflection curves of a polished, acidic etched mc-Si and alkaline etched mono-Si wafer [14].

2.2.2 Anti-Reflection Coating

Additional to the texture, an anti-reflection coating (ARC) is applied to the solar cell to further reduce reflection losses, this ARC is commonly made of a-SiN_x:H. It is not only an excellent anti-reflection coating, as it also provides bulk and surface passivation. The mechanisms of bulk and surface passivation are described in more detail in Chapters 7, 8 and 9. The optical properties of this dielectric layer depend on the deposition process conditions, which are discussed in Section 2.4 and in Chapter 7.

The optical properties can be expressed by the refractive index n and extinction coefficient k. For a-SiN_x:H layers, in which x varies between 0.18 and 1.7; n and k are shown in Figure 2.5. The data is obtained from spectroscopic ellipsometry measurements using the Tauc-Lorentz model [16]. The layers were deposited on double side mirror polished (DSP) (100) Si wafers using remote-Plasma Enhanced Chemical Vapor Deposition (remote-PECVD) equipment (MAiA) from Roth & Rau. More details on sample fabrication and analysis are given in Chapter 7.

Maximum light transmittance, and thus maximal J_{SC}, occurs if n of the ARC layer is between n of the Si wafer and air or encapsulant and glass. The effect of different a-SiN_x:H layers with respect to transmission can be modeled and the data can be used to predict the maximum J_{SC} possible [10, 11]. This is shown in Figure 2.6a for a mono-Si cell, assuming no recombination in the wafer or at the wafer surfaces and standard illumination conditions (1000 W/m^2 with spectral irradiance for an air mass of 1.5 at 25°C). Also the

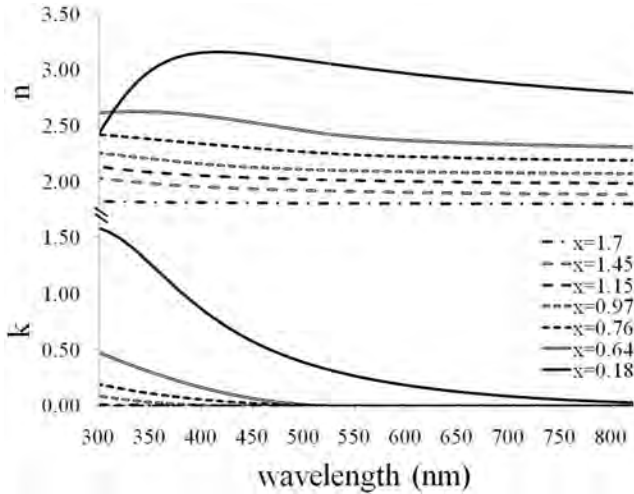

Figure 2.5: The refractive index n (top) and extinction coefficient (bottom) as function of the wavelength for various a-SiN_x:H layers.

parasitic absorption below 400 nm of industrial EVA, used to encapsulate the cells under the module glass [17], is not included. The maximal J_{SC} is 42.5 mA/cm^2 when using Si material [10, 11]. The corresponding and optimized layer thicknesses are given in Figure 2.6b. Figure 2.6 shows that a broad optimum exists for n in air, but a clear optimum at $n = 2.05$ is found when the cell is encapsulated with EVA and glass. Below this value, n becomes too close to the n of the encapsulant, while above 2.05 the parasitic absorption of the layer decreases the light transmission. Also, the required layer thickness per n differs significantly, but at $n = 2.05$ the layer thickness for in air and when encapsulated are the same. This result corresponds to what is found by others [17, 18].

The reflection of a textured mono- and mc-Si solar cell, excluding the scattered back reflection of the Ag fingers and busbars, coated with 70-75 nm a-SiN_x:H with $n = 2.05$, is shown in Figure 2.7. Also shown are the cells, excluding metal reflection, when encapsulated. This results in a significant decrease in total reflection, although the minimum reflection increases, as the glass itself has a reflection of close to 3.5 % over the full solar spectrum.

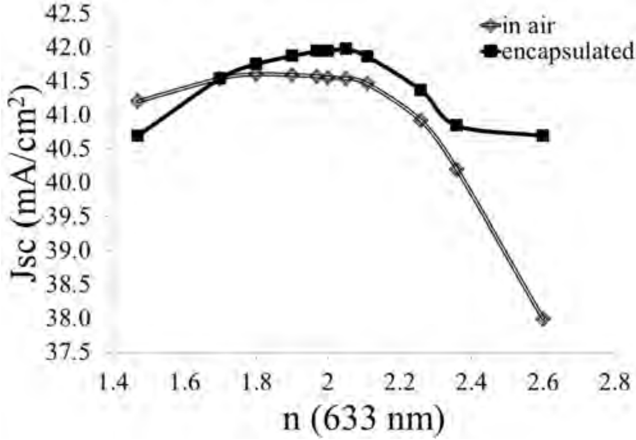

(a) Maximum J_{SC} as function of n at 633 nm.

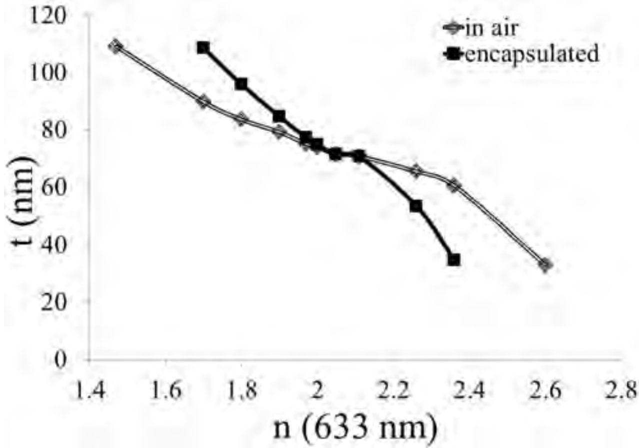

(b) Corresponding layer thickness as function of n at 633 nm.

Figure 2.6: Maximum J_{SC} and corresponding layer thickness of a-SiN_x:H as function of n (at 633 nm) for cells in air and encapsulated with EVA and glass. For n = 1.7 (at 633 nm) the data from a SiO_xN_y layer was used, for n=1.47 (at 633 nm) the data from a SiO_2 layer was used.

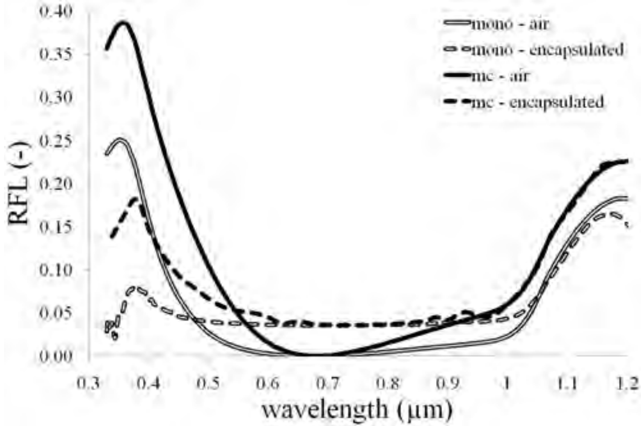

Figure 2.7: The reflection of textured mono- and mc-Si solar cells coated with 70-75 nm a-SiN_x:H with $n = 2.05$. Shown are the reflections in air en when encapsulated with EVA and glass.

2.3 Emitter formation

To allow generated electrons and holes to be collected in the solar cell, these charges need to be separated. This is done at the p-n junction, which is formed by introduction of a n-type dopant (emitter) in the p-type material. In industrial solar cell processing, the n-type element phosphorus (P) is generally used and is introduced in the silicon (Si) lattice by diffusion [19].

The diffusion process is executed in a furnace at temperatures between 800 and 900°C. The most common furnaces are either a tube furnace which uses $POCl_3$ as precursor or an in-line belt furnace which uses a H_3PO_4 deposition system as pre-station. During heating and in reaction with O_2, in both cases P_2O_5 is formed. P_2O_5 reacts with the Si surface in the following way [19]

$$2P_2O_5 + 5Si \rightleftharpoons 4P + 5SiO_2 \qquad (2.1)$$

P diffuses in both the formed SiO_2 and the Si lattice. At the interface between the phosphorus silicate glass (PSG) and Si, redistribution of P occurs due to differences in the chemical potential of P in the PSG and Si [19]. As the solid solubility of P in the growing oxide is lower than in the Si wafer, a pile-up of P at the silicon surface is formed. The pile-up depends on the rate of oxidation and amount of P and depends heavily on the precise processing conditions. Generally, due to processing conditions used, in in-line belt systems this pile up is significant, while in the $POCl_3$ process it is negligible.

Diffusion describes the process by which atoms move in a crystal lattice. An impurity in a lattice wanders in a series of random jumps. These jumps occur in all three dimensions, and a net flux of diffusing species results

if there is a concentration gradient [19]. The location of the P atoms in the Si lattice can be substitutional or interstitial. In the first case, the P atom has replaced a Si atom and occupies a lattice position in the Si crystal. In the second case, the P atom occupies a location between the lattice Si atoms. Diffusion is governed by two different mechanisms for P in Si. The first is the substitutional-interstitial ($S - I$) mechanism, which involves dopant interstitial diffusion by the kick-out and dissociative mechanism. The second is the substitutional diffusion by the vacancy mechanism [20]. Via the kick-out mechanism, the interstitial P atom moves into a substitutional site by displacing the lattice Si atom. The now interstitial Si atom is a so-called self-interstitial [19]. Via the dissociative mechanism the P atom moves from a substitutional site to an interstitial site, leaving behind a vacancy. This process depends on both the impurity concentration and crystal quality. In substitutional diffusion the P atom jumps from one lattice site to the next, if this adjacent site is vacant. Since the equilibrium concentration of vacancies is quite low, this means that substitutional diffusion occurs at a much lower rate than interstitial diffusion [19]. The mechanisms can be described by the following reactions

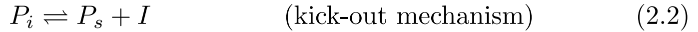

$$P_i \rightleftharpoons P_s + I \qquad \text{(kick-out mechanism)} \qquad (2.2)$$

$$P_i + V \rightleftharpoons P_s \qquad \text{(dissociative mechanism)} \qquad (2.3)$$

$$(P_s - V) \rightleftharpoons P_s + V \qquad \text{(vacancy mechanism)} \qquad (2.4)$$

where P_i and P_s denote interstitial and substitutional P impurities, and I and V are self-interstitials and vacancies; $(P_s - V)$ denotes the nearest-neighbor pair configuration in which P_s becomes mobile through site exchange with vacancies.

The different diffusion mechanisms combined cause the anomalous shape of P concentration in the diffusion profile of the emitter. In Figure 2.8 the total P concentration (N_{tot}) as determined by Secondary Ion Mass Spectroscopy (SIMS, see Section 4.1.2) on a mirror-polished (100) 1-5 Ω·cm Si wafer can be seen. Not all P is electrically active and this concentration (N_{el}) can be determined using the following empirical equation [21]

$$N_{\text{tot}} = N_{\text{el}} + 2.04 \cdot 10^{-41} N_{\text{el}}^3 \qquad (2.5)$$

The difference between the electrically active and total P concentration is electrically in-active P. Electrically in-active P consists of Si-P precipitates which act as recombination centers [22, 23].
The maximum carrier concentration and solid solubility depend on the process temperature. For process temperatures of 900°C an active carrier concentration of $3{\cdot}10^{20}$ cm^{-3} can be achieved in practical structures. Its solid solubility limit is close to 5-$6{\cdot}10^{20}$ cm^{-3} [19].

In the diffusion profile some characteristic features can be seen. The electrically active profile consists of an initial flat to gently sloped top region,

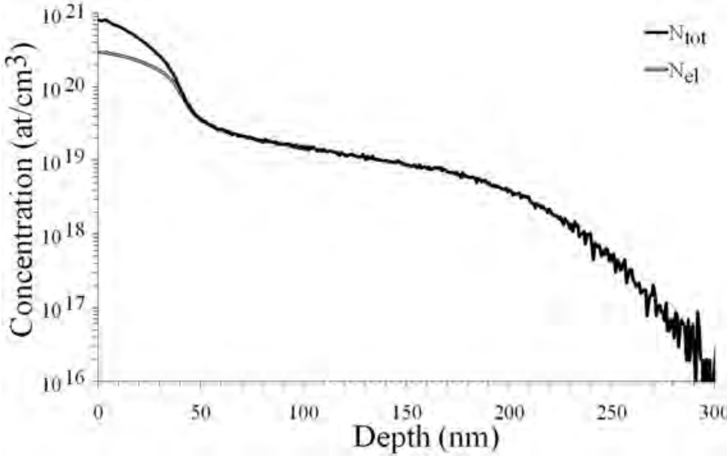

Figure 2.8: Total and active P concentration profiles as function of depth of a P-diffused emitter. Active P concentration is determined using Equation 2.5.

a kink at around $3{\cdot}10^{19}$ cm^{-3}, followed by a gently sloped region, and finally a tail part. Various empirical studies reveal relations between the diffusion profile and the diffusion mechanisms. Substitutional diffusion is dominant in the initial region where the P concentration is high and the vacancy mechanism is dominant. The region between kink and tail is governed mainly by the kick-out and to a lesser degree the dissociative mechanisms of diffusion. The diffusion in the tail region is dominated by the kick-out mechanism [20]. In addition to diffusion, P ions move by drift in the presence of an electric field. An electric field is internally generated during the substitutional diffusion of P at high doping levels. This field arises as the electrons have a much higher diffusion rate than the atoms and outrun them, creating a region containing an electric field. Due to this field the diffusivity doubles. When the P doping is less than a factor 10 higher than the base doping level, this field becomes too weak to have a significant effect on diffusion. This is thus of influence in the tail regime. Practically this means that Si wafers with a low base doping will have a deeper diffused P-profile than wafers with a high base doping [19]. Also, the diffusivities of the different mechanisms are temperature dependent, leading to different P-profiles. Diffusion at lower temperatures while extending diffusion time will lead to a shallower initial region and deeper tail, indicating that the diffusivities related to substitutional diffusion decrease faster with temperature than those related to the interstitial diffusion mechanisms [19, 20]. Furthermore, the solubility of other impurities, like Fe, is higher in the highly n-doped emitter and PSG compared to the bulk of the wafer. During the diffusion process these impurities diffuse to the emitter and PSG and are gettered there. This gettering process improves the lifetime of minority carriers in the bulk of the wafers.

While the recombination due to electrically in-active P is high, the presence of electrically in-active P is required for a good solar cell with screen-printed contacts. For this work, various emitters with different profiles were fabricated using the standard p-type mc-Si solar cell process. A strong relation is found between the maximum P concentration and the fill factor of the solar cell (*FF*). This can be seen in Figure 2.9. Relations between *FF* and other characteristic parts of the emitter profile were not found, indicating that indeed the surface doping is crucial. This relationship is not only dependent on the surface doping, but also to Ag paste used [24]. The surface doping concentration has been correlated to the Ag crystal growth on the surface [25], which explains the result found in Figure 2.9. See sections 5.4.3 and 5.4.5 for further results and process details.

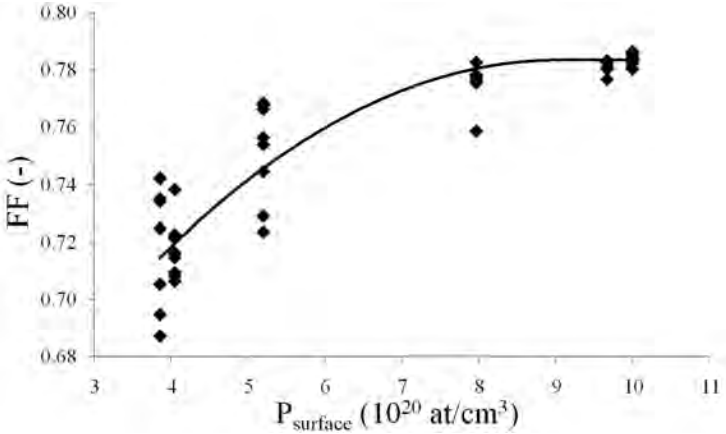

Figure 2.9: The relationship between the *FF* and the P surface doping. The line is a guide to the eye.

Often the sheet resistance (R_s) is used to characterize the emitter. The sheet resistance is related to the depth of the initial to gently sloped top region and the maximum concentration in that region [26].

2.4 a-SiN_x:H deposition

This section is divided into two parts. The first part describes the deposition technique of remote-Plasma Enhanced Chemical Vapor Deposition (remote-PECVD), while the second part describes the influence of different controllable parameters of the system on the resulting layer characteristics. The layer characteristics and the influence on the solar cell's output are described in Chapter 7. The specific interface created using remote-PECVD and the influence on the solar cell's output are described in Chapters 8 and 9.

2.4.1 Remote-PECVD

In this work, a-SiN_x:H is deposited using remote-PECVD. Two remote-PECVD systems are used, a SiNA and a MAiA system, both fabricated by Roth & Rau. The SiNA system is a prototype, while the MAiA system is an XS version of the industrial machines used in the solar cell industry. The layout of the MAiA system is shown in Figure 2.10, the layout of the SiNA system is discussed by Soppe *et al.* [27].

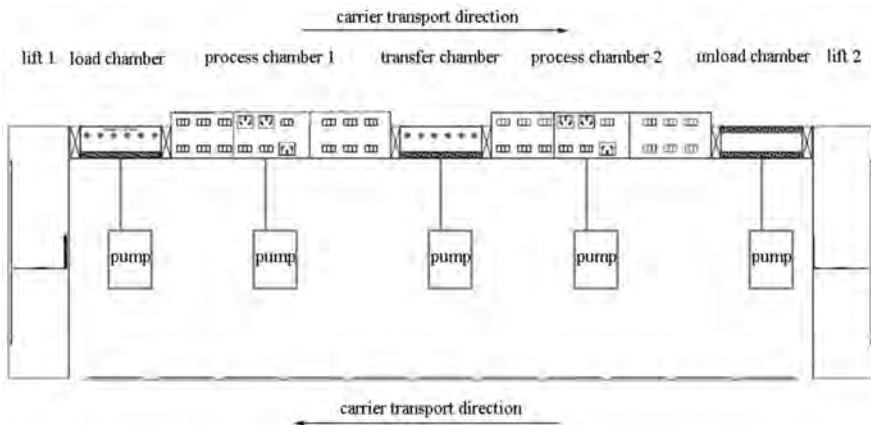

Figure 2.10: The layout of the MAiA remote-PECVD system by Roth & Rau.

In the MAiA system, the wafers are placed horizontally on the carrier tray (nine 156×156 mm^2 wafers per tray), which is positioned in lift 1. An automatic routine transports the tray through the system. In the load chamber (LC) a vacuum (10^{-3} mbar) is created, as is present throughout the system. The wafer is subsequently transported through process chamber 1 (PC1), the transfer chamber (TC), process chamber 2 (PC2) and the unload chamber (ULC). In the ULC, nitrogen gas (N_2) is purged to bring the pressure to atmospheric conditions. Subsequently, the tray is moved out and lift 2 transports the tray to ground level, where the tray is moved under the machine back to lift 1, where it is lifted again to the start position. The tray

is heated to process temperature in the transfer chamber when only PC2 is used. When also PC1 is used, the preheating is done in the LC and in the TC the temperature is maintained. Heating also is performed in the process chambers. In PC2 the a-SiN_x:H deposition is carried out. PC1 is used for the ammonia (NH_3) plasma pretreatments prior to a-SiN_x:H deposition in PC2, as described in Chapters 8 and 9. In both PCs two plasma sources for top-down and one plasma source for bottom-up deposition are available. In this work, only one top plasma source in PC1 and both top plasma sources in PC2 are used. The bottom plasma sources were not used during this study.

The layer deposition occurs in the region under the plasma source. The cross-section view and the principal mode of function of the plasma source are depicted in Figure 2.11.

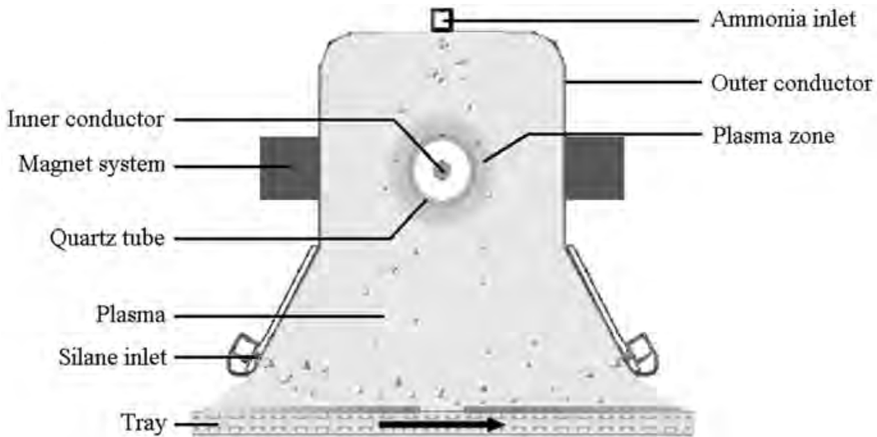

Figure 2.11: Cross-section view and principal mode of function of the plasma source for a-SiN_x:H deposition.

The linear microwave (MW) plasma source consists of a quartz tube with a Cu antenna (inner conductor) inside and is operated at a microwave frequency of 2.45 GHz. Permanent magnets are part of the system necessary for the plasma confinement. Typically, two different precursor gasses are used, NH_3 and silane (SiH_4). The NH_3 gas inlet is at the top, while the SiH_4 gas inlet is close to the wafer surface. Around the quartz tube containing the antenna a plasma is created. The reactive species from the plasma are used to deposit a-SiN_x:H on the wafers, while the tray containing the wafers moves through the plasma region. The high frequency used results in low plasma self-bias, combined with the fact that the wafers are not exposed to the plasma zone, results in hardly any ion bombardment of the wafers [28]. High depletion rates (typically more than 90%) are found for the precursor gasses, which indicates that the plasma is highly reactive.

The type of plasma in the MW system is a so-called surface wave sustained discharge. In the MW plasma source wave launchers feed the waves simultaneously from both ends of the tube. For sufficiently high microwave powers, the discharge extends along the full length of the tube and the superposition of the two linear decreasing plasma densities results in a constant axial plasma density along the entire tube, ensuring homogeneous deposition on the wafers on the tray [27]. Formation of standing waves is prevented by applying a pulsed mode for the microwave generation, in which different values for pulse duration and pulse repetition time ($t_{\mathrm{on}}/t_{\mathrm{off}}$) for opposite wave launchers are used. As the NH_3 gas inlet is above the antenna and that for the SiH_4 below, the NH_3 is dissociated in the MW plasma zone. As the gas inlet of the SiH_4 is close to the wafer surface, SiH_4 dissociation occurs both by interactions with the NH_x radicals in the plasma zone and by diffusion into the plasma zone where it can be dissociated by both NH_x radicals and electrons.

The species close to the Si surface which allow a-SiN_x:H growth on the wafer, have been identified as SiH_3 and NH_2 [27, 29, 30]. The surface Si atoms are firstly nitridated, as further described in Chapters 8 and 9, which determines the surface passivation. The subsequent a-SiN_x:H layer growth proceeds by the attachment of the SiH_3 radicals, which are subsequently nitridated by NH_2 [27, 29, 30].
The overall reaction for the formation of Si_3N_4 is [27]

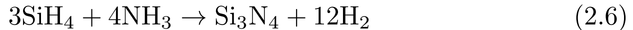
$$3SiH_4 + 4NH_3 \rightarrow Si_3N_4 + 12H_2 \tag{2.6}$$

The main dissociation chain of NH_3 is [27]

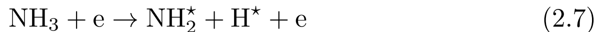
$$NH_3 + e \rightarrow NH_2^{\star} + H^{\star} + e \tag{2.7}$$

For SiH_4 the following dissociation reactions can be expected [27]

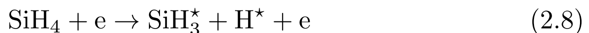
$$SiH_4 + e \rightarrow SiH_3^{\star} + H^{\star} + e \tag{2.8}$$
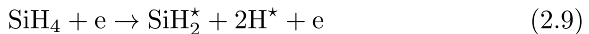
$$SiH_4 + e \rightarrow SiH_2^{\star} + 2H^{\star} + e \tag{2.9}$$
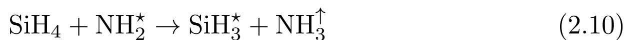
$$SiH_4 + NH_2^{\star} \rightarrow SiH_3^{\star} + NH_3^{\uparrow} \tag{2.10}$$

$$SiH_4 + H^{\star} \rightarrow SiH_3^{\star} + H_2^{\uparrow} \tag{2.11}$$

The * sign indicates that the species is a radical; the $\uparrow$ sign indicates that this species has an increased chance to escape from the plasma zone and its contribution to the deposition process is reduced. The composition of the deposited layer depends on the amount of $SiH_3^{\star}$ and $NH_2^{\star}$ present near the Si surface and is influenced by the reaction rates of the reactions described by Equations 2.8–2.11.

The total flow of gas and the ratio of gaseous species are the most important factors. With increasing SiH_4 flow, the $NH_2^{\star}$ formation rate remains

unaffected, but the rate of the reaction described by Equation 2.10 is increased, thus reducing the N content in the deposited layer [30]. For higher pressures the plasma is more confined to the quartz tube and the electron density is lower at more remote distances. This influences the deposition as for higher pressures the rates of the reactions described by Equations 2.8 and 2.9 are reduced, while the rates of the reactions near the substrate surface described by Equations 2.10 and 2.11 increase. As more NH_3 escapes from the plasma zone, more Si-rich layers are formed [27, 30]. Plasma power determines the flux of the $NH_2^{\star}$, allowing more nitrogen rich layers to grow for higher plasma power [30]. However, this is not confirmed in this work (see next section). The flux of reactive species arriving at the substrate determines the exact growth rate of the layer which is about 1-4 nm/s [28].

2.4.2 Tuning the layer characteristics

Variations in layer deposition were obtained by varying the following parameters: pressure (p = 0.1-0.5 mbar), temperature (T = 275-475 °C), total gas flow (Q = 200-1250 sccm), plasma power (P = 400-3320 W) and gas ratio NH_3/SiH_4 (R = 1-7). In all cases, the speed of the tray was kept constant, so the layer thickness found is a measure for the growth rate of the layer. Over 80 layers were fabricated and analyzed using FTIR and spectroscopic ellipsometry to extract the bond densities and optical parameters. For the analysis, the statistical program Statgraphics was used. The values of the deposition parameters of the layers were determined by iterative experiments, starting with two experiments with a screening design, followed by a response surface analysis design and finalized by optimization of the desired layer types: one with good and firing-stable surface passivating properties, one firing-stable with optimized anti-reflection and sufficient passivating properties for the front side of the solar cell.

The layer characteristics, which are found to be closely linked to each other, are the refractive index (n), extinction coefficient (k), deposited layer thickness (t), Si-N bond density, Si-H bond density, N-H bond density and Si-Si bond density. These correlations are shown in detail in Chapter 7. A higher n and a higher k are found to be correlated to a lower Si-N bond density, a higher Si-H bond density, a lower Si-H peak location in the Fourier Transform Infrared (FTIR, see Section 4.1.4) spectrum and a lower N-H bond density. Surface effects are correlated to the effective surface recombination velocity (SRV) and layer stability during the high temperature firing step affects the effective SRV after firing. The SRV is a measure for the surface passivation, a low value indicates a good surface passivation, and is explained in more detail in Chapter 3.

The main effects of the parameters, at 95% confidence level, are given in Table 2.2. In the analysis quadratic terms and interactions are taken into account. All correlations are linear, except for the effect the gas ratio has on

n and k, which shows a parabolic relation (strong quadratic term). Several interactions between parameters are found that are of influence, however these are not required for the overview and explanation of the main effects and are not given here.

Table 2.2: Main effects of varying set parameters on the layer characteristics. The varied parameters are plasma power (P), pressure (p), temperature (T), total gas flow (Q), and gas ratio NH_3/SiH_4 (R);
+ indicates a positive correlation, - a negative correlation, 0 indicates that no correlation is found; *bf* stands for before firing; *af* stands for after firing.

Characteristic	P	p	T	Q	R
n (633 nm)	0	+	0	+	-
k (400 nm)	0	+	0	0	-
t	+	0	0	+	0
SRV bf	+	-	+	+	-
SRV af	+	+	-	+	-

No effect on the layer composition is found by adjusting the power, but the growth rate increases with increasing power. As the flux of reactive species ($NH_2^\star$) arriving at the substrate is enhanced, nitridation is enhanced, which, when not controlled well, can have a detrimental effect on the *SRV*. Nitridation is the insertion of N into and adhesion of NH and NH_2 to the Si surface and will be discussed in more detail in Chapters 8 and 9.

With increasing pressure, n and k increase as the rates of the reactions described by Equations 2.8 and 2.9 are reduced, while the rates of the reactions described by Equations 2.10 and 2.11 are increased. When NH_3 is removed, more Si-rich layers are formed which have a higher n and k. Si-rich layers are less firing stable, so although the effective *SRV* before firing is decreased with higher pressure, the effective *SRV* after firing is increased.

No effect on the layer composition is found with increasing temperature. However, the temperature does have an effect on the layer stability as is indicated by the effective *SRV* before and after firing, however this effect is found to be very small compared to the effect the power and ratio have on the *SRV*. Overall, the temperature is not found to be a significant parameter in the range investigated.

The total flow is one of the most crucial parameters. With increasing flow the rates of the reactions described by Equations 2.10 and 2.11 are increased, so relatively more NH_3 needs to be added to keep constant layer characteristics (like n), so for similar R, n is increased. With increasing flow the flux of

species arriving at the substrate is enhanced, and hence the growth rate is increased. Increase of the total flow has a detrimental effect on the effective *SRV*, as the flux of the $NH_2^{\star}$ species is increased and thus the nitridation when not controlled well (see Chapters 8 and 9).

The ratio has a clear effect on both the layer characteristics and the interface structure. An increase in ratio leads to lower n, k and t. A lower t indicates a lower growth rate, and thus lower flux of the $NH_2^{\star}$ species and less nitridation, which results in a lower effective *SRV*, thus a better surface passivation.

So in general, first order adjustments of the characteristics of the layer can be done by adjusting the total flow, ratio and pressure, while surface passivation can be optimized by reducing the power and the total flow and increasing the ratio. More information on found correlations and more insight in how to tune the surface passivation further are given in Chapters 7, 8 and 9.

2.5 Contacting

In contacting of the solar cell with p-type base and n-type emitter, the approach to the front and the rear side are distinctly different. First the front side contacting is discussed, followed by the discussion on the rear side contacting.

2.5.1 Front Side Contacting

A standard front side contacting paste consists for 84-90 m% (percentage by mass) of Ag particles. The remaining 10-16 m% is solvents, organic binders and a lead oxide (PbO) containing glass frit. The paste is printed on the solar cell using screen-printing and dried at around 200°C to remove most of the solvents. During the subsequent high temperature firing step the actual contacting is done. A typical firing temperature profile is shown in Figure 2.12. The firing process takes about 1 minute. At temperatures below 550°C, the organics, mainly binders that still remained in the print, burn. At temperatures between 550°C and 700°C, the glass frit melts and wets the surface. The glass frit melt mainly consists of Pb_2SiO_4 in which Ag dissolves, creating $(PbO)_x(SiO_2)_y(Ag_2O)_z$ [31]. The melt etches the a-SiN_x:H via an oxidation and reduction reaction during which N_2 is released. Oxygen acts as a catalyst for this reaction [25]. After the complete layer is etched, the melt continues etching the Si. Due to the oxygen deficit upon etching of Si in the melt, the element that binds oxygen most weakly will fall out, this is Ag. The Ag will start to nucleate and form crystallites at the Si/a-SiN_x:H melt interface [31]. This occurs at temperatures above 700°C [25]. This also underlines the importance of the presence of oxygen during the firing process. The atmosphere used in the firing furnace is therefore typically air.

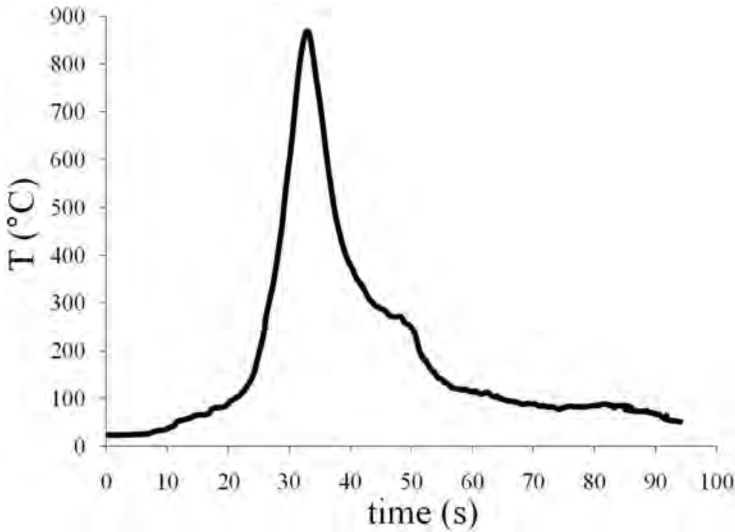

Figure 2.12: Firing temperature profile.

The electronic contact itself is believed to be created by a combination of two different mechanisms. The first is by direct contact between the Ag crystallites and the silicon or by quasi-direct connections where the glass layer is thinner than 1 nm (tunneling) [25]. The second is by tunneling through nano-Ag colloids which are present in the glass at the surface [32]. If this mechanism is dominant, good contact can be realized without crystallite formation.

2.5.2 Rear Side Contacting

Two different rear side pastes are commonly used in the solar cell production. The first is a paste that is Ag-based, which is printed as pads or full busbars, necessary in the soldering process during module integration. The composition and behavior resemble the Ag front side paste. The second paste is aluminum based and covers more than 97% of the rear side, giving a good contact and adequate surface passivation. This paste consists of about 77 m% of Al particles coated by a 150-200 nm thin Al_2O_3 layer; the remaining 23 m% are taken up by solvents, organic binders and bismuth (Bi) or Pb glass.

The Al paste is screen-printed on the cell and dried at around 200°C to remove the solvents and is subsequently simultaneously fired with the front and rear side Ag pastes. The firing process starts by burning off the organic binders. Above 660°C the glass frit and Al, within the stable particle shells, melt. While Si dissolves in the Al in the particles, Al moves out of the particles to the Si surface, forming an Al-Si liquid. On further heating more and more Si is dissolved in the liquid Al. At peak temperature the full

surface is covered by an Al-Si liquid. During cooling down, the back surface field (BSF) is formed as the Si from the melt recrystallizes epitaxially on the wafer surface, incorporating Al. As Al is a p-type dopant in Si, this newly formed layer is p^{++}-doped and effectively repels electrons, thereby passivating the rear side. The doping level of Al is between $1{\cdot}10^{18}$-$1{\cdot}10^{19}$ atoms/cm^3 depending on the maximum used temperature in the process, the BSF thickness is around 6-8 µm. Upon further cooling below the eutectic temperature of 577°C the liquid solidifies, which implies that in the originally only Al particles, now also Si is present. The remaining Al on the wafer surface will now form the eutectic layer and consists of around 12.5% Si and 87.5% Al [33, 34]. The final Al back contact consists of three main layers: the BSF, the eutectic layer and the porous Al-Si bulk. The latter consists of BiSi glass (3.3%), pores (14%) and Al-Si (87.5% Al and 12.5% Si) [34].

Chapter 3

Introduction to surface passivation

The recombination of minority carriers at the wafer surface has a detrimental effect on the performance of solar cells. To reduce this recombination, the wafer surface can be passivated by applying coatings to it; the characteristics of the interface between Si and the used coating determine the quality of the passivation. The most common deposited layer is a-SiN_x:H, but SiO_2 and AlO_x are also well known and used in solar cell manufacturing. The recombination rate at the interface, U_s, can be derived from the Shockley-Read-Hall formalism and is expressed as [35, 36]

$$U_{\mathrm{s}} = (n_{\mathrm{s}}p_{\mathrm{s}} - n_{\mathrm{i}}^2) \int_{E_{\mathrm{v}}}^{E_{\mathrm{c}}} \frac{v_{\mathrm{th}} D_{\mathrm{it}}(E) dE}{\sigma_{\mathrm{p}}^{-1}(E)(n_{\mathrm{s}} + n_1(E)) + \sigma_{\mathrm{n}}^{-1}(E)(p_{\mathrm{s}} + p_1(E))} \tag{3.1}$$

The parameters n_s and p_s are, respectively, the electron and hole density at the interface; n_i is the intrinsic carrier concentration; E_v and E_c are, respectively, the valence band edge level and the conduction band edge level, the difference defining the band gap [eV]; v_{th} is the thermal velocity of electrons; D_{it} is the density of states at the interface per energy interval [$cm^{-2}eV^{-1}$] and is directly related to the number of defects at the interface; n_1 and p_1 are statistical factors; σ_n and σ_p are, respectively, the electron and hole capture cross sections.

The recombination rate is dependent on defect levels (e.g. related to dangling bonds) which are distributed throughout the band gap. These levels are dependent on the structure and bond angles at the interface. This will be discussed in more detail in Chapters 9, 12 and 13 for the case of a-SiN_x:H and c-Si.

A common way to express the recombination, is by using the surface recombination velocity (*SRV* or S), which is defined as

$$S \equiv \frac{U_s}{\Delta n} \tag{3.2}$$

The parameter Δn is the excess carrier density [35–37].

S can be reduced by decreasing the number of interface defects (D_{it}), which is referred to as chemical passivation. S can also be reduced by decreasing the number of charge carriers, electrons and holes, as can be accomplished by an electric field and is called field effect passivation. In practice, the electric field is realized by the presence of fixed charge, Q_f, at the interface [37, 38] or by a gradient in the doping.

The presence of fixed charge at the interface leads to band bending. Three different effects of band bending can occur: accumulation, depletion and inversion. In case the majority charge carriers in the wafer are opposite in polarity to the fixed charge, the field will attract the majority carriers (increased density) and accumulation of these carriers will occur at the interface. Simultaneously, the minority carriers which are equal in polarity to the fixed charge, will be repelled from the interface (decreased density). So, S is significantly lowered. For equal polarity of the majority carriers and the fixed charge, the field will repel the majority carriers and simultaneously attract the minority carriers. Depletion of carriers occurs when the density of majority carriers at the interface is comparable to the density of the minority carriers because the field is not strong enough to repel the majority carriers sufficiently; consequently, as the density of majority carriers is not significantly lowered and the density of minority carriers is increased, S is high. Inversion of carriers occurs when the density of majority carriers at the interface is significantly lower than the density of the minority carriers, effectively making the minority carriers now the majority carriers at the interface. The difference in density between charge carriers is significant, thereby lowering S as in this case $n_\mathrm{s}p_\mathrm{s}$ (Equation 3.1) becomes small. Inversion is highly dependent on the doping level of the material. The higher the doping level, the higher Q_f must be to achieve inversion. For highly doped materials with the same polarity as Q_f the surface passivating quality will decrease because of depletion as the inversion state cannot be reached [39].

The effective minority carrier lifetime in the Si wafer, τ_eff, can be determined experimentally, see Section 4.1.7, and depends on the surface passivation quality, expressed as τ_surf, and bulk properties, expressed as τ_bulk (bulk lifetime), as follows

$$\frac{1}{\tau_\mathrm{eff}} = \frac{1}{\tau_\mathrm{bulk}} + \frac{1}{\tau_\mathrm{surf}} = \frac{1}{\tau_\mathrm{bulk}} + \frac{2S_\mathrm{eff}}{W} \tag{3.3}$$

The parameter S_eff is the effective surface recombination velocity and W is the thickness of the wafer.

S_eff and its relation to D_it and Q_f are shown in Figure 3.1 [37]. Also shown is $S_\mathrm{eff,max}$, which is defined as the value achieved for a very high value of $\tau_\mathrm{bulk} = 10$ ms. The dominant factor determining S_eff depends on the value of D_it. For low values of D_it, D_it is the dominant parameter determining S_eff, only higher values of Q_f can be seen to contribute to a significantly lower S_eff. For high values of D_it, the contribution of Q_f becomes more important in determining S_eff.

For bulk material like Float Zone material (FZ), which contains hardly any crystal lattice defects or impurities other than specifically used to dope the wafer, the bulk lifetime is only dependent on excess carrier concentration (Δn) and doping atom concentrations in the p-type (acceptor) N_A or n-type

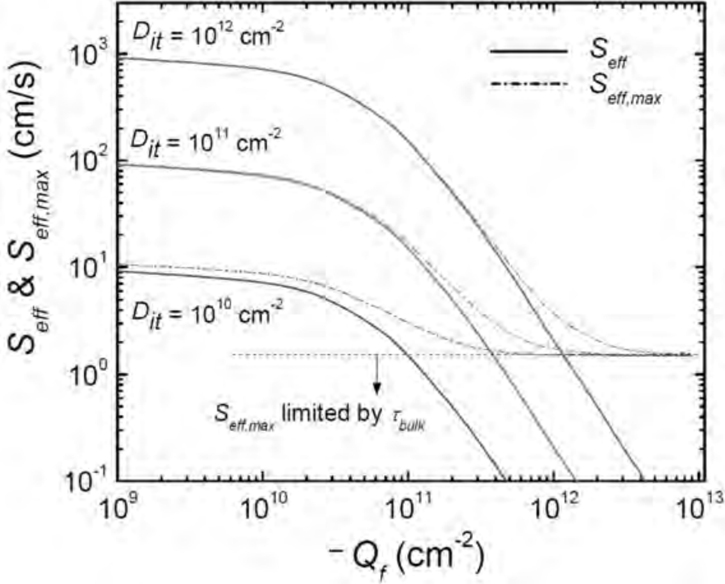

Figure 3.1: Calculated S_{eff}, $S_{\text{eff,max}}$ and the relation between Q_{f} and D_{it}, for a bulk resistivity of 2 Ω·cm p-type Si (doping of $7.2{\cdot}10^{15}$ cm^{-3}) and an excess carrier density of Δn = $5{\cdot}10^{14}$ cm^{-3} [37].

(donor) N_D material. The bulk lifetime can be calculated using the following semi-empirical formulas as found by Kerr *et al.* [40]

$$\begin{aligned}\frac{1}{\tau_{\text{bulk}}} &= (\Delta n + N_A)\left(6\cdot 10^{-25}(N_A)^{0.65} + 3\cdot 10^{-27}\Delta n^{0.8} + 9.5\cdot 10^{-15}\right)\\ \frac{1}{\tau_{\text{bulk}}} &= (\Delta p + N_D)\left(1.8\cdot 10^{-24}(N_D)^{0.65} + 3\cdot 10^{-27}\Delta p^{0.8} + 9.5\cdot 10^{-15}\right)\end{aligned} \tag{3.4}$$

For a p-type FZ wafer with a base resistivity of 2.5 Ω·cm ($N_D = 5.6{\cdot}10^{15}$ cm^{-3}) τ_{bulk} is 6.6 ms for an excess carrier concentration of $\Delta n = 1{\cdot}10^{15}$ cm^{-3}. For a n-type FZ wafer with a base resistivity of 3.5 Ω·cm ($N_A = 1.32{\cdot}10^{15}$ cm^{-3}) τ_{bulk} is 17.5 ms. It must be noted that experimentally, lifetimes above the values stated as maximum by Kerr *et al.* have been recorded, showing that the intrinsic lifetime can be higher in reality [41]. However, for common materials used in solar cells, like multi-crystalline and Czochralski (Cz) material, the bulk lifetime is much lower than in FZ material. This is due to high concentrations of impurities, like Fe, lattice defects and grain boundaries (the latter only for mc material).

Chapter 4

Experimental Methods

In this thesis different characterization methods are used, which are introduced in this chapter. Also, background information is given on the modeling approaches used in Chapters 10, 11, 12 and 13.

4.1 Characterization Methods

4.1.1 Transmission Electron Microscopy

Transmission Electron Microscopy (TEM) is a high resolution imaging method providing chemical and structural information on an atomic level. The technique uses electrons from an electron gun that are accelerated to high voltages and focused on the sample. The sample is so thin (a few tens to a few hundred nm) that it is transparent to the electrons. The transmitted electrons are used to form an image and as the sample is very thin, the beam does not fan out, allowing the resolution to be very high, approaching 0.08 nm.

Image contrast depends on scattering and diffraction of electrons in the sample. Scattering is stronger by heavy atoms than by light ones and thus provides information on the chemical structure of the sample. Bragg diffraction, due to the wave nature of electrons, occurs at the atomic planes in crystalline samples and provides structural information.

TEM has three primary imaging modes, which are bright-field, dark-field and high-resolution (HRTEM). Bright field images show only transmitted electrons and dark spots indicate heavy atoms, as these cause increased scattering. Dark-field images are made using a specific diffracted beam and thus provide structural information. HRTEM, also known as lattice imaging, gives structural information on the atomic level and is very important for interface analysis.

Due to inelastic collisions in the sample, the electrons lose energy. The measurement and analysis of the distribution of the energies of the transmitted electrons is named electron energy loss spectroscopy (EELS). The low energy loss peaks are primarily due to plasmons and in this way especially light atoms like P, O and N, can be detected. However, very light atoms like H are practically undetectable. EELS is primarily used to provide micro-analytical and structural information using the very high resolution of TEM [42].
Measurements shown in this study were made at the Technical University of Denmark (DTU) in cooperation with SINTEF, Norway.

4.1.2 Time-of-Flight Secondary Ion Mass Spectroscopy

Time-of-Flight Secondary Ion Mass Spectroscopy (ToF-SIMS) is used to analyze the composition of a material. The technique uses a pulsed primary ion beam that is focused on the sample surface removing ions from that surface. These so-called secondary ions are analyzed. The surface material is removed with steps smaller than 1 nm from an area smaller than 1 μm^2. The secondary ions are accelerated and their mass per location is determined by measuring the exact time at which the secondary ions reach the detector.

With ToF-SIMS different atoms, isotopes and molecular compounds can be detected with high accuracy (in the ppm range) and this allows elemental and chemical mapping on a sub-micron scale. However, it should be noted that only ions are detected, not neutral species. Qualitative results can be acquired for all elements. Obtaining a quantitative value of the density is not possible with the exception of a few elements like B, P, O and H. To be able to give a quantitative value for other elements and components, a reference material with known properties and density is needed to calibrate the ToF-SIMS system [42].

Accurate determination of the depth is done by using a reference sample with approximately the same matrix composition. Differences between the two samples will give an error in the depth determined. The escape depth of the sputtered atoms is a few monolayers, resulting in a small spread for the exact location where a chemical compound is found.

When comparing the chemical composition found within different materials, it should be noted that the number of secondary ions sputtered from the surface depends on the properties of the bulk material (like density) and can show strong variations. This is the so-called matrix effect and can give errors in the sputtered depth [42].

Measurements shown in this study were made at the department Test, Measurement and Analysis of MiPlaza, Philips Innovation Services in Eindhoven, the Netherlands.

4.1.3 X-ray Photoelectron Spectroscopy

X-ray Photoelectron Spectroscopy (XPS) is used to identify chemical species and states at the sample surface, enabling all elements except hydrogen and helium to be detected. X-rays (1-2 keV) are incident on the sample surface and eject electrons from the valence band. The electrons can be emitted from any orbital, including core level, for energies exceeding the binding energy. The measured energy of the ejected electron at the spectrometer, E_{sp}, is related to the binding energy E_{b}, by $E_{\mathrm{b}} = h\nu - E_{\mathrm{sp}} - q\phi_{\mathrm{sp}}$, where E_{F} is the

Fermi level, $h\nu$ is the energy of the primary X-rays, ϕ_{sp} is the work function of the spectrometer (3-4 eV) and q is the electron charge.
The found electron binding energy is characteristic for a specific chemical species and can thus be used to determine the elements involved. It is influenced by its chemical surroundings and can therefore be used to determine the chemical states of the element [42].

The emitted photoelectrons are from the top 0.5–5 nm of the sample, making XPS a surface sensitive analysis method. X-rays penetrate deeper in the sample, but electrons excited deeper in the sample cannot escape as the electrons recombine in the sample. Depth profiling is possible by ion beam sputtering or by tilting the sample [42].

Measurements shown in this study were made at SINTEF, Norway.

4.1.4 Fourier Transform Infrared Spectroscopy

Fourier Transform Infrared Spectroscopy (FTIR) is used to study fundamental vibrations and more specifically for this work to determine the bonds present in the layer as well as the densities of these bonds.

Fundamental vibrations are excitations of a molecule originally in the ground state. Normal vibrations are excitations of a molecule originally not in the ground state and are ignored in FTIR analyses. Excitations occur when infrared (IR) light that matches the energy difference between the ground and excited states, is absorbed. This absorption can be seen in the altered transmission (or reflection) spectrum of the passed (or reflected) light. The area of the absorbed peak, in the extinction coefficient (k) versus frequency (ω) plot, is a measure of the number of bonds or bond groups within the layer. Several vibrational modes have been identified for a-SiN_x:H and are listed in Table 4.1 [43].

In this work a Perkin Elmer Infrared Spectrometer, which can measure in transmission mode, is used. The samples consisted of double-side-polished (DSP) Si wafers coated with a single a-SiN_x:H layer. The extinction coefficient k is calculated by subtracting the transmission through the substrate from the sample measurement, so excluding absorption effects of the Si wafer.

The ratio between the light transmitted through the substrate/layer combination (T) and the light transmitted through the substrate (T_0) is related to k, ω and the layer thickness (t), through the Lambert-Beer law (for a homogeneous system only)

$$\frac{T(\omega)}{T_0(\omega)} = e^{-k(\omega)t} \tag{4.1}$$

The bond density can be calculated from the area of the absorbed peak in

Table 4.1: Vibration modes of a-SiN_x:H [43].

Bond	ω (cm^{-1})	K ($10^{19}cm^{-2}$)	vibration mode
Si-N	490	-	N-Si_3 stretching symmetric
	850	2	stretching asymmetric
	790	2	Si-N stretching in a locally distorted configuration
	1020	2	Si-N stretching of H-SiN_3
Si-H	630-650	-	Si-H wag-rocking
	2000-2300	2	Si-H stretching deconvoluted as:
	2000	7	H-Si-Si_3
	2060	11	H-Si-HSi_2
	2100	17	H-Si-NSi_2, Si-H surface mode
	2140	11	H-Si-SiN_2, H-Si-HSiN
	2170	40	H-Si-HN_2
	2220	20	H-Si-N_3
N-H	1150	2	N-H wag-rocking
	3340	12	N-H stretching

the $k(\omega)$ plot, using

$$[X - Y] = K \cdot \int_{-\infty}^{\infty} k d\omega \tag{4.2}$$

with $[X - Y]$ the specific bond density; ω the frequency expressed in wave numbers (cm^{-1}) and K the calibration constant.

It should be noted that the values of K for the various Si-H stretching modes are ambiguous, as they depend on the configuration and composition of the bonds surrounding the Si-H bond [44]. The other values are better defined.

For fast and accurate analysis of the FTIR spectra the in-house developed software programme "ECN FTIR fit program 1.4" by A.R. Burgers was used.

4.1.5 Spectroscopic Ellipsometry

Dielectric properties and thickness of the a-SiN_x:H layers can be determined using spectroscopic ellipsometry. Light with known and precise polarization (parallel component p and perpendicular component s) and intensity falls on the sample at a certain incident angle. The light reflected, both at the wafer surface and in the sample, will have changed polarization and intensity. The reflected light is captured and analyzed regarding the intensity and rotated p and s components.

A typical ellipsometry configuration is shown in Figure 4.1 [42, 45]. The data can be fitted by using different models, the most common ones being Urban, Sellmeier and Tauc-Lorentz [16, 46]. With the models the spectrometric refractive index (n), extinction coefficient (k) and the thickness (t) can be determined.

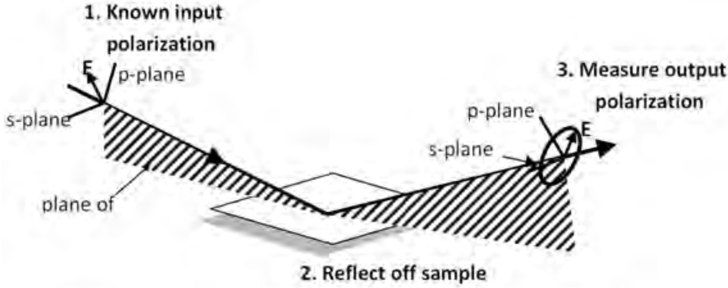

Figure 4.1: A typical ellipsometer configuration.

In this work a spectroscopic ellipsometer from Sentech was used. Measurements were performed in the range of 280-820 nm, and the data obtained between 300-820 nm was used for the fitting procedures.

4.1.6 Combining FTIR and Ellipsometry to extract atomic densities

Calculating the Si-Si bond density for a sample can be achieved by combining the refractive index n at 633 nm determined using ellipsometry and the [Si-N] bond densities found with FTIR, using [47]

$$[\text{Si-Si}] = \frac{n - n_{(\text{a-Si}_3\text{N}_4)}}{n_{(\text{a-Si:H})} - n}[\text{Si-N}] \tag{4.3}$$

with $n_{(\text{a-Si}_3\text{N}_4)}$ the refractive index of stoichiometric amorphous Si_3N_4 and $n_{(\text{a-Si:H})}$ the refractive index of a-Si:H. These values are respectively 1.9 and 3.3.
The atomic densities can now be calculated using [47]

$$\begin{aligned} [\text{H}] &= [\text{Si-H}] + [\text{N-H}] \\ 3[\text{N}] &= [\text{Si-N}] + [\text{N-H}] \\ 4[\text{Si}] &= [\text{Si-N}] + [\text{Si-H}] + 2[\text{Si-Si}] \end{aligned} \tag{4.4}$$

4.1.7 Minority Carrier Lifetime

Measuring the effective minority carrier lifetime (τ_{eff} [s]) is one of the most common methods to determine the quality of the bulk and surface passivation.

The relationship between the effective minority carrier lifetime, bulk lifetime (τ_{bulk} [s]) and effective surface recombination velocity (S [cm/s]) is [48]

$$\frac{1}{\tau_{\text{eff}}} = \frac{1}{\tau_{\text{bulk}}} + \frac{2S}{W} \tag{4.5}$$

with W the thickness of the Si wafer [cm].

The effective minority carrier lifetime can be determined using the Sinton Flashtester WCT-120 [49], which provides two options. For the first option, the system provides a fast decaying light flash, which causes an excess carrier concentration in the wafer. The induction caused by the decay of the excess carrier concentration is measured in the coil underneath the sample and is thus directly proportional to it. The data can be used to determine the effective minority carrier lifetime related to a well passivated surface. The second option the system provides is using a slowly decaying light flash, with the aim to obtain a balance between generated carriers and recombined carriers, effectively nullifying the induction caused by varying excess minority carrier concentrations (varying light intensities). The data can be used to determine the effective minority carrier lifetime related to a relatively poorly passivated surface [48, 50, 51].

4.1.8 CV-MIS

With the Capacitance-Voltage Metal-Insulator-Semiconductor (CV-MIS) method, several characteristics of the interface between Si and a dielectric insulator like a-SiN_x:H can be determined. These characteristics include the fixed charge (Q_{f}) and the density of interface traps (D_{it}), but also the resultant width of the accumulated or depleted region can be determined and the energy band diagram can be constructed [42, 52–54].

In the CV-MIS technique the capacitance (C) is measured as function of the applied gate voltage (V_G) of a Metal-Insulator-Semiconductor device. Superimposed on V_G is a small ac voltage, due to which charge is stored in the device. The total capacitance is a combination of this capacitance and the capacitance due to the fixed charge (C_{ins}) and is thus defined as: $C = C_{\text{ins}} + \frac{dQ}{dV}$. The fixed charge induces a shift from 0 V in the plot of C versus V_G, as shown in Figure 4.2, such that the location of the steep slope is transposed $\phi_{\text{ms}} + V_{\text{fb}}$. The parameter ϕ_{ms} is the difference in workfunction between the metal and the semiconductor and V_{fb} is the transposition due to the fixed charge. The typical curve appears as the capacitator is driven from inversion to accumulation conditions. The effect the D_{it} has on the capacitor is shown when this transition occurs; a more steep slope is related to lower D_{it}. The method on how to extract the exact values for Q_{f} and D_{it} are described by others [42, 52–54].

The CV-MIS response is extremely sensitive to the frequency of the small ac voltage. A low and high frequency is commonly used to extract Q_f and D_{it} [54]. However, the low-frequency measurement is very sensitive to leakage current [53] and is not suited when using a-SiN_x:H. Consequently, only the high frequency part (1 MHz) of the CV-MIS response is used in this work and interpreted using the Terman model [53–55]. In this work the device is a single a-SiN_x:H layer deposited on a double side mirror polished (DSP) FZ Si wafer, while on top of the a-SiN_x:H layer 300 nm thick aluminum (Al) gate contacts of various sizes (0.10–1.91 mm^2) are evaporated through a mask. On the full rear side of the Si wafer 300 nm Al is evaporated.

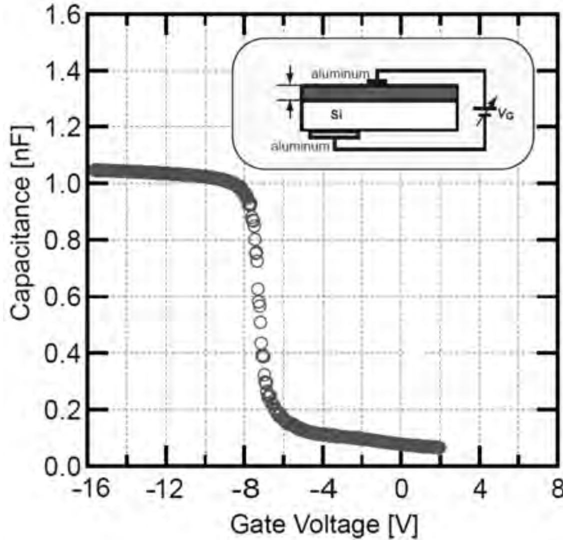

Figure 4.2: Example of a high–frequency CV-curve of the MIS capacitor.

4.2 Modeling Approaches

4.2.1 *Ab Initio* Density Functional Theory

Ab initio Density Functional Theory (DFT) is a quantum mechanical modeling method used to investigate the electronic structure of a system of atoms. The properties of a many-electron system can be determined by using functionals, which are functions of another function. In *ab initio* DFT these functionals are the spatially dependent electron densities.

Ab initio DFT is based on the quantum mechanical Thomas-Fermi (TF) theory for the electronic structure of many-body systems and improved by the two Hohenberg-Kohn (H-K) theorems. The first H-K theorem states that

ground state energy of a many-electron system is uniquely determined by the 3D-electron density. The second H-K theorem proves that the ground state electron density has minimal energy [15].

The density is obtained by integrating the wave function over the number of electrons and their positions in the system. The assumption (Kohn-Sham) that the system only consists of non-interacting electrons leads to the conclusion that the density is a summation of the wave functions of non-interacting single electron orbitals. These orbitals can subsequently be solved from the Schrödinger equation. All remaining interactions between electrons, like correlation and exchange energy, are contained in the exchange-correlation potential which is the functional derivative of the exchange-correlation energy functional, which can also be expressed in spatially dependent electron density. The energy of the system is thus completely described in functionals of the electron density [15].

In this study, *ab initio* DFT modeling is used to characterize the composition of bulk a-SiN_x:H and to examine the interface between a-SiN_x:H and c-Si. The computer program used to do the *ab initio* DFT modeling as presented in different chapters in this thesis is the Vienna Ab initio Simulation Package (VASP) [56]. The *ab initio* DFT modeling was performed by the group of the Faculty of Physics and Center for Computational Materials Science of the University of Vienna, Austria, under supervision of Prof. Dr. G. Kresse.

4.2.2 Force Field Molecular Dynamics

Force field Molecular Dynamics (MD) simulation generates atomic trajectories of a system of interacting particles, atoms and molecules. It does so by numerical integration of Newton's equation of motion, where the motion is determined by the interatomic potential energy. This reproduces the structural and conformational changes in time (nano to micro seconds), but not chemical reactions [57].

The potential energy calculations are based on two approximations. The first, the Born-Oppenheimer approximation, assumes that electrons react instantaneous to the motion of their nuclei; the second treats nuclei as point particles which follow classical Newtonian dynamics. The initial and boundary conditions, but also the ensemble and integrator parameters, are of importance for a good MD simulation. The ensemble and integrator parameters points to, respectively, the requirements on the distribution of initial conditions and the requirement that time-averaged solutions must approach the macroscopic thermodynamic average [57].

To obtain finer levels of detail, potentials based on quantum mechanics are used, where the bulk of the material is treated classically, but a small region as a quantum system, allowing it to undergo a chemical transformation [57].

In this study MD is used to examine the dynamics of the interface and adjacent area of a-SiN_x:H and c-Si. The results from the *ab initio* DFT calculations are used as input for the MD simulations. The MD simulations were performed by Dr. K.T. Butler from the Department of Materials Science and Engineering of the University of Sheffield, United Kingdom, under supervision of Prof. Dr. J.H. Harding.

Part II

High Efficiency Solar Cells

Chapter 5

17.9% Metal-wrap-through mc-Si solar cells resulting in world record module efficiency of 17.0%

M.W.P.E. Lamers[1], C. Tjengdrawira[1], M. Koppes[1], I.J. Bennett[1], E.E. Bende[1], T.P. Visser[1], E. Kossen[1], B. Brockholz[1], A.A. Mewe[1], I.G. Romijn[1], E. Sauar[2], L. Carnel[3], S. Julsrud[3], T. Naas[3], P.C. de Jong[1] and A.W. Weeber[1]

[1] ECN Solar Energy, P.O. Box 1, 1755 ZG Petten, the Netherlands
[2] REC Group, P.O. Box 594, 1302 Sandvika, Norway
[3] REC Wafer, Tormod Gjestlandsvei 41, 3908 Porsgrunn, Norway

Progress in Photovoltaics: Research and Applications **20**, 62–73 (2012).

Abstract

We obtained 17.9% cell efficiency on thin and large mc-Si REC wafers using ECN's Metal-Wrap-Through (MWT) concept. Optimization of several cell processing steps led to an increase of more than 2% absolute in cell efficiency compared with previously reported values [58]. With these cells 36-cell modules were manufactured at 100% yield in our industry scale module pilot line. The highest module efficiency obtained (as independently confirmed by JRC-ESTI) was 17.0% (aperture area), which was the world record end 2009 and early 2010 in its category. In this module the average encapsulated cell efficiency was 17.8%; the small difference demonstrates a main advantage of our integrated MWT cell and module technology.

5.1 Introduction

To reach grid parity, PV industry focuses on obtaining higher efficiencies, while simultaneously reducing material and process costs.[1] In this article we will show that this goal can be obtained with ECN's integrated metal wrap-through (MWT) cell and module concept. Both can be manufactured with a very high yield, which is another requirement to be industrially viable. To underline our motivation for developing the ECN-MWT cell and module concept, first conventional H-pattern processing and bottlenecks are explained.

Conventional solar cells are based on so-called H-pattern front side metalization: two large busbars with connecting fingers on the front side and two large busbars or pads on the full aluminum rear side.[2] In module fabrication the front and rear side of solar cells placed in series are interconnected with tabbing strips or ribbons. Several problems that reduce yield and efficiency can occur in H-pattern cell and module fabrication; some are illustrated in Figure 5.1.

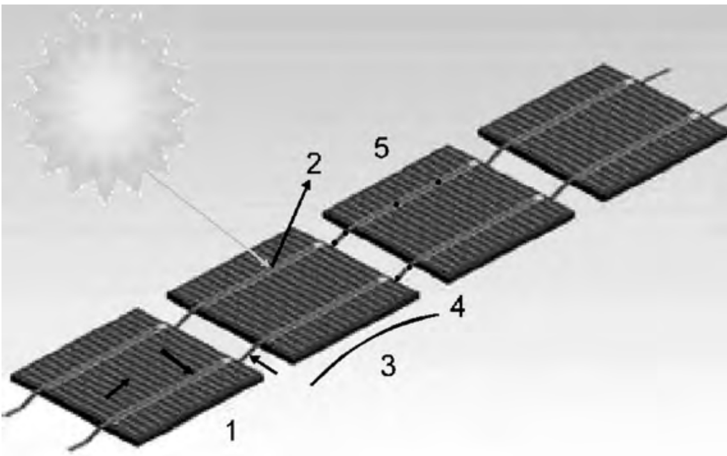

Figure 5.1: Problems in H-pattern module fabrication: series resistance in fingers and interconnection material (1), increase of shading losses if more busbars are used(2), cell bowing (3), cell breakage at edges (4) and at soldering points (5).

Higher efficiencies and related higher currents increase the series resistance losses in the module's interconnection material (1). A higher series resistance

[1] After the final submission of this paper, grid parity was reached in the Netherlands for both residential and commercial energy prices in respectively 2011 and 2012 as discussed in Chapter 1.

[2] Since the final submission of this paper, the design has been changed to the use of three and even five busbars.

loss is also caused by an increase in the finger length when larger cells are used (1). Reducing the finger length by using three busbars will generally increase the shading losses due to higher metalization coverage (2). Cell bowing due to the full aluminum rear-side metalization can lead to increased breakage during the module manufacturing process, in particular for thinner cells (3). Additional cell breakage can be expected at the edges of thin cells caused by the tabbing material used in conventional module manufacturing (4). Also, the soldering of the strips creates a highly stressed surface which may lead to increased breakages during module manufacturing (5). These drawbacks are overcome by the ECN-MWT cell and module concept. In Figure 5.2 a photo of an ECN-MWT cell is shown.

Figure 5.2: Photograph of a 243 cm^2 back-contacted MWT cell. The shown front side metalization pattern is owned by ECN.

In one cell, 16 unit cell structures (4×4) are used. In the middle of the unit cell structure a laser hole is drilled through which the emitter metal contacts are wrapped, realizing all electrical contacts on the rear. An illustration of the cross-section of the ECN-MWT cell can be seen in Figure 5.3.

Figure 5.3: Illustration of a cross-section of the MWT cell. More details are given by Weeber *et al.*, Bultman *et al.* and de Jong *et al.* [58–60].

The design of the metal patterning of the ECN-MWT solar cell is significantly different compared to MWT designs by other groups [61–63]. As already described above, the ECN-MWT cell uses unit cell structures while others use pattern design based on straight lines, resembling an H-pattern cell with very small or no busbars. In the ECN-MWT design only 16 holes are required, while others need much more holes (in the order of 100) because their design is based on lines. An additional advantage of the ECN-MWT design is that it allows a very easy up-scaling of the wafer size by a simple addition of more unit cell structures without increases in series resistance or shading losses. In previous work carried out by ECN and others [61–63], it was demonstrated that a significant gain in efficiency can be obtained using an MWT concept when compared to the conventional H-pattern processing. For the ECN-MWT cell and other MWT cell designs, the metalization front side coverage of about 5.5% resulted in a 2-3% relative gain in short-circuit current, J_{SC}, compared to an H-pattern cell with a metalization coverage of 7.5% [58–63].

For the ECN-MWT module manufacturing a low series resistance is obtained by contacting the cells to a conductive foil using a conductive adhesive. For H-pattern cells, it was already demonstrated using damp-heat and thermal-stress tests that the application of conductive adhesives between busbars and tabs provides low-stress interconnection and a highly stable contact [64]. ECN's MWT conductive foil for interconnection is covered with an isolation layer with local openings. At these locations the conductive adhesive is printed which connects the cell to the foil. This way of module fabrication of ECN-MWT solar cells results in a high yield, even for thin cells. As the cells are glued on the foil using a conductive adhesive no soldering stress or stress at the edges of the cells is present. Additionally, this method of module fabrication allows a higher packing density as no tabs are needed between the cells. Also, the required area for bussing can be omitted, as this is integrated in the function of the interconnection foil and thus no additional area is needed. The use of the conducting foil allows more efficient current collection over the whole cell area as compared to conventional 2 mm tabs. Finally, module manufacturing up to and including the lamination process can be done 3-8 times as fast (depending on module size) as conventional module fabrication. It has been demonstrated that a 2% relative gain in fill factor (FF) and a 1% relative gain in J_{SC} can be obtained at the module level [58, 65].
The module integration of these cells, where the advantage of the ECN-MWT cell concept is most evident, resulted in world record module efficiency for mc-Si of 17.0% [66]. At the time of writing, the world record module efficiency has been further increased by Kyocera using another MWT technology (17.3%) [67] and Schott Solar using an H-pattern PERC design (17.6%) [68].[3]

[3] After the final submission of this paper, the world record module efficiency for mc-Si has been further increased in recent years by Hanwha Q Cells using an H-pattern PERC design (18.5%) [69].

Cost calculations for the ECN-MWT module show PV module direct manufacturing costs of about 0.7-0.8 €/Wp[4], which is needed to enable grid parity [71].[5] Also, the IEC certificate 61215 was obtained for this method of module manufacturing [72].

5.2 ECN-MWT cell and module processing

Industrial ECN-MWT cell processing, which is based on screen-printing, closely resembles conventional industrial H-pattern processing; the main differences are the laser drilling, metalization and isolation of the holes. The cell process flow is given in Table 5.1.

Table 5.1: Industrial H-pattern and ECN-MWT solar cell processing on 243 cm^2 mc-Si wafers. The additional steps required to fabricate an ECN-MWT cell are printed in bold.

Process sequence mc-Si cells
Laser drilling of holes
Texture
Emitter formation
Glass removal and cleaning
Front-side a-SiN_x:H deposition
Screen-printing of the Ag front side, **Ag holes**, Ag rear side and Al rear-side metalization
Simultaneous firing
Laser isolation around the **holes** and edge

Cell manufacturing of the ECN-MWT cell starts with laser drilling of the holes. Removal of saw and laser damage is combined with a wet-chemical texturing step. Subsequently, emitter formation is carried out by high temperature phosphorus diffusion. After glass removal and cleaning, an a-SiN_x:H anti-reflection and passivation coating is applied on the front side of the wafer. Metallization at the front side, the holes and the rear side is done by screen-printing. The contacts are formed by a short high-temperature step (peak firing). The final step is laser isolation of the edge and around the holes.

[4]In the last few years, costs have dropped and are now around 4% lower than the production costs of H-pattern modules [70].

[5]After the final submission of this paper, grid parity was reached in the Netherlands as discussed in Chapter 1.

Module manufacturing using our automated pilot line has been reported before [73]. An illustrative image of a cell in the module, showing the different components, is given in Figure 5.4.

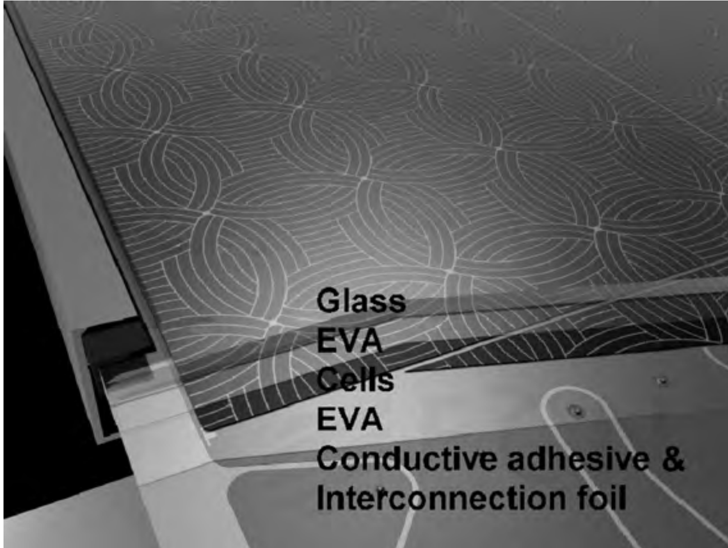

Figure 5.4: Illustrative image of the MWT module, showing the different components.

The module process flow is giving in Table 5.2. Process steps one to six can each be performed within one minute for a 60-cell module. The module build begins with the positioning of a patterned conductive foil on a carrier plate. The conductive adhesive (CA), which realizes the electrical contact between the foil and metalization of the cell, is printed on the foil. Before placement on the foil, the rear side encapsulant is perforated at the positions where the conductive adhesive is printed to allow contact between the cells and the conductive foil. Subsequently, the cells are individually picked from a stack by a robot and placed on the encapsulant and the foil such that the contacts on the cell make contact with the conductive adhesive. As a last step before lamination, the front side encapsulant and glass are placed on the front side of the cells. During lamination the encapsulation of the cells is finalized and the CA is simultaneously cured, which secures the electrical contact between the cells and the foil. This is shown in Figure 5.5. The module is finalized by the placement of the junction box and frame.

Table 5.2: Industrial ECN-MWT solar module processing.

Process sequence ECN-MWT module
Placement interconnection foil
Screen printing conductive adhesive (CA)
Puncturing rear-side sheet of encapsulant and placement on foil
Pick and place of ECN-MWT cells
Placement of front-side sheet of encapsulant
Placement of glass
Lamination
Finishing module assembly (adding junction box and frame)

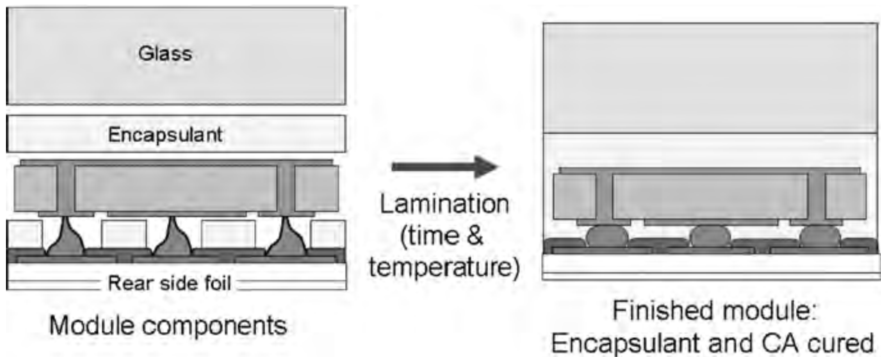

Figure 5.5: During lamination both the encapsulant and CA are cured.

5.3 Evolution of ECN-MWT cells

To show the progress made with ECN-MWT the efficiency distribution of different batches of mc-Si cells made in the last six years is depicted in Figure 5.6. This figure shows that since the first cells were processed in 2003, efficiencies have rapidly increased due to various improvements, which led to the definition of an ECN-MWT industrial process flow in 2006. The process steps for this flow are given in Table 5.1. Further optimizations in the process flow in 2008 and 2009 led to a top cell efficiency of 17.9%, an average cell efficiency of 17.8% on 36 cells and when integrated in module to a module efficiency on aperture area of 17.0%. During the same time period wafer size increased from 225 cm^2 to 243 cm^2 and cell thickness decreased from 240 µm to 160 µm. In the next section, the optimizations, made relative to the process flow as defined in 2006, are discussed.

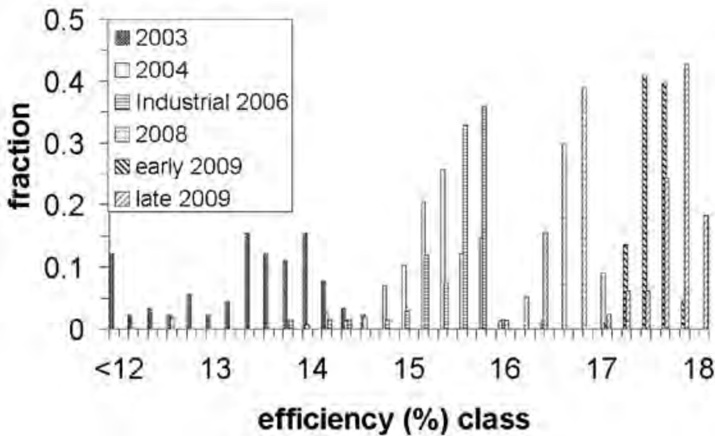

Figure 5.6: ECN-MWT efficiency throughout the years. When required, efficiencies are recalculated to the new spectrum as defined by Green *et al.* [74].

5.4 ECN-MWT cell process optimization

Between 2006 and 2009, the ECN-MWT processing has been optimized on several aspects and these are described in this section.

In all cases 1-1.5 Ω·cm 160 µm thin mc-Si p-type cells, sized 156×156 mm^2, were used, unless stated otherwise. The current-voltage (IV) measurements on cells were performed according to the ASTM-E948 standard [75] using the class AAA solar simulator at ECN and were measured or recalculated to the new spectrum as defined by Green *et al.* [74]. Implied open-circuit

voltage (implied V_{OC}) and emitter saturation current density (J_{0e}) were determined using a Sinton Consulting WCT-120 lifetime tester [76, 77]. a-SiN_x:H bond densities were determined using Fourier Transform Infrared (FTIR) spectroscopy. The bond densities were calculated by integrating the different absorption peaks over the frequency. Reflectance was measured using an integrating sphere.

5.4.1 Laser drilling of the holes

In the as-cut wafers 16 holes were drilled with a UV (355 nm) nanosecond laser system. The width variation in the holes was less than 10% and the width variation from hole to hole was less than 2%. The width of the hole is smaller than 500 µm.

5.4.2 Texturing

In previous work it was shown that the use of an improved acidic etch T2 for saw damage removal and surface texturing results in a low reflection (Figures 5.7 and 5.8) [78]. This texture gave a relative increase of 3% in J_{SC} compared to conventional acidic etch T1 on H-pattern cells. The use of the improved texture gives a similar result when applied on ECN-MWT cells.

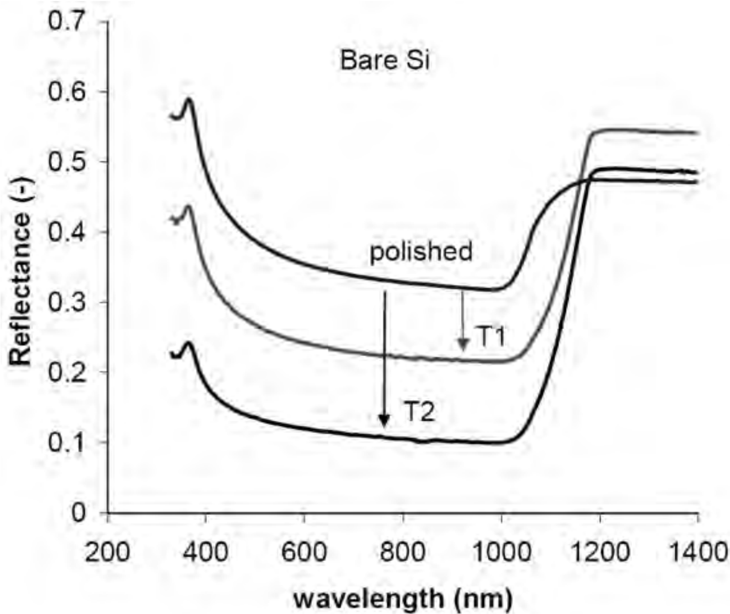

Figure 5.7: Reflectance of improved texture T2 as textured.

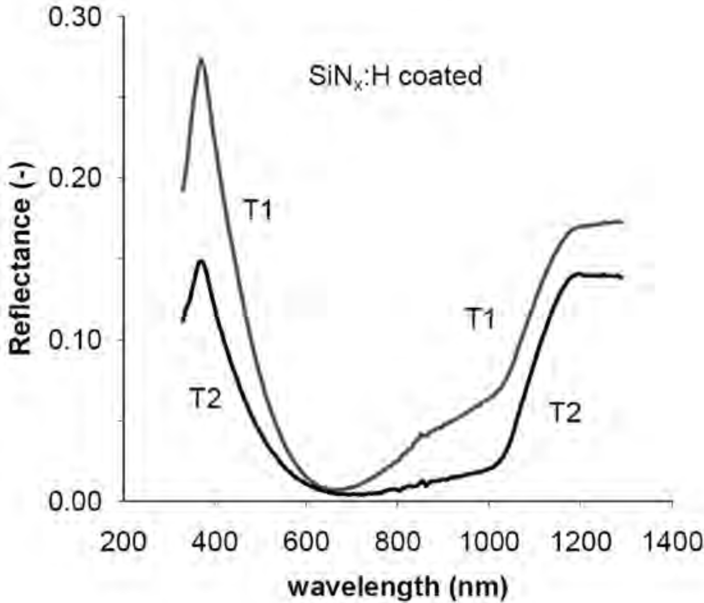

Figure 5.8: Reflectance of improved texture T2 when coated with a-SiN_x:H.

5.4.3 Emitter

The emitter determines the diode characteristics of the cell. V_{OC}, J_{SC} and FF are to a large amount dependent on the emitter quality. To improve the diode characteristics the emitter recombination current J_{0e} needs to be reduced; this will improve V_{OC} and J_{SC}. In Figure 5.9 the relation between J_{SC}/J_{0e} and V_{OC}, using the ideal diode law relation $V_{OC} \approx \ln\left(\frac{J_{SC}}{J_{0e}}\right)$, is shown for different emitters as measured on textured neighboring p-type mc-Si wafers and cells.

The determination of J_{0e} on neighboring mc-Si wafers as has been done here only serves to obtain a relative comparison and does not give an absolute value of J_{0e}, as this also includes material properties. It is also noted that the ideal diode law is not directly applicable to real solar cells. We use only the general relation between V_{OC}, J_{SC} and J_{0e} described in the ideal diode law.

A high recombination is related to a high concentration of phosphorus in the emitter. Increasingly higher doping levels result in increasingly higher Auger recombination [79]. Additionally, precipitates can form, band gap narrowing occurs and crystal defects are formed at high diffusion temperatures [80]. Reduction of the doping level will thus result in a lower recombination and therefore higher V_{OC} and J_{SC}. However, a high phosphorus doping concentration is required to secure a good contact with the metalization

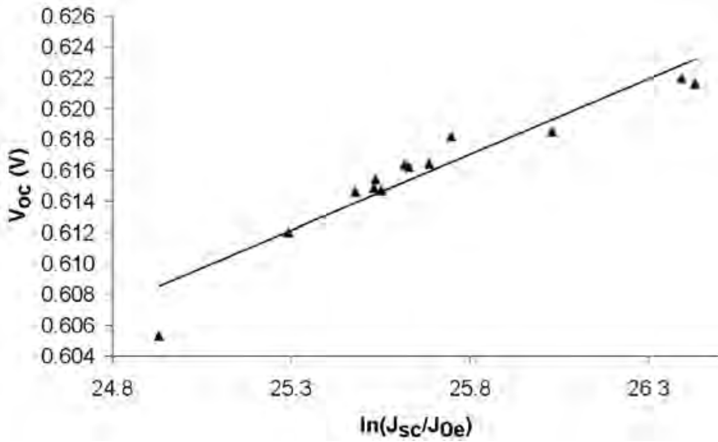

Figure 5.9: The relationship between J_{SC}/J_{0e} and V_{OC}.

and to obtain a high *FF*. The relation between the phosphorus surface concentration and *FF* as found for our emitters is depicted in Figure 5.10.

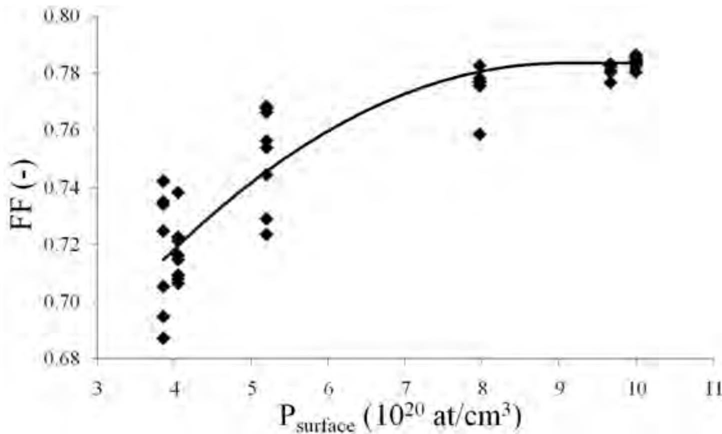

Figure 5.10: The relation between doping concentration of phosphorus at the surface and the *FF*.

Relatively simple optimization of the emitter can be done by reducing the depth of the highly doped region. In Figure 5.11 the doping profiles of two emitters are shown that have been characterized using Secondary Ion Mass Spectroscopy (SIMS), both having a high P-surface concentration. The first emitter is a conventional industrial in-line emitter which has a J_{0e} of 450 fA/cm^2 as measured on textured mc-Si. The second improved emitter is made in a $POCl_3$ tube furnace and has a J_{0e} of 275 fA/cm^2. This lower

J_{0e} is due to a significant decrease in dopant concentration at depths 30-70 nm from the surface. This lower J_{0e} resulted in an efficiency gain of 0.5% absolute, while maintaining a *FF* of 78%. The cell results are presented in Table 5.3.

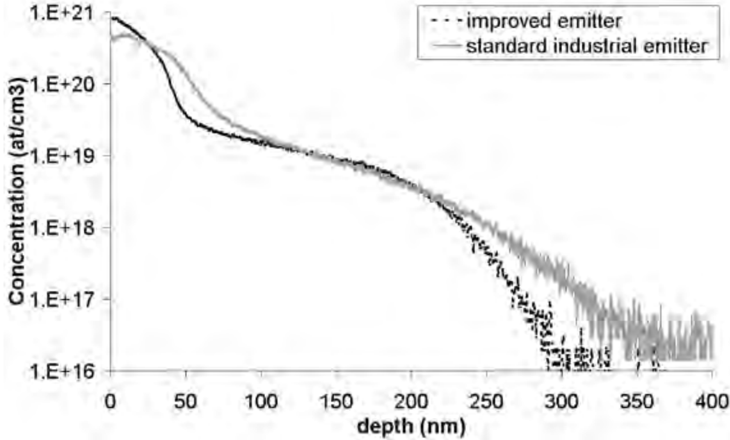

Figure 5.11: SIMS profiles of two emitters: a conventional industrial in-line emitter and an improved emitter.

Table 5.3: Cell parameters of neighboring H-pattern cells using two different emitters.

Average of nine cells	J_{SC} (mA/cm^2)	V_{OC} (mV)	*FF* (%)	Efficiency (%)
Improved emitter	34.5	615	78.0	16.6
Conventional emitter	34.0	605	78.1	16.1

5.4.4 a-SiN$_x$:H

a-SiN$_x$:H is commonly used as an anti-reflection coating. Additionally, the a-SiN$_x$:H provides bulk passivation by diffusion of hydrogen from the layer into the silicon and gives excellent surface passivation on n-type doped emitters due to both field and defect passivation. The composition of a-SiN$_x$:H can be optimized to obtain both good light in-coupling and optimal passivating qualities. The light in-coupling parameters (refractive index, thickness and low absorption) can be optimized with regards to the texture, the IQE of the cell and the glass and encapsulant used in the module fabrication. The

amount of bulk passivation required depends on the wafer quality, while the required surface passivation depends on the texture and emitter. Low quality mc-Si material needs very good bulk passivation to achieve maximum cell output; the bulk passivation property of the layer can be related to the Si-N bond density, the optimum value was found by Romijn *et al.* to be between $1.2{\cdot}10^{23}$ and $1.3{\cdot}10^{23}$ cm^{-3} as shown in Figure 5.12 [81].

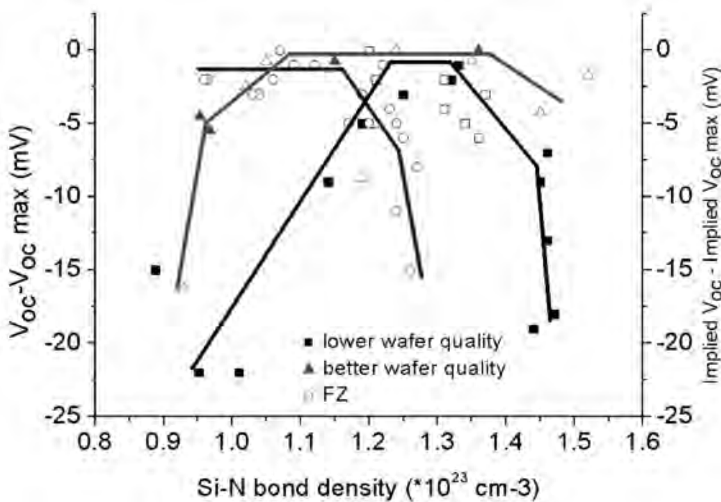

Figure 5.12: $V_{OC} - V_{OC}(\text{max})$ of mc-Si solar cells versus the Si-N bond density for lower and better mc-Si wafer quality and implied $V_{OC} - V_{OC}(\text{max})$ for half-fabricated FZ p-type wafers. The a-SiN_x:H layers were deposited using in-line Micro Wave Remote PECVD system. The lines are guides to the eye.

Lower Si-N bond densities correlate with a lower density and higher hydrogen content, whereas higher Si-N bond densities correlate with a higher density and lower hydrogen content [82,83]. An a-SiN_x:H layer with higher hydrogen content gives a very good surface passivation, but a more dense structure is required to avoid too much diffusion of H to the environment instead of to the Si bulk. Very good material quality (FZ material) does not require any bulk passivation and the (implied) V_{OC} depends primarily on the surface passivation. This requires lower Si-N bond densities below $1.15{\cdot}10^{23}$ cm^{-3}. In good quality mc-Si material a balance between bulk and surface passivation is called for, as can be seen in Figure 5.12. An optimum over a broad range for the Si-N bond density can be seen from $1.05{\cdot}10^{23}$ to $1.35{\cdot}10^{23}$ cm^{-3}.

By fine tuning the Si-N bond density as well as the light in-coupling parameters to the wafer quality, texture, emitter, IQE of the cell and the module components specific for high-efficiency ECN-MWT cells, a gain in

efficiency was achieved of at least 0.1% absolute compared to a broader range optimized a-SiN_x:H.

5.4.5 Emitter contacting

Emitter optimization is closely related to a good emitter contact. V_{OC} and *FF* can be reduced due to increased recombination at the metal-Si interface. Different screen-print pastes show different behavior. In Figures 5.13 and 5.14 this influence can clearly be seen in a comparison between two pastes on emitters with varying phosphorus surface concentration.

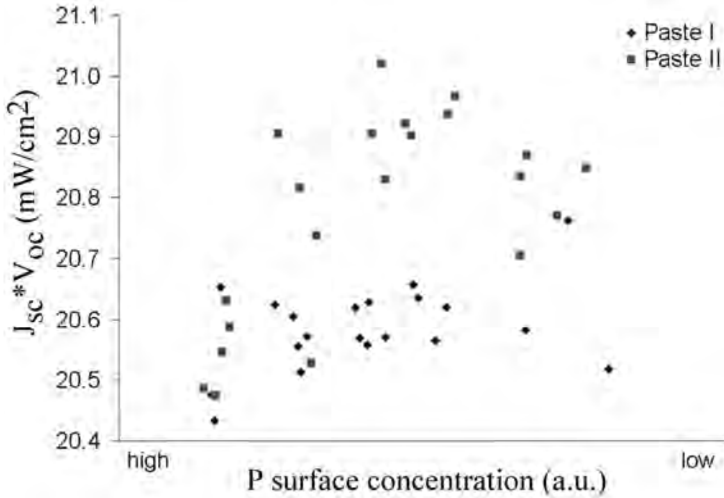

Figure 5.13: $J_{SC} \times V_{OC}$ as function of the P-surface concentration using two different front-side pastes on neighboring mc-Si cells.

Paste II shows a significantly higher $J_{SC} \times V_{OC}$, indicating that the recombination is lower at the interface between paste and emitter, while for Paste I this recombination is a clear dominant factor reducing the efficiency. In the experiment the two pastes gave similar *FF* and the line conductivity, width and height were comparable [24]. A reduction in $J_{SC} \times V_{OC}$ was observed when the phosphorus doping level of the emitter became too low. This may due to a bad contact and lower *FF* [84].

5.4.6 Metal wrap-through

The most significant difference between an ECN-MWT and an H-pattern cell is the metalization through the hole. By improving the conductivity through the holes by optimizing the metalization, the *FF* was significantly enhanced as was shown in previous work [85]. The metalization was improved by using the innovative plug paste which fills the hole with Ag. The increase

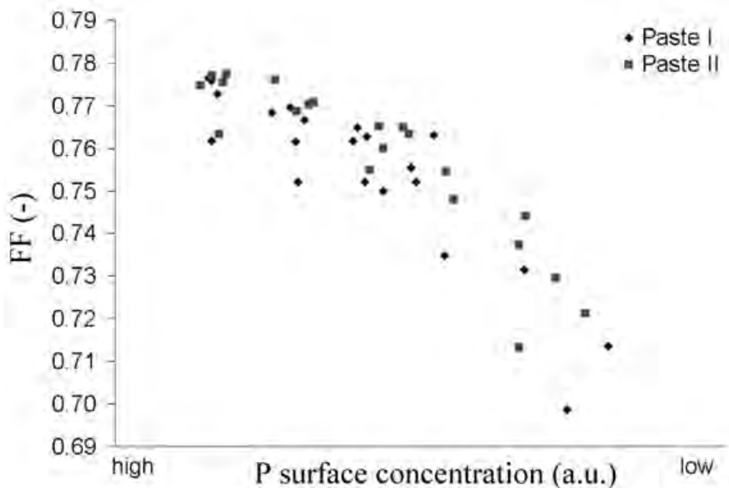

Figure 5.14: *FF* as a function of the P-surface concentration using two different front-side pastes on neighboring mc-Si cells.

in *FF* relative to the original ECN-MWT metalization as defined in 2006 (reference) is indicated in the Box-Whisker plot shown in Figure 5.15. The improved distribution of the *FF* is mostly related to significantly better process stability. The use of the plug paste is not limiting the *FF* as values up to 0.787 have been obtained with our ECN-MWT concept.

5.4.7 Rear side aluminum

The aluminum (Al) metalization on the rear side has the triple function of being the rear conductor, rear reflector and rear side passivation layer through the back-surface-field (BSF) formation. A good contact with the Ag rear pads needs to be realized, as these will be the connection points to the module foil. In Figures 5.16 and 5.17 the results of a comparison study between different Al pastes are shown.

The use of paste I and II resulted in an efficiency gain of 0.3% and 0.2% absolute compared to paste III. The gain was found in both J_{SC} and V_{OC}. In the EQE, IQE and reflection data an increase in the red response (starting at $\sim$ 900 nm) was observed. The improvements in rear side internal reflection for pastes I and II accounted for respectively relatively 0.5% and 0.3% increase in J_{SC} relative to paste III. The remainder of the efficiency increase is due to improvements in the BSF passivating quality as indicated by the IQE, shown in Figure 5.17. These improvements can be related to the quality of the pastes, for example when comparing the Al particle size. The Al particle size was significantly larger for paste II compared to paste I (unknown for paste III), while the Al percentage within the pastes was comparable and the

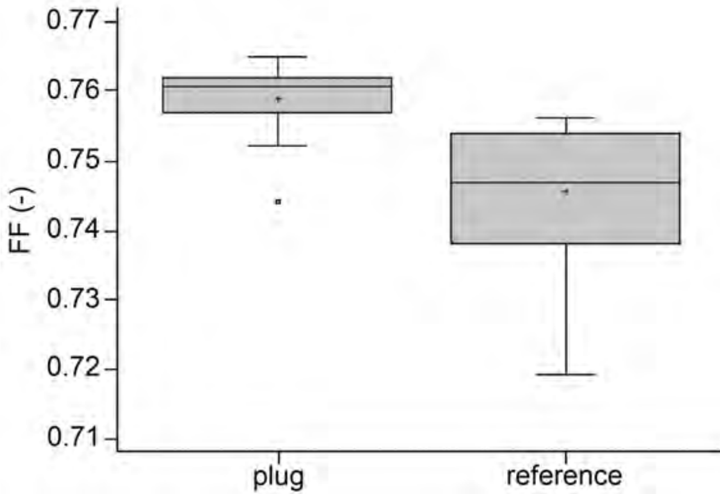

Figure 5.15: A significant improvement in FF is found when the holes are filled with an innovative plug paste as shown in this Box-Whisker plot.

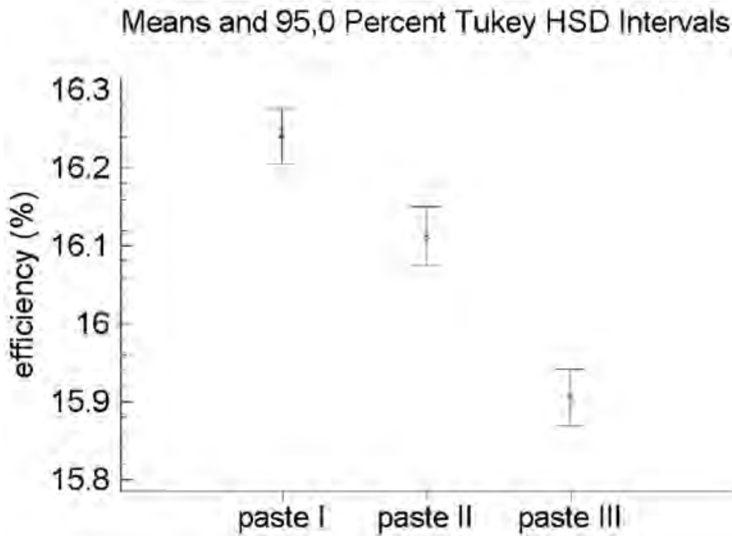

Figure 5.16: Efficiency obtained when using the different pastes.

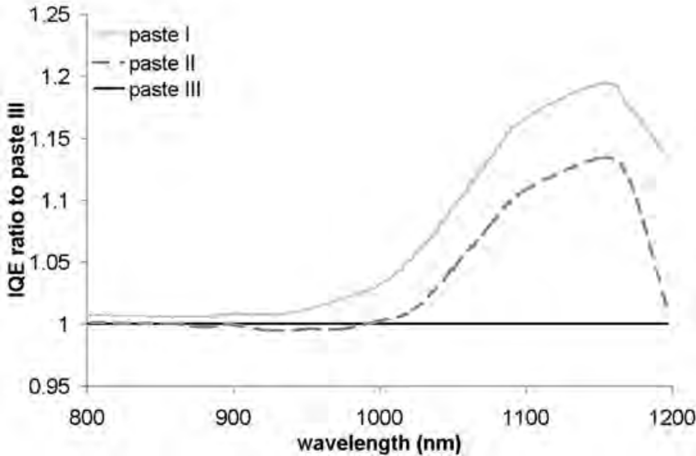

Figure 5.17: IQE ratio relative to paste III.

amount of paste applied similar. Pastes containing smaller Al particles have been shown to give a more homogeneous BSF and therefore higher J_{SC} [86].

5.4.8 Isolation

Isolation of the diode by laser scribing is a conventional method in the industry. Chemical isolation is also used as it typically leads to higher cell efficiencies. For the ECN-MWT cell, the edges and the holes need to be isolated. This means that not only the total length of laser grooves and the associated recombination is increased, but also that these recombination areas are positioned all over the cell's surface and not only at the edges. Reduction of the laser damage is thus important to improve cell output, as shown in Figure 5.18.

For the ECN-MWT cells, the standard laser process was optimized and compared to chemical isolation. Optimizing the standard laser process led to an enhanced *FF*. This can be explained by reduced laser damage as the optimized laser grooves are narrower (from 100 to 30 µm) and shallower (from 20 to 6 µm). Microscopic images of the two laser grooves are shown in Figure 5.19. The chemical isolation gave an even better performance, and led to the best fill and pseudo-fill factor.

5.4.9 Front side metalization pattern

The front side metalization pattern can be optimized when the following parameters are known: base resistance, emitter resistance, emitter contact resistance, line resistivity, line width and expected J_{SC} and V_{OC} (based on material quality and the used cell processes). Using these as input parameters

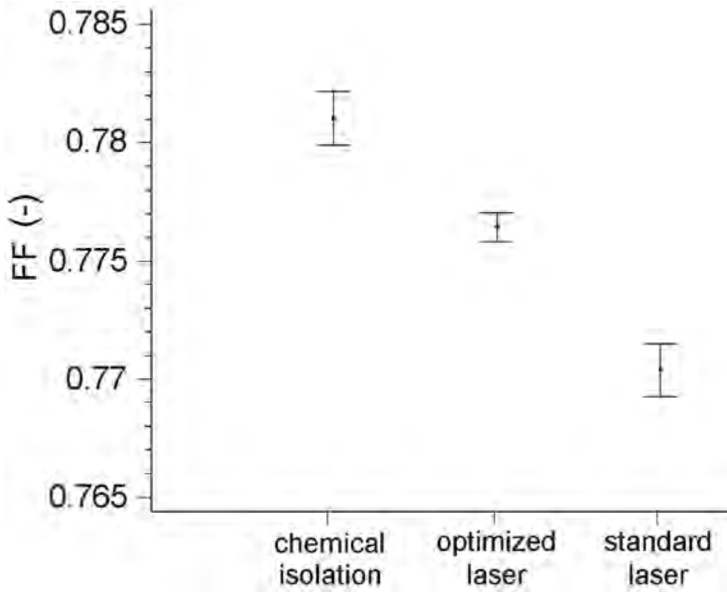

Figure 5.18: Different isolation methods and their effect on the *FF*.

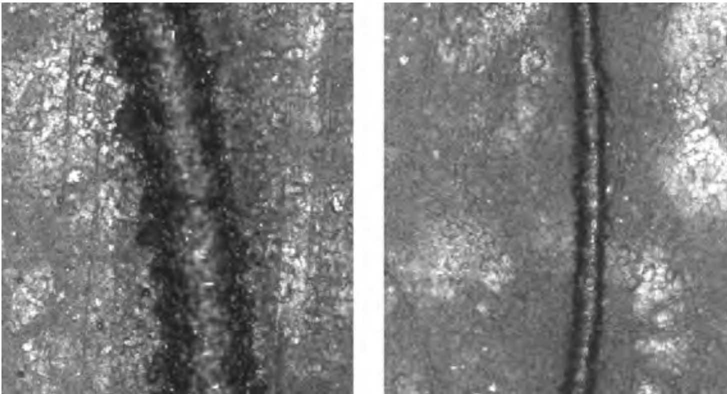

Figure 5.19: Left: Laser groove of standard laser. The groove is 100 µm wide and 20 µm deep. Right: Laser groove of optimized laser. The groove is 30 µm wide and 6 µm deep.

an optimal pattern for the ECN-MWT cells was calculated, leading to a relative reduction in the front side metalization area of close to 20% compared to the pattern as defined in 2006. This allowed an increase in $J_{SC} \times V_{OC}$ of 0.3% absolute.

5.4.10 Integration of optimized steps

Integration of all the optimized process steps, indicated by steps one to seven in Figure 5.20 and Table 5.4, should lead to an increase of close to 1.8% absolute as compared to the ECN-MWT process flow as defined in 2006. The average ECN-MWT cell efficiency in 2006 was 15.5%, therefore average cell efficiencies of 17.3% were to be expected.

Table 5.4: When separate gains in efficiency are added, an absolute increase in efficiency of 1.8% can be expected relative to the industrial process as defined in 2006.

No.	Process step	Absolute gain in efficiency (%)
1	Improve texture and lower reflection	0.3
2	Improve a-SiN_x:H anti-reflection coating	0.1
3a	Improve emitter contact	0.15
3b	Improve front-side metalization pattern	0.3
4	Improve emitter	0.5
5	Improve conductivity in holes	0.15
6	Improve p-type contact	0.1
7	Improve isolation	0.2
	Total	1.8

Integration of the found optimizations led to an average cell efficiency of 17.6% over 81 cells. This is an improvement of 2.1% absolute since 2006. The best cell had an efficiency of 17.9%. The cell efficiencies are shown in Figure 5.21.

The wafer material was p-type mc-Si provided by REC, sized 156×156 mm^2 with a base resistivity of 1-1.5 Ω·cm; the cell thickness was 160 µm. The wafer material was optimized by lowering the dislocation density. Two main reasons can be given for the discrepancy between the calculated 1.8% and the obtained 2.1%. These are the improved material quality and the positively mutual reinforcement of the multiple improvements.

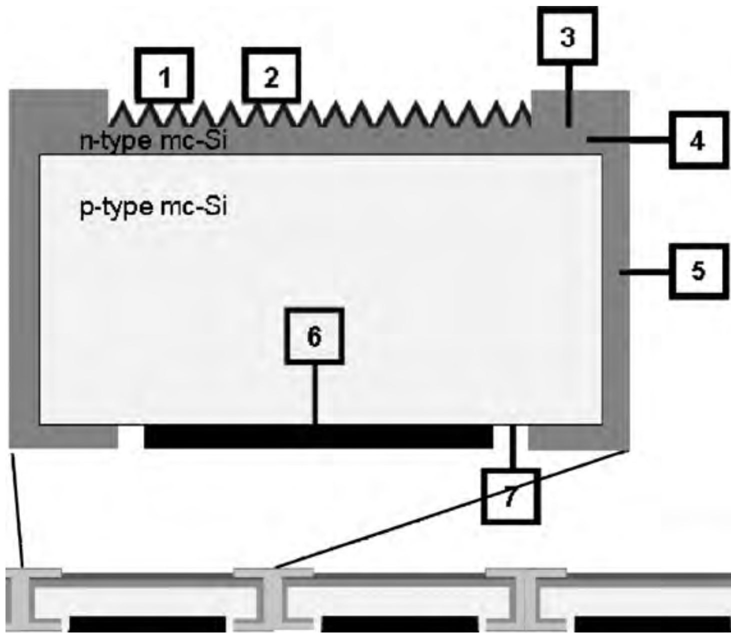

Figure 5.20: Locations of different optimizations in the ECN-MWT concept. Explanation of numbers is given in Table 5.4.

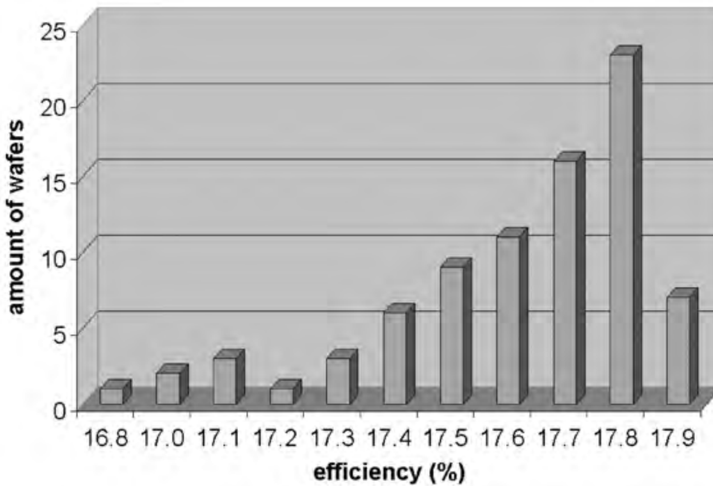

Figure 5.21: Cell efficiencies of MWT cells on REC material.

5.5 17% module efficiency

From the 81 processed cells, 36 cells were selected and integrated in a 9×4 ECN-MWT module. The module efficiency of 17.0% was independently confirmed by JRC-ESTI. Cell and module efficiencies are given in Table 5.5.

Table 5.5: Cell and module efficiencies. Cell efficiencies are measured with a class AAA solar simulator at ECN and module efficiency is independently measured by JRC-ESTI and corrected for spectral mismatch.

	Area (cm^2)	J_{SC} (mA/cm^2)	V_{OC} (mV)	FF (%)	Efficiency (%)
Best cell	243.36	36.41	0.632	77.8	17.9
Average 36 cells before encapsulation	243.36	36.37	0.631	77.4	17.8
Average 36 cells after encapsulation	243.36	36.94	0.630	75.0	17.2
Module (aperture area)	8885	36.41	22.67	75.0	17.0

The module aperture area was 0.8885 m^2. Multiple ECN-MWT modules were manufactured at ECN with 100% yield, also when thinner cells of 120 µm were used [87]. A photo of the module is shown in Figure 5.22.

The light in-coupling parameters of the cell are optimized for use under glass, allowing a higher J_{SC} in the module. Additionally, a special coating provided by Royal DSM N.V. was applied on the glass improving the light in-coupling even further, which increased J_{SC} with 1.6% absolute. Due to the high packing ratio of close to 99% in the module a very small loss of 1.4% in J_{SC} was found. Consequently, J_{SC} of the cells before encapsulation is comparable to J_{SC} of the finished module. A small loss of only 3% in FF was found due to the low resistance losses in the module components. The spectral response of an ECN-MWT cell and the module are given in Figure 5.23. It can be seen that the spectral responses are very similar, as is expected from the processing and the similar J_{SC}. The loss of wavelengths shorter than 400 nm can be explained by the absorption in the EVA.

Main losses in the ECN-MWT cell, compared to an ideal but simple spectral response are related to recombination at the surfaces, in the emitter and in the bulk of the cell, and to the non-optimal light confinement. Recombination at the front surface and in the emitter, and absorption in the a-SiN_x:H reduce the response below 550 nm. The non-optimal bulk of the cell and rear side properties (reflection and passivation) reduce the response for wavelengths above 900 nm.

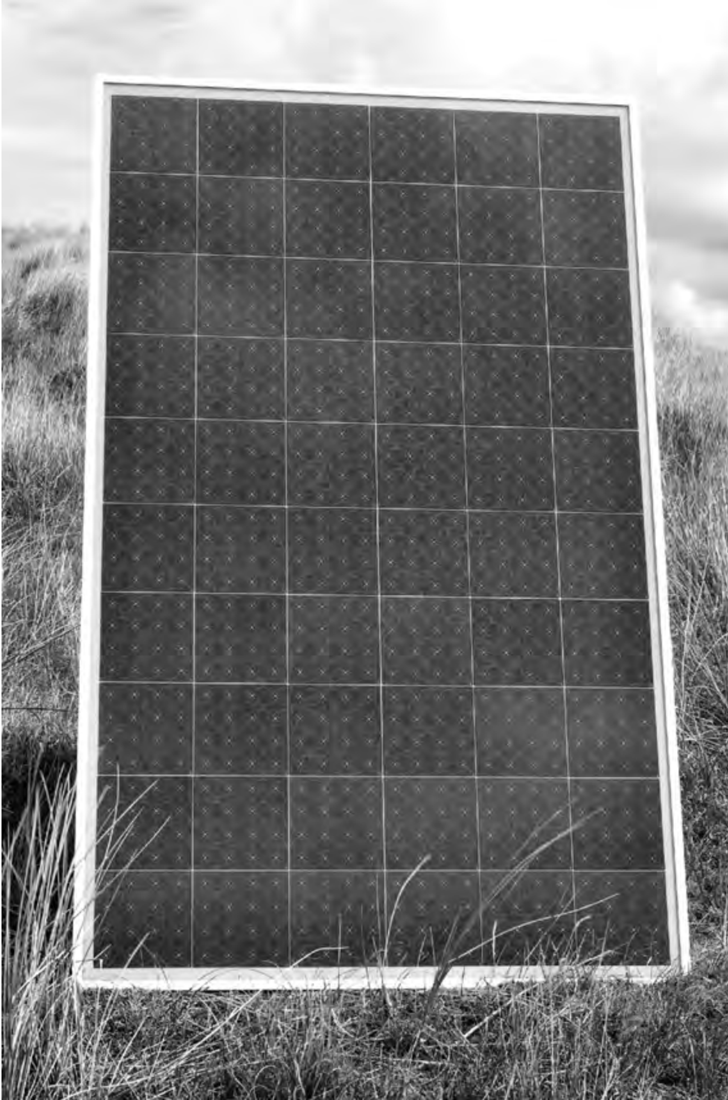

Figure 5.22: Photograph of a 60-cells mc-Si ECN-MWT module.

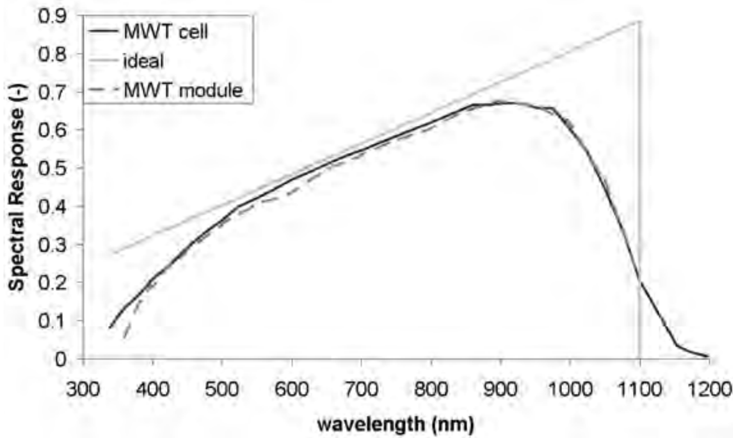

Figure 5.23: SR of an MWT cell and the MWT module. Also given is the idealized and simplified SR (QE=1).

5.6 Losses and gains

Characterization of the high efficiency ECN-MWT cells and the 17.0% module indicated three main topics in which a significant gain in efficiency can be obtained for the used material:

1. Transmission of light to improve J_{SC}.
2. Emitter recombination to improve J_{SC} and V_{OC}.
3. Rear side passivation and reflection to improve J_{SC} and V_{OC}.

5.6.1 Transmission of light

The transmission of light is reduced by several factors: on the module side by the reflection and absorption of the module glass and EVA, on the cell side by the reflection and absorption of the a-SiN_x:H and by the reflection at the cell surface.

Reflection losses on the module side can be reduced with an anti-reflection coating on the glass. The 17.0% module had a special anti-reflection coating from Royal DSM N.V. which gave a gain of 1.6% relative in J_{SC}. Absorption in the module is mostly related to EVA, which is used in conventional module manufacturing. EVA absorbs all light of wavelengths below 400 nm, which accounts a 1-2% relative loss in J_{SC} [17]. Replacing EVA with another encapsulant which absorbs significantly less, like silicone, can give a gain of 0.7-1.1% relative in J_{SC} depending on the quality of the glass and the response of the cell at short wavelength [88].

To reduce the reflection losses on the cell side an improved texture was used which increased J_{SC} with 3% relative as compared to conventional texturing [78]. To reduce reflections further, a stack of a-SiN_x:H layers with varying refractive indices can give an increase in J_{SC}. Modeling shows that an increase of at least 2% relative in J_{SC} on module level can be expected relative to the a-SiN_x:H layer currently used.

5.6.2 Emitter recombination

Emitter recombination can be reduced by integrating a selective emitter concept in the ECN-MWT processing. A selective emitter consists of a highly doped P emitter under the metal fingers to secure a good contact, while the P dopant level between the fingers is significantly reduced. With good surface passivation, reduction of the dopant level in the emitter results in a significant reduction of J_{0e} and therefore a significant increase in V_{OC} and J_{SC}. Based on modeling, a relative gain of 5% in V_{OC} and 1% in J_{SC} can be expected if the emitter recombination (including the surface) is the only limiting factor.

5.6.3 Rear side passivation and reflection

The rear side can be improved by replacing the Al-BSF with a passivating layer with a very high reflection. A SiO_x/a-SiN_x:H or SiO_x/AlO_x coating improves the rear side reflection from 77% to 90-95%, improving J_{SC} with 2.5% relative [89]. Combined with the improved rear side passivation, a total increase in J_{SC} of 3-4% has already been demonstrated. Due to the improved passivation also V_{OC} improves slightly around 1-2% relative [90–92].

Combining the different optimization steps can lead to efficiencies of over 20% on cell level and over 19% on module level. For mc-Si, 20.3% cell efficiency was demonstrated by Schultz *et al.* on small area and using special laboratory processes [93].

5.7 Conclusions

Improvements on all steps in the cell processing resulted in an efficiency increase of more than 2% absolute since 2006. The average efficiency of more than 80 mc-Si ECN-MWT cells, sized 243 cm^2, is 17.6% with a top efficiency of 17.9%.

Using 36 of these cells with an average efficiency of 17.8% a high module efficiency of 17.0% was obtained. This was the world record end 2009 and early 2010 in its category. Several modules, also using thinner cells, were made with 100% yield.

In the future, further improvements can be made in the ECN-MWT process flow by improving the front and rear side reflection and reducing the emitter and rear side recombination. With these improvements cell efficiencies over 20% and module efficiencies over 19% are within reach.

Acknowledgments This work was carried out in the framework of the Crystal Clear Integrated Project and the EOS-ES Starfire project. The EC and the Dutch AgentschapNL are both acknowledged for the financial support under respective contract numbers SES6-CT 2003-502583 and S063024. Royal DSM N.V. is acknowledged for the special anti-reflection coating on the module glass. The REC Group is acknowledged for their material and financial support.

Chapter 6

Towards 21% n-Cz IBC solar cells based on screen-printing

M.W.P.E. Lamers[1], A.A. Mewe[1], I.G. Romijn[1], E.E. Bende[1], Y. Komatsu[1], M. Koppes[1], D. Morecroft[2], M. Cascant[2], F.J. Castaño[2], A.W. Weeber[1], I. Cesar[1]

[1] ECN Solar Energy, P.O. Box 1, NL-1755 ZG Petten, the Netherlands
[2] Siliken Renewable Energy, Department of R&D, Ciudad Politécnica de la Innovación – UPV, Camino de Vera, 14 (46022) Valencia, Spain.

Proceedings of the 26th European Photovoltaic Solar Energy Conference and Exhibition, 2239-2242 (2011).

Abstract

Interdigitated Back Contact (IBC) cells have been fabricated at ECN laboratories with a best cell efficiency of 19.1%, using n-type Cz material and a process flow based on all-screen-printed patterning and metalization. Excellent current collection due to an optimized FSF is demonstrated by a J_{SC} value as high as 41.5 mA/cm^2, corrected for spectral mismatch, and a V_{OC} of 641 mV. The results show high pseudo fill factors (PFF) of above 81% but lower fill factors (FF) of below 72%.

6.1 Introduction

Driven by market pressure to increase cell efficiencies and decrease production costs, we have developed a process flow for Interdigitated Back Contact (IBC) cells which is compatible with low-cost industrial processes. The process flow comprises conventional screen-printing steps for patterning and metalization, avoiding more expensive approaches such as lithography [94–96].

High efficiencies (>20%) can be achieved in IBC cells mainly because all current collection contacts are located at the rear, which eliminates the problem of front shading losses. A schematic cross section of the IBC cell can be seen in Figure 6.1.

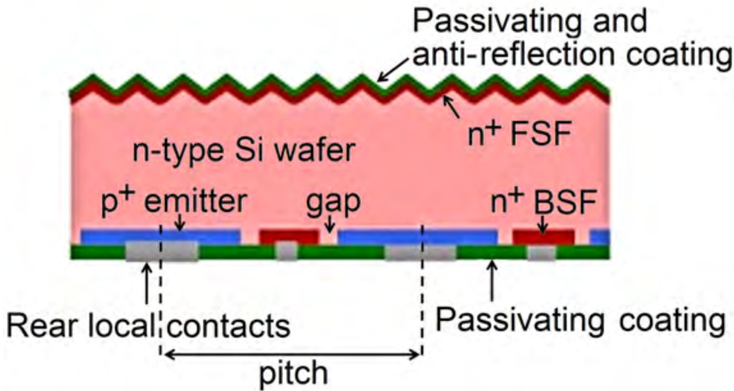

Figure 6.1: Schematic cross-section of an IBC cell, indicating the Front Surface Field (FSF), n^+-Back Surface Field (BSF), p^+-emitter, contacts and passivating layers. The definition of pitch and gap at the rear are also included. All contacts are located at the rear.

Although optical shading losses are eliminated, recombination losses occur in the regions without emitter as the transport distances towards the emitter become comparable to the local diffusion length. This effect is referred to as electrical shading [97]. To reach the high cell efficiencies, the device structure requires excellent surface passivation at the front and rear sides, as well as well-defined patterning of both n-and p-type regions at the rear of the cell and a high bulk lifetime (>1 ms). Narrow and abrupt contact areas will result in reduced resistive and recombination losses. These losses are determined by the minimum feature size, which is limited by the patterning method used. The top-down solution of lithography is able to achieve close to ideal contact regions but the current process is too expensive for high-volume manufacturing. On the bottom-up end, screen-printing is well demonstrated in PV manufacturing and it is therefore important to evaluate the limits in the efficiencies of IBC cells fabricated using this approach.

Since the emitter in IBC cells is located at the rear, an almost ideal surface passivation is required at the front as most charge carriers are created close to that interface. The formation of a high-quality Front Surface Field (FSF) is necessary, which should provide a shielding field effect with no added Auger recombination and the FSF should be well-passivated with a dielectric layer.

In this paper we present the IBC cell made at ECN using tube furnace diffusions, wet-chemical etching and cleaning, a PECVD and screen-printing (patterning and metalization) process steps alone. The efficiency limits of cells made with the fabrication process presented, are evaluated by studying the influence of the pitch and emitter fraction, and the effect of unpassivated contacts.

6.2 Solar Cell and Process Description

In Figure 6.2 the process flow used to fabricate the IBC cells at ECN is shown.

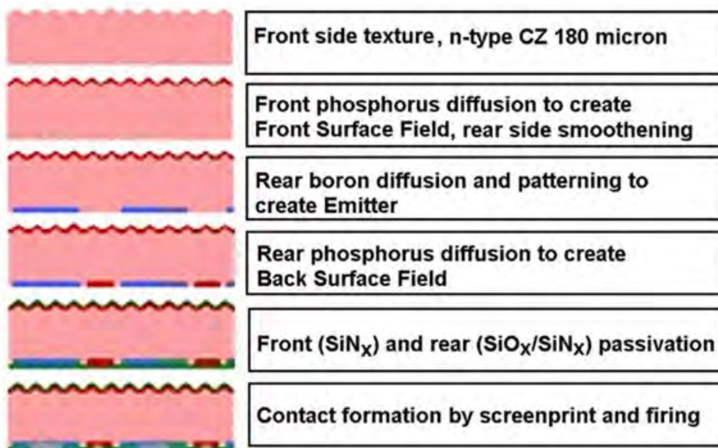

Figure 6.2: Process flow used for fabricating >19% interdigitated back contact solar cells at ECN.

To enable optimal light confinement, the front surface of the cells is textured (random pyramids) using alkaline etching while the rear surface is smoothened which also improves passivation. This wet-chemical process is followed by the FSF diffusion, mainly to reduce the recombination at the front side [98]. After FSF diffusion, the steps include masking, diffusion and patterning of the boron emitter and phosphorus BSF at the rear surface. Shunting is avoided by separating the emitter and BSF by a non-diffused gap. To ensure high efficiencies, front and rear side passivation need to be excellent. The IBC cells require a rear surface passivation solution for three different surfaces:

the highly doped p-type emitter, the highly doped n-type back surface field and the lightly doped n-type base. For this, the full rear side is passivated using a stack of SiO_2/a-SiN_x:H. The front side is passivated using a single layer a-SiN_x:H coating on top of the FSF. Subsequently, metalization on the BSF and emitter regions is done by screen-printing and contacting of both regions is achieved simultaneously by a short high temperature firing step. All patterning and metalization steps were executed using low-cost screen-printing methods. Contacting was achieved by so-called firing-through using an inline belt furnace. Depending on the pitch size, the metalization fraction on the rear side was varied between 7.5 and 11.3%, excluding busbars.

6.3 Solar Cell Optimization

Several aspects of the IBC solar cell can be optimized and in this paper results of various optimizations are presented. These include the FSF, the pitch and the emitter fraction. For the fabrication of the cells 3-4 Ω·cm n-type Cz grown Si material was used, for which the bulk lifetime exceeded 1 ms.

6.3.1 Front surface field optimization

The function of the front surface field is to reduce the recombination at the front side and improve lateral transport.[1] Recombination in the FSF should be minimal and the optimal n-type doping level was found to be $3{\cdot}10^{18}$ atoms/cm^3 [101–103]. Improved lateral transport by the FSF becomes increasingly important for larger pitches and higher base resistivity. For this, the optimal resistance for the FSF was found to be 150 Ω/sq. These specifications indicate that the FSF profile should be deep, close to 1 µm. In order to fabricate this by diffusion in an industrial process, a long process time is required which is undesired. For moderate to low bulk resistances and small pitches the additional value of the FSF for lateral transport is of less importance. Under these circumstances, a lightly doped and shallow FSF, with a high resistance in combination with good surface passivation, will give the highest cell output [98]. These specifications allow a short diffusion time in an industrial process.

At ECN 2D simulations of the FSF using Microtec software were performed. The related output of the IBC cell were modeled as a function of the surface doping level, depth and the surface recombination velocity (S) at the a-SiN_x:H/Si interface. For the simulations a pitch of 2 mm, emitter fraction of 90%, a bulk lifetime of 1 ms and a Gaussian diffusion profile of the FSF were assumed. In Figure 6.3 these modeling results are given for the FSF with a depth of 310 and 940 nm. It can be seen that J_{SC} is optimal at doping

[1] It should be noted that electrical shading is not reduced by using a n-type FSF, but can be reduced by application of a p-type front floating emitter [99, 100].

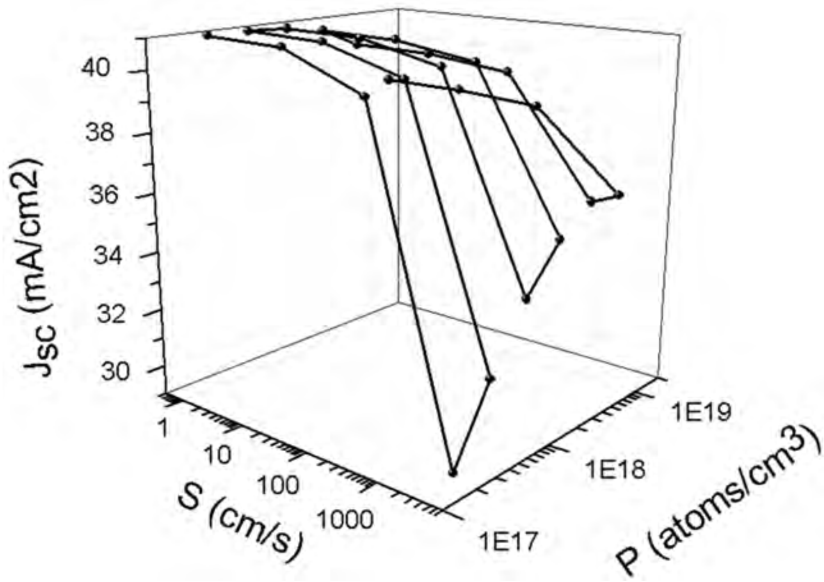

(a)

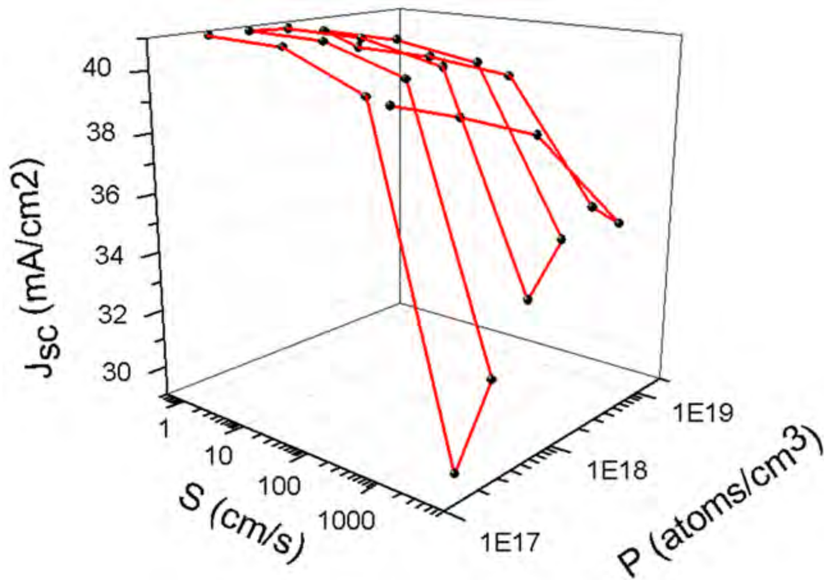

(b)

Figure 6.3: The relationship between the surface doping of the FSF (P), surface recombination velocity (S) and J_{SC} for a FSF which is a) 310 nm or b) 940 nm deep.

levels of $3{\cdot}10^{18}$ atoms/cm^3 for a wide range of S values, which shows that for this doping level the processing is expected to be most stable in terms of surface passivation. It was found that J_{SC} decreases for doping levels below $1{\cdot}10^{17}$ atoms/cm^3. The modeling also showed that for this surface doping level variations in depth of the FSF do not have a significant effect on J_{SC}. Furthermore, the modeling demonstrated that for a deeper FSF, J_{SC} more steeply declines for higher doping levels. This indicates that in processing a shallow FSF is more stable and will lead to higher J_{SC} on average.

Taking note of the increasing required processing time with increasing depth of the FSF and the more optimal process stability for a shallow FSF, it was therefore decided to use a shallow and a high resistance FSF with a surface doping level of $3{\cdot}10^{18}$ atoms/cm^3 which had a J_0 of 44 fA/cm^2 as measured on textured n-type Cz wafers. The sheet resistance was so high that it did not contribute to lateral transport. This FSF should lead to maximal J_{SC} and an optimal IQE.

6.3.2 Emitter fraction and pitch optimization

As shown in Figure 6.1, the rear side consists of the BSF, the emitter and the gap. The fraction of each region can be varied. The fractions multiplied by the pitch give the widths of the different regions. We present here the average of 10 cells per pitch and per emitter fraction. In Figures 6.4 and 6.5 the effect on V_{OC} and J_{SC} for two different emitter fractions is given. A clear improvement in J_{SC} is found for a larger emitter fraction. This is due to a reduction in recombination of minority carriers as the collection area is increased and the required diffusion distance of minority carriers is thus reduced. The values for V_{OC} are comparable to values found for other high efficiency screen-printed n-type Cz solar cells [104].

Using light beam induced current (LBIC) measurements, the Internal Quantum Efficiency (IQE) response of the cell can be mapped. In Figure 6.6 the IQE scan of one of the best IBC cells is shown for a wavelength of 976 nm. In Figure 6.7 a line scan of this image is given. This cell had a pitch of 2 mm, an emitter fraction of 80% and a BSF and gap width of 400 µm. A high IQE of 97% can be seen in the region of the emitter (blue), in the region of the BSF this is 82% (orange/red), with intermediate values in the gap (green). This difference of 15% is due to the electrical shading losses. This is significantly lower than was found by others who used a larger BSF and gap region [97, 98]. The lower IQE in the BSF region indicates that the passivation needs to be improved. The high doping levels of the BSF, required for good contacting, reduce the passivation of this region [105].

In Figure 6.8 the effect on the FF for three different pitches is given. No effect by the BSF width, gap width and emitter fraction on the FF was observed. A relatively low FF was found with a maximum value of 71.8%,

which decreased as contact spacing increased. Combining commonly reported FF values of around 79% with the obtained values for J_{SC} and V_{OC} in this work, would result in cell efficiencies well above 21%. The low FF is subject of our research effort. An estimate of the contribution of the series resistance is presented by Cascant *et al.* [96].

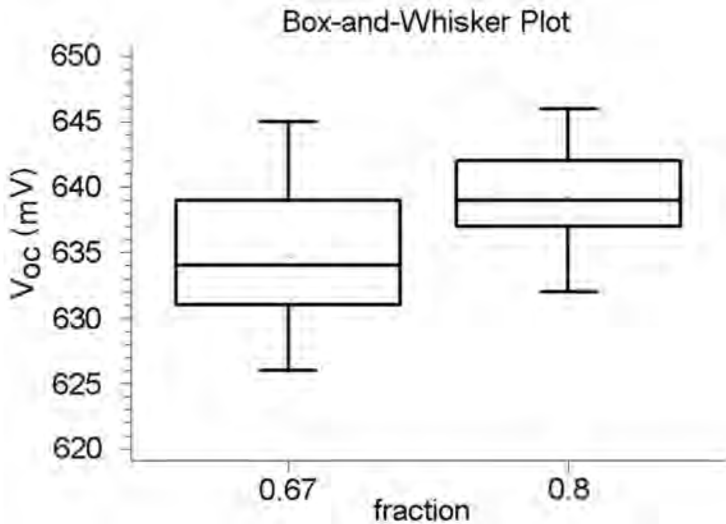

Figure 6.4: The effect on V_{OC} for two different emitter fractions.

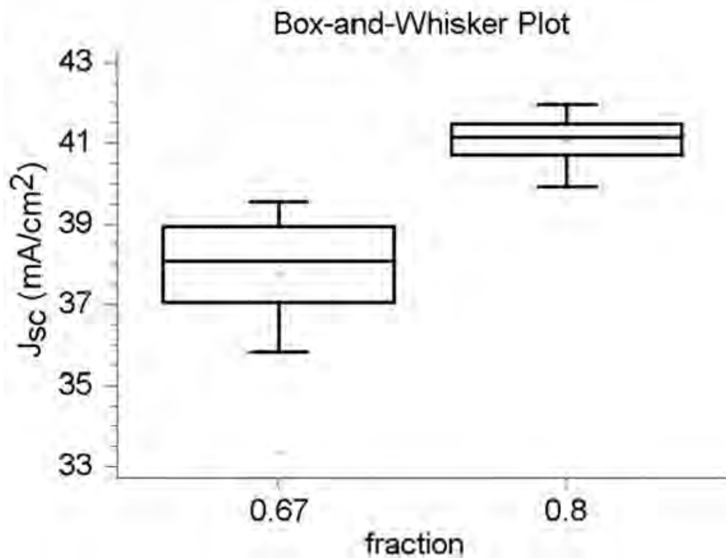

Figure 6.5: The effect on J_{SC} for two different emitter fractions.

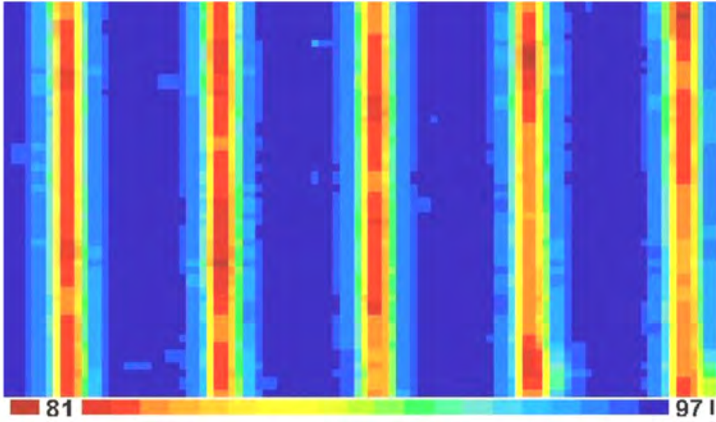

Figure 6.6: IQE measurement at 976 nm showing the local IQE. Highest IQE is shown in blue (emitter), lowest in red (BSF).

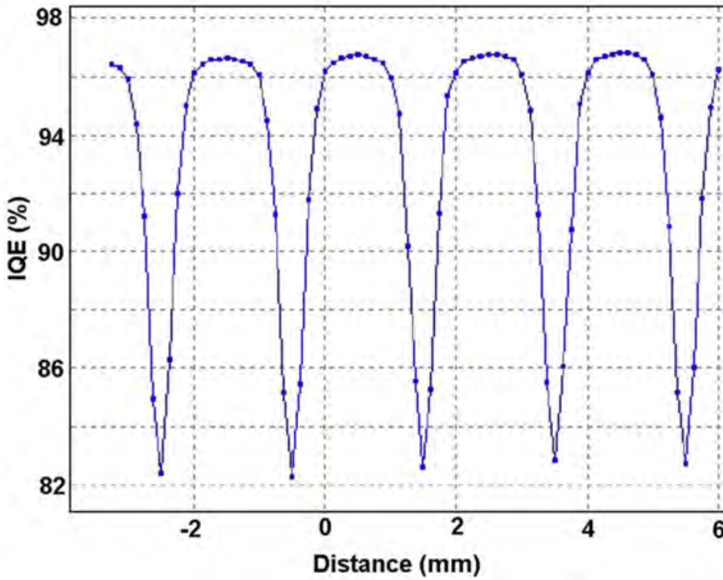

Figure 6.7: Line Scan of the IQE presented in Figure 6.6. Highest IQE is found for the emitter, lowest for the BSF.

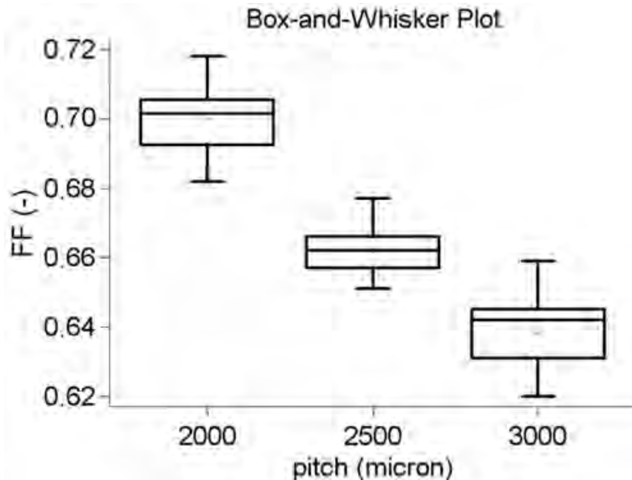

Figure 6.8: The effect on the *FF* for three different pitches.

6.4 Best Cell Results

The overall experimental results show that several factors play an important role in obtaining high efficiency. These factors are high quality FSF, high emitter fraction and a small pitch. Figure 6.9 shows both Internal Quantum Efficiency (IQE) and IV data of our best IBC cell. A summary of measured parameters corresponding to this best cell with 19.1% efficiency is given in Table 6.1. For this cell the emitter fraction was 80%, the pitch was 2 mm and the area 13.2 cm^2.

The IQE results are very good; approaching unity in a broad wavelength range, with characteristic drops in the blue response mainly due to absorption of light in the a-SiN_x:H layer, and in the red close to the band-gap limit. Excellent current collection is shown by a J_{SC} value as high as 41.5 ±1.2 mA/cm^2, as corrected for spectral mismatch. This J_{SC} is close to the maximal current which can be expected from IBC cells [98] and similar to what we obtain on Cz n-MWT cells, when corrected for the front side metalization [104]. This high J_{SC} can be related to the excellent FSF, low electrical shading losses and high-quality surface passivation as discussed before.

Table 6.1: Summary of the best cell parameters which gave an efficiency of 19.1%.

Pitch (mm)	Emitter fraction	J_{SC} (mA/cm^2)	V_{OC} (mV)	*FF* (%)	Efficiency (%)
2	0.8	41.5	641	72.0	19.1

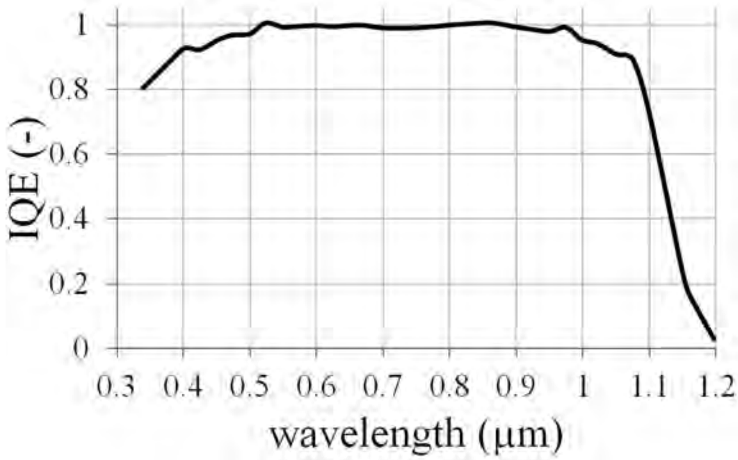

(a)

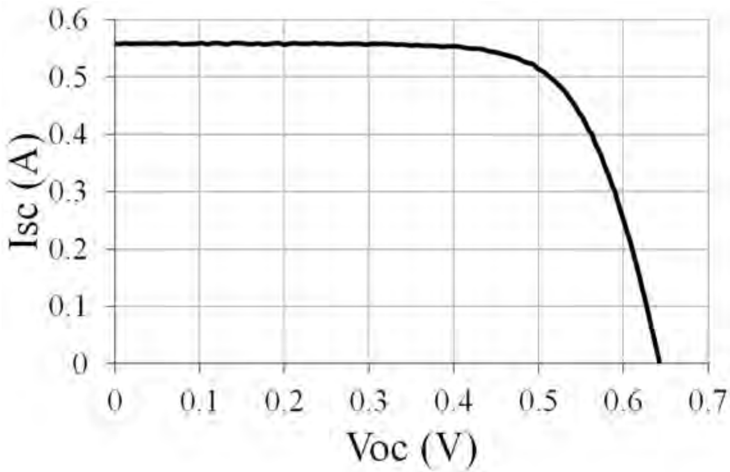

(b)

Figure 6.9: IQE (a) and IV (b) corresponding to the best IBC cell fabricated.

6.5 Conclusions

The results show that high-efficiency IBC cells, with a top efficiency of 19.1%, have been successfully fabricated using low-cost fabrication technologies such as screen-printing for patterning to create the p-n regions and metalization. In general the results show higher efficiencies for larger emitter fraction and smaller pitch, with best results in this study obtained for a large emitter fraction of 80% and a small pitch of 2 mm. The cell was passivated with a stack of SiO_2/a-SiN_x:H for the emitter, BSF and gap, and using an excellent FSF and obtaining low electrical shading losses, high J_{SC} values of 41.5 mA/cm^2 have been achieved. The IQE values are close to unity in a broad wavelength range. Combining commonly reported FF values of around 79% with the obtained values for J_{SC} and V_{OC} in this work would result in cell efficiencies well above 21%.

Part III

Analysis of the a-SiN_X:H layer and interface with c-Si

Chapter 7

Characterization of the a-SiN_x:H layer: bulk properties, interface with Si and solar cell efficiency

M.W.P.E. Lamers[1], K.T. Butler[2], P.E. Vullum[3], J.H. Harding[2], A.W. Weeber[1]

[1] ECN Solar Energy, P.O. Box 1, 1755 ZG Petten, the Netherlands
[2] University of Sheffield, Western Bank, Sheffield S10 2TN, United Kingdom
[3] SINTEF, Materials and Chemistry, Box 4760 Sluppen, NO-7465 Trondheim, Norway

Physica Status Solidi A **210**, 658-668 (2013)

Abstract

In this paper two front-side a-SiN_x:H layers that can be used in the solar cell industry are extensively characterized and their influence on solar cell efficiency is studied. Variations in layer build-up, atomic density, optical properties, surface passivation and passivation of defects and impurities in the wafer (bulk passivation) are discussed. The build-up of these two layers are considered against a background of over 80 a-SiN_x:H layers. These layers differ in stoichiometry, optical properties and surface passivation, as the refractive index is varied between 1.9 and 3.0. The validity of comparable data output of different characterization equipment is discussed as well. On solar cells, the effect of different layer build-up is investigated and it is found that a wide process window is allowed to obtain similar cell efficiencies with regard to the optical transmission, bulk and surface passivation.

7.1 Introduction

In wafer-based silicon solar cells, hydrogenated amorphous silicon nitride (a-SiN_x:H) is the standard anti-reflection and passivating layer, for both surface defects and defects and impurities in the bulk of the wafer. Commonly, the layer is deposited using plasma-enhanced chemical vapor deposition (PECVD). The physical properties of the layer have previously been correlated to cell output properties like the open-circuit voltage V_{OC} [81,82]. In general, the optimized a-SiN_x:H layer is a compromise between optical (anti-reflection and absorption) and passivating properties. Si-rich a-SiN_x:H layers show good surface passivation, but are highly absorbing and cannot be used for solar cell applications. N-rich layers show good optical properties, but are less effective in surface passivation. Additionally, sufficient N-H bonds must be present in the layer as H released by breakage of this bond during the high temperature firing, gives rise to passivation of defects and impurities in the bulk of the wafer (bulk passivation) [15,106,107]. Results of extensive characterization of different a-SiN_x:H layers deposited with various equipment have been published before [15,44,81,108]. Commonly, the a-SiN_x:H layer is approximated by a homogeneous composition. Bond densities, optical properties and atomic density are taken to be constant throughout the layer. However, variations in the layers do exist and can be small, which allow determination of the layer as homogeneous, or can be large, in which case the layer is inhomogeneous.

In this article a background data set is provided in which over 80 a-SiN_x:H layers are characterized. Against this background homogeneous and inhomogeneous layers are compared using extensive characterization. The effect of the build-up of the layers is related to the three functions of a-SiN_x:H on solar cells: as anti-reflection coating and as provider for bulk and surface passivation of the silicon wafer and solar cell.

7.2 Setting the background

7.2.1 Sample preparation

Samples were prepared using 275 µm thick p-type FZ (100) wafers and 500 µm thick p-type Cz (100) wafers, which were double side mirror polished with a base resistivity of respectively 2.5 Ω·cm and >20 Ω·cm. Remote PECVD using the MAiA system of Roth & Rau [109] was used to deposit 80-110 nm a-SiN_x:H layers on the wafers. Variations in deposition were obtained by varying the pressure (0.1-0.5 mbar), temperature (275-475°C), total gas flow (200-1250 sccm), plasma power (400-3320 W) and gas ratio NH_3/SiH_4 (1-7). These parameters influence the layer composition and are discussed in more detail in Chapter 4 and by Soppe *et al.* [27]. The wafers received a 1% HF dip before deposition. The Cz wafers were single

side coated, while the FZ wafers were coated on both sides. The first were used for Fourier transform infrared spectroscopy (FTIR) and spectroscopic ellipsometry measurements. The latter were used to determine the minority charge carrier lifetime measurements using the Sinton Consulting WCT-120 lifetime tester [49]. The lifetime was determined at a minority carrier density of $1{\cdot}10^{15}$ cm^{-3}. Subsequently, surface recombination velocity (SRV) was determined, taking into account the doping of the wafer [48]. FTIR bond densities were calculated from the spectrum using the conversion factors as found by Giorgis *et al.* [43]. It is noted that calibration constants needed to convert the data from the FTIR spectrum to the bond density cannot be regarded as exact [44], but they represent a good first approximation. Spectroscopic ellipsometry (280-820 nm) was performed at three angles of incidence (50°, 60°and 70°) and the layers were analyzed using the Urban model [46]. From the fit, the refractive index n and the extinction coefficient k were determined at respectively 633 nm and 400 nm. The approach used by Bustarret *et al.* [47] was used to calculate the Si-Si bond densities and atomic densities.

7.2.2 Optical properties, bond densities and passivation

The ellipsometry data of the layers could be fitted well with a single layer model and the spectral trends for n and k were comparable to what is commonly observed [108]. This indicates that the layers have a homogeneous build-up. In Figures 7.1a and 7.1b the bond densities of the layers, determined using FTIR, as a function of n at 633 nm are given. The range in n, 1.9 to 3.0, corresponds to x in a-SiN_x:H from 1.45 to 0.15 as is shown in Figure 7.1c. In this figure it can also be seen that k at 400 nm becomes zero for x $>$ 1.1, which corresponds to $n < 2.03$.
The variation around the trendline of the Si-Si bond density is small, which can be expected as the Si-Si bond density is calculated from n. For $n < 3.0$ the Si-Si bond density increases almost linearly when increasing n. The Si-N bond density is more or less constant for $n < 2.1$, but decreases linearly when increasing n. For $n < 1.9$, the Si-H bond density is negligible, but linearly increases until $n = 2.4$-2.5, after which this bond density is stable. By contrast, the N-H bond density is high for layers with low n, but rapidly decreases when increasing n, with the maximum curvature around $n = 2.0$. A transition of the dominant bond from N-H to Si-H is found at $n = 2.0$ (x = 1.15), which is similar to the transition point as found by Garcia *et al.* [110] and which has been identified as the percolation threshold of Si-Si bonds [111].

The atomic densities can be calculated from the bond densities [47] and from this result the total atomic density. In Figure 7.2, the total atomic density is given for the layers made with the MAiA system and is found to increase linearly with n, though the error is quite large.

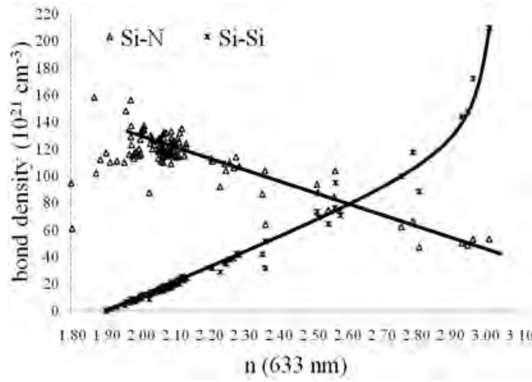

(a) The Si-N and Si-Si bond densities as a function of n.

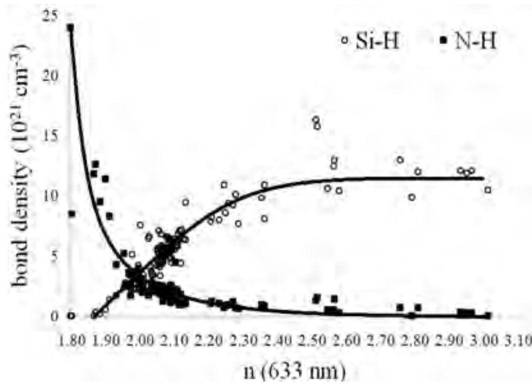

(b) The Si-H and N-H bond densities as a function of n.

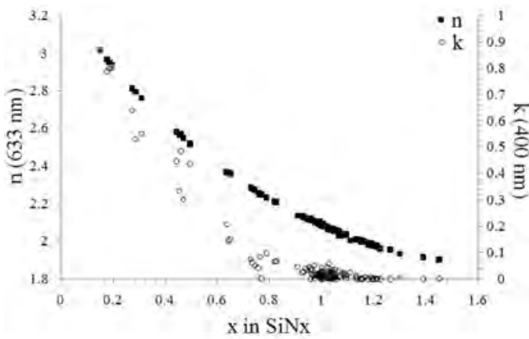

(c) The x in a-SiN_x:H and k as function of n.

Figure 7.1: Bond densities, k at 400 nm and x in a-SiN_x:H as function of n at 633 nm for over 80 layers.

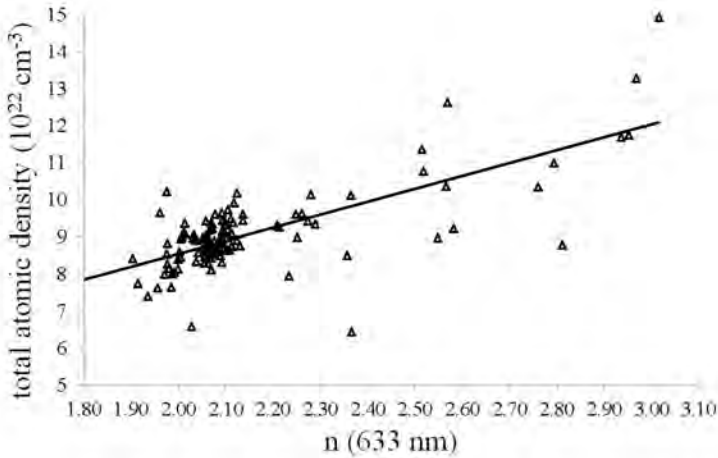

Figure 7.2: Total atomic density as function of n for the MAiA layers. The line is a guide to the eye.

From the data the atomic percentages of H, Si and N as found in the layers, are determined. They are given in Figures 7.3a and 7.3b as a function of n and the extinction coefficient k. A strong correlation exists between n and the atomic percentage of Si and N, as can be expected, but it is more or less independent of H. A minimum in H concentration can be seen around n = 1.9-2.0 as the N-H bond density rapidly decreases while the Si-H bond density increases much slower. At this point the main atomic bonding of H switches from N to Si. The minimum H percentage is around 5% and the maximum is around 15%. It must also be noted that the total H concentration increases with n, as the total atomic density increases. Regarding k, this parameter becomes zero for $n < 2.03$, which corresponds to atomic percentage of Si $< 45\%$. However at the transition point where the percentage of Si becomes larger than the percentage of N, k increases and increments linearly with larger percentages of Si.

In Figure 7.4 the effective SRV is given as a function of n. The SRV is determined for the samples before and after the high temperature firing step corresponding to the step that is needed to form the metal contacts in solar cell manufacturing. As can be seen, for low n the SRV is very high, but this drops quickly when increasing n. At around n = 2.1 low SRV values are obtained. The effective SRV remains stable for higher n. Variation due to the firing process or firing stability of the layers can not be claimed, since no distinct differences between the before firing and after firing state can be observed. Variations in the obtained effective SRV for similar n, can be linked to the Si-H bond density of the specific layer. In Figure 7.5 the Si-H bond density as function of the effective SRV is given for all layers with $2.0 < n < 2.15$.

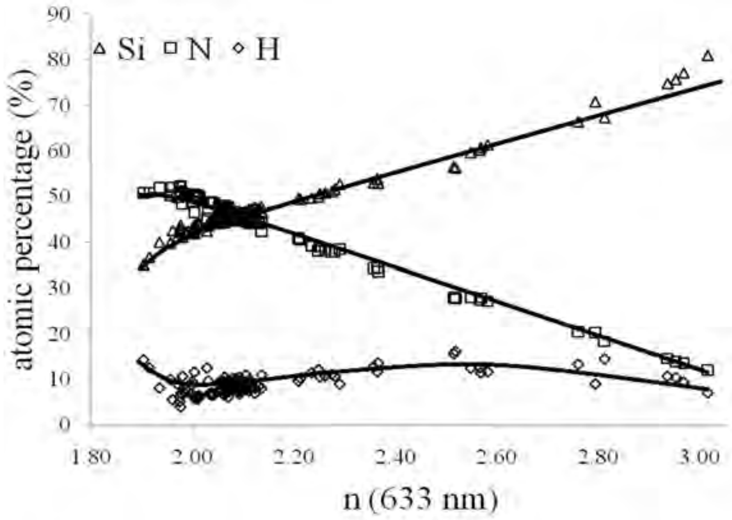

(a)

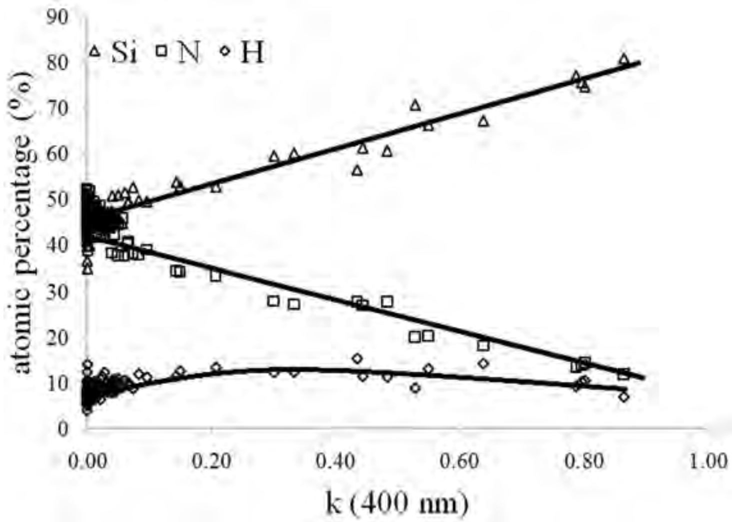

(b)

Figure 7.3: Atomic percentage of H, Si and N as function of a) n and b) k.

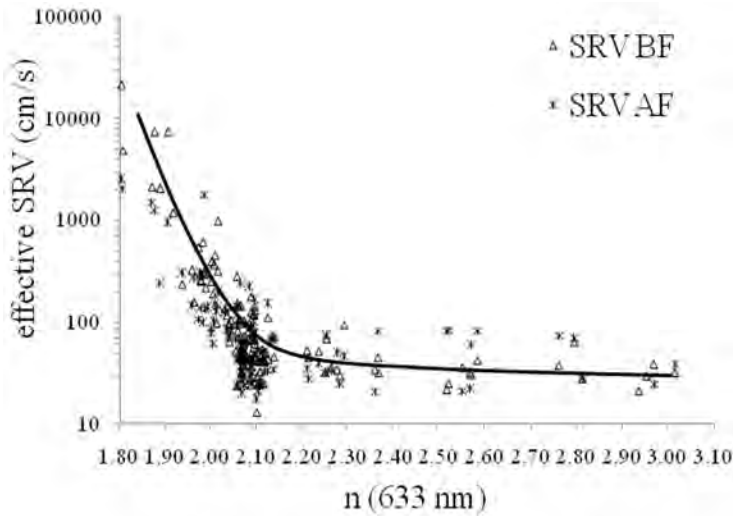

Figure 7.4: Effective *SRV* before (BF) and after firing (AF) as a function of n.

In this section a framework, linking various parameters, has been developed based on homogeneous layers. It is shown that with increasing n, the:

- Si-N bond density decreases linearly;
- Si-Si bond density increases linearly;
- N-H bond density declines very rapidly for $n < 2.1$; for $n > 2.1$, the decline rate reduces significantly and becomes linear;
- Si-H bond density first increases linearly, but stabilizes for $n > 2.4$;
- Total atomic density increases;
- Si content increases linearly;
- N content decreases linearly;
- H content varies between 5 and 15% and shows a minimum at $n = 1.9$;
- *SRV* is very high for low n, but decreases rapidly and stabilizes for $n > 2.1$.

7.3 Characterization accuracy

7.3.1 Homogeneity in the layer: atomic concentration measured by SIMS and FTIR/ellipsometry

In the previous section the results from FTIR and ellipsometry were combined to obtain more insight into the layer build-up and to obtain correlations between bonds, densities, stoichiometry, surface passivation and optical properties. In this characterization, a homogeneous build-up of the layer

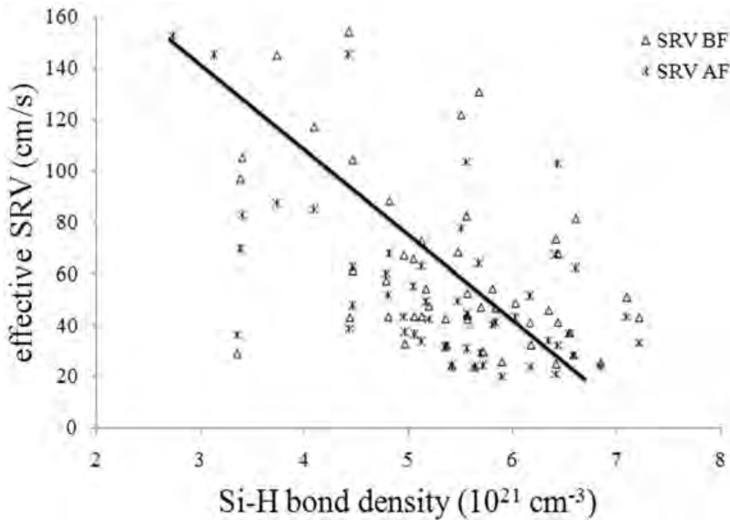

Figure 7.5: Effective *SRV* before (BF) and after firing (AF) as a function of the Si-H bond density for all layers with $2.0 < n < 2.15$. The line is a guide to the eye.

is assumed. Variations in layer build-up can have an effect on different properties, but are not considered in this approach. To study the layer build-up in more detail, samples fabricated with two different PECVD systems, the MAiA and the SiNA (also from Roth & Rau), are analyzed. Our SiNA system is a prototype and is described in more detail by Soppe *et al.* [27]. The MAiA layers can be approached as homogeneous in layer build-up, while the SiNA layers are inhomogeneous. Variations in layer build-up can be related to differences in gas flow distribution throughout the system. To compare homogeneous and inhomogeneous layers, for each type a passivating and a standard a-SiN_x:H layer were fabricated and analyzed in various ways. The two inhomogeneous layers were etched back in small steps, so the variations in bond densities and optical properties could be analyzed in a more detailed manner. Each etch step consisted of a 2 minute 9% HF dip, a 10 seconds 0.05% KOH dip and a 3 minute 1% HCl dip. After each etch step the layers were analyzed with lifetime measurements, FTIR and ellipsometry. For layers thinner than 15 nm the FTIR signal became weak, which limits the accuracy of the analysis of this data. Also, surface roughening due to the etch back process needs to be taken into account and can explain the variations around the line drawn in the figures.

The two inhomogeneous layers analyzed were optimized as a front side layer (standard a-SiN_x:H), with changing n from Si-side (at 0 nm) to air side (at 80-100 nm) from 2.4 to 2.0 and as a surface passivating layer (passivating a-SiN_x:H), with changing n from Si-side to air side from 2.8 to 2.4. The

change in n for both layers is discussed in Section 7.3.2. The Si-N, Si-H bond densities and Si-H peak location as a function of the remaining layer thickness for the two etched back inhomogeneous layers are shown in Figures 7.6, 7.7 and 7.8.

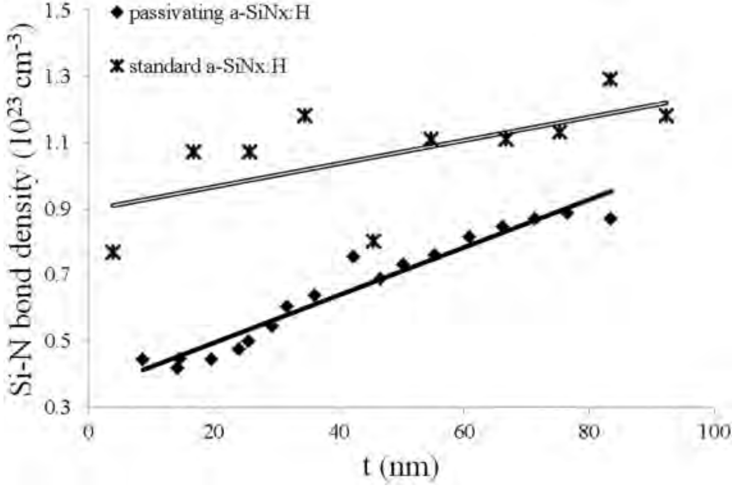

Figure 7.6: The Si-N bond density as a function of the remaining layer thickness t for the passivating and standard inhomogeneous layers.

The compositions of both layers clearly change. It can be seen that for the passivating layer a steep increase in Si-N bond density is found when moving from the Si-side to the air side, though the Si-H bond density and peak position remain stable. The relative composition of each part of the inhomogeneous layers follow the atomic composition as found for the homogeneous layers shown in Figure 7.3 very closely.

The H atomic concentration found for the investigated layers is compared to the calibrated H atomic concentration found by Time-of-Flight Secondary Ion Mass Spectroscopy (ToF-SIMS). For this, the bond densities needed to be calculated as function of the distance from the Si surface. A fit was made through the data points as shown in Figures 7.6 and 7.7. Using this fit, the bond density as function of the distance could be calculated using,

$$[X-Y] = \frac{d_{\mathrm{e}}[X-Y]_{\mathrm{e}} - d_{\mathrm{e}+1}[X-Y]_{\mathrm{e}+1}}{d_{\mathrm{e}} - d_{\mathrm{e}+1}} \tag{7.1}$$

with [X-Y] representing the bond density like Si-H or Si-N as function of the distance from the Si surface; $[X\text{-}Y]_{\mathrm{e}}$ the measured integral value of the bond density after etch step number e; $[X\text{-}Y]_{\mathrm{e}+1}$the measured integral value of the bond density after etch step number $e+1$; d_{e} the thickness of the layer after

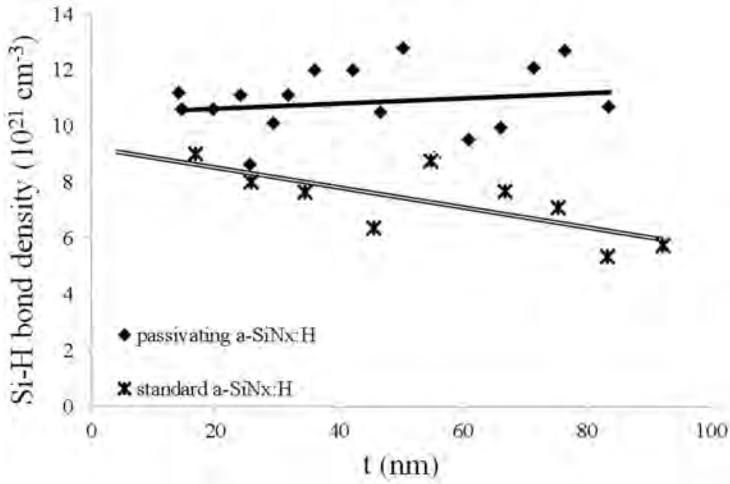

Figure 7.7: The Si-H bond density as a function of the remaining layer thickness t for the passivating and standard inhomogeneous layers.

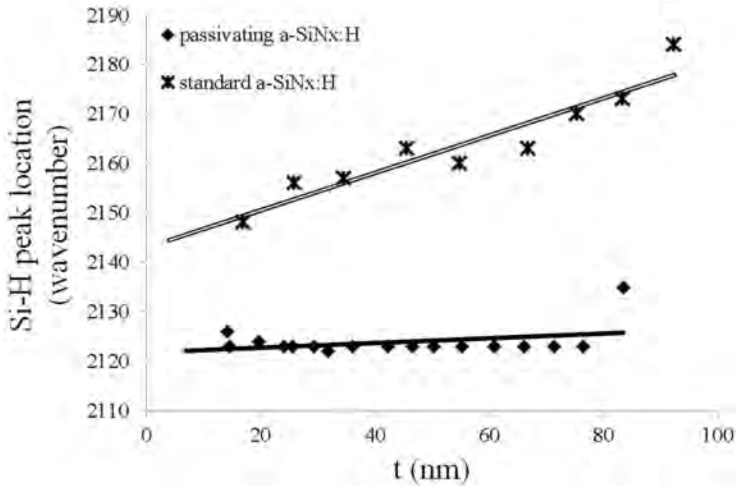

Figure 7.8: The Si-H peak location as a function of the remaining layer thickness t for the passivating and standard inhomogeneous layers.

etch step number e; d_{e+1} the thickness of the layer after etch step $e+1$. The results for the H concentrations are shown in Figure 7.9. As can be seen the H concentrations determined by ToF-SIMS and FTIR/ellipsometry are comparable. The variation throughout the layer in the inhomogeneous passivating layer is not large. This is as expected, as layers with low effective *SRV* ($n > 2.4$), even though fluctuating in n (n = 2.4-2.8), will give similar densities of Si-H bonds and hence similar H concentrations. The inhomogeneous standard layer, with n = 2.0-2.4, is expected to give a larger variation in H concentration which is found to be true. Moreover, the layers exhibit quite a high H concentration 5-20 nm from the Si interface, corresponding to 11% of the total atomic density. The homogeneous layer shows indeed on *average* a constant H profile. After closer examination variations in the layer can be observed suggesting a small change in composition at half thickness. This small variation can be related to the presence of two sources in the PECVD machine and the movement of the tray underneath these sources. The small variation occurs as the deposition is done at the boundary between the two sources.

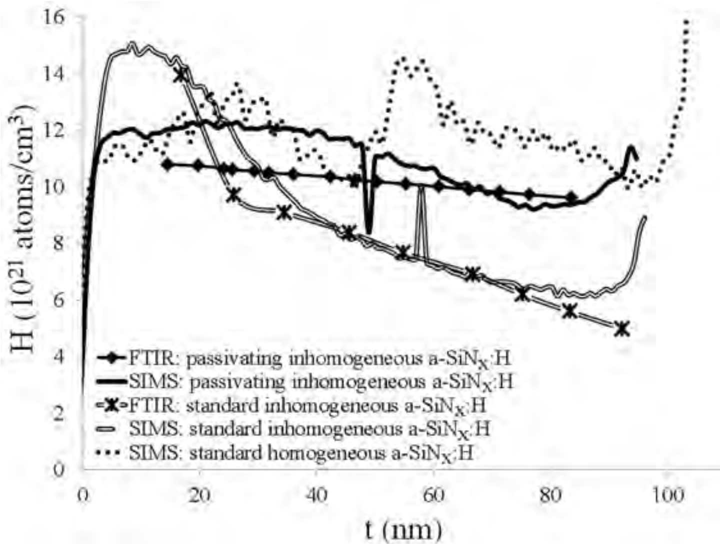

Figure 7.9: The H concentration in the standard homogeneous layer and passivating and standard inhomogeneous layers.

An estimation of the Si density in a-SiN_x:H can be obtained using ToF-SIMS. This is done by relating the average ^{30}Si signal of the c-Si bulk to the density of c-Si (2.329 g·cm^{-3}) and using this ratio to determine the Si density from the ^{30}Si peak signal in the a-SiN_x:H layer. The Si density as determined by ToF-SIMS and FTIR/ellipsometry is shown in Figure 7.10. As can be seen, the (uncalibrated) Si concentration determined by ToF-SIMS does not follow the same trend as the Si concentration determined by FTIR/ellipsometry, the

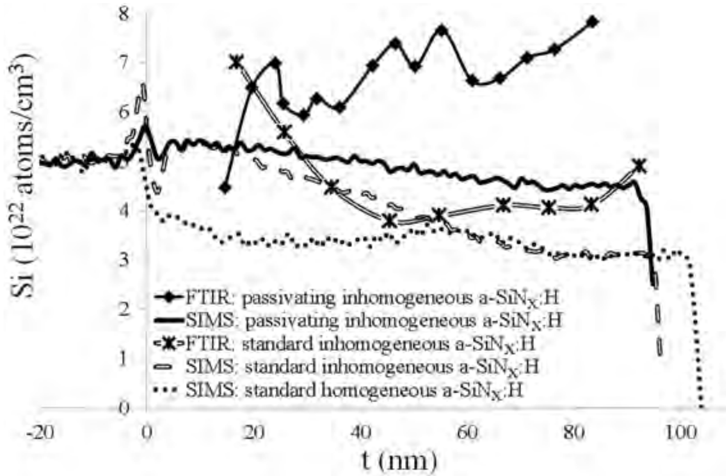

Figure 7.10: The Si concentration in the standard homogeneous layer and passivating and standard inhomogeneous layers.

absolute values differ as well. However, both measurements give a higher Si concentration for the passivating inhomogeneous layer than for the standard inhomogeneous layer, conform expectations. Also, a large increasing trend is found in Si in the inhomogeneous standard layer when moving towards the Si interface. The homogeneous layer shows a very constant Si concentration, except for a small peak at half thickness. The three layers show different behavior close to the interface and this can be related to matrix effects of SIMS measurements.

The ^{29}SiN signal, normalized by dividing by the average ^{30}Si signal in bulk c-Si, gives a profile of the Si-N bond density in the a-SiN$_x$:H. The ^{29}SiN/^{30}Si(c-Si bulk) signal as determined from the ToF-SIMS data is shown in Figure 7.11. The intensity of ^{29}SiN/^{30}Si(c-Si) is quite similar for all samples. For the inhomogeneous passivating layer an increase in ^{29}SiN is found, which is as expected as n decreases. While the homogeneous standard layer gives a constant value on *average*, clear but small variations in data can be seen. The inhomogeneous standard layer at first shows an increase, followed by a decrease in ^{29}SiN. Comparing Figure 7.11 to Figure 7.6, it can be seen that the reduction in N is similar for the inhomogeneous passivating a-SiN$_x$:H layer, but is quite different for the inhomogeneous standard a-SiN$_x$:H layer. In the next section two additional different methods to determine the exact Si and N content are used to analyze the layers and to discuss the results in more detail.

Regarding the comparison between homogeneous and inhomogeneous layers an initial conclusion can be made that variations in layer build-up occur for

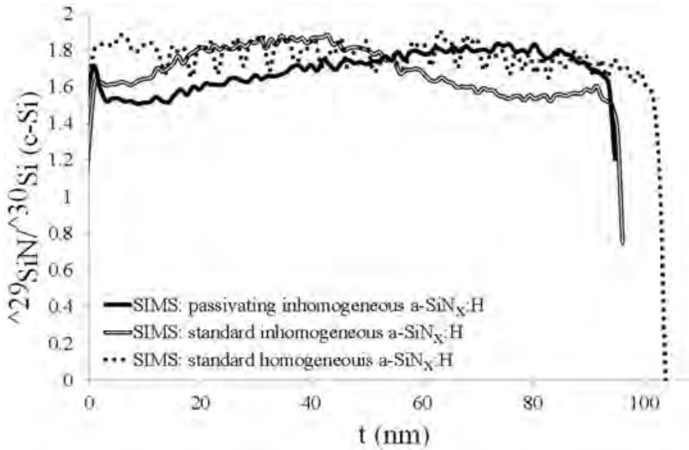

Figure 7.11: The ^{29}SiN/^{30}Si(c-Si bulk) signal of the standard homogeneous layer and passivating and standard inhomogeneous layers.

all the layers. However, in homogeneous layers the variations are relatively small and the composition is *on average* constant. In inhomogeneous layers similar variations can be found, however a clear trend is observed in these variations.

7.3.2 Homogeneity in the layer: atomic concentration measured by XPS, TEM and FTIR/ellipsometry

To further examine the exact Si and N content, the inhomogeneous standard layer was characterized with X-ray Photoelectron spectroscopy (XPS) and Transmission Electron Microscopy (TEM). The characterizations were performed at SINTEF. The XPS measurements were performed using Al Kα radiation ($h\nu$ = 1486.6 eV) combined with Ar$^+$ sputtering (2 keV, 1 mm^2 raster size) for depth profiling. Cross-section TEM specimens were prepared by mechanical polishing, dimpling and Ar$^+$-ion sputtering using liquid nitrogen to cool the sample. The acceleration voltage was progressively reduced to 1.0 keV during the final stage of the Ar$^+$-ion sputtering to minimize sample damage. TEM was performed on a JEOL 2010F operated at 200 kV. Compositional analysis was performed with X-ray energy dispersive spectroscopy (EDS) using a 0.5 nm in diameter electron beam.

In Figure 7.12 the atomic percentage (including only Si and N) as found by XPS, TEM and FTIR/ellipsometry are given for the inhomogeneous standard layer. The graph shows an undervaluation of the N concentration with TEM analysis, which is a known problem when characterizing low mass atoms. The trend, however, follows the SIMS profile, indicating that the discrepancy is constant. The percentages as measured by XPS and FTIR/ellipsometry

found for both Si and N are similar.

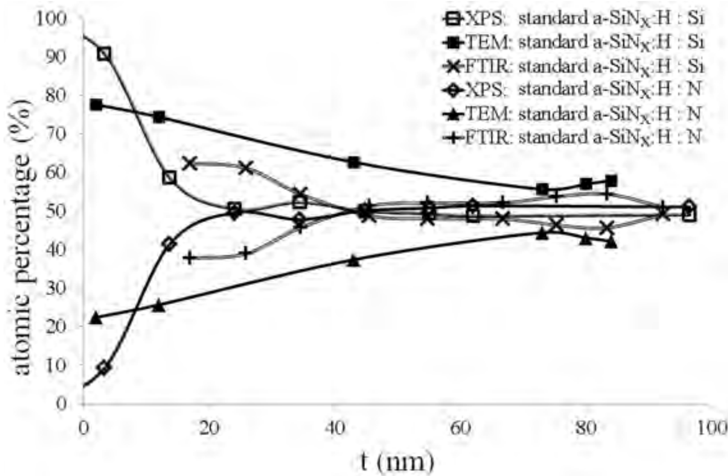

Figure 7.12: The Si and N atomic percentages in the inhomogeneous standard layer, characterized by XPS, TEM and FTIR/ellipsometry.

In XPS, depth is determined by etching rate which is assumed to be constant throughout the sample. However, for a sample with inhomogeneous build-up it is not constant.

To confirm this, the passivating inhomogeneous sample was also analyzed by XPS and these results, together with the FTIR/ellipsometry data, are shown in Figure 7.13. The atomic percentages as found by XPS and FTIR/ellipsometry are relatively comparable far from the Si interface, but close to this surface they deviate. Moreover, 15-20 nm from the interface no N is found in the layer, which indicates that the material should be a-Si:H. This is highly unlikely as measurements from FTIR, ellipsometry and ToF-SIMS contradict this. Moreover, the surface passivation quality of this layer is stable under firing, and does not deteriorate as expected for real a-Si:H layers, which should crystallize during the firing step. Therefore, a depth error is present in the XPS analyses of the layer. However, from the data obtained far from the interface, when only little depth etching was done, it can be concluded that the atomic percentages as found by FTIR/ellipsometry and XPS match.

Analyses of a-SiN_x:H layers by TEM, ToF-SIMS, XPS, FTIR and ellipsometry show a variation in the estimated Si, N and H content throughout the a-SiN_x:H layer. Variations within the layers themselves exist and can be identified, however, accurate quantification is difficult as the error can be quite large.

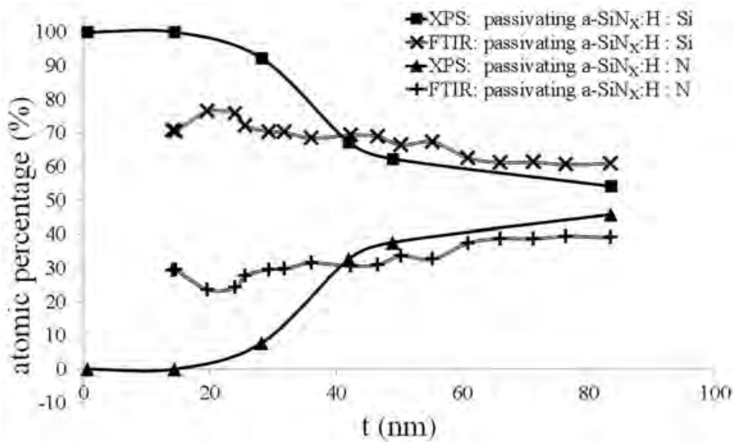

Figure 7.13: The Si and N atomic percentages in the inhomogeneous passivating layer, characterized by XPS and FTIR/ellipsometry.

7.3.3 Homogeneity in the layer: optical properties as determined by ellipsometry and spectral reflection

To maximize the short circuit current density, J_{SC}, of a solar cell, the a-SiN$_x$:H layer must not absorb light and minimize reflection to allow maximum transmission. For this reason, we examine the ellipsometry data in more detail and compare the predicted reflection of the generated model from the spectroscopic ellipsometry fit to the total reflection as measured using an integrating sphere. The measured reflection of the homogeneous layers closely matches the reflection simulated using the optical properties modeled by use of ellipsometry data (not shown). However, the reflection of the inhomogeneous layers is more complicated as the variation in the layer build-up determines the reflection. In Figure 7.14 the refractive index n and the extinction coefficient k of two layers, a passivating and standard layer, are given as a function of the thickness t. Two approaches were used to fit the ellipsometry data. Firstly by modeling the full layer as a double layer. Secondly by modeling each etched layer separately, creating a multiple stack layer. Both models show a clear decrease in n and k throughout the layers. A drop in both n and k is present close to the interface with Si. This can be related to the oxidation of the already exposed Si surface in the back-etching process, which interferes with the analysis. This drop might also be related to the presence of some residual native oxide grown on the Si surface after the 1% HF dip prior to a-SiN$_x$:H deposition, as was confirmed by ToF-SIMS.

In Figure 7.15 the reflection of the passivating a-SiN$_x$:H as measured by integrating sphere and the simulated reflections based on the ellipsometry

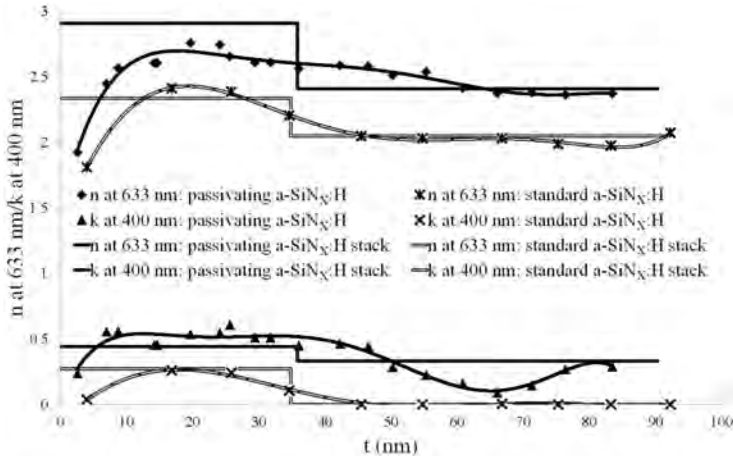

Figure 7.14: n and k as determined at 633 and 400 nm respectively as a function of t for the passivating and the standard a-SiN$_x$:H layer using two different approaches to modeling by ellipsometry: as double layer and as multiple stack layer, wherein each etched layer is modeled separately.

models are given. The fitted reflections match the measured data well. This leads to the conclusion that similar reflection curves can be obtained for layers with varying n and k in the layer itself.

7.4 Passivation

The use of a-SiN$_x$:H results in passivation of both the bulk and surface of a Si wafer. The former can be understood as H is released from the a-SiN$_x$:H layer, which diffuses into the Si wafer where it passivates defects. The latter can be understood as a combination of the reduction of the dangling bonds and thus the density of interface states (D_{it}) and the repulsion of the holes in the Si wafer by the positive fixed charges (Q_{f}), thereby reducing recombination at the interface between a-SiN$_x$:H and Si. In this section these aspects with respect to a-SiN$_x$:H are investigated.

7.4.1 Bulk passivation

Bulk passivation is the result of the release of H atoms during the high temperature firing step as N-H bonds break [15, 106, 107]. The atomic H diffuses through the a-SiN$_x$:H layer and Si wafer, and bonds to defects it encounters, thereby passivating them. Logically, layers with a high N-H density will release more H than layers with hardly any N-H. As can be seen in Figure 7.1b N-H rich layers have a low n. Atomic H formed in these layers can

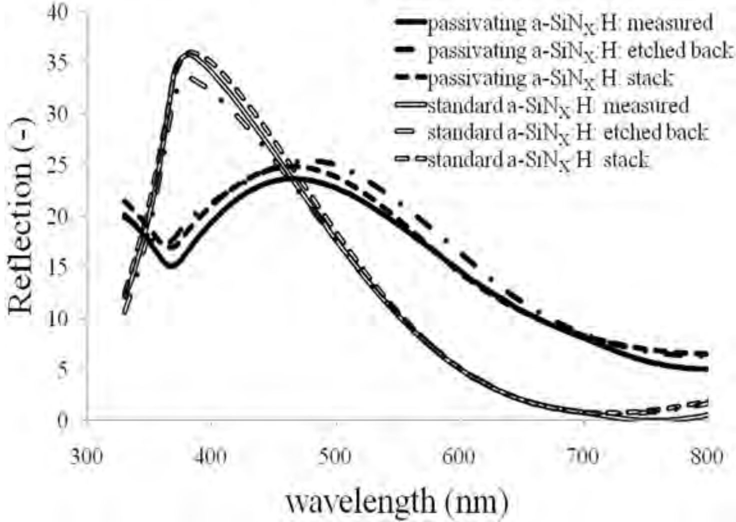

Figure 7.15: The measured reflection of the two a-SiN_x:H layers. Also the simulated reflection curves from the ellipsometery models are given.

easily form H_2, as these layers also have a low total atomic density as can be seen in Figure 7.2, thereby effectively reducing the concentration of atomic H in the layer. The formed H_2 is released to the outside world [15]. The resultant low atomic H concentration in the Si wafer has an unfavorable effect on V_{OC} of the solar cell. For high Si-N bond density (and low N-H bond density) the number of atomic H released from the layers is too small to passivate defects in Si, thereby effectively reducing V_{OC} [81]. An optimum has been found for layers with a Si-N bond density between 1.2 and $1.3{\cdot}10^{23}$ cm^{-3} [81]. The effect on solar cells significantly depends on the bulk quality of the Si wafer, i.e. the number of defects to be passivated.

7.4.2 Surface passivation

As Q_f and D_{it} are properties of the interface of a-SiN_x:H/Si, this indicates that they are determined by the initial growth of the a-SiN_x:H layer. More profoundly, Q_f is related to the interface structure between the materials (a-SiN_x:H and Si) causing a local-field effect as was described by Aspnes [112]. The origin of Q_f is linked to the so-called K- and N-centers [111, 113]. These centers are respectively *Si≡N_3 and *N=Si_2. * indicates that these centers can be neutral, positive, negative or bonded to H. Assuming that K- and N-centers are also present at the interface, this leads to the conclusion that Q_f is determined by the variation and volume fractions of K- and N-centers in the interface region of a-SiN_x:H and Si. The number of K-centers that are bonded to H can be related to the Si-H peak in a FTIR spectrum [43]. A peak location close to 2220 cm^{-1} indicates relatively more K-centers. Both

the K- and N-centers have also been identified as recombination centers and can therefore be related to D_{it}. Thus, when the concentration of (charged) K- and/or N-centers increases, Q_{f} becomes larger. Simultaneously, as the volume fraction of the centers rises, the number of (unpassivated) dangling bonds also increases and so D_{it} increases as well.

Selected homogeneous layers of the background data set were further analyzed. The peaks in the FTIR spectrum were deconvoluted to find the specific back bonds to Si-H and Si-N. The literature on the exact values needed to convert the area of the FTIR spectrum per bond to a density is not conclusive; we decided to show the data in terms of peak area of the bond density [44]. On both sides of the samples with single side a-SiN_x:H a 300 nm aluminum single layer was deposited to create Metal-Insulator-Silicon (MIS) structures. Q_{f} and D_{it} were determined using Capacitance-Voltage (CV) MIS analysis. The relations between the deconvoluted Si-H bond density in the H-Si-N_3 configuration (at 2220 cm^{-1}), the total Si-H bond density, the N-H bond density, the deconvoluted Si-N bond density in the locally distorted configuration (at 790 cm^{-1}) and the refractive index n (at 633 nm as determined with ellipsometry) are shown in Figure 7.16 (see also Chapter 8). Again the relations between the Si-N, Si-H and N-H bond densities are shown, as given in Figures 7.1a and 7.1b. It can be seen that the H-Si-N_3 bond and the Si-N bond in locally distorted configuration follow the same trend, with a maximum around $n = 2.3$. The relations between the effective SRV, Q_{f}, D_{it} and the refractive index n (at 633 nm as determined with ellipsometry) are shown in Figure 7.17.
A clear and positive correlation between Q_{f} and D_{it} is found. Furthermore, at low n, the Q_{f} is nearly absent and the effective SRV is determined by the (high) D_{it}. In Figure 7.16 it is seen that in these layers the H-bonded K-center is not present and distortion inside the layer is very low. With increasing n and decreasing SRV, Q_{f} and D_{it} increase as well, just like the H-bonded K-centers and distortion. This can be explained since, as the number of charged K-centers increases, the neutral dangling bonds (uncharged and non-passivated K-centers) increase as well. With even higher n, and low SRV, Q_{f} and D_{it} decrease again to a certain level, simultaneous with a drop in H-bonded K-centers and distortion in the layer. The effective SRV is a combined effect of Q_{f} and passivation of dangling Si bonds by H (high Si-H bond density) (see also Chapter 8) [114]. The latter relation is depicted in Figure 7.15.

Molecular dynamics (MD) simulations of the interface were performed at the University of Sheffield using de Brito Mota's [115] parameterization of the Tersoff potential [116]. The bonding patterns are found to depend on the stoichiometry. Also, increasing defective geometries and distortion are found to correlate with the increased presence of K- and N-centers at the interface as shown in Figure 7.16. Since charge carriers barely penetrate into the a-SiN_x:H region only the defect centers at the surface will be expected

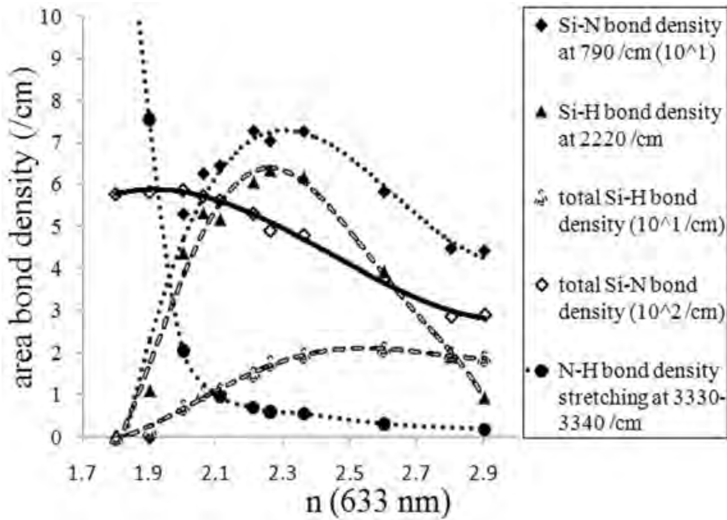

Figure 7.16: Relation between (the peak areas of) the Si-H bond density, the deconvoluted Si-H bond density at 2220 cm^{-1}, the Si-N bond density, the deconvoluted Si-N bond density at 790 cm^{-1} (distorted), N-H bond density and n (see Chapter 8).

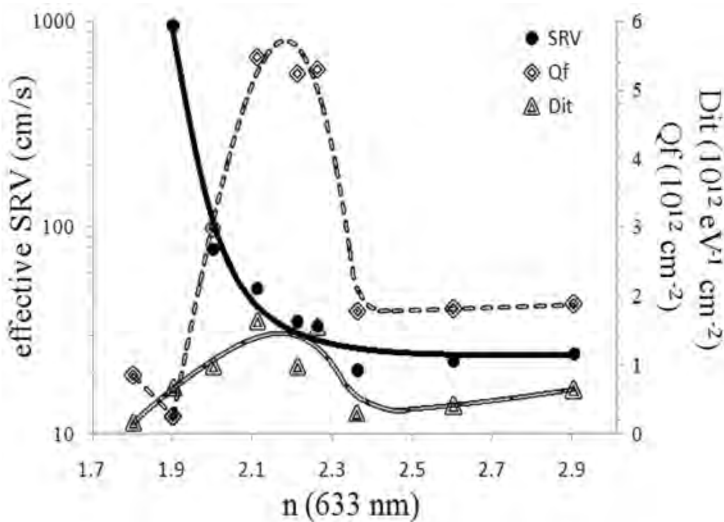

Figure 7.17: Relation between the effective SRV, Q_{f} and n.

to affect the recombination rates. The modeling methods and results are described in more detail in Chapters 10 and 11.

For inhomogeneous layers a correlation between the bulk properties and surface passivation is more complicated as the composition in the layer changes. To identify which part of the a-SiN_x:H layer determines the surface passivation the standard and passivating layers were etched back and the effective SRV was determined after each etch step. The results are given in Figure 7.18. As can be seen, effective SRV, and thus surface passivation, remains constant even for very thin layers, this indicates that the cause of passivation, that is Q_f, lies very close to the interface.

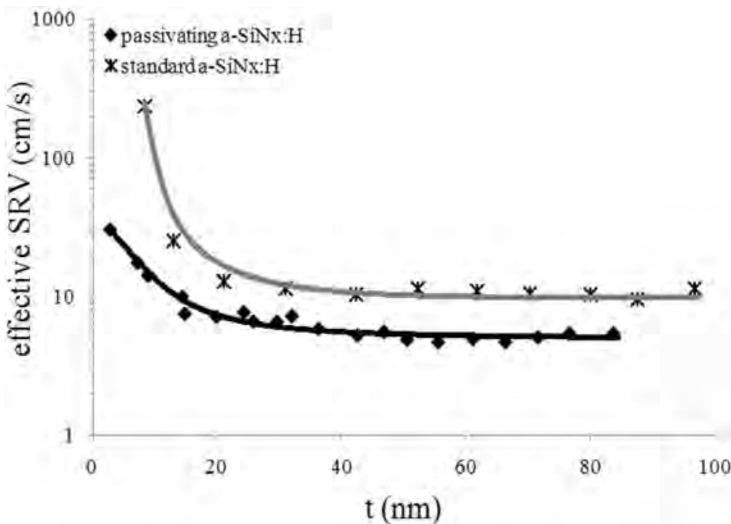

Figure 7.18: The effective SRV at 10^{15} cm^{-3} measured as a function of the distance to the Si surface.

7.5 Solar Cells

So far, we have shown the results of an extended investigation on a-SiN_x:H layers. Different aspects have come forward in analyzing different layers, especially when obvious inhomogeneities in the layer build-up are present. In this section the effect on p-type solar cells of these different layers is investigated. The wafers were 180 µm thick with a base doping of 1-2 Ω·cm, sized 156x156mm^2. The process flow used is described by Stassen *et al.* [117].

7.5.1 Light management

For optimal light management of a solar cell coated with a homogeneous standard layer, the refractive index must be close to 2.05 [17, 18]. For this n, absorption in the layer is negligible and transmission at optimum thickness is maximal. Fabrication of a stack layer, to reduce further the optical losses, can lead to higher J_{SC}. However, after encapsulation this difference becomes much smaller. To illustrate this, two p-type mc-Si cells are fabricated, one with the homogeneous standard layer, the other with the inhomogeneous layer. The reflections of these cells, corrected for the reflection losses by the front side metalization, are shown in Figure 7.19.

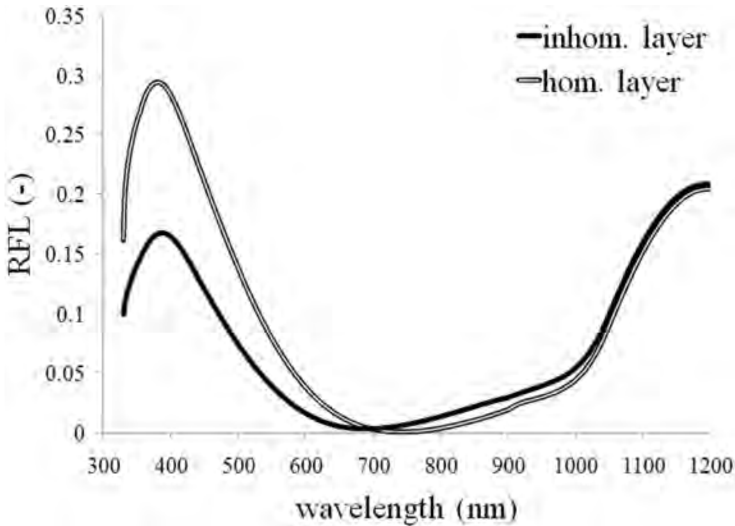

Figure 7.19: Reflection (RFL) of a mc-Si cell (excluding reflection from metalization) fabricated with an inhomogeneous and homogeneous a-SiN$_x$:H coating.

A clear difference is found in the reflection. The inhomogeneous layer absorbs part of the light with wavelengths below 600 nm, as determined by ellipsometry, which lowers the transmission. Also, for the homogeneous layer the reflection minimum is at a too high wavelength, which decreases J_{SC} (fabrication error). On the cell level the external quantum efficiency (EQE) is significantly higher for the inhomogeneous layer, but this difference reduces after encapsulation by EVA and glass. The EQE is shown in Figure 7.20. The difference still present after encapsulation is mainly related to the difference in reflection minimum. These results indicate that significant differences in reflection, and so significant variations in layer build-up, have minimal effect on solar cells after encapsulation.

In Table 7.1, the averaged solar cell parameters of five cells are given for two

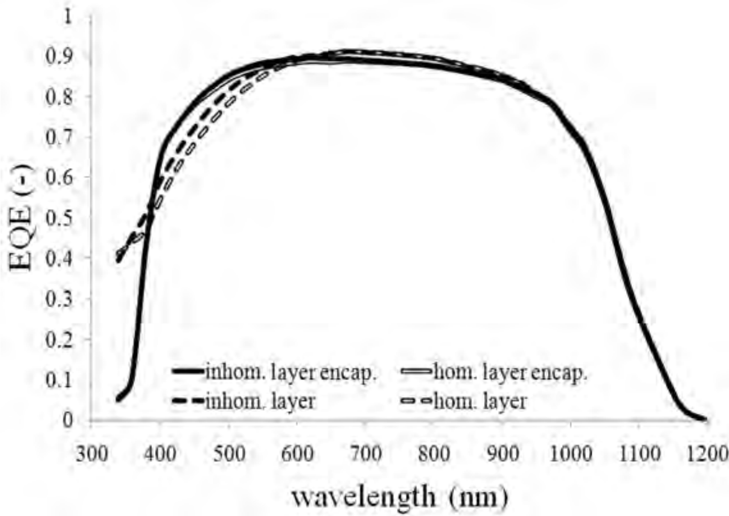

Figure 7.20: EQE before and after encapsulation of mc-Si cells fabricated with an inhomogeneous and homogeneous a-SiN_x:H coating.

material qualities and for both a-SiN_x:H layers.

Table 7.1: Average solar cell parameters of five cells using both lower and better material quality for two types of a-SiN_x:H layers.

Layer	Wafer quality	J_{SC} (mA/cm^2)	V_{OC} (mV)	FF (%)	Efficiency (%)
Inhomogeneous	Better	35.1	612	77.6	16.7
	Lower	35.2	610	77.4	16.6
Homogeneous	Better	34.7	610	77.4	16.4
	Lower	34.7	608	77.4	16.3

The difference in material quality was obtained by selecting material from both the bottom ('better') and the middle ('lower') of an ingot. The difference in material quality is related to the number of defects and impurities in the wafer which effect cell efficiency [118]. Comparing the cell results using the two different a-SiN_x:H layers, the main difference is in J_{SC}, which can be explained by the difference in reflection minimum. The difference in V_{OC} is related to surface passivation and explained in Section 7.5.3.

7.5.2 Bulk passivation: low versus good wafer quality

Solar cell efficiency is to a large extent determined by the wafer quality and thus by the properties of a-SiN_x:H to passivate defects in the bulk.

As discussed in Section 7.4.1, for excellent bulk passivation, the optimum Si-N bond density must be 1.2-1.3·10^{23} cm^{-3}. For the homogeneous layer, the N-H bonds are distributed evenly throughout the layer, whereas for the inhomogeneous a-SiN_x:H, the higher density of N-H bonds is found closer to the outer surface. To validate whether sufficient atomic H can reach the bulk Si, mc-Si cells were processed in four groups: three different homogeneous standard layers and one inhomogeneous layer were tested. Each group contained five wafers of lower and five wafers of better wafer quality, neighboring to the wafers discussed in Section 7.5.1 and also the same process flow was used. In Figure 7.21, two different box plots are shown, one representing the cell data for the lower quality material, the other representing the data for the better quality material. V_{OC}− V_{OC}(max) is shown as a function of the average Si-N bond density of the layers; V_{OC}(max) is the maximum V_{OC} found in the cells processed per a-SiN_x:H group.

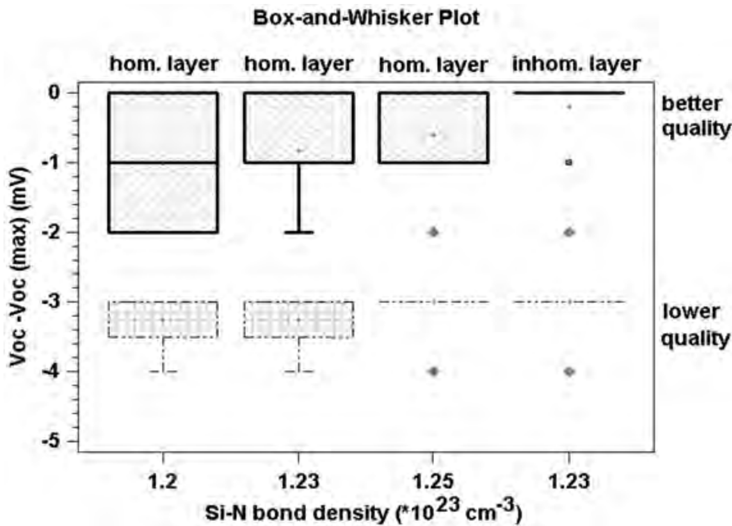

Figure 7.21: V_{OC} − V_{OC}(max) for inhomogeneous and inhomogeneous a-SiN_x:H layers as function of the average Si-N bond density of the layers.

No statistical difference is found, that is, the difference in V_{OC} between better and lower wafer quality is similar for all groups. As bulk passivation is determined by the N-H bonds, these results indicate that the position (or spread) of the N-H bonds in the layer is not important. This is in accordance with Boehme, who stated that the reduction of H during the dissociation processes is homogeneous throughout the film since any density gradient is instantly compensated for because of the high diffusivity of H [119].

7.5.3 Surface passivation

In a phosphorus emitter the number of minority carriers (holes) that are to be repelled from the surface is low, due to the field effect passivation of and the high recombination rate in the emitter. The *SRV* of the emitter itself was determined by Cuevas et al. [120] and for a standard high doped emitter, the effective *SRV* is between 10^4 and 10^5 cm/s. The inhomogeneous and homogeneous standard a-SiN$_x$:H layers give a different effective *SRV* on (100) DSP FZ, of 30 and 60 cm/s respectively, which is a significant difference in surface passivation. On the p-type cell level, this corresponds to a difference in 2-3 mV on average of more than 100 cells of both better and lower mc-Si quality and Cz material. The cells are modeled with PC1D [121] and the effect on V_{OC} as function of the effective *SRV* is shown in Figure 7.22, the experimentally obtained V_{OC} are also shown. The difference in V_{OC} for the two layers corresponds to the difference in surface passivation. The effect of Q_{f} is further described in Chapter 8.

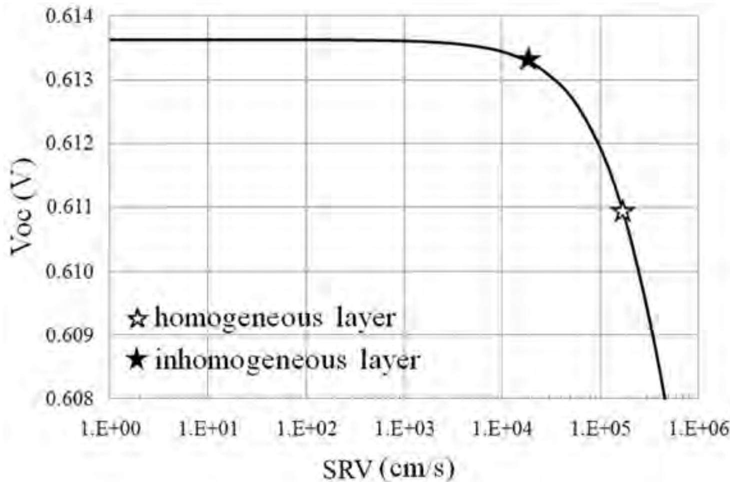

Figure 7.22: V_{OC} as function of *SRV* as modeled with PC1D. In the plot two points are given for the experimental data of the inhomogeneous and homogeneous layer.

7.6 Conclusions

Over 80 a-SiN$_x$:H layers are analyzed using FTIR, ellipsometry and QSSPC lifetime measurements to find a well-defined composition build-up of the layer for homogeneous layers. Clear correlations are found between optical properties n and k and the bulk properties like the Si-Si, Si-H, N-H and Si-N bonds and interface properties like Q_{f} and D_{it}. The real homogeneity

throughout both apparently homogeneous and inhomogeneous layers is investigated using FTIR, ellipsometry, ToF-SIMS, TEM and XPS. The results of using the different characterization equipment are compared and discussed. The effects of both homogeneous and inhomogeneous layers on solar cell efficiency are compared. It was found that small deviations in the layer do not have a large influence, but large variations in the composition will. It is also shown that reflection differences, giving a significant effect on cell level, can become insignificant after encapsulation. Bulk passivation for standard mc-Si solar cells is influenced by the N-H bond density and total mass density, but it is shown that the distribution of the N-H bonds in the layer is not critical. Surface passivation depends strongly on the composition of the a-SiN_x:H close to the interface and it is shown that differences in surface passivation can influence the V_{OC} of the solar cell. A difference of 2 mV was found.

The effective differences in solar cells performance, when encapsulated, for different a-SiN_x:H layers, are relatively small and give an indication of the wide process window for the a-SiN_x:H layers on the front side of solar cells.

Acknowledgments The authors acknowledge support from the European Commission Grant MMP3-SL-2009-228513, "Hipersol" as part of the 7th Framework Package, grant number 228513. Via our membership of the UK's HPC Materials Chemistry Consortium, which is funded by EPSRC (EP/F067496), this work made use of the facilities of HECToR, the UK's national high-performance computing service, which is provided by UoE HPCx Ltd at the University of Edinburgh, Cray Inc and NAG Ltd, and funded by the Office of Science and Technology through EPSRC's High End Computing Programme.

Chapter 8

Modification of interface properties of a-SiN_x:H and Si to improve surface passivation

M.W.P.E. Lamers[1], **K.T. Butler**[2], **J.H. Harding**[2], **A.W. Weeber**[1]

[1] ECN Solar Energy, P.O. Box 1, 1755 ZG Petten, the Netherlands.
[2] University of Sheffield, Western Bank, Sheffield S10 2TN, United Kingdom.

Solar Energy Materials & Solar Cells **106**, 17–21 (2012).

Abstract

Nitridation is the process in which, during the initial growth of a-SiN_x:H layers on Si surfaces, nitrogen is incorporated into the Si lattice near its surface. We show that this nitridation process affects the density of interface states (D_{it}) and fixed charges (Q_{f}) at the interface. These parameters determine the effective surface passivation quality of the layers. The nitridation can be tuned independently of the growth of a-SiN_x:H layers by using a plasma treatment prior to the actual a-SiN_x:H deposition. It is shown that Q_{f} can be varied from $2{\cdot}10^{12}$ to $15{\cdot}10^{12}$ cm^{-2} without changing the a-SiN_x:H deposition process. It is demonstrated that in our case and processing window, Q_{f} is the determining factor in surface passivation quality in the range of $2{\cdot}10^{12}$ to $8{\cdot}10^{12}$ cm^{-2}. For higher values of Q_{f}, D_{it} has increased significantly and has become dominant thereby reducing the passivation quality. It is shown that the passivation can be controlled independently of the a-SiN_x:H deposition process. In completed solar cells the effect of the controlled Q_{f} and D_{it} is studied. On n-type solar cells, due to increased depletion, increases in Q_{f} and D_{it} resulted in a drop in open-circuit voltage, V_{OC}, of over 20 mV. On p-type solar cells, where the Q_{f} results in accumulation, the effect was negligible.

8.1 Introduction

Hydrogenated amorphous silicon nitride (a-SiN_x:H) is the standard antireflection and passivating layer, for both surface and bulk defects, in wafer-based silicon solar cells. Commonly, the layer is deposited using plasma-enhanced chemical vapor deposition (PECVD). The physical properties of the layer have previously been correlated to cell output properties like the open-circuit voltage V_{OC} [81, 82]. In general, the optimized a-SiN_x:H layer is a compromise of optical (antireflection and absorption) properties, and bulk and surface passivation. Si-rich a-SiN_x:H layers show good surface passivation, but are highly absorbing and cannot be used for solar cell application. N-rich layers show good optical properties, but are less effective in surface passivation. In this paper our aim is to better understand the surface passivating properties and open ways to de-couple the surface passivating properties from the other properties (bulk passivation and optical) that should finally result in better solar cells. A qualification is made of the effect of surface passivation on solar cells depending on the dopant type and doping density at the surface, and independent of bulk passivation.

The total surface passivation is determined by the combined effect of two mechanisms: so-called chemical passivation by reducing the density of interface states (D_{it}) and field-effect passivation by the number of fixed charges (Q_f) at the interface with Si. A low D_{it} reduces the recombination rate at the interface. For Q_f the effect on surface passivation depends, besides other parameters, on the doping type and doping density [39]. For lightly doped material a high Q_f will increase the field-effect contribution to the surface passivation. For doping types with opposite polarity to the fixed charge, the field effect is governed by accumulation. For doped material with the same polarity the field effect is governed by inversion. For highly doped materials with opposite polarity to the fixed charge, a higher Q_f can (slightly) improve the surface passivation by accumulation. For highly doped materials with the same polarity as Q_f the surface passivating will decrease because of depletion. More information is given by Aberle [39].

As Q_f and D_{it} are properties of the interface of a-SiN_x:H/Si, this indicates that they are determined by the initial growth of the a-SiN_x:H layer. More profoundly, Q_f is related to the interface structure between the materials (a-SiN_x:H and Si) causing a local-field effect as was described by Aspnes [112]. This local field depends on the different polarizabilities of each material and the variation in volume density of these polarizabilities over distance at the interface. The different components in bulk a-SiN_x:H, which can be charged have been linked to the so-called K- and N-centers [113]. These centers are respectively $^*Si{\equiv}N_3$ and $^*N{=}Si_2$. * indicates that these centers can be neutral, positive, negative or bonded to H. Assuming that K- and N-centers also occur at the interface, this leads to the conclusion that Q_f

is determined by the variation and volume fractions of K- and N-centers at the interface region of a-SiN$_x$:H/Si. The number of K-centers that is bonded to H can be estimated from the Si-H peak in a Fourier transform infrared spectroscopy (FTIR) [43] spectrum and is correlated to Q_f and D_{it}. A peak location close to 2220 cm^{-1} indicates relatively more K-centers. Both the K- and N-centers have also been described as the origins of the dangling bonds at the interface and therefore related to D_{it} [113]. Therefore, when the concentration of (charged) K- and/or N-centers increases, Q_f increases correspondingly. Simultaneously, as the volume fraction of the centers is increased, the number of (unpassivated) dangling bonds also increases and, therefore, D_{it} increases as well. Additionally, it is shown in this paper that the Q_f might also be connected to local distortions in the SiN$_x$:H.

a-SiN$_x$:H, as described in this article, is deposited using remote-PECVD. In the plasma the process gases, typically SiH_4 and NH_3, are dissociated. Subsequently, a thin film a-SiN$_x$:H can now grow on the substrate surface. During the initial growth of a-SiN$_x$:H the surface is nitridated, which can be described as N-insertion into the Si surface. The interface region itself is approximately found to be 1-3 nm wide. Depending on the deposition temperature and gas flow of NH_3 different bonds and nitridation characteristics are obtained as observed by Dai *et al.* [122]. Up to temperatures of 300°C no surface alteration is observed. Above 350°C -NH_2 starts to adhere to the Si surface. Above 400°C N begins to be inserted into the Si-Si bonds of the surface of the Si crystal and the degree of this insertion increases with temperature. That this nitridation has indeed a direct relation with Q_f was shown by Takakura *et al.*, though no difference in D_{it} was observed [123].

In this article we will demonstrate the variations in Q_f and D_{it} for different SiN$_x$:H layers. Additionally, we show that different plasma pretreatments prior to SiN$_x$:H deposition cause different nitridation profiles and thus different surface passivating properties while applying the same a-SiN$_x$:H layer. The effect of the nitridation on the surface passivating properties for completed solar cells is shown as well. This indicates that separate control of bulk and interface properties of a-SiN$_x$:H is possible.

8.2 Layer study

8.2.1 General a-SiN$_x$:H

During a-SiN$_x$:H deposition, different gas ratios and temperatures determine both the initial growth conditions and bulk properties [27, 81, 114]. As the initial growth of the a-SiN$_x$:H layer determines both nitridation and the Q_f and D_{it} values, a clear correlation is found between the properties of the layer and Q_f and D_{it}. To show this, samples were prepared using 275 µm thick p-type

FZ (100) wafers, which were double side mirror polished with a base resistivity of 2.5 Ωcm. Remote PECVD was used to deposit 80-100 nm a-SiN_x:H layers with different composition on one side of the wafer. Deconvoluted bond densities were calculated from FTIR data, and after 300 nm aluminum deposition on the samples to create Metal-Insulator-Silicon (MIS) structures, Q_f and D_{it} were determined using Capacitance-Voltage (CV) MIS analysis. The relations between the Si-H bond density in the H-Si-N_3 configuration (at 2220 cm^{-1}), the total Si-H bond density, the N-H bond density, the Si-N bond density in the locally distorted configuration (at 790 cm^{-1}), the refractive index n (at 633 nm as determined with ellipsometry), the effective surface recombination velocity (SRV) and Q_f are shown in Figures 8.1a and 8.1b. A clear and positive correlation between Q_f and D_{it} is found and can be seen in Figure 8.1b. A similar relation between n, the Si-H bond density in the H-Si-N_3 configuration and the Si-N bond density in the locally distorted configuration was described by Demichelos *et al.* [124] and a similar trend between n and Q_f was found by Wolf *et al.* [125]. The results obtained in literature regarding the exact conversion values needed to convert the area of the FTIR spectrum per bond to a density is not conclusive, therefore we decided to show the data in peak area of the bond density [44]. The Q_f found in our experiments is relatively high. To confirm the validity of the results, a comparison was done with SiN_x:H fabricated with a batch PECVD, which showed similar values as obtained by Demichelos *et al.* [124]. Also, known Al_2O_3 layers were measured and comparative values were obtained.

With increasing N content in the layer, corresponding to a decreasing n, Q_f increases. This can be explained since, as the number of charged K-centers increases, the neutral dangling bonds (uncharged and non-passivated K-centers) increase as well. However, as the N-content in the SiN_x:H layer increases further ($n <$ 2-2.1) the layer becomes less distorted as the Si-N bond density at 790 cm^{-1} shows a steep decrease; also, the layer shows a sharp increase in N-H bond densities while the Si-H peak is very small or no longer observed in the FTIR spectrum. For these layers, the number of K-centers decreases as the distortion lowers, as consequently Q_f reduces. The effective SRV is a combined effect of Q_f and passivation of dangling Si bonds by H (high Si-H bond density). For optimal light management of a solar cell, the refractive index should be around 2.05 [17, 18]; for optimal bulk passivation a Si-N bond density of 1.2-1.3$\cdot 10^{23}$ /cm^3, which corresponds to a peak area of 560-580 cm^{-1}, is necessary in combination with sufficient N-H bonds [15, 81, 82]; these requirements can be met simultaneously but do not provide a low effective SRV as is clear from Figures 8.1a and 8.1b. To tune the effective SRV separately from the bulk properties, we focus on changing the N content (and thus K-centers) at the surface by tuning the nitridation prior to the bulk SiN_x:H layer deposition.

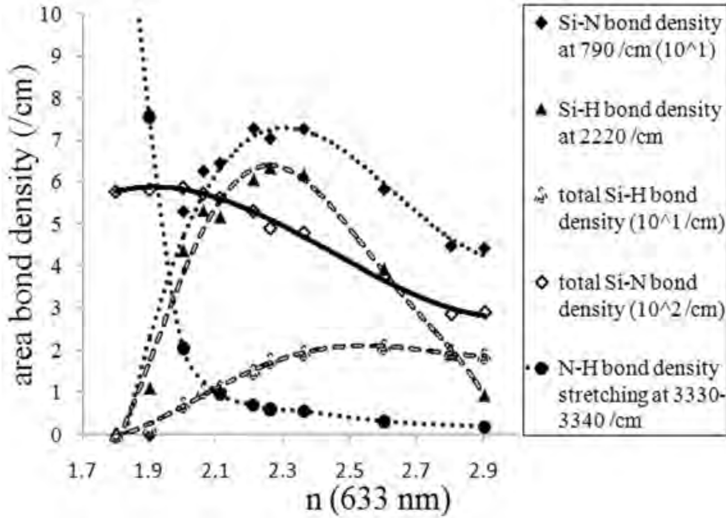

(a) Relation between (the peak areas of) the Si-H bond density, the deconvoluted Si-H bond density at 2220 cm^{-1}, the Si-N bond density, the deconvoluted Si-N bond density at 790 cm^{-1} (distorted), N-H bond density and n.

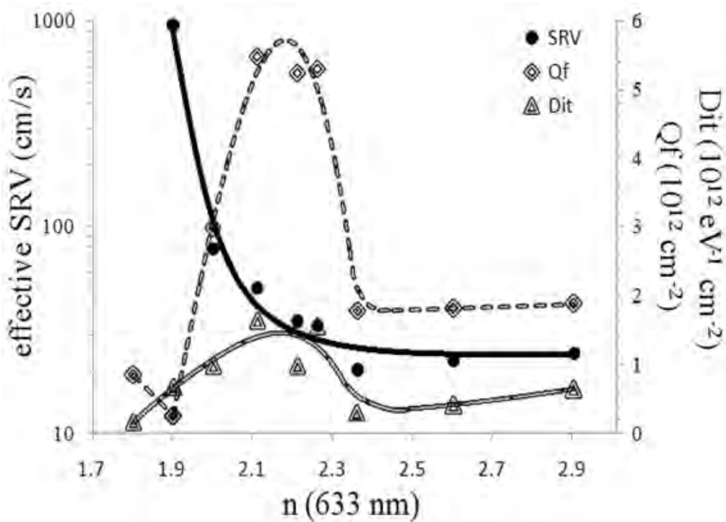

(b) Relation between the effective SRV, Q_f and n.

Figure 8.1: Relation between the bond densities, effective SRV, Q_f and n at 633 nm.

8.2.2 Nitridation of the Si surface

To study the effect of nitridation on passivation in more detail, various NH_3 plasma treatments prior to a-SiN_x:H layer deposition were done. To study possible dependence on dopant type and crystal orientation, two different materials were used: 275 µm thick p-type FZ (100) wafers, which were double side mirror polished with a base resistivity of 2.5 Ω·cm, and 275 µm thick n-type FZ (111) wafers, which were double side mirror polished too, but with a base resistivity of 3.5 Ω·cm. Shortly before nitridation, the wafers received an HF dip to remove the surface oxide. As mentioned above the total process consisted of a NH_3 plasma pretreatment to vary nitridation followed by a-SiN_x:H layer deposition. The latter was the same for all pretreatments. Both steps in the process were performed using a remote PECVD system. The effective lifetime of the minority carriers, which is determined by the bulk lifetime and surface passivating quality, was measured using symmetric test structures with nitridation and a-SiN_x:H coating on both sides. Samples with nitridation and coating on one side were used to determine Q_f and D_{it} using CV-MIS. NH_3 plasma pretreatments were carried out at temperatures between 300 and 500°C.

In Figures 8.2a and 8.2b the effect of the temperature of a NH_3 plasma on Q_f and D_{it} is shown. A positive correlation between Q_f and D_{it} is found. Already at 300°C a small effect can be seen, which suggests that the onset of nitridation might start at somewhat lower temperature than suggested by Dai [122]. The nitridation effect can be seen by the increase in Q_f. In Figure 8.2b, the effect on the effective *SRV* is shown. A lower effective *SRV*, thus better passivation, is obtained when the surface is slightly nitridated and so Q_f values up to about $8 \cdot 10^{12}$ cm^{-2} are seen, corresponding to pretreatment temperatures of 400 °C. In this case and according to Dai et al. [122], NH_2 starts to adhere to the surface, but no or hardly any insertion of N in the Si-Si bonds takes place. The reduction in effective *SRV* compared to samples without plasma pretreatment (nitridation) at 300°C might be related to the onset of nitridation of the thin native oxide present on the wafer surface. Above 450°C N insertion into Si-Si takes place, which corresponds to a higher effective *SRV* and is related to a further increase in Q_f and the now dominant high D_{it}. A maximum was found at 400°C for n-type (111) and at 300°C for p-type (100). The results clearly show that tuning of the effective *SRV* is possible, independently of the bulk properties of the SiN_x:H layer.

8.3 Solar cell study

8.3.1 Solar cell and semi-fabric processing

Solar cells and semi-fabrics were fabricated using both n-type monocrystalline (mono) Cz Si and p-type (multicrystalline (multi) Si and mono Cz Si) wafers to study the effect of the nitridation and fixed charge on the cell output.

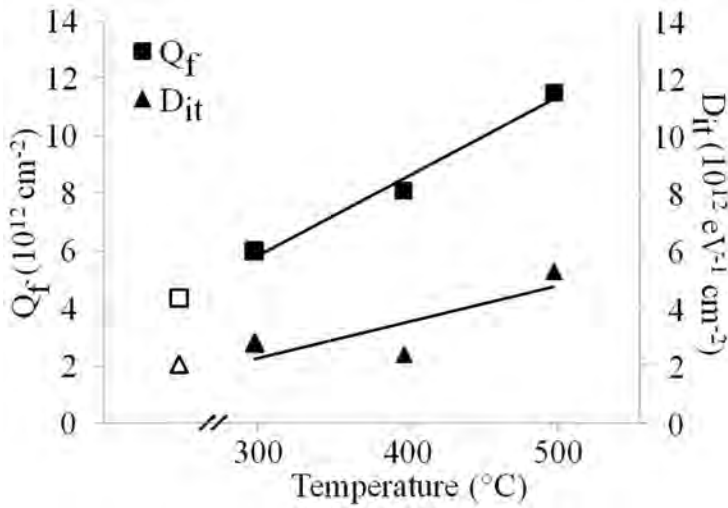

(a)

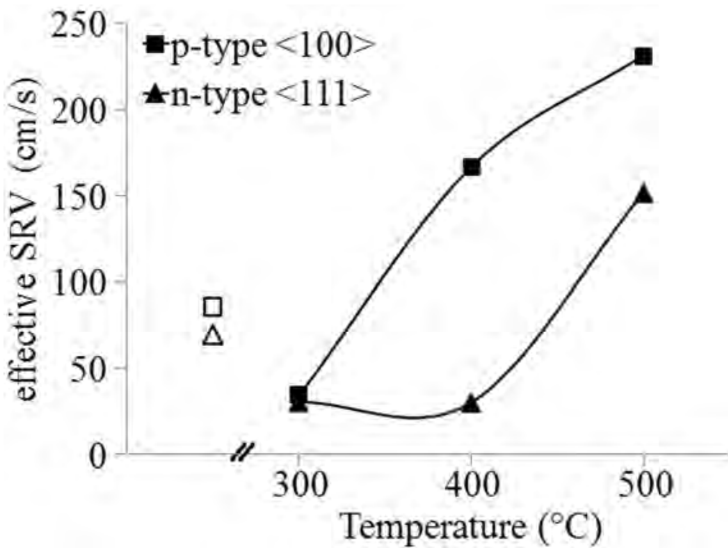

(b)

Figure 8.2: The effect of the temperature of a NH_3 plasma treatment on Q_{f} and D_{it} and effective SRV for a minority carrier density of $1{\cdot}10^{15}$ cm^{-3} as measured on p-type (100). Closed and open symbols are, respectively, samples with and without pretreatment. The lines are guides to the eye.

Semi-fabricated Si wafers were textured with an alkaline or acidic procedure for respectively mono and multi Si wafers. The emitter (boron for n-type base material and phosphorus for p-type) was created with a high temperature diffusion step. Subsequently, the glass was removed and the wafers were cleaned and passivated with SiN_x:H.

The structures of the fabricated n-type and p-type cells are shown in Figure 8.3.

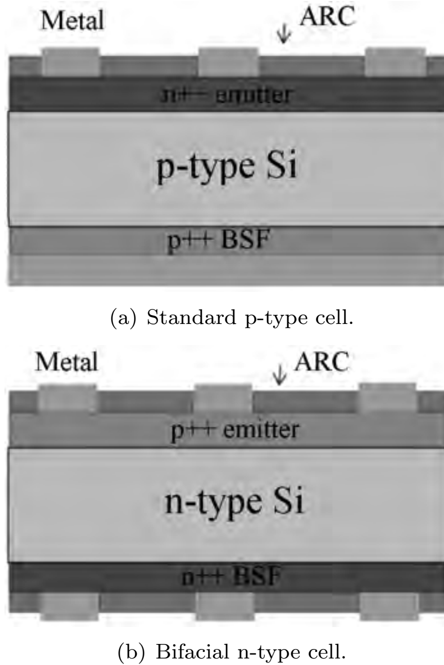

(a) Standard p-type cell.

(b) Bifacial n-type cell.

Figure 8.3: Structure of a solar cell.

For p-type cells the process started with an alkaline or acidic texture formation for respectively mono or multi Si wafers. The emitter was formed using $POCl_3$ diffusion and after glass removal and cleaning the wafers were passivated with SiN_x:H. Screen printing was used to apply the metalization. At the rear side the area was fully printed with aluminum and at the front side a silver H-pattern was used. Contacting is obtained by a co-firing procedure. The n-type cells were made using an alkaline texture, after which the boron emitter and phosphorus back-surface-field were created in high temperature diffusion steps. After glass removal and cleaning, the wafers were passivated on both sides with SiN_x:H. The contacting of the metal pastes was done in a co-firing procedure. The processes are described in more detail by the author *et al.* [24] and by Weeber *et al.* [126] respectively. Prior to the a-SiN_x:H layer deposition on the front side, the cells are given a plasma NH_3 pretreatment to alter Q_f and D_{it}.

The square p-type multi Si wafers were 210 µm thick with a base resistivity of 1.3 Ω·cm. The 180 µm thick and square p-type Cz mono Si had a base resistivity of 1.3 Ωcm. The semi-square n-type Cz mono Si had a base resistivity of 2.5 Ω·cm and were 180 µm thick. All wafers were sized 156×156 mm^2.

8.3.2 Effect of doping density

Two types of base doping are currently used within the silicon solar cells industry. These are phosphorus (n-type) and boron (p-type). The required emitters of these solar cells are of opposite character to the base doping, respectively boron and phosphorus. For n-type emitters the positive fixed charge of the SiN_x:H will result in accumulation. For p-type emitters the positive fixed charge will result in depletion, and in case of low doping, in inversion, which in final solar cells will induce inversion layer shunting, as shown by Dauwe [38]. The extent of the effect of the surface passivation, significantly depends on the quality of the emitter. High recombination rates in the emitter will reduce any effect of surface passivation to insignificant. This is also reflected in the Shockley-Read-Hall formalism in which the surface recombination significantly depends on the doping density [35]. Therefore, the effect of doping must be included in order to examine the effect of Q_f on the cell output.

8.3.3 Relation Q_f and implied V_{OC}

The V_{OC} is directly related to passivation and hence this factor has been chosen to show. In Figure 8.4a, V_{OC} is given as a function of Q_f for n-type cells, both modeled with PC1D and experimentally found. As Q_f and D_{it} increase simultaneously with increased nitridation, the trend in V_{OC} is due to the combined effect of increased D_{it} and increased depletion caused by higher Q_f. With increasing positive fixed charge more depletion occurs at the interface, reducing V_{OC} up to 20 mV. Also the effects in other cell parameters like J_{SC} and FF were very significant, a drop of 2 mA/cm^2 and 1% in FF were found. This strong effect, independent of the a-SiN_x:H deposited, shows the extent of the influence of the surface passivation. PC1D simulations of the cell were in accordance with the cell results and showed that for negative fixed charges the V_{OC} is not limited by the surface passivation, but by the recombination in the emitter itself.

A similar observation can be made for p-type solar cells, as shown in Figure 8.4b. Implied V_{OC} as determined from p-type mono semi-fabricated which had a standard emitter with a high surface doping of $8 \cdot 10^{20}$ atoms/cm^3 as determined with Secondary Ion Mass Spectroscopy (SIMS), showed not to be influenced by Q_f due to different nitridations. To illustrate the effect of the maximal doping of the emitter PC1D modeling [121] was done and

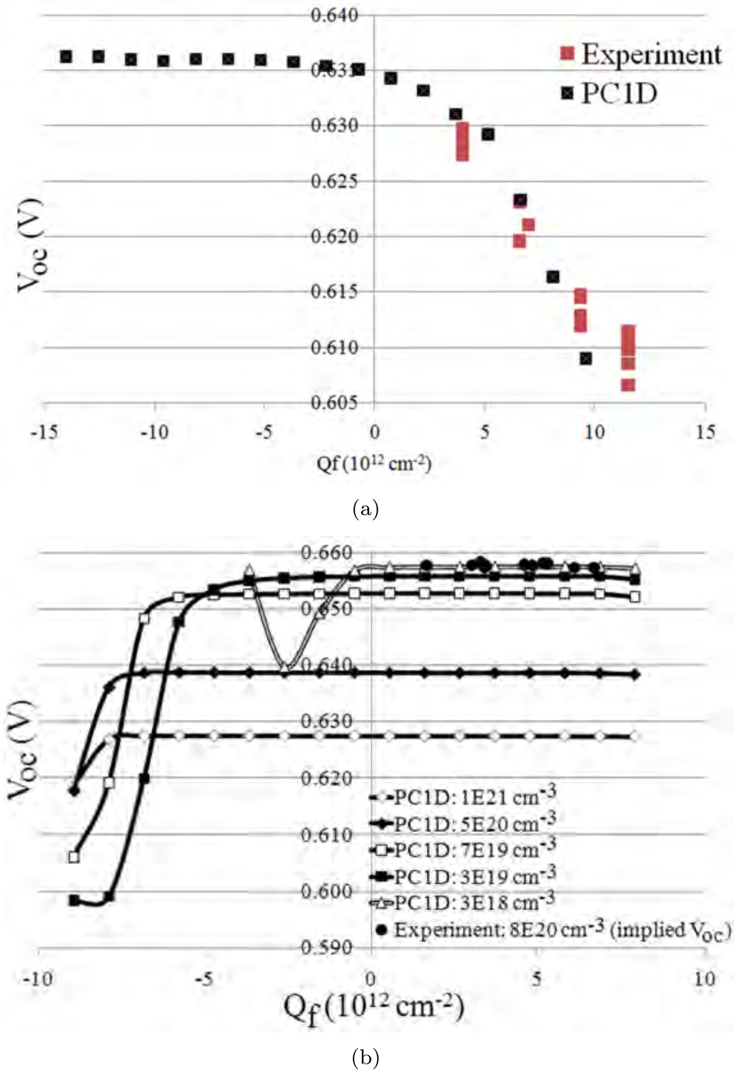

Figure 8.4: The V_{OC} of the n-type solar cells (a) and p-type solar cell (b) as function of Q_{f} both modeled in PC1D and measured experimentally. For the p-type solar cell the modeling results are given for different values of the phosphorus surface concentration, as well as experimental data for a phosphorus surface concentration of $8{\cdot}10^{20}$ atoms/cm^3.

shown here as a function of the fixed charge. For the simulations a p-type cell was modeled, using a stack of two Gaussian curves to simulate the doping of the phosphorus emitter with a depth of 300 nm. The base resistivity for the p-type wafer was 1.3 Ω·cm. The lifetime of the minority carriers in p-type wafer material was taken to be 200 µs. It can be seen that due to the high doping level of phosphorus and the high recombination rate in the emitter, the dependence on surface passivation is negligible, even surface passivation schemes with negative fixed charges, like shown by Hoex [127], can be used to coat the surface. However, with reducing doping density in the emitter, the sensitivity for the surface passivation increases and with negative fixed charges the V_{OC} will reduce again due to depletion at the interface. For a low doping density of $3{\cdot}10^{18}$ atoms/cm^3 even inversion will occur, but due to inversion layer shunting this will further reduce the solar cell efficiency. This effect of shunting cannot be simulated with PC1D.

8.4 Modeling of the SiN_x:H/Si interface

Molecular dynamics (MD) simulations of the effect of increased nitridation were performed using de Brito Mota's [115] parameterization of the Tersoff potential [116]. Heavier nitridation increases the recombination inside the Si crystal. This correlates with the increased presence of K- and N-centers at the interface as shown in Figure 8.5. Since charge carriers will hardly penetrate into the a-SiN_x:H region only the defect centers at the surface will be expected to affect the recombination rates. As the N gradient width is increased from 2 up to 5 nm the defect concentration moves steadily away from the interface. The plots show a clear increase in volume fraction of both the K- and N-centers, which correlate to the experimentally found increase in Q_f and D_{it} due to heavier nitridation. The modeling and results are described in more detail in Chapter 10.

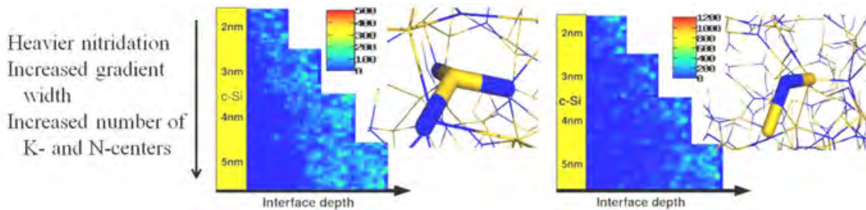

Figure 8.5: Molecular Dynamics Simulations of nitridation on: (left) K-centers; (right) N-centers. In the figures the a-SiN_x:H is represented in blue, the c-Si bulk is yellow and the legends refer to the density of K- and N-centers identified by analyzing the simulation trajectories. The subfigures (horizontal and bar-like) in each plot with 2, 3, 4 and 5 nm gradient width show that heavier nitridation results in an increased number of K and N centers.

8.5 Conclusions

The incorporation of N into the Si surface is a process called nitridation. This nitridation is closely related to the density of interface states (D_{it}) and fixed charges (Q_f), which are parameters that determine the surface passivation quality in a solar cell. Increasing the nitridation by use of a plasma treatment prior to a-SiN$_x$:H deposition alters Q_f from $2{\cdot}10^{12}$ to $15{\cdot}10^{12}$ cm^{-2} and the correlated D_{it} from $2{\cdot}10^{12}$ to $16{\cdot}10^{12}$ eV^{-1} cm^{-2}.

In completed solar cells the effect of the controlled Q_f and D_{it} is studied. On n-type solar cells, due to increased depletion, increases in Q_f and D_{it} resulted in a drop in open-circuit voltage, V_{OC}, of over 20 mV. On p-type solar cells, where the Q_f results in accumulation, the effect was negligible. The effects on both types of solar cells were confirmed with PC1D modeling.

Molecular dynamics modeling of the nitridation effect shows that with increased nitridation the volume and fraction of the K- and N-centers in the Si bulk increase and are located in the first few nm from the interface. This correlates to the experimentally found increase in both Q_f and D_{it}.

Acknowledgments The authors acknowledge support from the European Commission Grant MMP3-SL-2009-228513, "Hipersol" as part of the 7th Framework Package, grant number 228513. Via our membership of the UK's HPC Materials Chemistry Consortium, which is funded by EPSRC (EP/F067496), this work made use of the facilities of HECToR, the UK's national high-performance computing service, which is provided by UoE HPCx Ltd at the University of Edinburgh, Cray Inc and NAG Ltd, and funded by the Office of Science and Technology through EPSRC's High End Computing Programme.

Chapter 9

The interface of a-SiN_x:H and Si: Linking the nano-scale structure to passivation quality

M.W.P.E. Lamers[1], L.E. Hintzsche[2], K.T. Butler[3], P.E. Vullum[4], C-M. Fang[2], M. Marsman[2], G. Jordan[2], J.H. Harding[3], G. Kresse[2], A.W. Weeber[1]

[1] ECN Solar Energy, P.O. Box 1, 1755 ZG Petten, the Netherlands
[2] University of Vienna, Faculty of Physics and Center for Computational Materials Science, Sensengasse 8/12, A-1090 Vienna, Austria
[3] University of Sheffield, Western Bank, Sheffield S10 2TN, United Kingdom
[4] SINTEF, Materials and Chemistry, Box 4760 Sluppen, NO-7465 Trondheim, Norway

Solar Energy Materials & Solar Cells, **120**, 311–316 (2014).

Abstract

Surface passivation by hydrogenated amorphous silicon nitride (a-SiN_x:H) is determined by the combined effect of two mechanisms: so-called chemical passivation by reducing the density of interface states ($D_{\rm it}$) and field-effect passivation as a result of the number of fixed charges ($Q_{\rm f}$) at the interface with Si. These are related to the K defect center: *Si≡N_3. Defects near the interface (in both Si as in a-SiN_x:H), modeled by force field Molecular Dynamics (MD) and *ab initio* Density Functional Theory (DFT), can be related to $Q_{\rm f}$ and $D_{\rm it}$ measured experimentally using CV-MIS (Capacitance-Voltage Metal Insulator Semiconductor). The compositional build-up at the interface as is determined by HRTEM (High Resolution Transmission Electron Microscopy) and modeled by MD correspond to each other; a gradual change from Si to the bulk a-SiN_x:H composition in the first 2 nm of the a-SiN_x:H layer. At the c-Si side a highly distorted layer (about 1-3 nm) caused by the insertion of N and/or H is found. The adhesion of N at the Si surface and insertion of N in the first few nm's of the Si substrate is called nitridation and can be altered by using a NH_3 plasma prior to a-SiN_x:H deposition. HRTEM image analysis shows that by varying the nitridation of the Si surface the amount and penetration depth of N in the first few nm's of the Si substrate were altered. Using MD modeling, it is shown that this process changes the amount of K-centers at the surface, which explains the variation in $Q_{\rm f}$ and $D_{\rm it}$ that is found experimentally. *Ab initio* DFT studies of a-SiN_x:H (x=1.17) show that K-centers and Si atoms in distorted configuration, are the dominating defects resulting in a higher $D_{\rm it}$. For lower x (x=1) the $D_{\rm it}$ caused by K-centers increases, which is also observed experimentally.

9.1 Introduction

Hydrogenated amorphous silicon nitride (a-SiN_x:H) is the standard antireflection and passivating layer, for both surface and bulk defects, in wafer-based silicon solar cells. The passivating properties of the layer have previously been correlated to cell output properties like the open-circuit voltage V_{OC} [81, 82]. The total surface passivation is determined by the combined effect of two mechanisms: so-called chemical passivation by reducing the density of interface states (D_{it}) and field-effect passivation as a result of the number of fixed charges (Q_f) at the interface with Si. A low D_{it} reduces the recombination rate at the interface. For Q_f the effect on surface passivation depends, besides other parameters, on the doping type and doping density [39]. As Q_f and D_{it} are properties of the interface of a-SiN_x:H/Si, this indicates that they are determined by the initial growth of the a-SiN_x:H layer. The relation between Q_f, D_{it} and the a-SiN_x:H layer properties was discussed in Chapter 8.

Q_f is related to the interface structure between the materials (a-SiN_x:H and Si) causing a local-field effect as was described by Aspnes [112]. This local field depends on the different polarizabilities of each material and the variation in volume density of these polarizabilities over a certain distance at the interface. The different components in bulk a-SiN_x:H, which can be charged have been linked to the so-called K- and N-centers [113]. These centers are respectively *$Si{\equiv}N_3$ and *$N{=}Si_2$, * indicates that these centers can be neutral, positive, negative or bonded to H. Assuming that K- and N-centers also occur at the interface, may lead to the conclusion that Q_f is determined by the variation and volume fractions of K- and N-centers at the interface region of a-SiN_x:H/Si.

In this paper our aim is to better understand the surface passivating properties by examining the interface both on electrical and physical properties, and comparing the results to force field Molecular Dynamics (MD) and *ab initio* Density Functional Theory modeling. We show that the compositional build-up at the interface as is measured and modeled correspond to each other; a gradual change from Si to the bulk a-SiN_x:H composition in the first 2 nm of the a-SiN_x:H layer. At the c-Si side a highly distorted layer (about 1-3 nm) caused by the insertion of N and/or H is found. The adhesion of N at the Si surface and insertion of N in the first few nm's of the Si substrateT is called nitridation and can be altered by using a NH_3 plasma prior to a-SiN_x:H deposition. We show by High Resolution Transmission Electron Microscopic (HRTEM) image analysis that by varying the nitridation of the Si surface the amount and penetration depth of N in the first few nm's of the Si substrate were altered. Using MD modeling, we show that this process changes the amount of K-centers at the surface, which explains the variation in Q_f and D_{it} that is found experimentally. Furthermore, with *ab initio* modeling we

show that a large amount of H is present at the surface, needed to passivate the dangling Si bonds. Even more, we propose that the location of Q_f is stretched over the interface, starting a few nm in the c-Si to around 2 nm in the a-SiN_x:H, the magnitude can be altered by changing the concentration gradient, more specifically of N in the c-Si. This can be achieved by using a NH_3 plasma prior to a-SiN_x:H deposition.

9.2 Results

9.2.1 A graded interface

a-SiN_x:H was deposited by remote Plasma Enhanced Chemical Vapour Deposition (PECVD) on a double side mirror-polished (100) 2.5 Ω·cm p-type and (111) n-type 3.5 Ω·cm FZ Si substrates, 275 µm thick. Cross-sectional TEM specimens were prepared by mechanical polishing, dimpling and Ar^+-ion sputtering using liquid nitrogen to cool the sample. The acceleration voltage was progressively reduced to 1.0 keV during the final stage of the Ar^+-ion sputtering to minimize sample damage. TEM was performed with a JEOL 2010F operated at 200 kV. The HRTEM image of the (100) sample is shown in Figure 9.1.

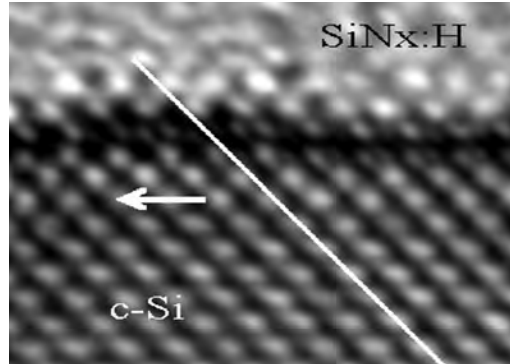

Figure 9.1: HRTEM image of a-SiN_x:H/c-Si interface of the (100) sample.

A white line is drawn over the high amplitude periodic signal. It is observed that the first few atomic layers of c-Si at the surface show a distorted expanded crystal structure and that the high amplitude signal is shifted left and lowered in intensity. This indicates the presence of large strain and the possible insertion of other smaller atoms. A dark band is seen at the interface, which can indicate that light atoms, like N and/or H, are present. Such a dark band is not visible at a SiO_2/c-Si interface [128]. Large strain was also found in the (111) oriented sample as shown in the inverse fast Fourier transformed (FT) image (Figure 9.2c), and corresponds to the dark band in Figure 9.2a. No such strain was found in the c-Si bulk (Figure 9.2b).

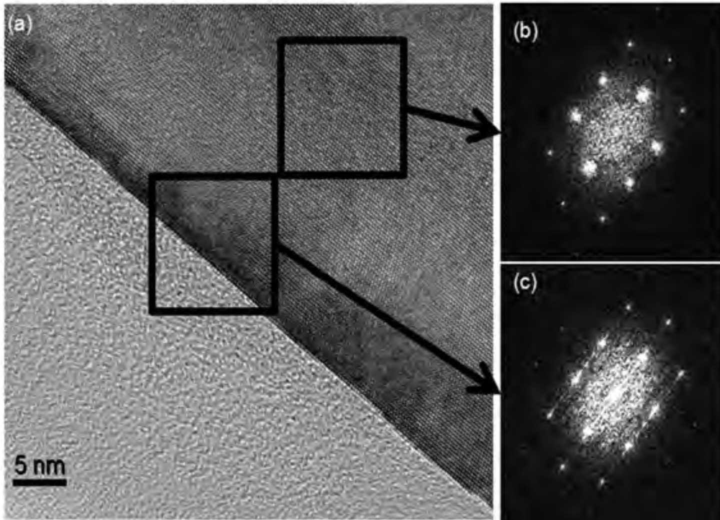

Figure 9.2: (a)HRTEM image of a-SiN_x:H/c-Si interface of the (111) sample; (b) FT image of c-Si; (c) FT image of the interface of a-SiN_x:H and c-Si.

On the a-SiN_x:H side of the interface a 2 nm wide gradient was found in the plasmon loss energy with Electron Energy Loss Energy Spectroscopy (EELS) as shown in Figure 9.3. In the figure it can be seen that the plasmon loss energy increases from 17.0 eV to 19.8 eV over 3 nm (from -1 nm to 2 nm). From the high-loss region of the EELS spectrum also the chemical composition can be determined and this shown in Figure 9.4. Park *et al.* showed a relation between the plasmon loss energy and the composition of a-SiN_x:H [129] and we found that this relation is also valid for the interface. The relation between plasmon loss energy and composition combined with the increase in plasmon loss energy occurring at the Si side (1 nm) indicates the presence of N in the first few nm's of the Si substrate, besides H. The presence of N was also found in the first few nm's of the Si substrate by Ikarashi *et al.* [130]. The composition is determined from the $L_{2,3}$ peak onset in the high-loss region of EELS (around 99 eV) and it could not be found to change for $t < 0.5$ nm; this indicates that the N content is relatively low.

9.2.2 Nitridation, Q_f, D_{it} and K-centers

In the plasma, the precursor gasses to deposit a-SiN_x:H, typically SiH_4 and NH_3, are dissociated. Subsequently, a thin film a-SiN_x:H can now grow on the substrate surface. During the initial growth of a-SiN_x:H the surface is nitridated, which can be described as the adhesion of N at the Si surface and insertion of N in the first few nm's of the Si substrate. This nitridation is temperature dependent. Typically, adhesion of $-NH_2$ to the Si surface

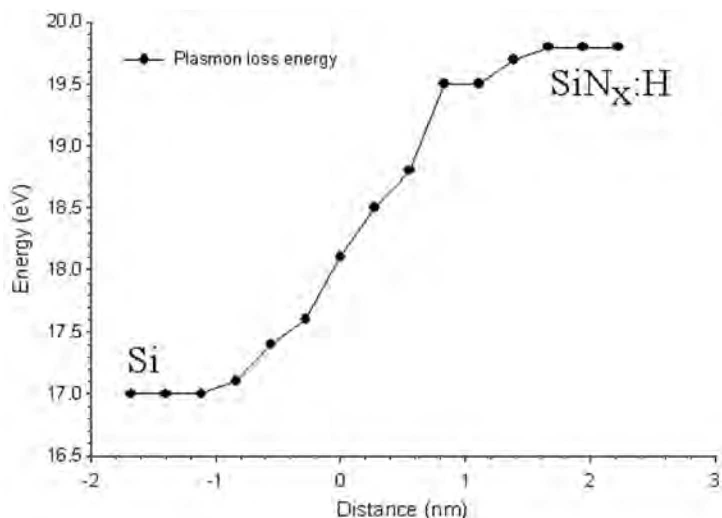

Figure 9.3: The plasmon loss energy over the interface of the (100) sample. The interface is at 0 nm.

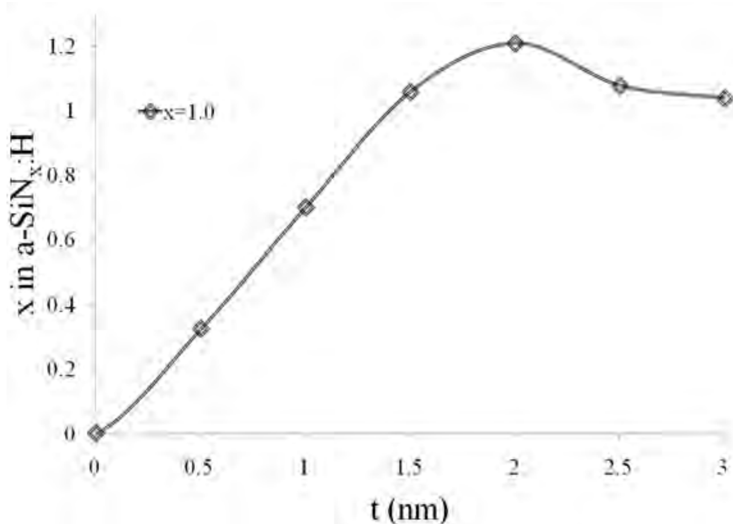

Figure 9.4: Experimentally determined change in composition at the interface in a-SiN$_x$:H of the (100) sample. The interface is at 0 nm.

starts above 350°C, N insertion into the Si-Si bonds begins above 400°C and this increases with temperature [122]. To study the effect of nitridation on passivation in more detail, NH_3 plasma pretreatments prior to a-SiN_x:H layer deposition were performed on 275 μm thick p-type FZ (100) wafers, which were double side mirror polished with a base resistivity of 2.5 Ω·cm. Shortly before nitridation, the wafers received a short HF dip to remove the surface oxide. Samples with nitridation and coating on one side were used to determine Q_f and D_{it} using CV-MIS. CV-MIS samples were prepared by evaporating 300 nm aluminum on the full area of the uncoated rear side and circular dots with varying sizes (0.1 - 1.91 mm^2) on the coated front side. The thickness of the a-SiN_x:H layer was determined using spectroscopic ellipsometry. NH_3 plasma pretreatments were carried out at temperatures between 300 and 500°C. In Figure 9.5 the effect of the temperature of a NH_3 plasma on Q_f and D_{it} is shown (see also Chapter 8).

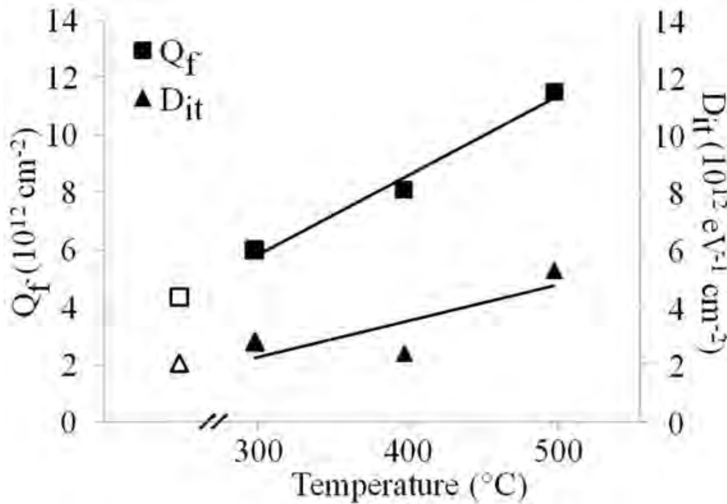

Figure 9.5: The effect of the temperature of a NH_3 plasma treatment on Q_f and D_{it} on p-type (100). Open and closed symbols are samples without respectively with pretreatment. The lines are guides to the eye (see Chapter 8).

A positive correlation between Q_f and D_{it} is found. It can be seen that already at 300°C a small effect is visible, which suggests that the onset of nitridation might start at somewhat lower temperature than suggested by Dai *et al.* [122]. The nitridation effect can be seen by the increase in Q_f and D_{it}. The relation between nitridation, measured lifetime and solar cell efficiency is shown elsewhere by the authors (see Chapter 8). The nitridation effect is also observed by analyzing the plasmon loss energy as was measured with an EELS line scan on the samples as is shown in Figure 9.6.

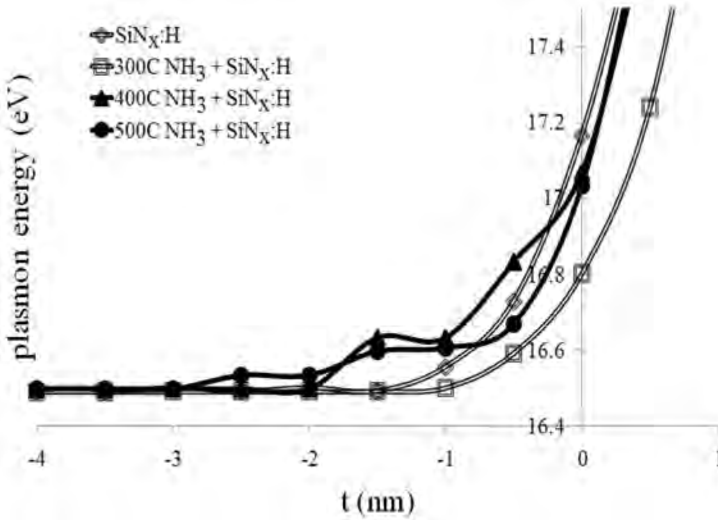

Figure 9.6: Plasmon loss energy over the interface for different treatments of NH_3 prior to a-SiN_x:H deposition. Each line represents the averaged value of three line scans.

For NH_3 treatments a rise in plasmon loss energy is found on the c-Si side of the interface, signaling a larger incorporation of N with increasing temperature. This result is confirmed by MD simulation on graded interfaces. It shows a higher amount of N in a-SiN_x:H at the interface with Si, which leads to a higher defect concentration as is shown in Figure 9.7. This higher defect concentration results in higher Q_f. Also, the MD modeling which compares a sharp interface with a graded one, shows that gradual interfaces show significantly lower defects (see Chapter 10).

A clear gradient in the composition of a-SiN_x:H at the interface is found and also the presence of N is detected at the silicon side of the interface. With the NH_3 plasma pretreatment the nitridation of the Si surface is altered as shown by an increase in plasmon loss energy at the c-Si side of the interface. Experimentally, it is found that this corresponds to an increase in Q_f, while MD modeling shows an increase in K-centers. The variation in volume density of the K-centers at the interface creates a local field, which we propose is the cause of the macroscopically detected Q_f. The location of Q_f is stretched over the interface, starting a few nms in the c-Si to around 2 nm in the a-SiN_x:H. Furthermore, Q_f can be altered by changing the concentration gradient, more specifically of N in the c-Si. This can be achieved by using a NH_3 plasma prior to a-SiN_x:H deposition.

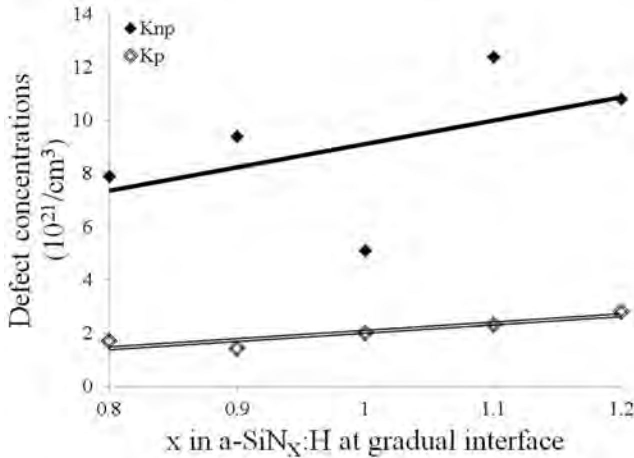

Figure 9.7: MD simulations of defect concentrations at gradual interfaces for increasing N concentration at the interface (higher x value); p refers to passivated meaning the defect has a H atom bonded, np indicates non-passivated.

9.2.3 Hydrogen and D_{it}

To increase further the understanding of the interface, *ab initio* density functional theory (DFT) studies for the interface of a-$Si_3N_{3.5}H_{0.8}$ and c-Si were performed. For the modeling 100 atoms of a-$Si_3N_{3.5}H_{0.8}$ and 56 c-Si atoms were used. a-$Si_3N_{3.5}H_{0.8}$ is the configuration of the standard a-SiN_x:H layer placed on the front side of solar cells, as determined by the authors (see Chapters 7 and 12), and the orientation of the c-Si part was (111). The amorphous structures were generated by heating the samples up to about 2500 K and then cooling them down by using two different cooling strategies. For the first strategy, the samples were cooled continuously until the systems are completely frozen. This was typically the case at a temperature of about 1500 K. Afterwards, the structure was relaxed at 0 K. About 30 interface structures have been obtained in this way. For the second strategy, about 500 samples were relaxed immediately to ground state. To prevent an intermixture of the c-Si and a-SiN_x:H part, the degree of freedom of the c-Si atoms during the molecular dynamics simulations was adjusted. While the c-Si atoms in the middle of the c-Si part stayed always fixed, the c-Si atoms of the two outermost c-Si layers could either move in all directions or only in directions parallel to the interfaces. This led to systems with either gradual or sharp interfaces. Figure 9.8 shows the averaged concentration of Si, N, and H of quenched samples with sharp interfaces (sharp, quenched), cooled samples with sharp interfaces (sharp, annealed), and cooled samples with gradual interfaces (gradual, annealed). The figure also shows the typical bonding structures of a c-Si/a-SiN_x:H interface.

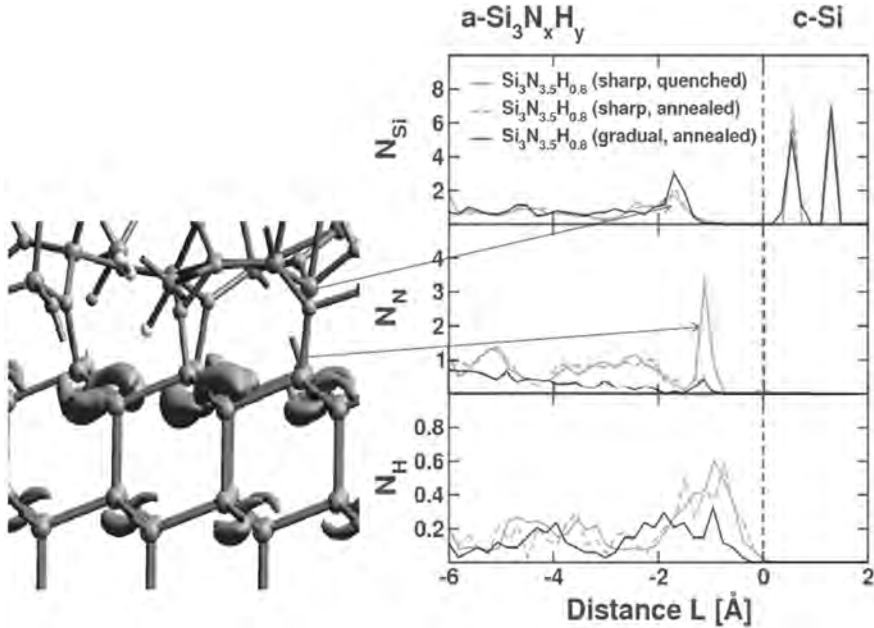

Figure 9.8: Results of *ab initio* theory studies regarding the structure and concentrations at the a-$Si_3N_{3.5}H_{0.8}$/c-Si interface.

It can be seen that for a-$Si_3N_{3.5}H_{0.8}$ with constant material properties a higher concentration of N and H is found at the interface, while for a gradient interface, the interface mostly consists of H. This might explain the dark band found in the HRTEM results. In contrast to experimental measurements, no N is found in the c-Si due to placed restrictions on the atom movement during the simulations. Moreover, the dimensions of *ab initio* model structures are still very small compared to real systems. While the models contain about 150 atoms and cover the length scale of a few angstrom, real systems contain about 10^{23} atoms and demand a description at nanometer-scale. Also, initial growth of a material in a plasma cannot be modeled by *ab initio* methods.

In Figure 9.9 the Density of States (DOS) of a-$Si_3N_{3.5}$ (x = 1.17) and a-Si_3N_3 (x = 1) are shown. For decreasing x, the band gap shrinks, and the DOS increases due to K-centers (solid lines) and distorted Si units (broken lines) (see Chapter 13). The inclusion of H decreases the density of states in the gap further (compare black and grey lines). The states caused by N-centers were found to lie outside the bandgap and we can conclude that N-centers do not have an effect on the D_{it}. These observations can be interpreted in several ways. It is for example a well-known fact that the optical absorption increases when the band gap shrinks. Therefore, the absorption for a-Si_3N_3 must be higher than for a-$Si_3N_{3.5}$, which is generally known. We furthermore

suppose that the number of defect states, which are mainly K-defects, are directly related to important passivation properties such as D_{it} and Q_f. The D_{it} is further increased by distorted Si units. Finally, the reduction of defects due to hydrogen agrees perfectly with experimental findings as shown in Chapter 13.

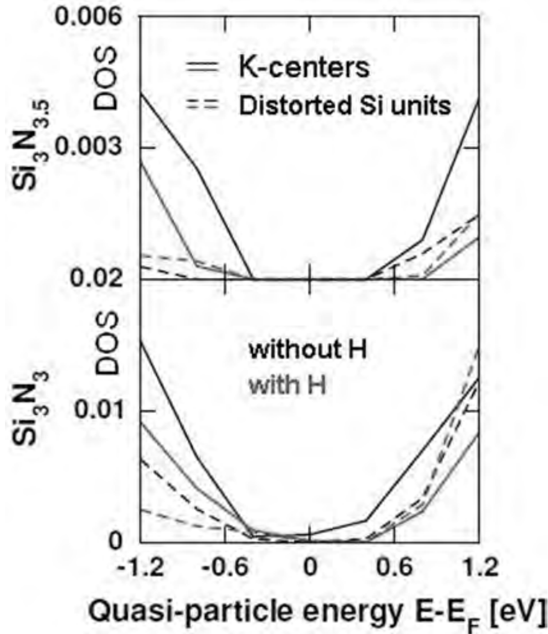

Figure 9.9: The Density of States (DOS) of a-$Si_3N_{3.5}$ and a-Si_3N_3 close to Fermi-level. The total DOS is related to K-centers and distorted Si units (full and broken lines). Additional hydrogen (grey lines) reduces the amount of electronic defect states in the gap (see also Chapter 13). Note that the y-axes are differently scaled.

The observations described above correspond to the ones found experimentally on bulk a-SiN_x:H. FTIR (Fourier Transform Infra Red) spectroscopy data for layers with different composition are shown in Figure 9.10 (see also Chapters 7 and 8) and it can be seen that the concentration of distorted Si-N bond increases for x = 1 compared to the one for x = 1.17. Simultaneously, the H-Si-N_3 (passivated K-centers) concentration increases. These increases can be related to higher values for Q_f and D_{it} as shown in Figure 9.11.

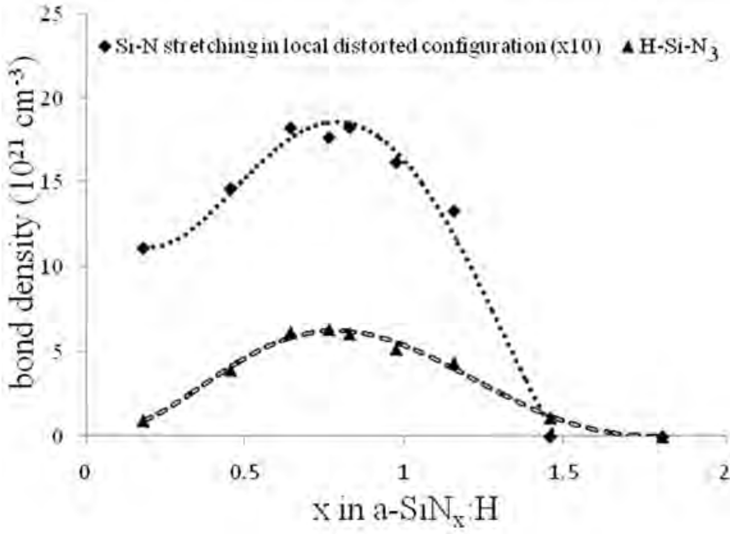

Figure 9.10: The bond densities of H-Si-N_3 and Si-N stretching in local distorted configuration (see Chapters 7 and 8).

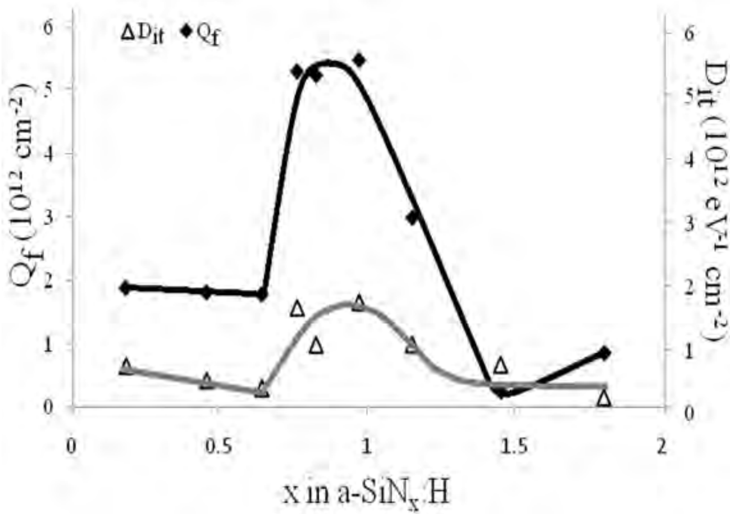

Figure 9.11: Relation between Q_{f}, D_{it} and x. The lines are guides to the eye.

9.2.4 Effect on solar cells

The effect of NH_3 plasma treatments and temperature prior to a-SiN_x:H deposition indicate that, depending on the surface doping, a significant effect on solar cells can be expected. As the increase in plasmon loss energy in the c-Si is found to be an indication of N insertion in the c-Si and that this also is found for surfaces without an additional NH_3 plasma treatment (see Figure 9.3), it is expected that significant nitridation may occur during standard a-SiN_x:H deposition. Therefore, we can conclude that both the NH_3 flow and temperature used in the standard a-SiN_x:H deposition will determine the final Q_f and D_{it}. However, for p-type cells with highly doped n-type emitter fabricated using NH_3 plasma treatment (300-500°C) prior to front side a-SiN_x:H deposition we did not observe a difference in cell performance (see Chapter 8). This indicates that these variations in surface passivation do not change the effective passivating quality of the front side for this cell design. Contrarily, in n-type cells with a p-type emitter fabricated using NH_3 plasma treatment (300-500°C) prior to front side a-SiN_x:H deposition a significant effect on the cell characteristics could be seen (see Chapter 8). A variation of 20 mV was observed. This indicates that the used temperature and NH_3 flow during a-SiN_x:H on p-doped surfaces significantly influence cell performance. No cell experiments were performed regarding the rear side of p-type cells as an increase in Q_f and D_{it} has been shown to have a detrimental effect on cell performance [38]. More details and results for p-type and n-type cells together with modeling are shown in Chapter 8.

9.3 Conclusions

The atomic structure of a-SiN_x:H layers is linked to the passivation quality, expressed by Q_f and D_{it}. Both parameters can be measured by using CV-MIS and they can be related to defect states on both sides of the a-SiN_x:H/c-Si interface, which is confirmed by using MD simulations. Dependent on the modeling technique this can be done at nanometer-scale as well as at atomistic scale. There is a good agreement between HRTEM observations of the a-SiN_x:H/c-Si interface and corresponding different model structures. We find a gradual change from c-Si to bulk a-SiN_x:H within the first 2 nm of the amorphous part. This change is associated with highly strained and distorted c-Si layers (within 1-3 nm) and with the insertion of N and H. The adhesion of N at the Si surface and insertion of N in the first few nm's of the Si substrate is called nitridation and can be altered by using a NH_3 plasma prior to a-SiN_x:H deposition. HRTEM image analysis shows that by varying the nitridation of the Si surface the amount and penetration depth of N in the first few nm's of the Si substrate is altered. Using MD modeling, it is shown that this process changes the amount of K-centers, which explains the variation in Q_f and D_{it} which was found experimentally. Based on experimental and modeling results, it is proposed that the change in the volume density of K-centers may be the origin of Q_f. Consequently, the

location of Q_f is stretched over the interface, starting a few nm in the c-Si to around 2 nm in the a-SiN_x:H. Q_f can be altered by changing the concentration gradient of N in c-Si. This can be achieved by using a NH_3 plasma prior to a-SiN_x:H deposition. *Ab initio* DFT studies of a-SiN_x:H (x = 1.17) show that K-centers are the dominating defects and that its amount increases for lower x (x = 1). The D_{it} is further increased by distorted Si units. This observation is also in good agreement with experimental results.

Acknowledgments The authors acknowledge support from the European Commission Grant MMP3-SL-2009-228513, "Hipersol" as part of the 7th Framework Package, grant number 228513. Via our membership of the UK's HPC Materials Chemistry Consortium, which is funded by EPSRC (EP/F067496), this work made use of the facilities of HECToR, the UK's national high-performance computing service, which is provided by UoE HPCx Ltd at the University of Edinburgh, Cray Inc and NAG Ltd, and funded by the Office of Science and Technology through EPSRC's High End Computing Programme. Supercomputing time on the Vienna Scientific cluster (VSC) is gratefully acknowledged.

Part IV

Background: Modeling of the a-SiN_X:H layer and interface with c-Si

Chapter 10

Molecular dynamics studies of the bonding properties of amorphous silicon nitride coatings on crystalline silicon

K.T. Butler[1], M.W.P.E. Lamers[2], A.W. Weeber[2], J.H. Harding[1]

[1] Department of Materials Science and Engineering, Sir Robert Hadfield Building, Mappin Street, Sheffield S1 3JD, UK.
[2] ECN Solar Energy, P.O. Box 1, 1755 ZG Petten, the Netherlands.

Based on *Journal of Applied Physics* **110**, 124905 (2011).

Abstract

In this paper we present molecular dynamics simulations of silicon nitride, both in bulk and as an interface to crystalline silicon. We investigate, in particular, the bonding structure of the silicon nitride and analyze the simulations to search for defective geometries which have been identified as potential charge carrier traps when silicon nitride forms an interface with silicon semiconductors. The simulations reveal how the bonding patterns in silicon nitride are dependent upon the stoichiometry of the system. Furthermore we demonstrate how having an 'interphase', where the nitrogen content in silicon gradually reduces towards pure silicon across a boundary region, as opposed to an interface where an abrupt drop exists in nitrogen concentration at the boundary, can result in significantly different numbers of carrier traps.

10.1 Introduction

The deposition of amorphous silicon nitride (a-SiN_x:H) on silicon in photovoltaic cells has become a popular strategy. In solar cells they were first used due to their properties as an anti-reflective coating (ARC). The presence of an ARC in crystalline silicon (c-Si) solar cells is important as a clean c-Si surface reflects more than 35% of incident light. The presence of an ARC allows for effective utilization of this light. That the inclusion of an a-SiN_x:H layer increases the performance of solar cells by more than would be expected merely from its role as an ARC has been explained by its ability to reduce the rate at which excess charge carriers recombine at the semiconductor surface [131], a property known as passivation. Thus a-SiN_x:H coatings address the two major loss mechanisms in solar cells, namely optical and electrical losses. Due to these dual beneficial properties for the improvement of photovoltaics as well as its importance in metal-oxide-semiconductor field effect transistors (MOSFETs) [132] the silicon nitride/silicon interface has been the subject of much research since the early 1990's [133–135].

Much of the work done on ARC development to date has focused on finding the optimal ratio of N to Si (i.e. the value of x in a-SiN_x:H) in order to maximize the percentage of incident light trapped in the c-Si [136]. There is a balance to be achieved between reducing reflection and reducing the amount of light absorbed by the ARC. If the effects of absorption of light were ignored, a value of n = 2.3 - 2.4 would be optimal. However, layers with n in this range have a high absorption; in order to reduce the amount of light absorbed in the ARC it is necessary to reduce the number of Si-Si bonds (i.e. higher values of x and thus lower n). The optimal value of n is between 2.03 and 2.08 (x = 1.02 - 1.08) [17, 123].

A considerable amount of experimental work has been done in characterizing the stoichiometric Si_3N_4/Si(111) interface. Much of this effort has been concentrated on identifying the types of surface reconstruction and charge transfers involved at the interface. 7×7 [135], 4×4 [137], 8/3×8/3 [138] and 8×8 [133] reconstructions have all been observed. The a-SiN_x:H/Si(100) interface has been studied by electron paramagnetic resonance (EPR) [139], which revealed the major electron trap in the interface layer to be due to under-coordinated Si. Further studies, see also Chapter 9, of this interface with transmission electron microscopy (TEM) showed that N atoms were present on the c-Si side of the interface up to the second layer [122, 130]. Such penetration of N, into the c-Si layer is also known to be extremely sensitive to the conditions during the deposition of the ARC [123].

In a-SiN_x:H a number of geometrical defects have been identified which have important implications for the electronic structure, two of the most important, the so-called K- and N-centers are shown in Figure 10.1. The

K-center consists of a Si bound to three N atoms with a dangling bond ($N_3 \equiv$ Si) and is observable by electron spin resonance (ESR) [140]. A defect center due to an under-coordinated N atom ($Si_2 =$ N) has also been observed [141]. These assignments have also been supported by *ab initio* calculations [142].

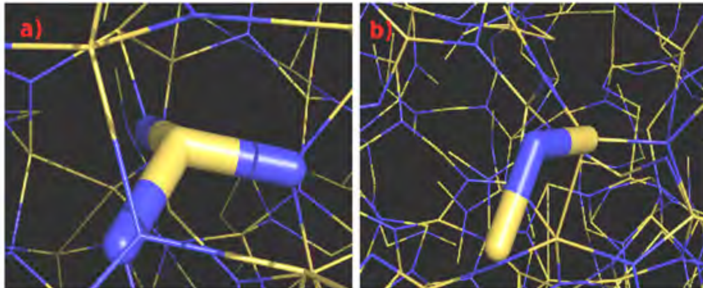

Figure 10.1: Important defect geometries in the a-SiN_x:H layer. a) the K-center, where Si is bonded to three N atoms with one dangling bond. b) the N-center, where N is bonded to two Si atoms with one dangling bond.

In this paper we simulate the Si(100) interface in contact with a-SiN_x:H at an atomistic level. a-SiN_x:H layers with x = 0.8, 0.9, 1.0, 1.1 and 1.2, incorporating 20 at.% (atomic percent) H are simulated. For each value of x we simulate both a clean interface, with an abrupt a-SiN_x:H/c-Si partition and a gradual interface with a gradient of x across a distance of 20 Å. We shall refer to these interfaces as clean and gradual interfaces respectively. We perform a topological analysis of the trajectories generated in our molecular dynamics (MD) simulations. We calculate the radial distribution functions (RDFs) for bulk a-SiN_x:H comparing to previous theoretical work, as a validation of our method and investigate bonding patterns in the interfacial regions of our models to identify and quantify defect centers, revealing a clear difference in the frequency of occurrence and degree of passivation of K- and N-centers at clean and gradual interfaces.

10.2 Methods

10.2.1 Generating a-SiN_x:H

All interactions in the system were modeled using Tersoff type potentials [116]. We use the parameterization of these potentials developed by de Brito Mota *et al.*, which were previously used to simulate a-SiN_x:H [115, 143]. All MD simulations presented in this paper were run using the DLPOLY code [144].

The first step in our procedure is to generate samples of a-SiN_x:H. This is achieved by randomly placing Si and N atoms in a simulation cell, subject to certain inter-atomic separation criteria, in the correct ratio. The cell volumes were set by estimation of the required density, from a linear interpolation between the density of c-Si and c-Si_3N_4. The details of the simulation cells are presented in Table 10.1.

In order to generate the amorphous samples the initially random configurations were run at 2500 K for 0.5 ns with a time-step of 1 fs in the NVT ensemble. After this simulation, the systems were quenched to 350 K at a rate of $3 \cdot 10^{11}$ K/s. We tested various quenching rates on samples of a-Si_3N_4 and found that this was the fastest rate at which no significant increase in the number of defects present in the sample was observed.

We then add 20 at.% H (Table 10.1) to the simulation cells and equilibrate, again in the NVT ensemble at 2500 K for 0.5 ns. In this instance a reduced time-step of 0.2 fs is employed due to the presence of H. The systems were quenched as above.

Table 10.1: Numbers of atoms in the simulation cells used to generate the a-SiN_x:H.

x	Si Atoms	N Atoms	H Atoms	Density (g/cc)
0.8	415	332	187	2.86
0.9	409	368	194	2.92
1.0	404	404	202	2.98
1.1	400	440	210	3.04
1.2	394	473	217	3.10

10.2.2 Generating a-SiN_x:H/c-Si interfaces

In order to generate clean and gradual interface structures two different procedures were followed. To generate the clean interface the amorphous sample was placed in a cell at the (100) surface of a 20 layer thick slab of c-Si. The a-SiN_x:H was placed 2.5 Å away from this surface and dynamics were performed at 2500 K for 0.1 ns, with the c-Si held in position. The a-SiN_x:H layer was then gradually moved closer to the surface, each time repeating the procedure until the energy of the system started to increase relative to the previous step. Having thus identified the minimum energy separation, the top two layers of the c-Si were un-locked (as illustrated in Figure 10.2) and dynamics were performed for a further 0.5 ns at 2500 K. The system was then quenched at the same rate as previously to 350 K, where dynamics were performed for a further 0.5 ns to generate statistics.

To generate the system with the gradual interface, the minimum energy separation from the previous step was used again. In this instance, however, the top 10 layers of c-Si were unlocked before performing the dynamics at 2500 K. This results in the N atoms from the a-SiN_x:H penetrating into the c-Si layer, which also melts and becomes distorted. After 0.5 ns at 2500 K the system is annealed to 350 K as described above, and run for 1 ns at 350 K to generate statistics.

All bond pattern analyses were performed using the R.I.N.G.S. code [145]. During this analysis two atoms are said to be bonding if the inter-atomic separation is within the first peak of the partial radial distribution function.

10.3 Results and discussion

10.3.1 Bulk a-SiN_x:H

All total and partial RDFs for the bulk samples of a-SiN_x:H at each value of x are shown in Figure 10.3. As the value of x increases, the first peak, which occurs at 1.80 Å, increases systematically, having values of 2.09, 2.20, 2.22, 2.25 and 2.26 at $x = 0.8$, 0.9, 1.0, 1.1 and 1.2 respectively. It is clear from comparison with the partial RDFs that this peak is due to the first peak of the Si-N RDF. As x increases, the first peak of the Si-Si RDF, at around 2.5 Å, is also seen to decrease dramatically due to the fact that N atoms replace Si atoms as nearest neighbors in the amorphous network. In the N-N RDF there are no N-N nearest neighbor pairs. This because the N-N interaction within the potential parameterization used is set to zero and is also representative of the physical situation, where N-N bonds would result in molecules of N_2 which would not be incorporated into the a-SiN_x:H network.

The RDFs obtained from our simulations are much closer in character to those obtained by Alvarez and Valladares using first principles simulations [146] than those obtained using the same Tersoff potential as ourselves produced by de Brito Mota *et al.* [143]. We believe that this is due to the fact that the methodology which we have used to produce the a-SiN_x:H is much closer to the annealing methodology of the former than the Monte-Carlo based methodology of the latter. This gives us an increased degree of confidence in the ability of this Tersoff parameterization to simulate the properties of a-SiN_x:H.

We now compare the bonding patterns from our simulations with the experimentally determined values [147]. We note that in this case we are comparing the results of our simulations which include hydrogen to the experimental results containing hydrogen. Figure 10.4 shows the total coordination numbers of Si and N in the various a-SiN_x:H samples as x

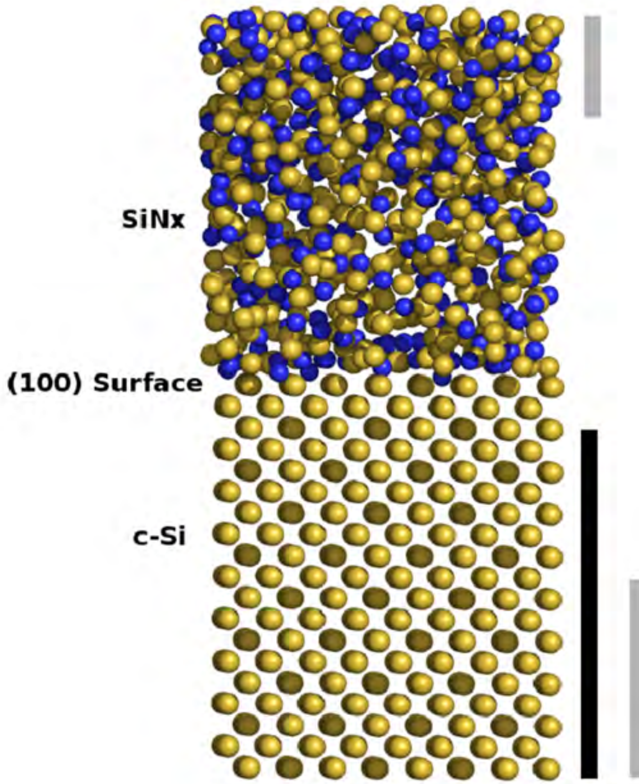

Figure 10.2: Simulation cell setups for creating clean and gradual interfaces. The lines to the right indicate the z coordinates over which atoms are frozen during interface generation. The dark line is c-Si frozen during clean interface generation, the grey line is c-Si frozen during gradual interface generation. The line at the top represents a-SiN_x:H frozen during all simulations. In the figure the color coding is as follows: Si (yellow); N (blue).

increases, we concentrate on the range $x = 0.8$ - 1.2, whilst the experimental results of Guraya *et al.* [147] (see Figure 10.4) cover a much wider range. In the graph of the partial coordinations the pairs A-B represent the number of atoms B bonded to atom A. In this case the atoms are said to be bonded if the inter-atomic separation is within the first peak of the partial RDF. These results are presented with the experimentally determined values of Guraya *et al.*, who obtained the values from x-ray photoemission spectroscopy.

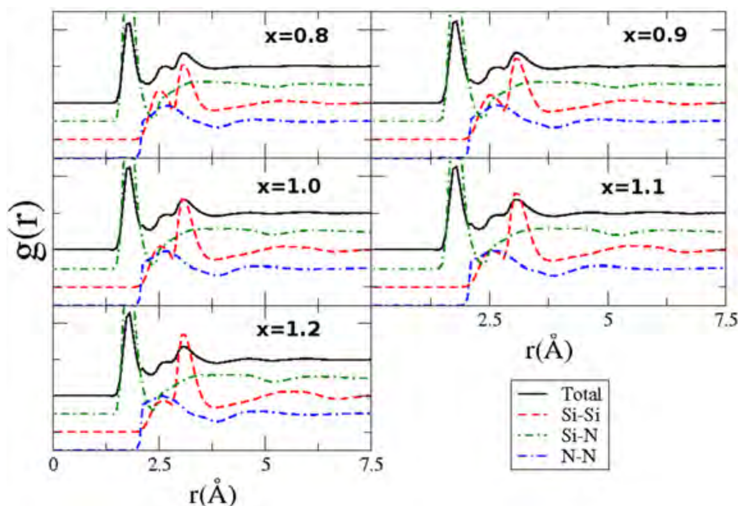

Figure 10.3: Total and partial radial distribution functions of a-SiN$_x$:H samples at values of x from 0.8 - 1.2. Note that individual RDFs have been offset by 0.5 on the y-axis for clarity.

Our bonding patterns match very well with the experimental data. We observe in our simulations that N and H bond almost entirely to Si, with very low quantities of N-H bonding, as observed in the experimental data (see Chapter 7). Also we observe that the number of N atoms bonding to a Si center increases in a linear manner with the value of x and the opposite is true of number of Si atoms bonded to a Si center, which decreases linearly with increasing x, this is also found experimentally as shown in Chapter 7. This is an indication that the Si nearest neighbors in the network are replaced by N atoms as x increases. As in previous theoretical and experimental studies the coordination of the N atoms is largely unaffected by the varying x [143, 146, 147].

The above results demonstrate that using our melting and quenching regime we can generate reliable a-SiN$_x$:H structures. The trends observed in bonding patterns and the RDFs are in excellent agreement with previous *ab initio* and experimental studies [146, 147]. We now proceed to use the samples thus generated and the methodologies established in order to model the interface between a-SiN$_x$:H and the Si(100) surface.

10.3.2 Clean a-SiN$_x$:H/c-Si interfaces

We first examine interfaces with an abrupt change in the N concentration at the interface with c-Si, which we refer to as clean interfaces. For this analysis we consider the a-SiN$_x$:H layer within 1 nm of the c-Si layer. In Figure 10.5 we can see that at $x = 0.8$ the total coordination number of Si is roughly

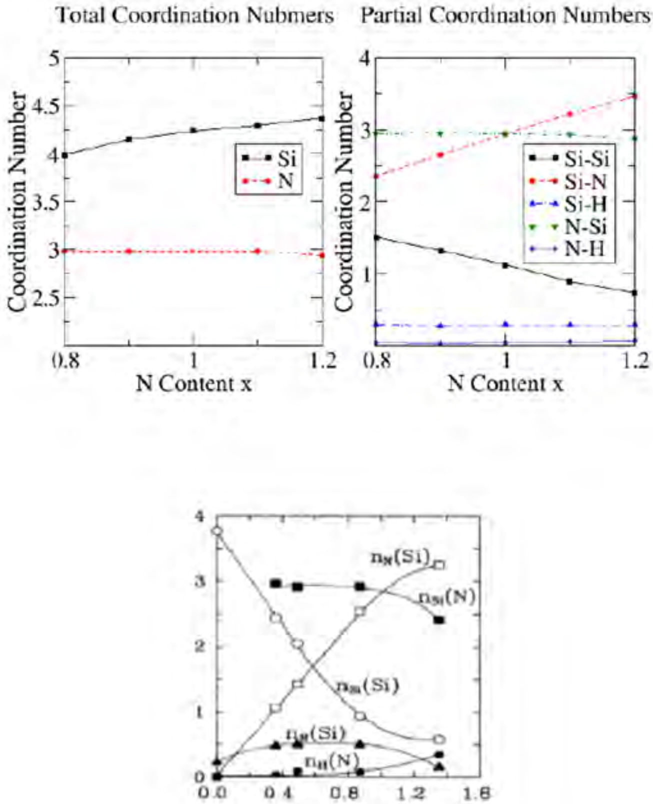

Figure 10.4: Upper: Total and partial coordination numbers for Si and N atoms from simulation. A-B means the number of atoms of B bonded to center A. Lower: Partial coordination numbers from the experimental study of Guraya *et al.* [147]. n_B(A) refers to the number of atoms of B bonded to center A.

the same as that in the bulk sample, however as x increases, although the coordination of Si does increase, this increase is not as pronounced as in the bulk sample. The coordination number of N remains constant as x increases, as was observed in the bulk samples. However, the coordination number of N is slightly decreased with respect to bulk samples by ~ 0.1. Whilst these changes may seem minor, closer inspection of the bonding patterns, from the partial coordination numbers, reveals a significant difference in bonding. The number of nearest neighbor N atoms for each Si center is decreased, varying from 1.6 to 2.5 across the range of x values. N coordination is again largely accounted for by Si atoms, with a slight increase in the number of N-H bonds. The values for Si-H are very similar to those in the bulk a-SiN_x:H.

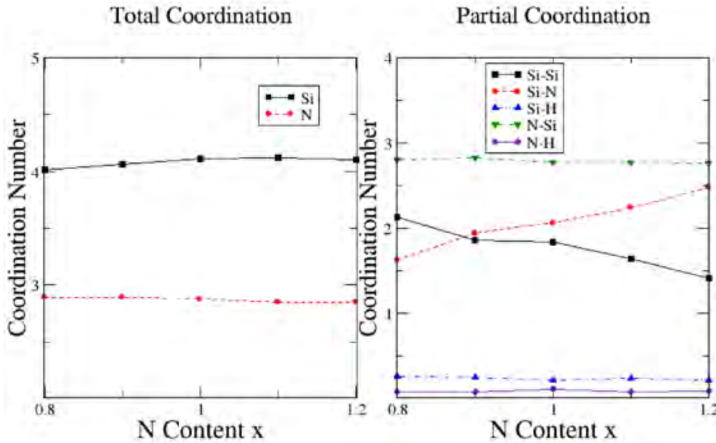

Figure 10.5: Total and partial bond densities in a-SiN_x:H close to the clean interface with c-Si as a function of nitrogen content (x).

We now consider the presence of bonding defects which are important in solar cells in terms of electrical performance. The two states in particular which we consider are the K- and N-centers which were described in the introduction. Passivation of these defects by H is very important, therefore we consider how these defects are passivated in our simulations. The results are presented in Table 10.2. Considering the total density of K-centers, the most striking feature is a sharp increase in the number after $x = 1.1$. It is interesting to note that this change occurs at the percolation limit of a-SiN_x:H [111], at which point the properties of a-SiN_x:H are known to alter in a non-linear fashion with varying x [148]. These results match well with the observation that above the percolation limit the density of Si dangling

Table 10.2: Defect center concentrations, in 10^{21} cm^{-3}, at the clean interfaces across the x range in a-SiN$_x$:H. p refers to passivated meaning the defect center has a H atom bonded, t refers to total and is passivated plus un-passivated centers.

x	0.8	0.9	1.0	1.1	1.2
K^t	9.3	18.0	17.9	29.0	33.6
K^p	3.6	5.5	6.1	12.3	12.1
N^t	17.8	19.3	27.7	27.8	32.6
N^p	7.6	8.5	13.2	11.2	12.8

bonds can increase [111]. The presence of H leads to passivation of these dangling bonds by bonding of H to the under-coordinated Si center. The results in Table 10.2 indicate that, in the presence of 20 at.% H, between 30 and 40% of the K-centers at the interface are passivated in our simulations.

The density of N-centers shows a similar large jump as the K-center density, however this occurs at $x = 1.0$, slightly before the percolation limit. We note, however, that below the percolation limit defects on N-centers are unlikely to be noticeable as the band structure is dominated by Si bands and the N-center is not in the band-gap [111]. Interestingly the N-centers are passivated to a larger degree, between 40 and 50%, than the K-centers. This is despite the fact that, from Figure 10.5, the degree of Si-H bonding is larger than the degree of N-H bonding, indicating that H bonds more selectively to under-coordinated N than under-coordinated Si. This supports the hypothesis that the reduction in density of paramagnetic Si dangling bonds observed upon increasing annealing temperature is a result of charge transfer between paramagnetic defects, rather than the passivation of dangling Si bonds by hydrogen [149].

10.3.3 Gradual a-SiN$_x$:H/c-Si interfaces

So far, we have considered only clean interfaces with an abrupt drop in the N concentration at the c-Si surface. In reality there is often a layer of gradual depletion of the N concentration. The width of this layer varies significantly depending on the deposition method, and can also vary within a single sample. However, this layer is typically between 1-3 nm wide (see Chapter 9). In order to simulate the effect such a gradual depletion may have on the structure of the a-SiN$_x$:H and the interface, we consider a number of systems which were set up as described in Section 10.2. We should point out that in the case of the simulations the width of the layer is restricted to around 2 nm (see Figure 10.6), which we choose as being representative of the experimental range. We are aware, however, that the slope and width of

the gradient may play an important role in determining the structure in this region, the effect of the width shall be considered in future studies. For now we shall restrict ourselves to establishing the difference in structure between the clean and gradual interfaces.

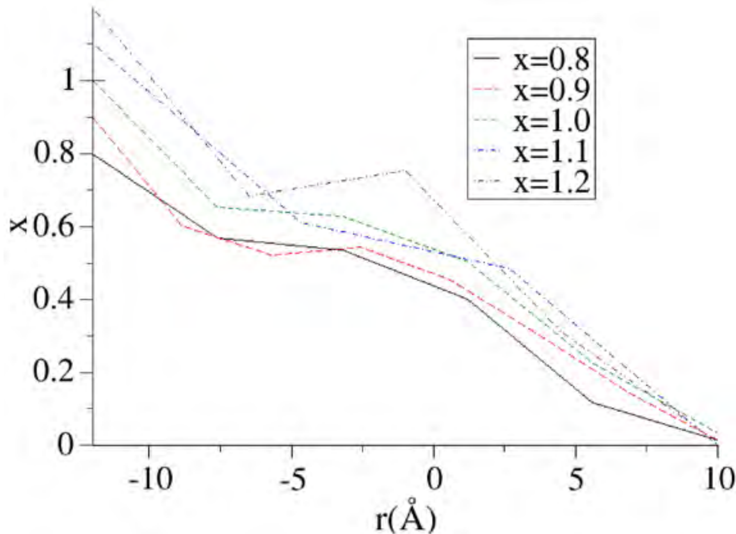

Figure 10.6: Value of x in a-SiN_x:H across the various simulated interfaces.

As was the case for the clean interface, the total Si coordination number (see Figure 10.7) is similar to the bulk at $x = 0.8$, and remains more or less constant across the stoichiometry range. At the gradual interface, the coordination number of N is very similar to that in the bulk samples. The number of N atoms bonded to Si is decreased with respect to the bulk and clean interface values, obviously due to a lower N content near the interface with c-Si in the gradual interface system. The hydrogen coordination numbers to both Si and N are reduced with respect to both the bulk and the clean interface, suggesting that the degree of passivation of dangling bonds may be reduced in a gradual interface. We now consider this specifically relating to the K- and N-centers.

Table 10.3 presents the density of K- and N-centers found in the gradual interface systems. The total density of K-centers at $x = 0.8$ is slightly larger in the gradual interface than the clean interface. However, as we go to larger values of x the total density does not increase as rapidly as in the clean interface systems. Thus, for all values of $x > 0.8$ the total density of K-centers is reduced in the gradual interface. As suggested by the coordination numbers, the degree of passivation of K-centers is significantly reduced in the gradual interface ranging between 15 to 30%. However, despite the reduction in the degree of passivation, the density of un-passivated K-centers is still lower in

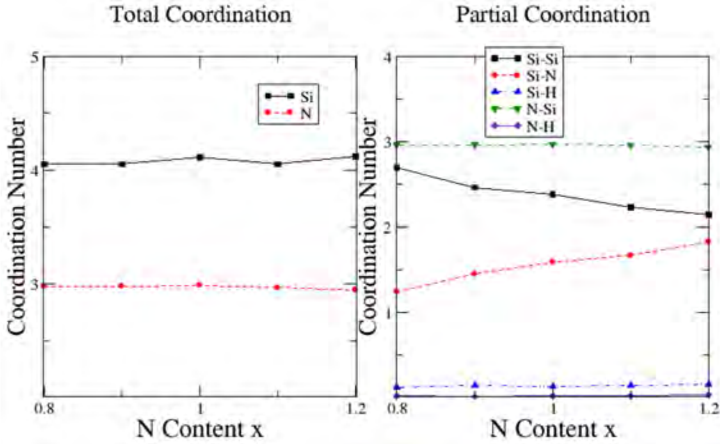

Figure 10.7: Total and partial bond densities in a-SiN_x:H close to the interface with c-Si as a function of nitrogen content (x) in systems with a N gradient.

Table 10.3: Defect concentrations, in $10^{21}cm^{-3}$, at the gradual interfaces across the x range in a-SiN_x:H. p refers to passivated meaning the defect center has a H atom bonded, t refers to total and is passivated plus un-passivated centers.

x	0.8	0.9	1.0	1.1	1.2
K^t	9.6	10.8	7.1	14.7	13.6
K^p	1.7	1.4	2.0	2.3	2.8
N^t	3.2	2.7	3.2	5.3	8.8
N^p	1.9	1.2	1.7	2.2	3.3

the gradual interfaces compared to the clean ones for all values of $x > 0.8$. The total density of N-centers on the other hand is greatly reduced across the composition range. This is because the density of N-centers within 1 nm of the c-Si is reduced in the gradual interface and the coordination numbers suggested that N-centers were more fully bonded in the gradual than in the clean interface. This indicates that the gradual interface can be expected to have improved electrical performance to the clean interface.

10.4 Conclusions

In this paper we have demonstrated that using the Tersoff potential the structure of a-SiN_x:H can be simulated in excellent agreement with *ab initio*

and experimental structures. We demonstrate that using a methodology based on melting the sample and quenching it, a better representation of the true amorphous structure can be obtained compared to previous studies which used Monte-Carlo methods to generate a-SiN_x:H using the Tersoff potential [143].

We have then used this methodology to simulate a-SiN_x:H interfaces with the Si(100) surface. We have simulated this for both a clean interface and for a gradient of N concentration across the boundary. To our knowledge this is the first systematic theoretical examination of the effect of a-SiN_x:H stoichiometry on the structure of the a-SiN_x:H/c-Si interface, as well as the first time a system with a N gradient across the interface has been modeled atomistically. The results of the simulations have implications for future optimization of the a-SiN_x:H layer in high performance c-Si solar cells.

The simulations reveal that in the case of a clean interface higher values of x in a-SiN_x:H correspond to increased densities of both K- and N-centers at the interface, although these centers are to some extent passivated by the presence of H. The implementation of a gradual interface resulted in a significant reduction in K- and N-centers, except for the $x = 0.8$ where a small increase in K-centers is found. For higher x, more K- and N-centers, passivated and non-passivated, are found. Experimentally, however, it is found that K_p is lower for higher values of x in the range investigated by us [150]. Other aspects that influence the build-up of the interface, like the width of the gradual interface, need to be evaluated. The influence of the width of the gradual interface is studied in Chapter 11.

Acknowledgments The authors acknowledge support from the European Commission Grant MMP3-SL-2009-228513, "Hipersol" as part of the 7th framework package, grant number 228513. In addition we would also like to thank our reviewer for an insightful critical reading of the original manuscript.

Chapter 11

Molecular dynamics studies of graded a-SiN_x:H at the interface with Si for improved surface passivation

K.T. Butler[1], J.H. Harding[1], M.W.P.E. Lamers[2], A.W. Weeber[2]

[1] Department of Materials Science and Engineering, Sir Robert Hadfield Building, Mappin Street, Sheffield S1 3JD, UK.
[2] ECN Solar Energy, P.O. Box 1, 1755 ZG Petten, the Netherlands.

Based on *Journal of Applied Physics* **112**, 094303 (2012).

Abstract

The effects of an interface gradient in nitrogen concentration on a number of important properties of amorphous hydrogenated silicon nitride / crystalline silicon (a-SiN_x:H/c-Si) interfaces in the context of solar cell devices are investigated using molecular dynamics simulations. We simulate interfaces with a gradient of nitrogen which goes from a-$SiN_{1.2}$ to Si over widths from 2-9 nm, in the presence of 10 at.% hydrogen, to recreate the conditions present when a-SiN_x:H layers are deposited onto c-Si by plasma enhanced vapor deposition. We examine how changing the width of the nitrogen gradient can affect a number of atomic level structural properties which influence the performance of solar cells. We examine the trajectories of our simulations to search for certain geometries which have previously been identified as being important at this interface. The fixed charge at the interface is shown to increase with the width of the gradient. The results demonstrate how altering the width of the N layer can affect the efficiency of a-SiN_x:H as a passivation layer, and we suggest an optimal gradient width of in the region of 2 nm.

11.1 Introduction

In order for high performance solar cells to attain ever-increasing efficiencies, one of the key considerations is an improvement in the lifetimes of charge carriers in the semiconductor. A major source of decreased carrier lifetimes is recombination of charge carriers at defects located at the semiconductor surface. For this reason the topic of improved surface passivation has become one of the major areas of research in all areas of high-performance solar cell technology today [151–154]. One of the most common layers used for surface passivation is hydrogenated amorphous silicon nitride (a-SiN_x:H). We investigate the use of this material, with a stoichiometric gradient at the crystalline silicon (c-Si) surface as an improved alternative to abrupt a-SiN_x:H/c-Si interfaces.

The use of a-SiN_x:H represents one of the most important technological advances in solar cell technology. This is due to its ability to fulfil the dual roles of an anti-reflective coating (ARC) and surface passivation layer for c-Si [155]. The a-SiN_x:H layer functions as the passivation layer by reducing the number of defective states at the c-Si surface, thus lowering the recombination rate at the surface. The electrical performance of a-SiN_x:H passivation layers have been studied by means of deep-level-transient spectroscopy (DLTS) [156–158]. These studies reveal three different defect states (labeled A-C) which play a role at the a-SiN_x:H/c-Si interface. Based on the DLTS measurements and theoretical analysis of the measured dependence of recombination rate on the excess carrier density, it was established that the defect labelled C dominates the recombination rate [159]. This defect has been identified as a Si center bound to three N atoms with one dangling bond. This center has also been identified as an important defect state in bulk a-SiN_x:H [140]. In accordance with common practice this defect will be referred to herein as the K-center, see inset on Figure 11.1 for a graphical representation.

Another feature of the a-SiN_x:H layer which affects the electrical performance of a device is the presence of a positive fixed charge (Q_f) at the interface with c-Si. It has been demonstrated that high values of Q_f in a-SiN_x:H result in improved effective surface recombination velocities [160, 161]. The major contribution to Q_f has been shown to be due to the presence of the K-center [159]. Thus the K-center plays two contradictory roles in passivation by a-SiN_x:H in solar cells. On one hand it acts as a recombination center, decreasing performance, on the other hand, it acts as a center for fixed charge increasing performance.

The nature of the a-SiN_x:H/c-Si interface determines the passivation obtained. For example, a gradual interface, where the concentration of N changes gradually to zero over a finite distance from the bulk a-SiN_x:H to the c-Si, shows different qualities than a clean interface where there is an abrupt

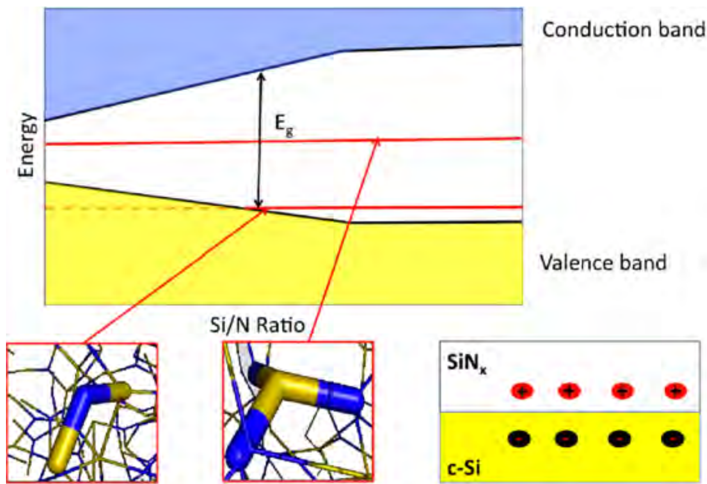

Figure 11.1: (Top) Schematic representation of the a-SiN_x:H band structure as a function of the Si/N ratio. The red lines represent defect energy levels due to K- and N-centers. (Bottom left) The structure of the N-center one N atom (blue), bonded to 2 Si atoms (yellow), with one dangling bond. (Bottom Centre) K-center, one Si atom bonded to 3 N atoms with one dangling bond. (Bottom right) Representation of the formation of an inversion layer of negative charge in c-Si, due to fixed positive charge in the a-SiN_x:H layer.

change from a-SiN_x:H to c-Si. Previously we have demonstrated how a graded a-SiN_x:H/c-Si interface can result in a significant lowering of K-center density at the interface (see Chapter 10). We have also shown how it is possible to control the incorporation of N into the c-Si surface by a process of nitridation (see Chapters 8 and 9), before deposition of the a-SiN_x:H layer. This allows for the introduction of a controllable N gradient in the device, giving control of the Q_f and density of interface states (D_{it}), independent of the a-SiN_x:H layer.

In this paper we provide a model for how the level of nitridation affects the important features of the a-SiN_x:H in a solar cell. We use a topological analysis of molecular dynamics (MD) simulations to investigate the effect of the gradient layer introduced by nitridation on the density of Si-Si and Si-H bonds. We then estimate the fixed charge in the a-SiN_x:H, by calculating the density of K-centers. Finally we combine our model for defect distributions with Shockley-Reed-Hall (SRH) recombination statistics [35, 36] to provide a model for how the carrier trapping rate is affected by the width of the N gradient layer introduced by nitridation.

11.2 Computational Methods

In order to represent the interaction between the atoms in our system we have used the Tersoff potential, as parametrized by de Brito Mota *et al.* [115, 143] for a-SiN_x:H. To generate amorphous a-SiN_x:H structures we used a melt and quench methodology which we have verified previously (see Chapter 10). Starting from a random configuration of atoms in a simulation cell with dimensions chosen to match the experimental density of $SiN_{1.2}$, 3.10 g/cc. The random configuration is then run, using a timestep of 0.2 fs, for 0.5 ns at 2500 K in the canonical (NVT) ensemble to achieve a well equilibrated system. The system is then quenched to 350 K at a rate of $3{\cdot}10^{11}$ K/s.

The amorphous sample generated is then placed in contact with the (111) surface of a slab of c-Si. To generate the gradient interface we re-run the system again at 2500 K for 0.5 ns and quench to 350 K at the same rate. During this simulation, parts of the c-Si and a-$SiN_{1.2}$:H layers are held in a fixed position. In each case the atoms allowed to move during the molecular dynamics simulation on either side of the interface are within half of the desired gradient interface width. The inter-diffusion of Si and N which takes place during this step results in a N gradient across the desired width, represented schematically in Figure 11.2, which re-creates the effects of nitridation before application of the a-$SiN_{1.2}$:H by PECVD experimentally. The final compositions of the simulation cells used in this study are presented in Table 11.1.

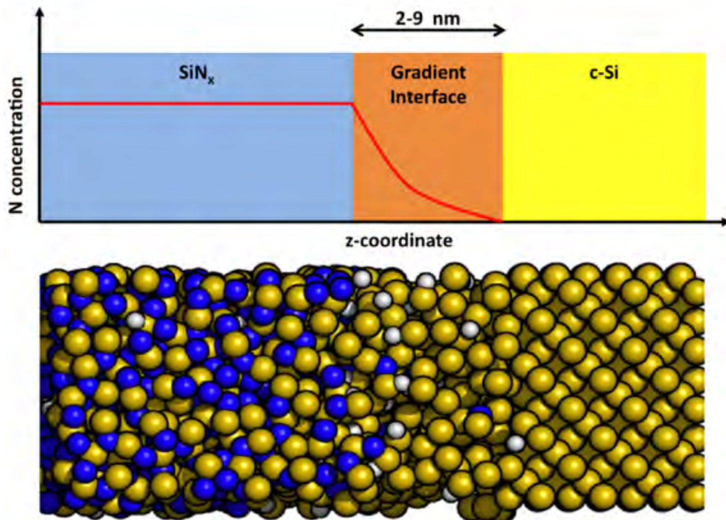

Figure 11.2: System composition in our simulations. A layer of $SiN_{1.2}$ is on the left hand side of the system, this is linked to a layer of pure c-Si through a layer with a gradually reducing value of x in a-SiN_x:H. The width of the gradient interface layer is varied from 2 to 9 nm. In the figure the color coding is as follows: Si (yellow); N (blue); H (white).

In order to search for defects in our system we have used the R.I.N.G.S software package [145] to analyze the trajectories of our equilibrium MD simulations of the interfaces. Within this analysis the coordination of an atomic center is defined by the number of neighboring atoms which are said to be "bonded" to that atom. The bonding is defined as the inter-atomic separation being within the first peak of the pair correlation function of the two atoms defined for a-SiN_x:H. Having thus defined the coordination of each atom it is a simple task to count and map the defective centers in the simulation.

11.3 Results and discussion

11.3.1 Fixed charge

As we explained in the introduction, the presence of Q_f is desirable as it reduces the minority carrier density in the c-Si interface region with a-SiN_x:H, thus reducing the recombination rate and increasing the minority carrier lifetime. In the following section we will consider how the nitridation profile affects the fixed charge.

Table 11.1: Compositions of the cells used to create samples of a-SiN_x:H for the different interface widths, showing number of Si, N and H atoms and the volume of the cell.

Sample	# Si	# N	# H	Volume [Å^3]
2nm	406	487	99	9435
3nm	507	609	124	11794
4nm	609	730	149	14153
5nm	710	852	174	16512
6nm	811	974	198	18870
7nm	1095	913	223	21229
8nm	1014	1217	248	23588
9nm	1116	1339	273	25947

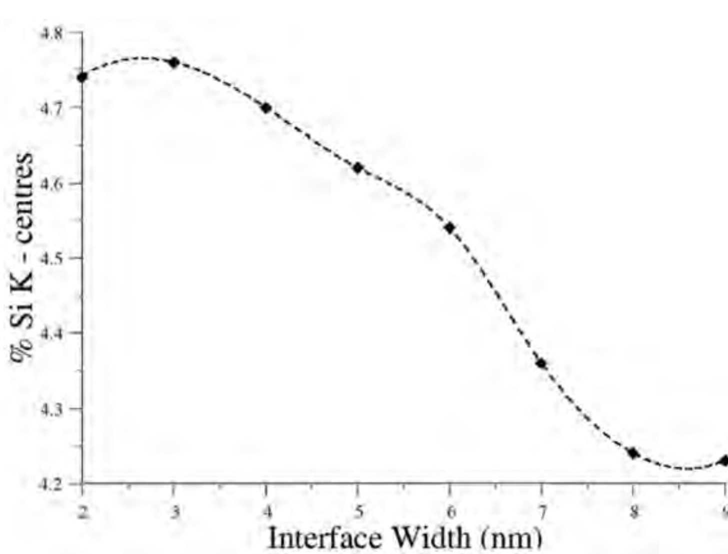

Figure 11.3: The percentage of Si atoms which have K-center topology as a function of the width of the N gradient region.

We analyze the trajectories of our MD simulations to identify K-centers, which are defined as under-coordinated Si-centers bonded to three N atoms. We define Si-N and Si-Si bonds based on the first peak of the pair correlation functions, as described in a previous study (see Chapter 10). In our samples the bulk region of a-$SiN_{1.2}$:H will have the same density of fixed charge in each system, thus any differences will be due to different levels of fixed charge in the gradient region. Therefore, we consider only the first 9 nm of the a-SiN_x:H layer in each sample in this analysis, since the remainder of the a-SiN_x:H will be the same from the point of view of Q_f concentration. The results are presented in Figure 11.3.
We can see from Figure 11.3, that there is a peak in the number of K-centers at an interface width of between 2 and 3 nm. We note that not all K-centers will be positively charged and contributing to the fixed charge in the a-SiN_x:H layer, therefore our analysis does not provide an absolute value for the value of Q_f. However, we think that it is reasonable to assume that the larger the number of K-centers the higher the fixed charge will be under otherwise identical circumstances. Thus the comparison of the number of K-centers in the various systems gives an indication of how much they will contribute relatively to the fixed charge. Our simulations show that an interface width larger than 3 nm would be expected to reduce the fixed charge.

11.3.2 Trap density

We now consider how the distribution of defects is affected by the gradient at the interface. Figure 11.4 shows how the distribution of two important defects in the a-SiN_x:H layer depends on the width of the layer of a-SiN_x:H. Increased density of interface states (D_{it}) at the semiconductor/insulator interface result in reduced carrier lifetimes. Thus it is desirable to minimize D_{it} at the interface in order to improve device performance. Figure 11.4 plots the density of K-centers mentioned previously across the various interfaces. Clearly from this figure the wider interface gradients lead to a reduction of the K-center density at the interface. Figure 11.4 plots the density of N-centers with a dangling bond, which have also been identified as possible trap states in a-SiN_x:H [141,142]. Again the density of these defects close to the interface is reduced when the interface gradient is increased.

11.3.3 Effects of the gradient interface on recombination

We now present a simplified model, based on our calculated trap densities, and estimations of the carrier concentrations, of the degree to which we would expect recombination to occur in the various gradient interfaces.

As Si is an indirect band-gap semiconductor, the dominant source of recombination will be bulk traps. Recombination can be considered as a process of electron and hole capture, which can be described by Shockley-Read-Hall (SRH) statistics [35]. According to the SRH model

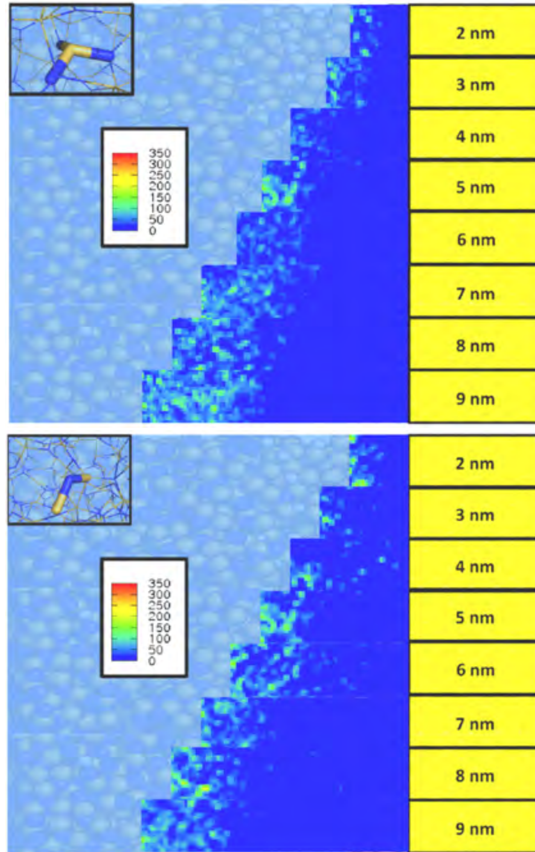

Figure 11.4: Plots of the density of important geometrical defects across the gradient layer in the a-SiN_x:H/c-Si interface. The graph shows (vertical) gradients with widths from 2 nm (top) to 9 nm (bottom). $x = 1.2$ in a-SiN_x:H (light blue region to the left) and decreases linearly to $x = 0$ on the right (c-Si interface) for each width. The top plot shows K-center density, the bottom plot shows N-center density. Insets on each plot show a graphical representation of the defect in question, the legends show the number of instances of the defect center in each volume region during the MD simulation.

the rate of capture is given by

$$U = \left[1 - \exp\frac{E_t - E_n}{k_B T}\right] f_{pt}\rho_T \times \int_{e_c}^{\infty} f(E)N(E)c_n(E)dE \qquad (11.1)$$

Here E_t is the energy of the trap and E_n is the quasi Fermi level. We consider the system under the condition of zero bias, where the quasi-Fermi level is equal to the intrinsic Fermi level (E_{F_n}), and is located almost at mid-gap for non-doped systems. f_{pt} is the probability that a trap is empty (thus available to any carrier) and ρ_T is the trap density. The integral runs from the bottom of the conduction band (e_c) to all higher levels and the terms in the integrand are the fraction of states occupied by electrons ($f(E)$), the number of quantum states ($N(E)$) and the probability per unit time that an electron will be trapped by a given trap ($c_n(E)$). In our analysis we replace the integral of $f(E)N(E)dE$ by a carrier density ρ_n. The density of carriers, in a non-degenerate n-type semiconductor, is given by [162]

$$\rho_n = 2\left(\frac{2\pi m_{de} k_B T}{h^2}\right)\exp\left(\frac{-E_{F_n} - E_V}{k_B T}\right), \qquad (11.2)$$

where E_V is the energy of the valence band minimum. Since the Fermi energy for an intrinsic semiconductor lies very close to the middle of the band-gap, and as we do not expect the a-SiN$_x$:H layer to have a significant dopant population we estimate the value $E_{F_n} - E_V$ to be half the of the band-gap. m_{de} is the effective mass of an electron in the conduction band.
Therefore we re-write Equation 11.1 as

$$U = \left[1 - \exp\frac{E_t - E_n}{k_B T}\right] f_{pt}\rho_T\rho_n \times \int_{e_c}^{\infty} c_n(E)dE \qquad (11.3)$$

The value for m_{de} in c-Si is $0.33m_{\mathrm{e}}$ [162] and that in a-SiN$_x$:H is $\sim 0.5m_{\mathrm{e}}$ [163–165]. The variation of the band-gap of a-SiN$_x$:H with stoichiometry has been calculated by Robertson [166]. In Figure 11.5 we present the variation of the band-gap with stoichiometry and the resultant variation in carrier concentration in the a-SiN$_x$:H layer as calculated using Equation 11.2.

Subsequently, the trap density is calculated from the trajectories of the MD simulations, with the active trap density defined as

$$\rho_{\mathrm{T}}(z) = \rho_{\mathrm{K}}(z) + \rho_{\mathrm{N}}(z)\delta, \qquad \delta = \begin{cases} 1 & \text{if} \quad x \geq 1, \\ 0 & \text{if} \quad x < 1 \end{cases} \qquad (11.4)$$

where $\rho_{\mathrm{K}}(z)$ is the density of K-centers not passivated by hydrogen, $\rho_{\mathrm{N}}(z)$ is the density of N-centers not passivated by hydrogen and the delta function is 1 when x in a-SiN$_x$:H is larger than 1 and 0 when x is less than 1, to reflect the fact that below $x = 1$ the N-center is no longer active in the band-gap of a-SiN$_x$:H as illustrated in Figure 11.1. This predicts very little contribution to trapping from N-centers in the gradient interface, since by the time the

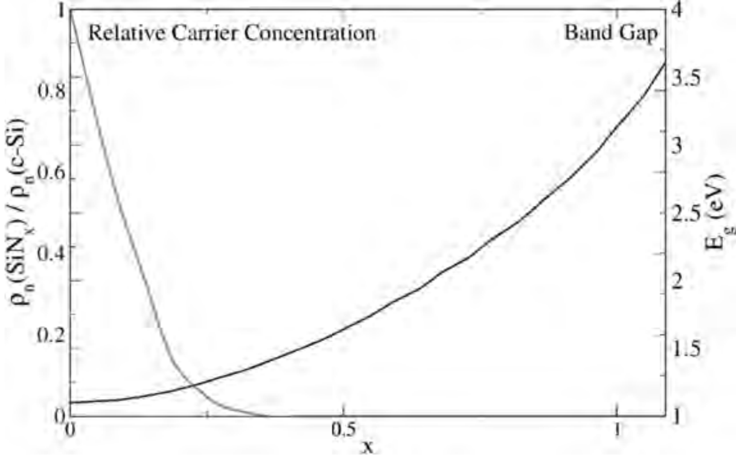

Figure 11.5: Band-gap dependence on the stoichiometry of a-SiN_x:H, as calculated by Robertson [166], and the resultant electron carrier population normalized by the carrier population in pure c-Si, calculated from Equation 11.2.

band-gap is wide enough for the N-center to be active, the carrier population is vanishingly small.

Thus we ignore the contribution from N-centers to trapping in gradient interface systems. The rate of capture at the K-center will depend on the difference between E_t and E_n in Equation 11.1, as we have already stated $E_\mathrm{n} = E_{\mathrm{F_n}}$ at zero bias. Since $E_{\mathrm{F_n}}$ is located at almost mid-gap as is E_t for the K-center [111], and given that the band-gap opens almost symmetrically about mid-gap [166] across the a-SiN_x:H composition range, this dependence will not change across the composition range either. Thus we can say that the probability of a carrier being trapped will be proportional to the trap density and the carrier density in the system

$$P_\mathrm{T} = \alpha \int_0^Z \rho_\mathrm{T}(z)\rho_\mathrm{n}(z)dz \tag{11.5}$$

where the integral is calculated from the a-SiN_x:H/c-Si interface at zero, to the edge of the a-SiN_x:H layer at Z. The constant of proportionality is

$$\alpha = \left[1 - \exp\frac{E_\mathrm{t} - E_\mathrm{n}}{k_\mathrm{B}T}\right] f_\mathrm{pt} \int_{e_\mathrm{c}}^\infty c_\mathrm{n}(E)dE, \tag{11.6}$$

and does not change across the composition range. P_T/α for the various interface widths at zero bias is plotted in Figure 11.6.

As can be seen from Figure 11.6, the introduction of a gradient interface results in a significant drop in the trapping probability for both N- and K-centers.

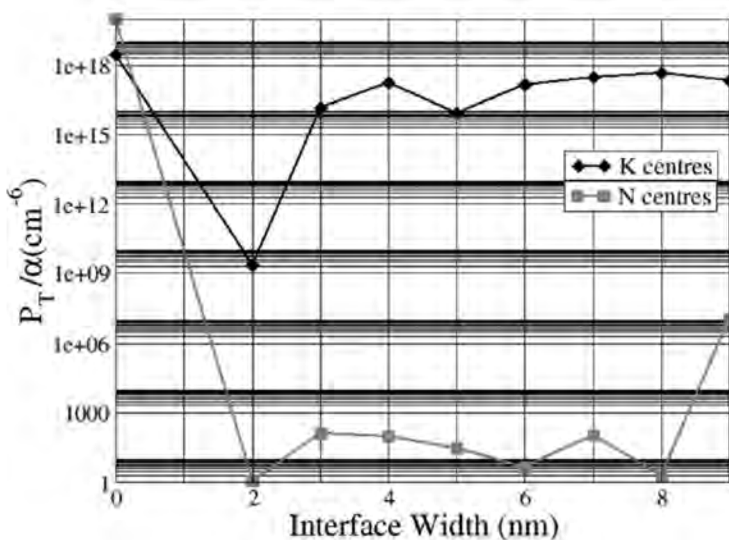

Figure 11.6: Probabilities of carrier trapping at defect centers depending on interface gradient thickness, calculated from Equation 11.5.

The number of N-centers drops to almost zero, implying that N-centers will play almost no role as recombination centers in gradient interface systems. The trapping probability for K-centers begins to rise again, by three orders of magnitude, with the introduction of a gradient wider than 2 nm. Given our earlier findings regarding the relation between fixed charge and the gradient width our simulations suggest that a gradient introduced by nitridation can have a beneficial effect on the performance of a solar cell, but that the degree of nitridation must be limited and an optimal width of the gradient region is around 2 nm.

11.4 Conclusions

In conclusion, we have performed molecular dynamics simulations to investigate the effect of a N density depletion layer at the interface between c-Si and a-SiN_x:H. In particular we have concentrated on how the width of the depletion layer affects the density and distribution of a number of bond types and defect states which have previously been shown to be important for the performance of solar cells when a-SiN_x:H is used.

By considering the density of K-centers and the locations of K- and N-centers we believe that these results suggest that a gradual interface with a gradient in ρ_N can be designed to improve device efficiency. Furthermore we believe that the results suggest that there must be an optimal width of the ρ_N

gradient, which would result in the best balance between layer stability, fixed charge and concentration of recombination centers at the interface. Although we realize that the complexity of the factors which affect operational solar cells means that we can only consider a small number of important aspects, we believe that our simulations suggest that an a-SiN_x:H gradient layer of around 2 nm would provide the best compromise between layer stability and electrical performance.

Acknowledgments The authors acknowledge support from the European Commission Grant MMP3-SL-2009-228513, "Hipersol" as part of the 7th Framework package, grant number 228513. Via our membership of the UK's HPC Materials Chemistry Consortium, which is funded by EPSRC (EP/F067496), this work made use of the facilities of HECToR, the UK's national high-performance computing service, which is provided by UoE HPCx Ltd at the University of Edinburgh, Cray Inc and NAG Ltd, and funded by the Office of Science and Technology through EPSRC's High End Computing Programme.

Chapter 12

Density functional theory study of the structural and electronic properties of a-$Si_3N_{4\text{-}x}$:H

L.E. Hintzsche[1], C.M. Fang[1], T. Watts[1], M. Marsman[1], G. Jordan[1], M.W.P.E. Lamers[2], A.W. Weeber[2], G. Kresse[1]

[1] University of Vienna, Faculty of Physics and Center for Computational Materials Science, Sensengasse 8/12, A-1090 Vienna, Austria
[2] ECN Solar Energy, P.O. Box 1, 1755 ZG Petten, the Netherlands

Physical Review B **86**, 235204 (2012)

Abstract

We present *ab initio* density functional theory studies for stoichiometric as well as non-stoichiometric amorphous silicon nitride, varying the stoichiometry between $Si_3N_{4.5}$ and Si_3N_3. Stoichiometric amorphous Si_3N_4 contains the same local structure as crystalline Si_3N_4, with Si being fourfold coordinated and N being threefold coordinated. Only few Si-Si and N-N bonds and other defects are found in stoichiometric silicon nitride, and the electronic properties are very similar to the crystalline bulk. In over-stoichiometric Si_3N_{4+x}, the additional N results in N-N bonds, whereas in under-stoichiometric $Si_3N_{4\text{-}x}$ the number of homopolar Si-Si bonds increases with decreasing N content. Analysis of the structure factor and the local coordination of the Si atoms indicates a slight tendency towards Si clustering, although at the investigated stoichiometries phase separation is not observed. In the electronic properties, the conduction band minimum is dominated by Si states, whereas the valence band maximum is dominated by lone pair N states. Towards Si rich samples, the character of the valence band maximum becomes dominated by Si states corresponding to Si-Si bonding linear combinations. Adding small amounts of hydrogen, as typically used in passivating layers of photovoltaic devices, has essentially no impact on the overall structural and electronic properties.

12.1 Introduction

Hydrogenated amorphous silicon nitride (a-$Si_3N_{4\text{-}x}$:H) is commonly used in the solar cell industry because it has three desirable properties. It serves as anti-reflection coating and enhances light transmission, it is the main source of hydrogen (H) for passivating the silicon (Si) wafer and it chemically and physically passivates the surface [167]. The properties of a-$Si_3N_{4\text{-}x}$:H can be easily varied by changing the deposition parameters like the gas flow of NH_3 and SiH_4, allowing the three properties to be tuned enhancing solar cell efficiency [27]. The material is most commonly fabricated by plasma enhanced chemical vapor deposition (PECVD) [43, 167, 168], but other deposition methods like sputtering are used as well [147, 169].

Structural properties have been experimentally determined by Aiyama *et al.* and Misawa *et al.* using X-ray and neutron scattering [170,171]. Furthermore, trapping centers have been investigated by electro paramagnetic resonance (EPR) measurements by Lenahan *et al.* and Warren *et al.* [140, 141]. As experiments are limited to microscopic and macroscopic investigations, it is difficult to link them to structural and electronic properties at the atomic scale. In order to fill this gap, computer simulations are performed to establish realistic atomic models and relate them to the observed macroscopic properties.

First insight into silicon nitrides at the atomic scale was provided by the seminal studies of Robertson *et al.* in the 90s [111, 166, 172, 173]. Robertson *et al.* applied tight binding methods to small, essentially crystalline model systems and investigated defect induced changes in the electronic properties. These results are still helpful, but, with the advances in *ab initio* density functional theory, it is possible to study the properties of amorphous silicon nitrides in much greater detail and using better founded approximations.

In more recent computer simulations, typically a small selection of a-$Si_3N_{4\text{-}x}$:H configurations were produced in order to investigate the structural, electronic, optical as well as vibrational properties [115, 146, 174–183]. Few of these studies even examined the materials properties for different nitrogen concentrations [146, 176, 182] and the effect of hydrogenation [115, 178, 179]. Nevertheless, the number of considered models was generally very small making statistically meaningful analysis difficult.

In order to build amorphous model structures different strategies are adopted. A common strategy is to assemble small subunits and clusters with proper short range order (SRO) into a continuous random network (CRN) [175] or Bethe lattice [178, 184]. Furthermore, bond switching methods can be applied to the crystalline samples until they become reasonably amorphous [179, 185].

Although very small defect concentrations are achievable by these strategies [185], the most common and maybe most unbiased method to determine amorphous structures is by cooling the samples from the melt. This can be done by either Monte Carlo (MC) [115, 176, 177] or Molecular Dynamics (MD) [146, 174, 179–183, 186] simulations.

Matter of fact, all simulations need to rely on a potential energy surface to calculate jump probabilities and forces during the cooling and relaxation. *Ab initio* methods are very desirable but incur great computational cost [146, 179–181, 183], and hence many simulations are performed using different types of semi-empirical potential models (e.g. Tersoff, Thight Binding, Keating, Busing, Born-Mayer-Huggins) [115, 174–176, 178, 182, 186]. Both methods can be also combined in order to save computation time and/or to simulate larger systems. In this case, the samples are annealed using fast empirical potentials, and, afterwards, the electronic properties are calculated with more accurate *ab initio* methods [177, 186].

In this work, we present large-scale *ab initio* molecular dynamics studies on stoichiometric and non-stoichiometric Si_3N_{4-x} including up to 10 at.% H. Typically, we prepare three carefully quenched reference configurations with about 200 atoms for each considered stoichiometry. To allow for a statistically meaningful evaluation of defect related properties, 1000 small structural models with 100 atoms are then prepared for each stoichiometry. The main focus of the present work is an evaluation of the small models against the larger models, as well an evaluation of the average structural properties such as the pair correlation function, angular distribution function, structure factor, general features of the electronic density of states as well as the average local coordination of the atoms. A detailed analysis of the defect related properties is presented in Chapter 13.

12.2 Modeling Setup

12.2.1 Compositions, concentrations and densities

Non-stoichiometric amorphous silicon nitrides exhibit large density variations which seemingly depend strongly on the applied preparation conditions [168, 187, 188].

Here we mainly focus on amorphous silicon nitrides as used in solar cell industry and decided to determine the densities from the data published by Ippolito *et al.* [182]. We found it helpful to plot the average experimental volume per atom versus the nitrogen concentration, as shown in Figure 12.1. The volumes would lie on a straight line, if Vegard's law was observed [189]. Indeed, within the experimental uncertainties, this relation seems to hold very well, but the fit deviates from the volume of crystalline silicon in the Si

rich case by more than 2%. Increasing the slope improves this behavior for the Si rich case (full line) without deteriorating the root mean square error for the amorphous samples significantly. The final densities and volumes, as obtained from the fitted experimental data, are summarized in Table 12.1.

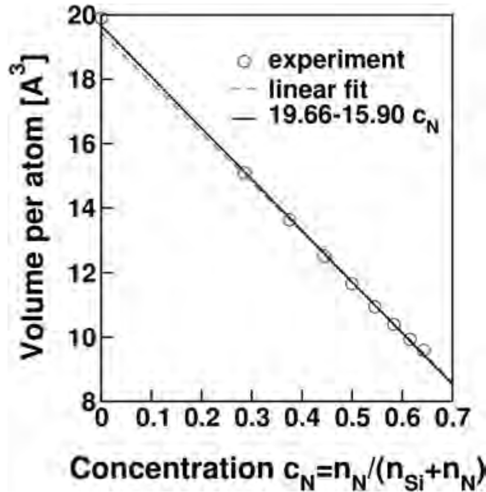

Figure 12.1: Volume per atom as a function of the N concentration $c_{\mathrm{N}} = n_{\mathrm{N}}/(n_{\mathrm{N}} + n_{\mathrm{Si}})$. The broken line shows the best linear fit to the experimental values (circles). The full line was obtained by readjusting the fit such that the density of crystalline Si is more accurately reproduced. This has only a slight effect on the root mean square error. The experimental data points for $\mathrm{Si_3N_x}$:H are from Guraya *et al.* [147], the density for crystalline Si is from Ashcroft *et al.* [190].

The second issue to address is the influence of hydrogen on the volume. The experimental data were almost always measured in the presence of substantial amounts of H approaching up to 25 at.% [147]. Remarkably, however, hydrogen seems to influence the volume only very little. For instance, although for the data shown in Figure 12.1, the H content varies from $15 - 25$ at.%, the deviation from Vegard's law is hardly noticeable, and for $\mathrm{Si_3N_4}$ the volume of the amorphous structure agrees within few percent with the volume of crystalline $\beta{-}\mathrm{Si_3N_4}$. This observation is reinforced by considering the small covalent radius of hydrogen. Even if we double the covalent radius, $d_{\mathrm{H}} = 2r_{\mathrm{covalent}} = 0.62$ Å (this value corresponds to the H-H bond length), and determine the corresponding volume, $V_{\mathrm{H}} = 4\pi d_{\mathrm{H}}^3/3 \approx 1$ Å^3, we obtain only small corrections to the volume. If the concentration was 20 at.% H, it would take up at most 3% of the entire volume. This is certainly a rather crude consideration, since one could argue that hydrogen disrupts the usual bonding topology of the network and therefore might yield

Table 12.1: Densities ρ and volumes per atom of Si_3N_x as studied in the present work. The densities were derived from experimental values as shown in Figure 12.1 (see also Guraya *et al.*) [147]. The table also shows the supercell volumes and the number of silicon n_{Si} and nitrogen atoms n_N in the considered supercells.

	$Si_3N_{4.5}$	Si_3N_4	$Si_3N_{3.5}$	Si_3N_3
ρ [g/cm^3]	3.22	3.14	3.06	2.98
volume per atom [Å^3]	10.12	10.57	11.10	11.71
$n_N/(n_{Si}+n_N)$	0.60	0.57	0.54	0.50
large supercell vol. [Å^3]	1973	1999	2020	2014
n_{Si}	78	81	84	86
n_N	117	108	98	86
small supercell vol. [Å^3]	1012	1033	1020	1077
n_{Si}	40	42	42	46
n_N	60	55	50	46

a significantly larger volume increase, but neither the experimental data nor any of our results seems to support this idea. Most likely, hydrogen simply accommodates in the network at defective or highly strained sites and hence causes only negligible changes in the volume.

To determine the hydrogen concentration typically found in a-Si_3N_{4-x}:H layers used in the fabrication of industrial solar cells, over 80 different Si_3N_{4-x}:H samples were prepared with plasma-enhanced-chemical-vapor deposition (PECVD) at the Energy Research Centre of the Netherlands. A more detailed description of the PECVD method is given by Soppe *et al.* [27]. The samples were analyzed using Fourier transform infrared spectroscopy (FTIR) and ellipsometry (see also Chapter 7). From this data, the atomic concentration was extracted using the approach described by Bustarret *et al.* (see Figure 12.2) [47]. We expect that the hydrogen concentration is rather low for the stoichiometric case and, although the data show a large scatter towards the right side of the graph (Si_3N_4), and the hydrogen concentration increases again for over-stoichiometric samples (Si_3N_{4+x}), we decided to perform the simulations for the Si_3N_4 case without hydrogen. For the other, nitrogen deficient cases, we performed simulations without hydrogen and with approximately 13 at.% H. This seems to be well within the experimental range, which lies between 10 and 15 at.% H for the considered stoichiometries.

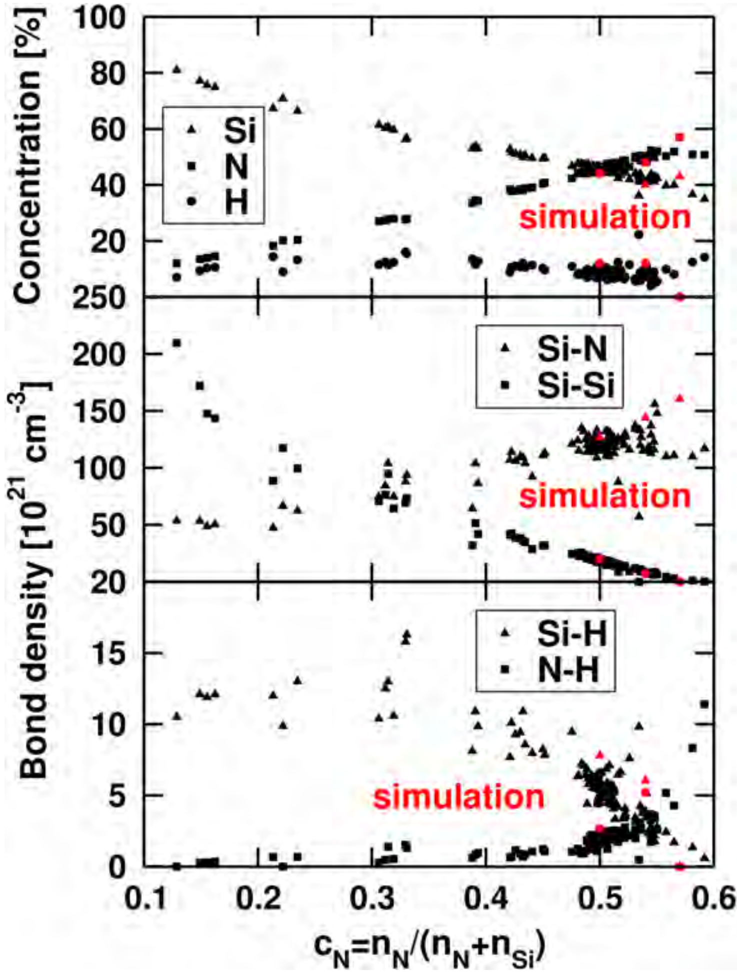

Figure 12.2: Atomic concentration and bond densities estimated for plasma-enhanced-chemical-vapor depositioned (PECVD) silicon nitride. The dependency of the nitrogen concentration c_N is shown. The stochiometric case (Si_3N_4) is to the right. The values of Si_3N_4, $Si_3N_{3.5}H_{0.8}$ and $Si_3N_3H_{0.8}$, obtained by simulations, are marked with red symbols.

12.2.2 PAW potentials and technical parameters

All calculations presented in this work were performed using the Vienna *ab initio* simulation package (VASP) and projector augmented wave (PAW) potentials in the implementation of Kresse and Joubert [191–194].

Since our aim was to perform large scale simulations, we decided to construct special PAW potentials optimized for the specific application in mind. To this end, we chose for the PAW potentials the largest possible core radius that did not degrade the quality of the results noticeable. We found that core radii of 2.0 and 1.9 a.u. (2.5 and 2.4 a.u.) for the *s*-partial (*p*-partial) waves for N and Si, respectively, lead to acceptable results. For Si the *d*-potential was chosen as local potential, whereas for N the all-electron potential was smoothed inside a sphere with a radius of 0.8 a.u.. These potentials allowed to obtain converged total energies at a plane wave kinetic energy cutoff of about 150 eV. Results for bulk Si are essentially indistinguishable from more accurate PAW potentials, whereas results for Si_3N_4 are slightly deteriorated compared to accurate reference calculations, but the errors remain fairly small. The Si_3N_4 volumina of the bulk crystalline phases (α, β and γ) are reproduced to within 1.5%, and the relative energy difference between the α and γ phase, which is 1.05 eV per formula unit using accurate reference potentials, is reproduced to within 0.03 eV. The largest errors are observed for the zone centered phonons, where discrepancies of the order of 5.0% for some high frequency branches are observed, whereas the predicted DFT Kohn-Sham band-gaps agree within 2 % with the accurate reference potential. All in all, the differences between the accurate reference potentials and the soft potentials are of the same order as the differences between the local density approximation and gradient corrected density functionals, which we believe to be a reasonable threshold. Furthermore, for liquid $Si_3N_{3.5}$ only small differences were found for the pair-correlation function and angular distribution function at 3000 K (see Figure 12.3). For over-stoichiometric samples, however, the N-N distance is shifted by 0.2 Å to larger bond distances using the soft potentials, but this will not change the results for the experimentally relevant under-stoichiometric samples. This makes us confident that the present potential will give accurate results and is certainly far superior to conventional molecular dynamics potentials such as the Tersoff potential [182]. All simulations presented here have been performed with Brillouin sampling at the Γ-point, and the PBEsol functional was used [195].

Compared to the standard potentials requiring 400 eV cutoff, the savings are about a factor five, and they allow us to perform much longer simulations than otherwise possible.

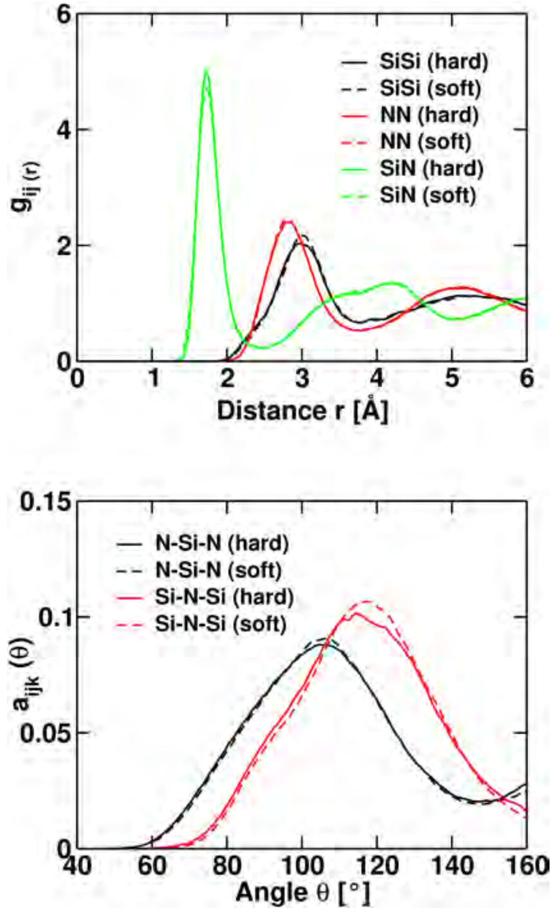

Figure 12.3: The PC functions $g_{ij}(r)$ and angular distribution functions $a_{ijk}(\Theta)$ of a-$Si_3N_{3.5}$ at 3000 K compared for different potentials. The soft potential (150 eV) used in our calculations gives nearly the same results as the harder reference (300 eV).

12.2.3 Large simulation cells, slow annealing

Our initial strategy was to determine representative samples by simulated annealing using fairly large simulation cells with a total supercell volume of about 2000 Å^3. Table 12.1 summarizes the corresponding supercell volumes and the number of atoms we employed.

All systems were initially molten at 4000 K and then the temperature was gradually decreased until the atomic configuration started to freeze in. In all simulations, a time step of 1.5 fs was adopted, and the mass of hydrogen was increased to ten atomic mass units. This mass increase will change the dynamics of the system, but has no influence on the explored configuration space, as the partition function factorizes into a momentum and configuration dependent part, with the later one being independent of the masses.

The "freezing" temperature was strongly dependent on the stoichiometry, as demonstrated in Figure 12.4, where the diffusion constant is plotted versus the temperature. When the value drops significantly below $0.05 - 0.1$ Å^2/ps, it is difficult to determine accurate diffusion constants. Monitoring the mean square displacement for these cases indicates jump diffusion occurring every few ps. It is likely that this is defect mediated, since the network can easily re-adjust and re-link at defects, and, consequently, the defect might migrate through the network. But a detailed investigation of this issue is beyond the scope of the present work. Stoichiometric Si_3N_4 freezes in at about $3000 - 3100$ K on a timescale of $20 - 40$ ps, which we observed repeatedly for several simulations at different system sizes, and the freezing goes along with the geometrical defects being progressively removed during the annealing. Usually the system locks in when two or zero defects are present in the sample (for topological reasons the defects always come in pairs for stoichiometric Si_3N_4). The observed amorphization temperature seems to be significantly larger than the experimental estimates of about 2000 K [196, 197]. But we note that the melting temperature of silicon nitride cannot be measured, since the solid decomposes into atomic and molecular Si and N before melting sets in (gas pressure of Si).

Matter of fact, our simulations are also hampered because of the short timescales and system sizes that are accessible to us: once all defects are cured, the system locks in. In real experimental samples, the density of mobile defects will only exponentially approach zero, sustaining diffusion at much lower temperatures. Furthermore, we believe that the experimental samples are never perfectly stoichiometric. Even being slightly off-stoichiometric, diffusion is enhanced since some defective bonds (e.g. Si-Si bonds) or coordination defects prevail. For $Si_3N_{3.5}$ and $Si_3N_{4.5}$, amorphization occurs at roughly 2600 K, whereas, for Si_3N_3, the freezing occurs at roughly 2300 K. We also note that jump diffusion is well possible below these temperatures, but these events are very rare on the timescales accessible to us. Finally, addition of

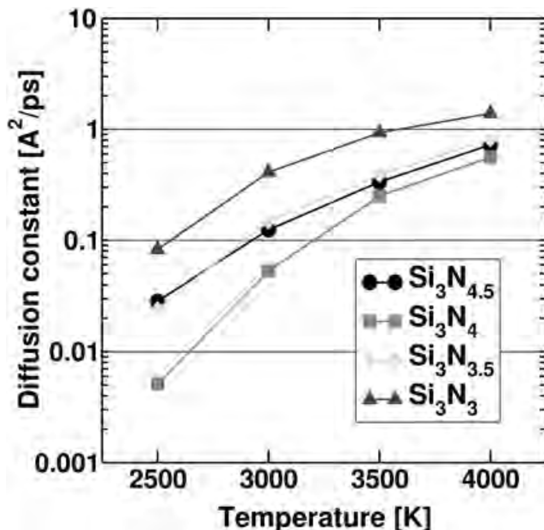

Figure 12.4: Diffusion constants for Si_3N_x at different temperatures. Stoichiometric Si_3N_4 (red squares) always shows the highest freezing temperature.

10 at.% H, generally lowers the amorphization temperature by another 200 K (not shown).

The adopted temperature profiles are shown in Figure 12.5. In retrospect, we could have fine-tuned the cooling history somewhat for each stoichiometry, for instance by progressively elongating the runs when approaching the freezing temperature, but we believe that this will change the final results only little. In order to prepare a set of samples, we extended the simulation runs at 3500 K (Si_3N_4) and 3000 K (Si_3N_{4-x}:H) followed by the same annealing history as for the original samples. In this manner, three samples were generated for a-Si_3N_4, a-Si_3N_3, a-$Si_3N_{3.5}$. For the less relevant a-$Si_3N_{4.5}$ and the hydrogenated samples only a single large representative structure was generated.

12.2.4 Small simulation cells

The drawback of the strategy adopted above is that it is difficult to generate any statistics for the defect related properties. Even with three samples, we cannot determine how likely the formation of a certain defect class is. To complement the simulations of the large systems, we therefore performed simulations for smaller systems containing about 100 atoms. In this case, the simulation was run for up to 1 ns just above the freezing temperature, and every 500-1000 steps a configuration was quenched into the closest local minimum using a standard minimization procedure. This approach allowed

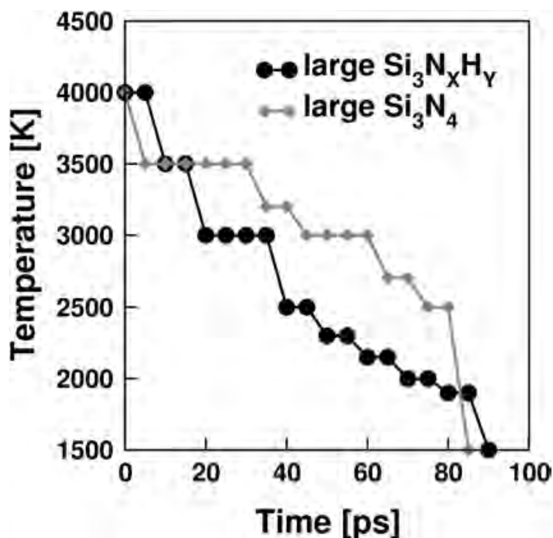

Figure 12.5: Annealing history adopted in the present work for the large Si_3N_x systems. Because Si_3N_4 freezes at about 3100 K, the system was equilibrated for 30 ps at 3500 K, then the system was cooled to 3000 K and annealed at this temperature until most defects were removed. For the other stoichiometries 20 ps annealing was performed at 3000 K, and then the temperature was gradually decreased to 2000 K equilibrating at each temperature for 10 ps.

us to generate about one thousand reasonably independent samples for each stoichiometry. The corresponding runs typically required four weeks on 32 cores each.

In Figure 12.6, we show the acquired mean square displacements (MSD) of four different stoichiometries. The diffusion constants are roughly similar and constant over the simulation time. Lowering the temperature by 50 – 100 K usually resulted in rapid freezing of the structures. The chosen stoichiometries correspond roughly to the same stoichiometries as those considered for the large systems. Only for the "stoichiometric" case, we removed one N atom resulting in a stoichiometry of roughly $Si_3N_{3.9}$ in order to avoid that all defects accidentally annihilate, which might have resulted in a "lock-in" at temperatures even above 3100 K.

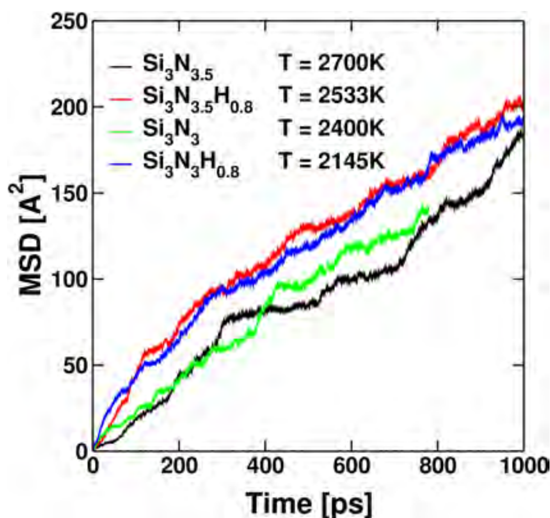

Figure 12.6: Mean square displacements (MSD) of four different $Si_3N_{4\text{-}x}$:H ensembles. The averaged temperature is given after the system label. The temperatures were adjusted to keep the ensembles just above the freezing temperature. In some cases, the temperature had to be increased and the simulation restarted before the freezing, when accidental freezing occurred.

12.3 Structural properties

The main focus in this chapter is on general structural properties, whereas a detailed analysis of the electronic properties of defects and defect statistics is given in Chapter 13. In the following sections we evaluated the pair correlation function, structure factor, angular distribution function and the local bonding topology at the Si and N sites.

12.3.1 Pair correlation function

The pair correlation (PC) functions for the quenched amorphous samples are shown in Figure 12.7. For the large systems, the results were averaged over three samples (except for $Si_3N_{4.5}$, where only a single structure was generated), whereas for the small systems the average was done over about 1000 samples. In addition to the PC function, we analyzed the average number of nearest neighbors by integration of the partial PC functions between 0 and the first minimum $r_{\rm min}$ in the respective function (see Table 12.2):

$$N_{\rm ij} = \rho_{\rm h(j)} \int_0^{r_{\rm min}} dr\ 4\pi r^2\ g_{\rm ij}(r). \tag{12.1}$$

Table 12.2: The partial coordination numbers $N_{\rm ij}$ evaluated for small ensembles. $N_{\rm ij}$ specifies for atom i the number of nearest neighbors of type j.

	$Si_3N_{4.5}$	Si_3N_4	$Si_3N_{3.5}$	Si_3N_3
$N_{\rm SiN}$	4.16	3.95	3.57	2.99
$N_{\rm SiSi}$	-	-	0.38	1.01
$N_{\rm NSi}$	2.77	3.02	3.00	2.99
$N_{\rm NN}$	0.30	-	-	-
	$Si_3N_{3.5}H_{0.4}$	$Si_3N_{3.5}H_{0.8}$	$Si_3N_{3.5}H_{1.7}$	$Si_3N_3H_{0.8}$
$N_{\rm SiN}$	3.51	3.47	3.40	2.97
$N_{\rm SiSi}$	0.48	0.35	0.33	0.93
$N_{\rm NSi}$	2.94	2.91	2.85	2.97
$N_{\rm NN}$	-	-	-	-
$N_{\rm HSi}$	0.51	0.51	0.47	0.70
$N_{\rm HN}$	0.48	0.44	0.38	0.24
$N_{\rm HH}$	0.04	0.06	0.13	0.06

Also the mean bonding distance $\bar{d}_{\rm ij}$ and the standard deviation $\sigma_{\rm ij}$ were evaluated by integrating up to the first minimum (see Table 12.3).
The first important observation is that the PC functions of the small (black solid lines) and the large systems (black broken lines) are very similar, in particular, at large distances beyond the first nearest neighbor. This is a little bit counterintuitive, since we would rather expect differences at long distances due to finite size effects, but at large distances we only recognize slightly more scatter for the large system, which points towards insufficient sampling over different configurations. However, at the distance of the first nearest neighbor, the PC function for the large systems shows somewhat more pronounced and narrower peaks for N-N and Si-Si. We believe that this is related to the slower and more careful annealing performed for the large systems. Recall that the small systems were created by directly quenching from the melt. In all other respects, the small systems seem to adequately

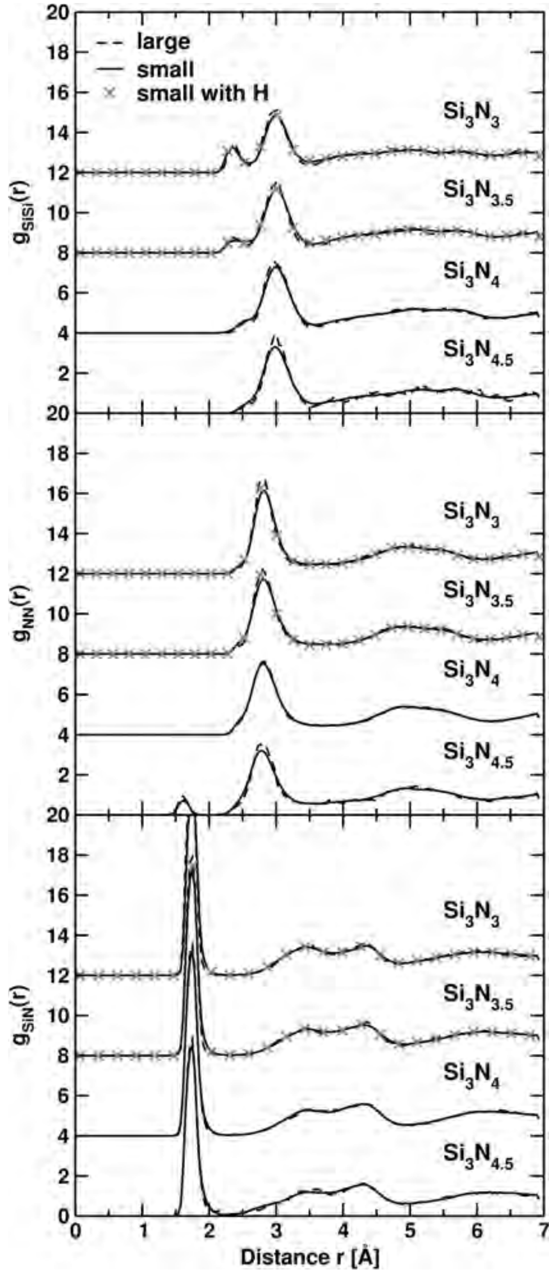

Figure 12.7: Partial pair correlation functions $g_{ij}(r)$ for the small (full line) and the large Si_3N_x:H systems (broken line). Hydrogen (crosses) leaves the PC function largely unchanged.

Table 12.3: Mean bonding distances and standard deviations and position of the minimum in the pair correlation function of the Si_3N_x evaluated for small ensembles (all values are in Å). For the non-stoichiometric systems, peaks emerge at short distance corresponding to direct Si-Si and direct N-N neighbor atoms at 2.4 Å and 1.6 Å, respectively.

Si-Si	$Si_3N_{4.5}$	Si_3N_4	$Si_3N_{3.5}$	Si_3N_3
1st $\bar{d}_{SiSi}$	-	-	2.40	2.38
1st σ_{SiSi}	-	-	0.10	0.10
1st r_{min}	-	-	2.57	2.59
2nd $\bar{d}_{SiSi}$	3.00	2.99	3.02	3.02
2nd σ_{SiSi}	0.22	0.24	0.19	0.19
2nd r_{min}	3.56	3.56	3.53	3.49
N-N	$Si_3N_{4.5}$	Si_3N_4	$Si_3N_{3.5}$	Si_3N_3
1st $\bar{d}_{NN}$	1.62	-	-	-
1st σ_{NN}	0.06	-	-	-
1st r_{min}	1.98	-	-	-
2nd $\bar{d}_{NN}$	2.86	2.89	2.90	2.89
2nd σ_{NN}	0.26	0.26	0.25	0.23
2nd r_{min}	3.54	3.62	3.63	3.58
Si-N	$Si_3N_{4.5}$	Si_3N_4	$Si_3N_{3.5}$	Si_3N_3
1st $\bar{d}_{SiN}$	1.75	1.75	1.75	1.75
1st σ_{SiN}	0.09	0.08	0.07	0.07
1st r_{min}	2.26	2.30	2.30	2.30

represent the amorphous structure, and specifically finite size effects at large distances are largely absent in the small simulation cell, at least at the level of the PC function.

The second remarkable observation is that hydrogen, in the low concentrations considered here, has virtually no discernible effect on the PC function (compare full line with red crosses). It rather seems that hydrogen only participates as a "spectator" decreasing the connectivity and increasing self-diffusion, with no dramatic effect on the *average* structural properties of the amorphous structure, as evaluated by the PC function. For $Si_3N_{3.5}H_{0.8}$ and $Si_3N_3H_{0.8}$, the mean hydrogen bonding distances are 0.77 ± 0.01 Å for $\bar{d}_{HH}$, 1.50 ± 0.07 Å for $\bar{d}_{HSi}$, and 1.11 ± 0.04 Å for $\bar{d}_{HN}$.

The present PC functions agree very well with previous simulations. The Si-N PC functions shows a pronounced peak at 1.75 Å, which hardly shifts with varying stoichiometry, and in fact, the entire Si-N PC function is almost entirely independent of stoichiometry. Inspection of Table 12.2 shows that each N atom forms three bonds, whereas the number of bonds formed by the Si atoms is always very close to four (sum of N_{SiN} and N_{SiSi}). For stoichiometric Si_3N_4, the Si-Si PC function shows one strong peak at 3.0 Å, which is related to the distance between Si atoms in Si-N-Si triangles, and similarly the N-N PC function shows a peak at 2.90 Å related to N-Si-N triangles. The other feature worthwhile mentioning is the small shoulder in the Si-Si PC function around 2.6 Å. As already discussed by Giacomazzi *et al.*, it is mostly related to planar Si-N-Si-N squares [180]. For sub-stoichiometric $Si_3N_{4\text{-}x}$ this peak seems to develop into a pronounced shoulder around 2.4 Å, but in fact, the origin of this shoulder are direct Si-Si bonds, as shown in the number of direct Si-Si neighbors N_{SiSi} in Table 12.2, which increases from 0.38 in $Si_3N_{3.5}$ to 1 in Si_3N_3. Likewise direct N-N bonds form in over stoichiometric Si_3N_{4+x}, as indicated by a value of $N_{NN} = 0.3$ in $Si_3N_{4.5}$. The absence of direct N-N neighbors in stoichiometric and sub-stoichiometric $Si_3N_{4\text{-}x}$, and likewise the absence of direct Si-Si neighbors in stoichiometric and over-stoichiometric Si_3N_{4+x} is a clear indication for the strong ordering tendency in silicon nitrides, as direct bonds to the same species are only formed if the material contains too much Si (Si-Si bonds) or too much N (N-N bonds). In summary, the amorphous structures are characterized by (i) fourfold coordinated Si atoms and threefold coordinated N atoms, with (ii) a strong tendency towards hetero-coordination and formation of Si-N bonds. The partial coordination numbers also reveal that hydrogen indeed disrupts the normal network topology of silicon nitride. For $Si_3N_{3.5}H_{0.8}$, it forms bonds with both Si and N atoms, whereas for $Si_3N_3H_{0.8}$ bonds are predominantly formed to Si atoms. Of course such bonds reduce the number N-Si bonds, for instance N_{NSi} drops from 3.0 to 2.91 in $Si_3N_{3.5}H_{0.8}$, and the sum $N_{SiSi}+N_{SiN}$ decreases from 4 to 3.9 when hydrogen is added in $Si_3N_3H_{0.8}$.

To investigate the dependence on the H content, we also performed calculations for concentrations of 6 at.% and 20 at.% H for $Si_3N_{3.5}$. As can be recognized from Table 12.2 the probability that hydrogen attaches to silicon or nitrogen is pretty much independent of the H content but changes with stoichiometry. For $Si_3N_{3.5}$ and Si_3N_3, about 50% and 70% of the H bonds to Si, respectively, whereas the number of hydrogen bonded to nitrogen decreases with decreasing N content. These results agree well with experiments (compare Figure 12.2 bottom panel, also see Guraya *et al.* and Garcia *et al.* [110, 147]). It is also quite clear and not unexpected, that the number of H "dimers" increases with the H content, but it remains fairly small up to about $10 - 15$ at.% H.

For stoichiometric Si_3N_4, we can compare the present bonding distances and the bonding angles with experimental data obtained by Aiyama *et al.* and Misawa *et al.* [170, 171] and with results from the simulations performed by Giacomazzi *et al.* and Jarolimek *et al.* [180, 181]. The present mean values have been calculated by averaging the bond length over the bonds up to the first minimum r_{min} tabulated in Table 12.3. Our mean distances are 3.0 Å for $\bar{d}_{\text{SiSi}}$, 2.9 Å for $\bar{d}_{\text{NN}}$ and 1.75 Å for $\bar{d}_{\text{SiN}}$. These values agree very well with previous experiments and simulations, as shown in Table 12.4.

Table 12.4: Reference values for the bond lengths in a-Si_3N_4 obtained by experiments and simulations (all values are in Å).

Reference	1st $\bar{d}_{\text{SiSi}}$	2nd $\bar{d}_{\text{SiSi}}$	2nd $\bar{d}_{\text{NN}}$	2nd $\bar{d}_{\text{SiN}}$
Aiyama *et al.* [170]	–	3.00	3.00	1.75
Misawa *et al.* [171]	–	3.01	2.83	1.73
Giacomazzi *et al.* [180]	2.42	3.03	2.76	1.73
Jarolimek *et al.* [198]	2.35-2.41	3.10	2.90	1.76

For Si rich samples, the direct Si bond distance is located at 2.4 Å, again in excellent agreement with previous simulations for amorphous Si_3N_x:H (and in good agreement with simulations for amorphous Si) [180, 181, 198].

Over-stoichiometric $Si_3N_{4.5}$ was investigated by Ippolito *et al.* using Tersoff potentials finding a peak in the N-N PC function around 1.3 Å [182]. In view of our present value of 1.62 Å this seems a little bit too short, but we have already emphasized that this peak distance is somewhat overestimated due to the use of a very soft N potential. After relaxation using harder potential, the mean distance moves to 1.45 Å, which is still larger than the value for the Tersoff potential. Our present simulations, also agree with previous *ab initio* simulations in predicting no direct N-N neighbors in stoichiometric and sub-stoichiometric $Si_3N_{4\text{-x}}$, whereas the previous force field simulations

showed direct N-N bonds even in slightly sub-stoichiometric Si_3N_{4-x}. This clearly points towards some deficiency in the Tersoff force fields.

12.3.2 Angular distribution function

In Figure 12.8, we show the angular distribution functions for different Si_3N_x compositions, with and without hydrogen. As before for the pair correlation function, hydrogen influences the angular distribution function very little. Regardless of stoichiometry, the main peaks are located at mean angles of 110° for silicon, and 120° for nitrogen. The value of $120° = 360°/3$ is in perfect agreement with the value expected for a flat triangle formed by three Si atoms surrounding a central N atom. This again confirms that the local bonding topology of nitrogen changes very little compared to crystalline Si_3N_4, where each N atom is surrounded by three Si atoms forming a coplanar triangle. This is also consistent with the electronic configuration of nitrogen, forming three sp^2 hybrid orbitals that interact with the three Si neighbors, and one out of plane lone pair p orbital that is doubly occupied and oriented perpendicular to the NSi_3 plane. Furthermore, a second peak is visible at 90° in the angular distribution function. This peak stems from N-N neighbors in a planar Si-N-Si-N arrangement, as shown in the inset.

The bond angle distribution for silicon is strongly peaked at a mean angle of 110°. This again agrees perfectly with the expected tetrahedral bonding angle of 109.5°. As for nitrogen, this suggests that the Si atoms may maintain their sp^3 hybridization forming bonds with the four neighboring atoms. These are N atoms in the stoichiometric case, and possibly few Si atoms in the sub-stoichiometric case Si_3N_{4-x}. Again a clear secondary peak is visible at 90° related to the planar Si-N-Si-N arrangement already mentioned above. For both silicon and nitrogen this peak loses intensity when moving to sub-stoichiometric compositions. This relates well to the observation that the number of Si-N-Si-N square configurations decreases when the amount of nitrogen deviates from the perfect stoichiometry Si_3N_4.

12.3.3 Structure factor

Information about long range order and density fluctuations are most easily investigated by an ensemble average of the Faber-Ziman structure factor $S(\mathbf{k})$ [199–202].

$$S(\mathbf{k}) = \frac{1}{N} \left\langle \sum_i \sum_j \exp[-i\mathbf{k}(\mathbf{r}_i - \mathbf{r}_j)] \right\rangle, \qquad (12.2)$$

where $\mathbf{k}$ are wave vectors and N is the total number of atoms and $\mathbf{r}_i$ are the atomic positions. Consistent with the finite supercell, we evaluated the structure factor on a grid of reciprocal lattice vectors $\mathbf{k}$ that are compatible with the applied supercell (and not by a Fourier transformation of the

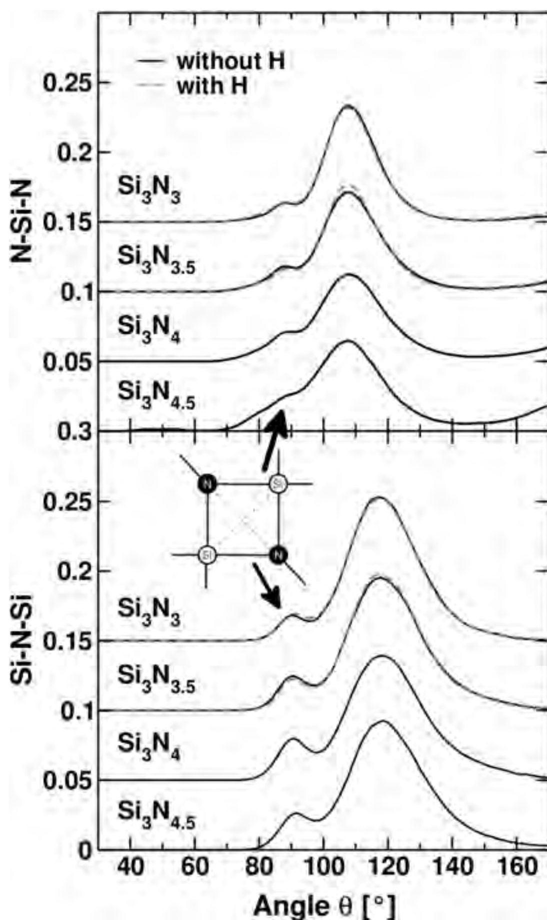

Figure 12.8: The angular distribution functions of the $\measuredangle_{\mathrm{SiNSi}}$ and $\measuredangle_{\mathrm{NSiN}}$ angles for the small Si_3N_x:H systems. The functions are normalized by the total number of counts and by a factor of $1/\sin(\theta)$, which amplifies contributions at 0° and 180°. The normalization is chosen such that a completely random distribution of angles would yield a straight line. Two Si and two N atoms arranged in a square result in pronounced peaks at 90°.

pair-correlation function). From the structure factors $S(\mathbf{k})$ on the grid, the isotropic structure factor is calculated by averaging over different $\mathbf{k}$ orientations and properly weighing each contribution:

$$S(q) = \frac{\int S(\mathbf{k})\, \delta(|\mathbf{k}| - q)\, d^3k}{4\pi q^2}. \tag{12.3}$$

The partial structure factors for each atom type $S_{\alpha\alpha}(\mathrm{q})$ were obtained by summation over one atom type in Equation 12.2. To calculate the partial structure factors $S_{\alpha\beta}(q)$ with $\alpha \neq \beta$ we use the implicit equation

$$S_{\alpha+\beta}(q) = \sum_{\alpha\beta} (c_\alpha c_\beta)^{\frac{1}{2}} S_{\alpha\beta}(q), \tag{12.4}$$

where c_α is the concentration of atom type α and $S_{\alpha+\beta}(q)$ is the total structure factor of both atom types [201].

In Figure 12.9 the structure factors are shown for the large supercells, since the small simulation cells result in a fairly coarse reciprocal space grid, causing a non-monotonic behavior (qualitatively the results are, however, similar as one would expect from the close agreement for the pair correlation function).

In general, the structure factors change little with composition, and in all cases, the main peak is observed at 2.2 Å^{-1} which agrees with the results of Jarolimek *et al.* [181]. The corresponding wavelength is roughly 2.8 Å agreeing well with the typical Si-Si and N-N distances in the pair correlation function. This indicates that the peak is mostly a residual of the Fourier transform of the first peak in the pair correlation, rather than a true long range order. Remarkably the SiN structure factor shows a strong anti-correlation at this wavelength, indicating a moderate medium range order with alternating Si-N-Si-N planes where the distance between the Si-Si and N-N planes is roughly 2.8 Å. This medium range order clearly decreases when moving off stoichiometry, most likely because Si-Si bonds are introduced into the network necessarily causing a disruption of the alternating planes.

The other important observation is the increase of the NN structure factor S_{NN} towards small wave vectors $\mathbf{q}$, with decreasing Si content. A similar increase is also observed for the small samples (not shown). Such an increase usually indicates the onset of long range density fluctuations, i.e. there are regions in our simulation cell, where N accumulates and regions where N becomes depleted. For sufficiently large simulation cells and sufficiently long simulation times, one might observe phase separation into a Si rich part with few N impurities, and a close to stoichiometric $\mathrm{Si_3N_4}$. For the simulation cells and stoichiometries considered here, this effect was however hardly noticeable in real space. As shown in the next section, some residual of the phase separation is observable even in the local coordination upon careful investigation.

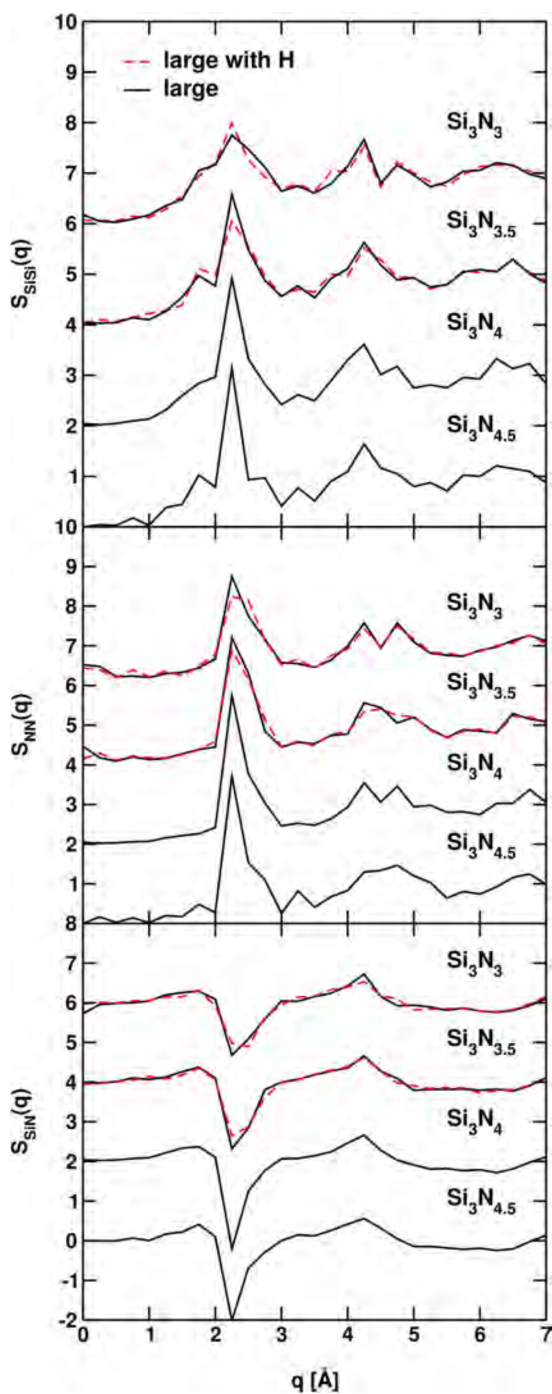

Figure 12.9: Partial Faber-Ziman structure factors $S_{\alpha\beta}$(q) for the large Si_3N_x:H systems.

12.3.4 Clustering or simple percolation

We now briefly return to the analysis of the local bonding properties of Si. As we have already shown in Table 12.2 most Si atoms have four nearest neighbors, whereas the N atoms are all threefold coordinated. Furthermore Table 12.2 shows that N atoms form bonds exclusively to Si in the stoichiometric and sub-stoichiometric case $Si_3N_{4\text{-x}}$ (N_{NSi}). In the absence of H, this allows to estimate the partial Si coordination number to be $N_{SiSi} = x$, which is indeed roughly observed in Table 12.2.

If the formation of Si-Si bonds were random, we would expect that the distribution of fourfold coordinated Si atoms with n nitrogen and $(4 - n)$ silicon neighbors would be roughly binomial

$$p(n) = \frac{4!}{n!(4-n)!} \left(\frac{x}{4}\right)^{(4-n)} \left(\frac{4-x}{4}\right)^{n}. \tag{12.5}$$

In Figure 12.10 we show the actual distribution of the bonding topology of fourfold coordinated Si atoms and compare it with the binomial distribution that would be expected if the formation of Si-Si bonds was entirely random. The most notable observation is that we would not expect any Si atoms with three Si neighbors in $Si_3N_{3.5}$, and no Si atoms with four Si neighbors in Si_3N_3, however, the actual analysis shows that such atoms exist. This is a sign that Si prefers either exclusively N neighbors or exclusively Si neighbors, which is consistent with our previous analysis of the structure factor and supports the claim that a tendency towards phase separation exists, although in the present case, it manifests itself only in the form of a slight tendency towards Si clustering, that goes beyond what one would expect for a random percolating network.

12.4 Electronic properties

12.4.1 Density of states

The silicon and nitrogen projected electronic density of states (DOS) is provided in Figure 12.11, together with the DOS of crystalline β-Si_3N_4, which was already discussed by Kresse *et al.* [203]. Averaging was done over all small samples (approximately 1000 for each stoichiometry). To align the individual DOS for different configurations and stoichiometries, we have chosen the average nitrogen 1s core level energies as reference.

Since the local short range order of a-Si_3N_4 is very similar to β-Si_3N_4 we expect similar electronic properties as in the crystalline phases, which is indeed confirmed (compare with broken line in Figure 12.11). As for structural properties, we again find that hydrogen has virtually no discernible influence on the average electronic properties, a more detailed discussion of

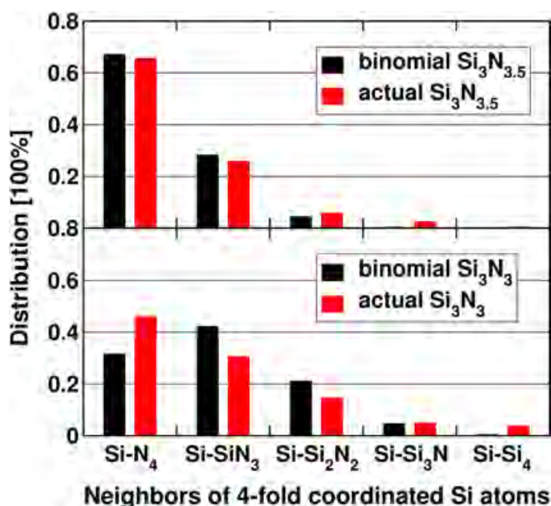

Figure 12.10: Detailed analysis of the bonding topology for fourfold coordinated Si atoms. The actual probability of finding a Si atom coordinated to n N and $(4-n)$ Si atoms is shown. Also shown is the distribution that one would expect if the formation of a Si-Si bond were entirely random. Excess probabilities are found towards the two end points in particular for Si_3N_3, which is consistent with a tendency towards Si clustering and "phase separation".

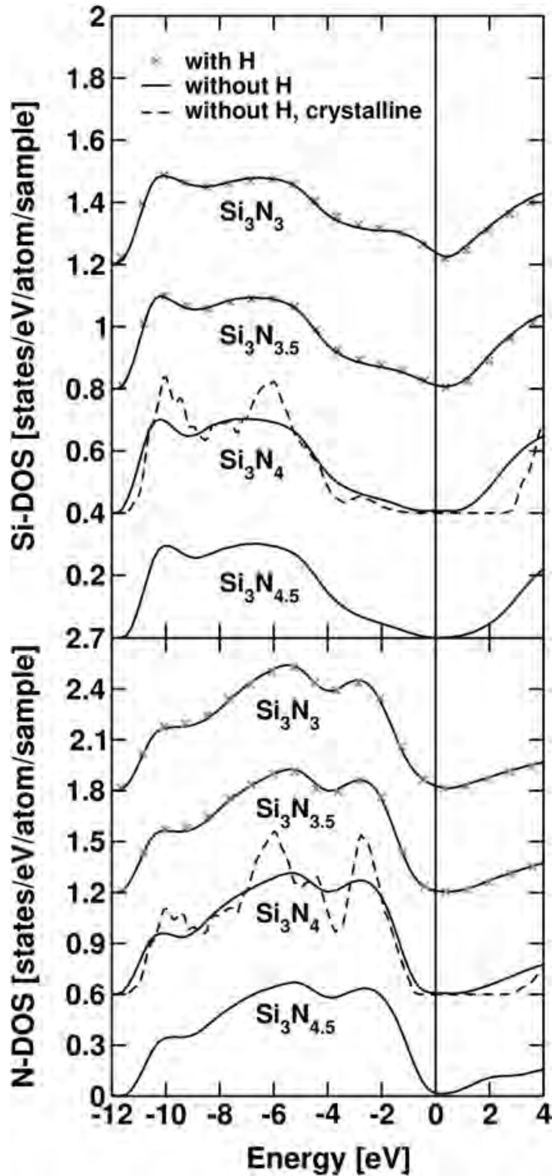

Figure 12.11: Site projected electronic DOS for Si and N atoms in the small Si_3N_x:H systems. The broken line corresponds to the DOS of crystalline β-Si_3N_4. The density of states are aligned in a such a way that the N core levels have always the same energy. The Fermi-levels are located exactly at the minimum of the individual DOS.

the properties of the defect states close to the Fermi-level is given in Chapter 13.

The lowest valence band is made up by N 2*s* states (not shown). The second lowest sub-band (-11 to -4 eV) is predominantly made up by bonding N 2*p* states. As already discussed, N atoms are located in an almost planar triangular configuration with three Si neighbors (NSi_3). The N 2*p* band is made up by two *p* orbitals per N atom, and shows significant hybridization with Si *p* states in particular at energies around -10 eV. The final sub-band below the Fermi level at -2.5 eV is dominated by the non-bonding N 2*p* states (one orbital per N atom) that is oriented out of the plane formed by the NSi_3 triangle. This band shows only very little hybridization with Si. As the Si concentration increases, a marked change is observed in the DOS below the Fermi-level with a significant increase in the Si DOS and little to no changes in the N DOS.

In stoichiometric Si_3N_4, the dominant contribution to the electronic states below the Fermi-level is stemming from the N 2*p* lone pair orbitals, however, for $Si_3N_{4\text{-x}}$ the Si DOS increases rapidly with decreasing N content. This property is easily understood to result from the increase in the number of Si-Si bonds. The bonding anti-bonding splitting for a Si-Si bond is far smaller than for the shorter Si-N bond: for a Si-N bond, the bonding Si-3*p* N-2*p* linear combination is pushed at least -3 eV below the Fermi-level, whereas for a Si-Si bond, the bonding linear combinations is located just below the Fermi-level. Matter of fact, this also relates to the smaller band-gap in crystalline Si or amorphous-Si (compared to Si_3N_4).

We thus expect that valence band defect states have important contributions from Si-3*p* states in sub-stoichiometric $Si_3N_{4\text{-x}}$, whereas N related lone pair states dominate in stoichiometric Si_3N_4. The other notable observation is that the Fermi-level is pushed upwards by 0.5 eV, as the stoichiometry changes from Si_3N_4 to Si_3N_3, in agreement with the less electronegative character of Si. Again we stress, that we have aligned the electronic DOS at the N 1*s* core level, but this seems to be a rather sensible approach, since the local coordination of the N atoms remains virtually unchanged from Si_3N_4 to Si_3N_3.

12.4.2 Inverse participation ratio

It is commonly expected that the inverse participation ratio (IPR) increases for states in the gap (see e.g. Justo *et al.* [177]). In the present case, we show the results only for the large systems, because the values for the small

systems remain more bounded. The IPR is calculated as

$$p_n^{-1} = \frac{N \sum_{j,l} \left| \psi_{n,l}(\mathbf{r}_j) \right|^4}{\left(\sum_{j,l} \left| \psi_{n,l}(\mathbf{r}_j) \right|^2 \right)^2} \tag{12.6}$$

where $\psi_{n,l}(r_j)$ is the projection of the orbital n onto the atomic site j and angular quantum number l. The sum is performed over all atoms j and the angular momentums l, whereas N is the total number of atoms. If all atoms participate in an electronic state n, p_n^{-1} becomes equal to one, and, if the state is completely localized on one atom, p_n^{-1} approaches N.

Figure 12.12 shows the partial (N and Si) resolved DOS and the IPR for a-Si_3N_4 and a-Si_3N_3. For stoichiometric a-Si_3N_4, we found very localized states at the valence band edge and a DFT band-gap of about 2 eV. Furthermore, for the considered snapshot no defect states are visible in the gap, in agreement with results of Giacomazzi *et al.* [180]. As discussed above, the band-gap becomes smaller and the DOS increases close to the Fermi-level when moving off stoichiometry, in particular, the Si DOS increases around the Fermi-level, in accordance with the observations made already in the previous section. It is also clearly visible that this results in much weaker localization, and smaller IPR values for the states at the valence and conduction band edges as well as in the band-gap.

12.4.3 Optical band-gap

A three step procedure following roughly the experimental methods is used to determine the optical band-gap. In the first step, we calculated the absorption coefficient $\alpha(E)$ from the independent particle dielectric function calculated using density functional theory orbitals and one-electron energies [204–206].

Second, we determine the DFT optical band-gap either as E_{04}, the energy value where the absorption coefficient α reaches the threshold of 10^4 cm^{-1}, or as the Tauc band-gap E_T where the linear regression of the linear regime of $\sqrt{\alpha E}$ crosses the energy axis. In our case the linear regime is between 6 and 9 eV. The corresponding data are shown in Figure 12.13 and are explained in more detail by Tauc, Robertson *et al.* and Zanatta *et al.* [166, 207, 208].

Finally, we applied the GW_0 approximation [209–212] to a set of 40 representative slowly cooled samples for each stoichiometry in order to correct the DFT band-gaps which are well known to underestimate experimental quasi-particle band-gaps. The GW_0 calculations were performed by iterating the eigenvalues in the Green's function until selfconsistentcy was reached [213, 214]. The orbitals were kept fixed to the Kohn-Sham orbitals. We

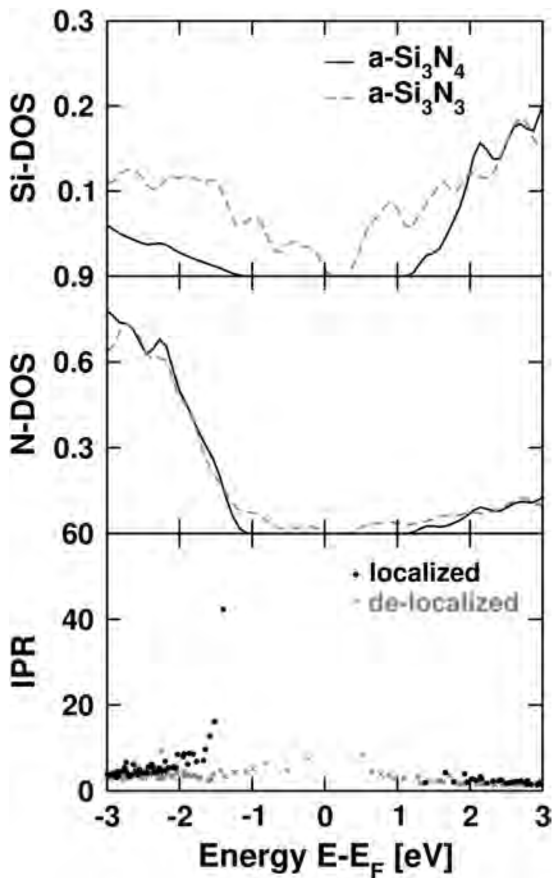

Figure 12.12: Density of states projected onto Si and N atoms and the inverse participation ration (IPR) for a-Si_3N_3 (red) and a-Si_3N_4 (black).

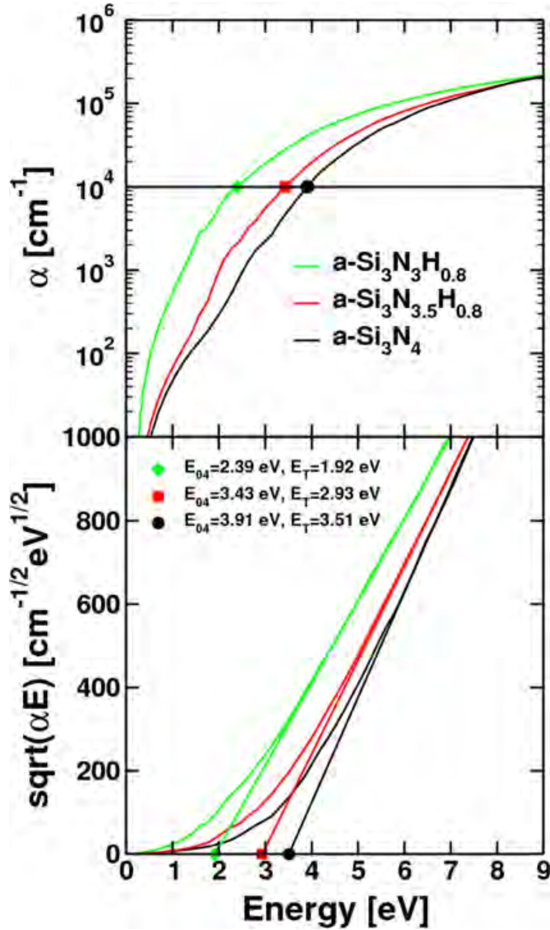

Figure 12.13: Optical band-gap of $Si_3N_xH_y$ estimated by applying a threshold of 10^4 cm^{-1} to the absorption coefficient α and by using the Tauc linear regression [207]. The bisections give the corresponding results E_{04} and E_T.

included typically 3500 unoccupied states, and one calculation required about two hours on 64 cores. Doubling the number of unoccupied orbitals increased the quasiparticle band-gap by less than 100 meV. The calculational details are otherwise similar to Kresse *et al.* [203].

Figure 12.14 shows that the unoccupied states of $Si_3N_{3.5}$, with and without hydrogen, are rigidly shifted upwards by 1.17 eV compared to the occupied states. Furthermore, in the vicinity of the gap the GW_0 quasi-particle energies exhibit a slightly increased slope compared to the DFT one-electron energies. This slope is almost constant for the valence band and conduction band states and amounts 1.13. Disregarding the corrections for the slope, we can simply add an optical band correction of $\Delta = 1.17$ eV to the DFT values E_{04} and E_T. The scissor gap corrections Δ for the other systems are summarized in Table 12.5.

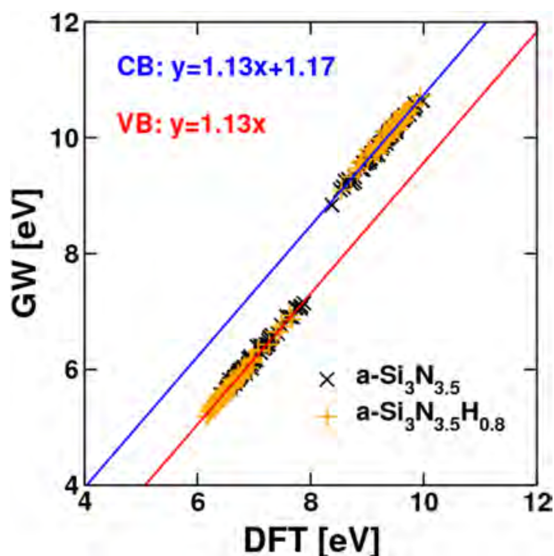

Figure 12.14: The eigenvalues of the highest occupied and lowest unoccupied orbitals for DFT and GW_0 calculations. The latter opens a gap of 1.17 eV between lowest occupied and highest unoccupied orbital, and increases the slope.

In Figure 12.15, we compare the corrected data of E_{04} and E_T with the experimental results obtained by Guraya *et al.* [147]. As one can see the values of E_{04} are generally greater than E_T, but both lie only slightly below the experimental reference, and follow the experimental data quite well. We note in particular the sharp decrease of the band-gap, when one approaches the stoichiometry of Si_3N_3, which is a result of the increasing number of Si-Si

bonds, the resultant percolation network and accompanied by a change of the valence band states from N lone pair to Si-Si bonding linear combinations (compare Figure 12.11). In passing we note, that a scissor correction will not modify the density of states presented in Figure 12.11, but for a trivial upshift of the conduction band states and an opening of the gap between the valence band and conduction band states.

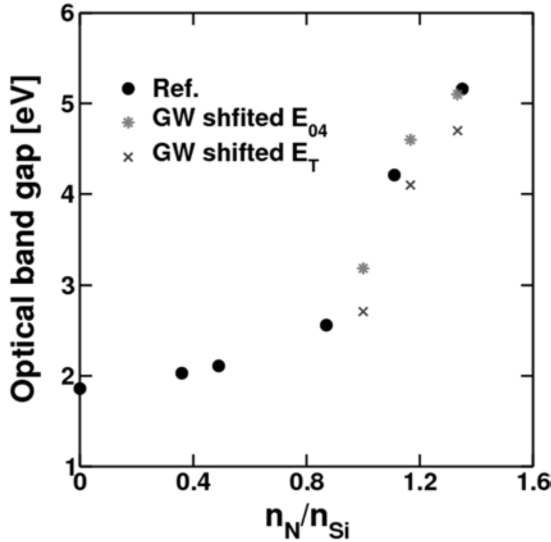

Figure 12.15: Comparison of calculated optical band-gap values (see Figure 12.13) with experimental values obtained by Guraya *et al.* [147]. As described in the text, the calculated values are shifted by a corresponding GW_0 correction (compare Figure 12.14 and Table 12.5).

Table 12.5: Parameter obtained by fitting the linear function $y = kx + \Delta$ to the and GW_0 quasi-particle energies as a function of the DFT one-electron energies for a-$Si_3N_xH_y$ (compare Figure 12.14). The scissor correction Δ is added to the optical DFT band-gap values determined in Figure 12.13.

	$Si_3N_3H_{0.8}$	$Si_3N_{3.5}H_{0.8}$	Si_3N_4
k	1.18	1.13	1.12
Δ [eV]	0.79	1.17	1.19

12.5 Conclusions

The present work shows a detailed study of a-$Si_3N_{4\text{-x}}$:H using first principles methods. Preparation of the samples proceeded via simulated annealing using *ab initio* molecular dynamics. We have chosen this approach in order to avoid ambiguities between the creation of the configurations and evaluation of the electronic properties, since we expect that the electronic properties are strongly intermingled with the structural properties, in particular at defect sites. Conventional pair or many body potentials have often difficulties to describe this relation, since the electronic properties are determined in a complicated non-trivial manner by the local environment around the defect.

As already emphasized from the outset, the present study concentrates on the "average" structural properties, paying little attention to details about the defect concentrations and electronic defects states in and close to the gap. This is left for future studies. However, the structural models determined in this work are expected to form an excellent basis for such studies.

We have shown that the average structural properties and electronic properties are faithfully reproduced using fairly small ensembles containing only 100 atoms. Using soft potentials with a plane wave cutoff energy of 150 eV (resulting in typically $40-50$ plane waves per atoms) we were able to perform calculations for up to 1 ns with reasonably modest computational resources. For each considered stoichiometry, amorphous model structures were prepared by rapidly quenching about 1000 structures from the molecular dynamics simulation into the closest local minimum. We compared these structures with larger calculations performed for systems with 200 atoms, and the results were found to be essentially identical for the small and large systems.

Analysis of the structural properties reveals that amorphous Si_3N_x is characterized by fourfold coordinated Si atoms and threefold coordinated N atoms, with a very strong tendency towards hetero-coordination and formation of Si-N bonds. Si-Si and N-N bonds are only encountered, if a Si or N surplus, respectively, exists, but even then each Si and N tries to maintain its fourfold and threefold coordination, respectively.

Analysis of the structure factor clearly showed the onset of density fluctuations in the N concentration, indicating N rich and N poor areas in the simulation cells. This observation in reciprocal space, was also confirmed by the analysis of the local bonding properties of Si atoms. A clear fingerprint for clustering is the number of Si atoms with three Si neighbors in $Si_3N_{3.5}$ and the number of Si atoms with four Si neighbors in Si_3N_3. If the formation of Si-Si bonds were entirely random, no such atoms would be expected. However, we observe a significant fraction in both cases. Although, the tendency towards clustering is not overwhelmingly strong for the preparation routes we have taken here, it is something to keep in mind for real passivation layers. To put this argument

in context, one should remember that crystalline sub-stoichiometric silicon nitrides Si_3N_{4-x} do not exist, and hence it can be only entropy that drives against phase separation in the amorphous layers, whereas energy favors phase separation into pure Si and Si_3N_4.

The evolution of the electronic properties of Si_3N_{4-x} is also quite remarkable. In the stoichiometric compound, the conduction band maximum is dominated by N lone pair states, whereas the valence band minimum is dominated by Si *p* states. However this changes drastically when decreasing the N content, causing the formation of Si-Si pairs as well as the formation of larger Si clusters (percolation, as well as clustering as described above). Within a Si pair or cluster, the bonding anti-bonding splitting is reduced compared to a Si-N bond, and thus the conduction band becomes progressively dominated by Si bonding contributions. Likewise we expect that the valence band edges will be dominated by states originating from Si pairs or larger clusters (reduced bonding anti-bonding splitting). We finally note that with decreasing N content the localization of the defect states at the valence and conduction band edges decreases strongly. This is in full accordance with the picture developed above. As the Si cluster size increases, the defect states will start to spread over the Si cluster with a resultant reduced inverse participation ration. It was also found that the band-gap reduces slightly from Si_3N_4 to $Si_3N_{3.5}$, but shows a sharp decrease for Si_3N_3, that we relate to the already described formation of larger Si clusters in Si_3N_3.

We expect that such clusters are of uttermost importance for understanding the properties of the passivation layers used in industrial solar cells. The electronic states of clusters are not well localized and extend over several Si atoms, electronically the corresponding defects states are expected to be located in the same energy range as the valence and conduction bands in crystalline Si, and hence tunneling into these states from the Si substrate is possible. We note in passing that, since such clusters are entirely missing in stoichiometric Si_3N_4, stoichiometric Si_3N_4 seems to be a unsuitable model for the materials used as passivation layers in industrial solar cells.

We have also analyzed the impact of hydrogen on silicon nitrides in detail. Remarkably, it has no visible impact on the averaged properties such as the pair correlation function, the structure factor or the electronic density of states. In agreement with common chemical intuition, we have noticed, however, that hydrogen can attach to a N or Si atom, terminating a dangling bond. This is in accordance with the commonly accepted picture that it helps to reduce the number of electronic defect states in the gap, although a more careful analysis of the electronic properties of defects is required to fully resolve this issue.

Acknowledgments This work is part of the HiperSol project (High Performance Solar Cells) funded by the European Commission Grant No.

MMP3-SL-2009-228513. We thank the project members for their support and inspiring discussions.

Chapter 13

Density functional theory study of defects and defect healing in a-$Si_3N_{4\text{-}x}H_y$

L.E. Hintzsche[1], C.M. Fang[1], M. Marsman[1], G. Jordan[1], M.W.P.E. Lamers[2], A.W. Weeber[2], G. Kresse[1]

[1] University of Vienna, Faculty of Physics and Center for Computational Materials Science, Sensengasse 8/12, A-1090 Vienna, Austria.
[2] ECN Solar Energy, P.O. Box 1, 1755 ZG Petten, the Netherlands.

Physical Review B **88**, 155204 (2013).

Abstract

We present an *ab initio* density functional theory study. of the dominant defects in hydrogenated amorphous silicon nitrides covering different stoichiometries, the influence of hydrogen and the influence of the annealing history. Whereas nitrogen (N) lone pair states dominate the valence band edge in stoichiometric a-Si_3N_4, we find that K-centers, threefold coordinated silicon (Si) atoms, and Si-Si bond related states dominate electronic defect contributions in the gap for nitrogen deficient a-Si_3N_{4-x}. Hydrogen saturates the dangling Si bonds, significantly reducing the number of electronic defects related to under-coordinated Si atoms.

13.1 Introduction

Amorphous silicon nitrides are widely used in industry, for example as anti-wear coatings on mechanical tools as well as protective layers in the semiconductor industry. Also in wafer-based silicon solar cells, the hydrogenated amorphous silicon nitride (a-$Si_3N_{4\text{-x}}H_y$) is the standard anti-reflection and passivating layer, for both surface and bulk defects [167, 215]. In general, the a-$Si_3N_{4\text{-x}}H_y$ layer is a compromise of optical (anti-reflection and absorption) properties, and bulk and surface passivation. Si-rich a-Si_3N_{4-x}:H layers show good surface passivation quality, but are highly absorbing and cannot be used for solar cell application. N-rich layers show good optical properties, a fair amount of Si-H and N-H bonds must be present, since both bonds supply H atoms that can cure electronic and structural defect states in bulk Si [83, 107].

The present study aims at determining the dominant defect class in hydrogenated silicon nitride, at improving the understanding of the nature of recombinations in silicon nitride, at improving the understanding of the nature of recombination centers in silicon nitride [140, 141, 215, 216]. Robertson *et al.* suggested the under-coordinated Si atom (K-center, $^*\text{Si} \equiv \text{N}_3$) being the dominant defect class already in the 1980s [172], and this has been subsequently confirmed by most experiments [140, 141, 217–222]. However, tight binding methods used by Robertson *et al.* do not meet the modern standards of *ab initio* techniques, and experiments yield only indirect evidence on defects, with direct microscopic atomic scale information mostly lacking. Ultimately, atomic scale insight obtained by modern first principles simulations is highly desirable to gain a more detailed understanding of silicon nitrides.

To characterize and investigate defects theoretically on the atomic scale, *ab initio* density functional theory (DFT) is nowadays indisputably the method of choice. However, defects are a minority species in the sense that most atoms maintain their preferred bonding topology. As we discussed in more detail elsewhere (see Chapter 12), with very few exceptions nitrogen atoms are found in a flat triangular configuration with three Si neighbors, whereas almost all Si atoms maintain the perfect fourfold coordinated tetrahedral bonding configuration in a-$Si_3N_{4-x}H_y$, regardless of the stoichiometry and hydrogen content (see Figure 13.1a). Furthermore, for stoichiometric a-Si_3N_4, all Si atoms are solely surrounded by N atoms, and only when the nitrogen content decreases, homo-polar Si-Si bonds form. It is then a matter of simple arithmetic to show that each Si atom will have x Si and $4-x$ N neighbors in a-Si_3N_{4-x}, as long as the tetrahedral and triangular local coordination of Si and N, respectively, prevails. These values are indeed confirmed in our simulations and agree with the common experimental assumptions (see Chapter 12).

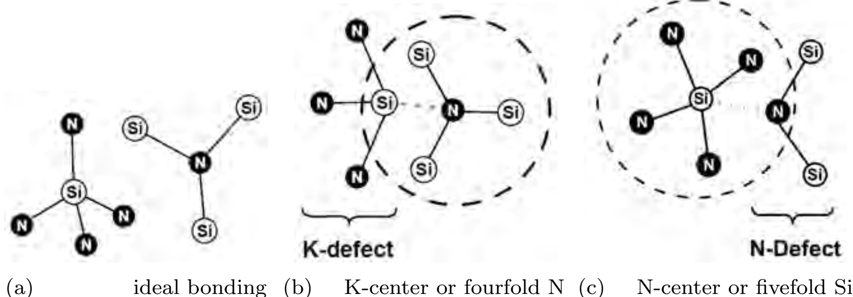

(a) ideal bonding (b) K-center or fourfold N (c) N-center or fivefold Si

Figure 13.1: Common geometrical bonding topologies of Si and N atoms in Si_3N_{4-x}. a) Ideally coordinated Si and N atoms have four and three neighbors, respectively, b) the K-center can be either counted as a threefold coordinated Si or fourfold coordinated N; c) likewise the N-center can be either counted as a fivefold coordinated Si or twofold coordinated N-center.

Geometric defects and electronic states in the gap are rarely found, *i.e.*, typically zero or at most one electronic defect state is observed for a supercell with 100−200 atoms. Hence, a meaningful statistical analysis cannot be drawn from a single model, and conclusions based on limited configuration sampling might be misleading. Literature retrieval, however, shows that this "single model" approach is often adopted to date, if the models are prepared entirely using *ab initio* DFT and cooling from the melt [146, 180, 181, 183, 223–228]. Well aware of these limitations, researchers prepare models of amorphous structures employing force fields (see Chapter 10) [115, 174–176, 182, 186, 229, 230] or continuous random alternating networks [178, 179, 185], but this is not entirely satisfactory either. Geometrical defects will often result in broken bonds, which are not well described by force fields, and even though the models can be re-optimized using DFT, it remains disputable whether different defect classes are properly statistically distributed in force field generated models.

Ultimately, it seems that an "all-in-one" *ab initio* DFT approach may be best suited, albeit with increasing significant computational costs. One purpose of the present study is to show that such calculations are possible nowadays and allow obtaining detailed insight for a technologically relevant material.

13.2 Method

In the present work, we use the Vienna *ab initio* simulation package (VASP) [193], the PBEsol functional [195], and fairly soft projector augmented wave (PAW) potentials [191, 231] for Si and N. These soft potentials allow reducing the energy cutoff to about 150 eV, resulting in typically 50 plane waves per

atom. We have tested these for the bulk and liquid Si_3N_{4-x}. In comparison to accurate reference potentials, we find only few percent differences for the volume, band structure, phonon frequencies and the pair correlation function (see Chapter 12). To allow for sufficiently long molecular dynamics simulations, we sample the electronic band structure at the Γ-point only and limit the models to relatively small supercells containing about 100 atoms. This is a compromise, but on the level of the pair correlation function and angular distribution function no statistically relevant differences to 200 atom models were found (see Chapter 12).

Three stoichiometries a-Si_3N_4, a-$Si_3N_{3.5}$ and a-Si_3N_3 were investigated, where the last two were studied with and without 12 at.% hydrogen (for details see Chapter 12). The first composition is chosen as it represents the stoichiometric form of amorphous silicon nitride, whereas the other two represent technological relevant nitrides. 1000 amorphous models have been created for each stoichiometry, by performing a 1 ns *ab initio* molecular dynamics run 50 K above the onset of amorphization) (2700 to 2100 K depending on stoichiometry) with a timestep of 1.5 fs, and rapidly quenching (relaxing) structures every pico second into the closest local minimum. These ensembles are from now on termed “rapidly quenched”. Additionally, for each stoichiometry, 30 models have been generated by slowly annealing the structures from the melt into the amorphous state, lowering the temperature by 1000 K in 75 ps. At the lowest temperature, diffusion was absent as monitored by the mean square displacement. Finally the structures were again relaxed, and we refer to these structures as “slowly cooled”.

It is obvious, from Figure 13.2, that slow annealing results in a much narrower energy distribution. Except for a-$Si_3N_{3.5}H_{0.8}$, the slowly cooled ensembles hardly exhibit lower energy structures than the rapidly quenched ensembles (left shoulders are identical). This suggests that we could have obtained similar results, by re-weighting the 1000 rapidly quenched ensembles, and we used this alternative to crosscheck our general conclusions.

An automated routine is adopted to characterize the defect related properties. Since we are mainly interested in the properties of electronic states in the vicinity of the band-gap, we concentrate on the three highest occupied and three lowest unoccupied states for each structure. We have inspected whether these electronic states are strongly localized on individual N or Si atoms and whether these atoms correspond to a geometrical defect. In fact, in about 65% of the cases, the electronic defect state is indeed localized on or close to a geometrical defect. Geometrical defects are determined by first building a nearest neighbor list using a fairly large radial cutoff. In the second step, for over-coordinated atoms, the longest bond is removed from the list until all atoms are either ideally coordinated or under-coordinated (compare Figure 13.1). Hence over-coordinated atoms are converted into neighboring under-coordinated atoms, leaving the total defect density unmodified. This

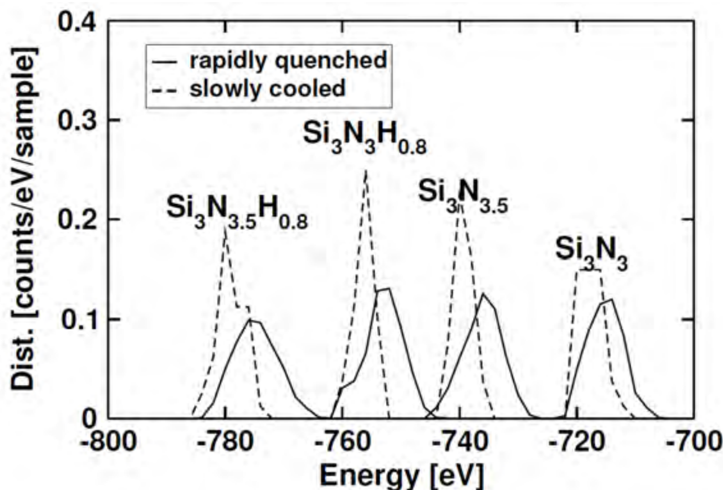

Figure 13.2: Distribution of internal energy for considered ensembles. Slow annealing (broken line) results in a significantly narrower internal energy distribution than the rapid quenches (full line).

corresponds to the experimental notion that the only defects are K-centers (threefold coordinated Si atoms) and N-centers (twofold coordinated N atoms).

13.3 Results

13.3.1 Defect classification

For prototype defects, the charge density and the local electronic DOS are shown in Figure 13.3. In our simulations, the most common defect is the K-center, which corresponds to a single threefold coordinated Si atom (see Figure 13.3a)). The electronic defect state is a dangling sp^3 orbital pointing towards the missing N atom. The defect state can be either occupied (red line) or unoccupied (blue line), and the one electron energy can be located anywhere in the gap, or gradually merge into the conduction or valence band, accompanied by a reduction in localization. Hence, at most one out of two geometrical K-centers will result in an electronic defect state in the band-gap, and a strict one-to-one correspondence between geometrical defects and electronic defect states in the gap does not exist.

The second class of defect states are related to Si-Si bonds or larger Si networks or Si chains. Compared to the Si-N bond, the Si-Si bond results in a much reduced bonding anti-bonding splitting. If the local tetrahedral Si

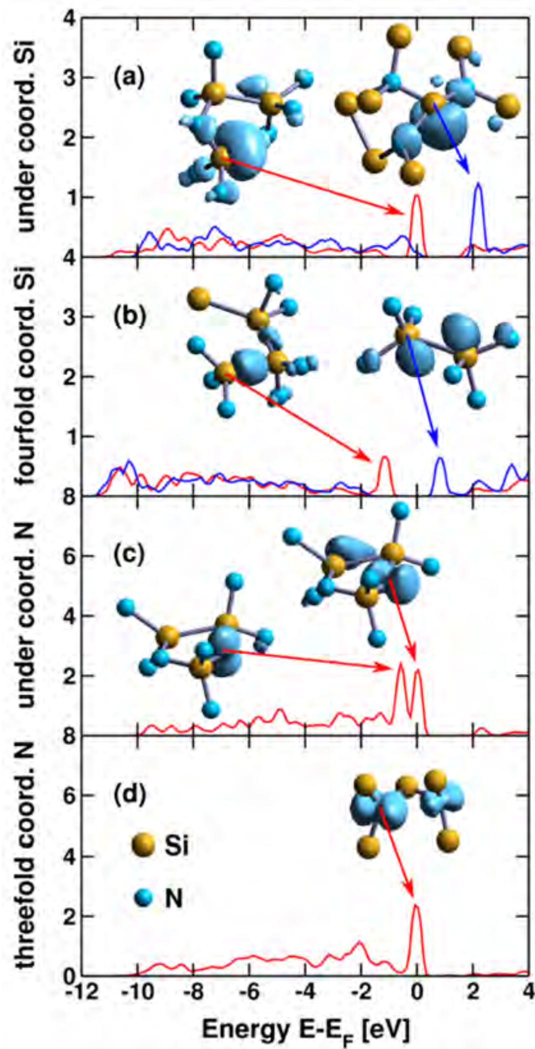

Figure 13.3: Local structure around selected geometrical defects and electronic density of states (DOS) evaluated at the corresponding sites (origin of arrow): a) Si-dangling bond (K-center), b) bonding and anti-bonding states on fourfold coordinated Si, c) N lone pair and dangling bond (N-center), and d) lone pair on threefold coordinated N. Also shown is the charge density corresponding to the peak in the DOS. The contributions to the DOS can be either occupied (red line) or unoccupied (blue line).

environment is distorted or a Si-Si bond is particularly short or long, electronic states in the band-gap are introduced. Examples for such defect states are shown in Figure 13.3b. For strong local distortions, sp^3 orbitals hybridize less efficiently with neighboring atoms and the charge distribution is sometimes reminiscent of K-centers. Furthermore, as the nitrogen content decreases, the number of homopolar Si-Si bonds grows, and larger Si percolation networks develop (see Chapter 12) [181]. Within such a Si network, some bonding or anti-bonding Si $3p$ linear combinations can move into the gap (Figure 13.3b left). Using an automatic procedure, Si-Si states are difficult to distinguish from other states related to a distorted Si environment, as both defect classes are intermingled. Visual inspection of the charge density, however, suggests that the majority (over 70%) of the gap states that cannot be assigned to under-coordinated atoms are localized on Si-Si bonds. This observation is similar to a recent finding of Khomyakov *et al.* for amorphous silicon (a-Si) [232].

N-centers, twofold coordinated N atoms, are rarely found and they are entirely absent in the slowly cooled nitrogen deficient samples. In the nitrogen deficient case, a surplus of Si atoms exists, and Si atoms grab any existing N-dangling bond. Although N-centers are only present in small numbers in the rapidly quenched ensembles, we, nevertheless, show their electronic properties in Figure 13.3c. N-centers are characterized by two localized peaks doubly occupied states close to the valence band edge. Ideally, nitrogen in Si_3N_{4-x} adopts a flat coordination with three Si neighbors forming sp^2 hybrid orbitals that develop bonding and anti-bonding linear combinations with the three neighboring Si atoms. The remaining two electrons form a lone non-bonding pair perpendicular to the NSi_3 plane. This state corresponds to the left peak. The second peak is the dangling bond state related to the broken N-Si bond. The energetic ordering of these two states depends on the local geometry and can interchange.

The final class of defects are distorted N-centers (N-Si_3) shown in Figure 13.3d. A strong local distortion or unfavorable electronic environment can shift the N lone pair states up into the band-gap. This is again a fairly rare defect species as well, always doubly occupied, and energetically close to the valence band edge.

In short, the dominant defects causing gap states are K-centers and tetrahedrally coordinated, but distorted Si-Si bonds or Si percolation networks (see Figure 13.3a-d). This result leads to the important question how the defect concentration changes with stoichiometry and annealing history.

13.3.2 Energy and defect resolved density of states

In Figure 13.4, we analyze the averaged defect contributions to the valence and conduction band tail. The black lines correspond to the number of states

localized on under-coordinated atoms, whereas the red lines correspond to the electronic DOS on ideally coordinated atoms. To obtain more realistic quasi-particle energies (x-axis), we have calculated GW_0 corrections for about 100 selected models. For $Si_3N_{3.5}H_y$ and $Si_3N_3H_y$, the corrections simply shift the unoccupied states up by $\Delta = 1.17$ eV and $\Delta = 0.79$ eV, as demonstrated in Figure 13.5.

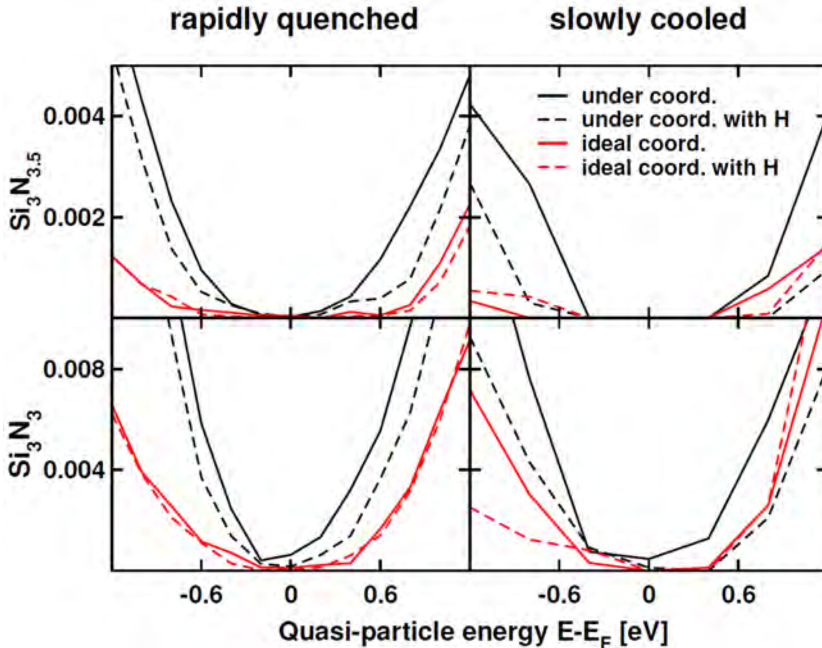

Figure 13.4: The DOS of $Si_3N_3.5$ and Si_3N_3 close to Fermi-level for rapidly quenched (first column) and slowly cooled (second column) ensembles. The total DOS is assigned to atoms with under and ideal coordination (black and red lines). Additional hydrogen (broken lines) reduces the amount of electronic defect states originated from under-coordinated atoms.

Obviously, the lowest defect density is observed in slowly cooled $Si_3N_{3.5}H_{0.8}$ (upper right panel, dashed lines), whereas the highest defect density is observed in rapidly quenched a-Si_3N_3 (lower left panel, full lines). Furthermore, increasing the nitrogen deficiency increases the defect density (compare upper and lower row and note the different scale). This is related to an increase of the number of Si-Si bonds causing a reduced bonding-antibonding splitting, a reduction of the band-gap, and a concomitant increase of the defect density. Finally, hydrogen significantly decreases the number of defect states in the gap (compare full and dashed lines), in particular for the slowly cooled samples.

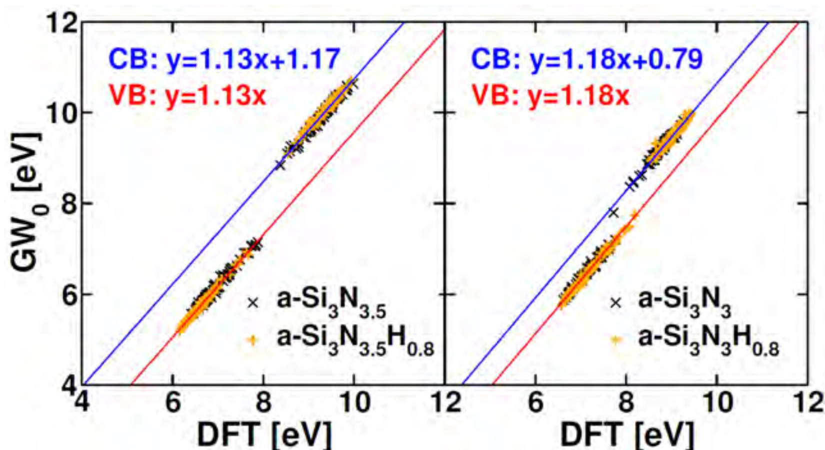

Figure 13.5: The eigenvalues of the lowest occupied and highest unoccupied orbitals for DFT and GW_0 calculations.

To obtain more qualitative results on defect related states, we have integrated the defect densities of Figure 13.4 between -1.2 eV and 1.2 eV and show the results in Figure 13.6. The cooling rate has a strong influence on the number of coordination defects (black full bars compared to hatched bars), whereas it has remarkably little influence on the number of electronic defect states related to ideally coordinated atoms (red bars). Hydrogen also mainly cures the coordination defects, and influences the number of electronic defect states related to ideally coordinated atoms very little. This is easy to understand as the coordination defects are mainly K-centers, and hydrogen can easily attach to a K-center resulting in a $N_3 \equiv$ Si-H center.

13.4 Discussion and conclusions

Our present results can be easily rationalized and are in good agreement with the present experimental evidence and prevailing assumptions. The first important observation is that defects in amorphous silicon nitride do not possess one unique energy position in the gap, but the energy resolved defect density rather decays from the band edges towards mid-gap (see Figure 13.4). The second observation is that, in the absence of hydrogen, the occupied as well as unoccupied defect states are clearly dominated by K-centers (threefold coordinated Si atoms) as experimentally agreed. However, somewhat unexpectedly, at least one third of the electronic defect states are related to states localized on topologically ideally coordinated Si sites. Furthermore, slower cooling and hydrogen strongly reduce the number of K-centers, but hardly changes the number of defect states localized on ideally

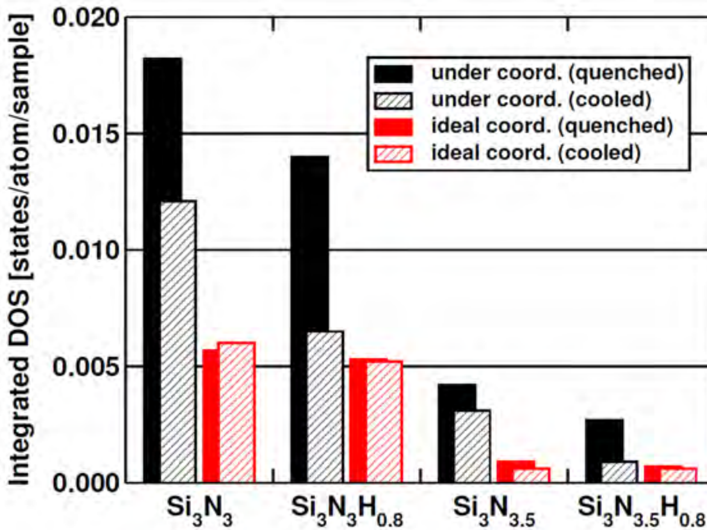

Figure 13.6: Coordination defects and ideally coordinated defects within the band-gap area of a-$Si_3N_xH_y$. Although most defects are under-coordinated atoms, the difference to ideal-coordinated atoms becomes, however, minor for the slowly cooled samples with H.

coordinated Si atoms. Thus, topologically ideally coordinated, but distorted, Si atoms might be equally important as K-centers whenever hydrogen is present. This result closely resembles the previous observations for amorphous hydrogenated Si [232] and necessitates a careful reconsideration of data for a variety of amorphous materials.

Methodologically, we have demonstrated that *ab initio* techniques and todays computational resources can be utilized effectively to sample the configuration space of amorphous structures. Since, geometrical defects and electronic properties are strongly intertwined, a consistent treatment of structure generation and electronic analysis is required.

Acknowledgments This work is funded by the European Commission Grant No. MMP3-SL-2009-228513 as part of the HiperSol project (High Performance Solar Cells). Supercomputing time on the Vienna Scientific Cluster (VSC) is gratefully acknowledged.

Summary

To improve market competitiveness and enhance market penetration of photovoltaic applications, researchers and industry experts world wide develop various cell and module technologies in order to increase efficiency and reduce costs. Two technologies are discussed in this thesis: Metal Wrap-Through (MWT) cell and module technology and Interdigitated Back Contact (IBC) cell technology.

In MWT technology, the emitter-contact metalization of the front side is wrapped through holes in the wafer to the back side, thereby effectuating both the emitter and base contact on the cell back. This thesis shows that optimization of several cell processing steps led to an increase of more than 2% absolute in cell efficiency. These optimizations can be divided into three different groups. The first group incorporates light management, which contains the surface texture, hydrogenated amorphous silicon nitride (a-SiN_x:H) layer deposition and rear side metalization (internal reflection). The second group incorporates recombination, which is determined by the a-SiN_x:H layer, emitter and front side contact, rear side contact and isolation of the holes. The third group incorporates (metal) conductivity, which corresponds to the front side metalization pattern and hole conductivity. By integrating these optimized process steps a cell efficiency of 17.9% was reached on thin and large mc-Si wafers. With these cells, 36-cell modules were manufactured at 100% yield in an industry scale module pilot line. The highest module efficiency obtained (as independently confirmed by JRC-ESTI) was 17.0% on aperture area, which was the world record in its category at the end of 2009 and the beginning of 2010. In this module the average cell efficiency was 17.8%, demonstrating only a very small cell-to-module loss of close to 1%. Further optimizations that may improve the efficiency of the MWT cells were identified as light transmission to the cells at the front side (on module level), internal light reflection at the rear side, recombination at the front side in the emitter and recombination at the rear side of the solar cell.

A type of cell which may obtain a high efficiency by reduction of the recombination losses is the IBC cell. In this cell, both the emitter and base regions and their contacts are positioned at the rear side. Consequently, the front side can be optimized to minimize recombination, while maximizing light transmission as there are no longer reflection losses from the front side metalization. This thesis describes the fabrication of an IBC cell, using n-type Czochralski (Cz) silicon material and a process flow based on all-screen-printed patterning and metalization. By minimization of the front surface recombination, a cell efficiency of 19.1% was reached. For the short circuit current, J_{SC}, an excellent value of 41.5 mA/cm^2 was obtained, which is close to the maximal obtainable value of 42.5 mA/cm^2 for silicon. The low front surface recombination was the result of an interplay between the low recombination in the internal electric field region at the front side

(Front Surface Field, FSF) and a very good surface passivation obtained with a-SiN_x:H.

One of the most limiting factors to increase solar cell efficiency further is the charge carrier recombination at the surfaces. The most common surface passivating layer for n-type regions in solar cells is a-SiN_x:H. This layer provides excellent surface passivation, in addition to its functions as an anti-reflection coating to enhance light transmission to the cell and as a source of hydrogen for passivating bulk defects and impurities in the wafer. Although commonly used, full understanding of the interface of this layer with Si is still lacking. Also, so far, separate tuning of the interface and bulk properties of the a-SiN_x:H layer was not possible, and usually a compromise is made. For improved understanding of the properties and characteristics of the a-SiN_x:H layer, over 80 different a-SiN_x:H layers were analyzed, deposited using two different remote Plasma Enhanced Chemical Vapor Deposition (PECVD) machines. The various layers, all homogeneous in build up, differed in stoichiometry, optical properties and surface passivation, as the refractive index was varied between 1.8 and 3.0. Strong correlations were found between bond densities, optical properties, bulk passivation and surface passivation within a layer. To improve light transmission and tune surface passivation, a gradient in the refractive index of the layer was created. This type of inhomogeneous layer was compared to the homogeneous layer type. Both types were optimized for use in solar cells and were analyzed and compared in their effect on solar cells. No differences in bulk passivation and only minor differences in surface passivation and light transmission were found. This showed that a wide process window is allowed for the build-up within a layer, in which similar cell efficiencies can be obtained.

Surface passivation is determined by the combined effect of two mechanisms, so-called chemical passivation by reducing the density of interface states (D_{it}) in the band gap and field-effect passivation by increasing the number of fixed charges (Q_{f}). These are related to the K-defect center (*Si≡N_3) at the interface between a-SiN_x:H and Si. During the initial growth of a-SiN_x:H, nitrogen is incorporated into and adhered to the Si lattice near its surface, a process called nitridation. It was shown that the nitridation can be tuned independently of the growth of a-SiN_x:H layers by using a NH_3 plasma treatment prior to actual a-SiN_x:H layer deposition. It was found that Q_{f} could be varied from $2{\cdot}10^{12}$ to $15{\cdot}10^{12}$ cm^{-2} without changing the a-SiN_x:H deposition process, thus allowing for the passivation quality to be tuned separately from the a-SiN_x:H layer properties. Using the NH_3 plasma pretreatment, both Q_{f} and D_{it} increased with increasing temperature. It was demonstrated that Q_{f} was the determining factor in surface passivation quality in the range of $2{\cdot}10^{12}$ to $8{\cdot}10^{12}$ cm^{-2}. At higher values of Q_{f}, D_{it} increased significantly and became dominant, thereby reducing the passivation quality. In completed solar cells the effect of the controlled Q_{f} and D_{it} was studied. On n-type solar cells, which have a p-type emitter where increases in

Q_f and D_it result in an increased depletion of charge carriers, increases in Q_f and D_it resulted in a drop in open circuit voltage, V_OC, of over 20 mV. On p-type solar cells, which have a n-type emitter where increases in Q_f result in an increased accumulation of charge carriers, the effect was negligible.

A detailed image of the compositional build-up of the interface between a-SiN_x:H and Si was obtained by characterization with High Resolution Transmission Electron Microscopy (HRTEM). A gradual change from Si to the bulk a-SiN_x:H composition in the first 2 nm of a-SiN_x:H was found. Modeling by force field Molecular Dynamics (MD) and *ab initio* Density Functional Theory (DFT) are in agreement with this result. HRTEM also showed the presence of a highly distorted layer (about 1-3 nm) inside the c-Si lattice, caused by the insertion of N and/or H. Analysis of the HRTEM results showed that by varying the nitridation by changing the temperature of the NH_3 plasma pretreatment, the amount and penetration depth of N in the first few nm's in the Si substrate were altered. Using MD modeling, it was shown that this process changed the number of K-centers at the surface, which explains the varying Q_f and D_it found experimentally. *Ab initio* DFT studies of a-SiN_x:H ($x = 1.17$) showed that K-centers and Si atoms in distorted configuration were the most important defects, resulting in a higher D_it. For lower x ($x = 1$) the D_it caused by K-centers increases. Both results were confirmed experimentally.

Nederlandse Samenvatting

Om het concurrentievermogen en marktaandeel van fotovoltaïsche toepassingen te verbeteren, ontwikkelen wetenschappers en industrie-experts wereldwijd verschillende zonnecel- en moduletechnologiëen om de effciëntie te verbeteren en kosten te verminderen. Twee typen technologiëen worden onderzocht in dit proefschrift: de Metal Wrap-Through (MWT) cel- en moduletechnologie en de Interdigitated Back Contact (IBC) celtechnologie.

In MWT technologie wordt de contactmetallisatie van de emitter via gaten in de wafer naar de achterzijde geleid, zodat zowel de emitter- als de basismetaalcontacten op de achterkant van de cel gelegen zijn. In dit proefschrift is aangetoond dat optimalisatie van verschillende processtappen hebben geleid tot meer dan 2% absolute verbetering van de celefficiëntie. Deze optimalisatiestappen kunnen verdeeld worden in drie verschillende categoriën. De eerste categorie omvat het beheren van de lichtinkoppeling, die de oppervlaktetextuur, de gehydrogeneerde amorf silicium nitride (a-SiN_x:H) laag en de achterzijdemetallisatie (interne reflectie) behelst. De tweede categorie omvat de recombinatie, die bepaald wordt door de a-SiN_x:H laag, de emitter, de voor- en achterzijdecontacten en de isolatie van de gaten. De derde categorie omvat de (metaal)geleiding, die beïnvloed wordt door het metallisatiepatroon aan de voorzijde en de geleiding door de gaten. Door deze optimaliseerde processtappen te integreren is een celefficiëntie bereikt van 17.9% op dunne en grote mc-Si wafers. Met deze cellen zijn, zonder breuk, modules van 36 cellen gemaakt met een industriëel geschaalde modulefabricage proefopstelling. De hoogst behaalde module-efficiëntie is (onafhankelijk bevestigd door JRC-ESTI) 17.0% op apertuuroppervlak. In zijn klasse was dit een wereldrecord aan het eind van 2009 en het begin van 2010. In deze module is de gemiddelde celefficiëntie 17.8%, wat een klein verlies van cel naar module laat zien van ongeveer 1%. Overige optimalisaties die de efficiënties van MWT cellen kunnen verbeteren zijn geïdentificeerd als lichttransmissie naar de cellen aan de voorzijde (op moduleniveau), interne lichtreflectie aan de achterzijde, recombinatie aan voorkant in de emitter en recombinatie aan de achterzijde van de zonnecel.

Een type cel dat is ontworpen voor onder meer het reduceren van de voorzijderecombinatie is de IBC cel. In deze cel bevinden zowel de emitter- als de basisgebieden en hun contacten zich aan de achterzijde. Dit betekent dat de voorzijde vrij is om geoptimaliseerd te worden om recombinatie te minimaliseren, waarbij gelijktijdig maximale lichttransmissie kan worden verkregen omdat er niet langer metaal aanwezig is wat een deel van het zonlicht reflecteert. Dit proefschrift beschrijft de fabricage van een IBC cel, gebruikmakend van n-type Czochralski (Cz) silicium materiaal en een proces gebaseerd op zeefdrukken voor de patroonvorming en metallisatie. Door de recombinatie aan de voorzijde te minimaliseren, is een celefficiëntie

van 19.1% bereikt. Voor de kortsluitstroom, J_{SC}, is een uitstekende waarde behaald van 41.5 mA/cm^2 wat dichtbij de maximaal haalbare waarde van 42.5 mA/cm^2 voor silicium ligt. De lage voorzijderecombinatie was het resultaat van een samenspel van een lage recombinatie door het interne elektrisch veldgebied aan de voorzijde (Front Surface Field, FSF) en een zeer goede oppervlaktepassivering waarbij a-SiN_x:H werd gebruikt.

Een van de meest beperkende factoren om zonnecelefficiëntie verder te verhogen is de ladingsdragersrecombinatie aan de grensvlakken. De meest gebruikte oppervlaktepassiveringslaag voor n-type gebieden in zonnecellen is a-SiN_x:H. Deze laag zorgt voor uitstekende oppervlaktepassivering, naast zijn functies als antireflectielaag om de lichttransmissie te verbeteren en als een bron van waterstof voor de passivering van bulkdefecten in de wafer. Ondanks de standaardrol van deze laag in productieprocessen, is er nog steeds geen volledig begrip van het grensvlak van deze laag met Si. Ook was het tot nu toe niet mogelijk om de kenmerken van het grensvlak en de laag zelf apart te optimaliseren, en wordt er normaal gesproken een compromis gesloten. Om een beter begrip van de kenmerken en karakteristieken van de a-SiN_x:H laag te krijgen, zijn meer dan 80 verschillende a-SiN_x:H lagen geanalyseerd, die gedeponeerd zijn met twee verschillende Plasma Enhanced Chemical Vapor Deposition (PECVD) machines. De verschillende lagen, allen homogeen in opbouw, in brekingsindex variërend tussen de 1.9 en 3.0, verschilden in stoichiometrie, optische eigenschappen en oppervlaktepassivering. Sterke correlaties zijn aangetoond tussen de bindingsdichtheid, optische eigenschappen, bulkpassivering en oppervlaktepassivering binnen een laag. Om de lichttransmissie te verbeteren en de oppervlaktepassivering te optimaliseren, werd er een gradiënt in de brekingsindex van de laag gemaakt. Dit type inhomogene laag is vergeleken met het homogene laagtype. Beide typen zijn geoptimaliseerd voor gebruik in zonnecellen en zijn geanalyseerd en vergeleken op invloed bij zonnecellen. Er zijn geen verschillen in bulkpassivering en alleen minieme verschillen in oppervlaktepassivering en lichttransmissie gevonden. Dit laat een breed procesgebied voor de opbouw van een laag zien waarbinnen een gelijke zonnecelefficiëntie kan worden behaald.

Oppervlaktepassivering wordt bepaald door het gecombineerde effect van twee mechanismen, zogeheten chemische passivering door de dichtheid van oppervlaktetoestanden (D_{it}) in de bandgap te reduceren en veldeffectpassivering door toename van de vaste oppervlaktelading (Q_{f}). Deze mechanismen zijn gerelateerd aan het K-defect centrum (*$Si{\equiv}N_3$) in het grensgebied tussen a-SiN_x:H en Si. Tijdens de initiële groei van a-SiN_x:H, wordt stikstof geïncorporeerd in het Si rooster bij het oppervlak en gebonden aan dit oppervlak door middel van adhesie; dit proces wordt nitridatie genoemd. In dit proefschrift is aangetoond dat de nitridatie onafhankelijk van de groei van de a-SiN_x:H lagen kan worden geregeld door gebruik te maken van een NH_3 plasma voorbehandeling vóór de eigenlijke groei van

de a-SiN_x:H laag. Er is aangetoond dat Q_f gevariëerd kan worden van $2{\cdot}10^{12}$ tot $15{\cdot}10^{12}$ cm^{-2} zonder dat het a-SiN_x:H depositieproces zelf moet worden aangepast, dus dat de passivering kan worden gevarieerd onafhankelijk van de a-SiN_x:H-laag kenmerken. Gebruikmakend van de voorbehandeling met een NH_3 plasma, werden zowel Q_f als D_{it} verhoogd met toenemende temperatuur. Ook is gedemonstreerd dat Q_f de belangrijkste factor is in oppervlaktepassivering in het gebied van $2{\cdot}10^{12}$ tot $8{\cdot}10^{12}$ cm^{-2}. Voor hogere waarden van Q_f nam D_{it} significant toe en werd dominant, waarbij de passivering afnam. In zonnecellen is het effect van een aangepaste Q_f en D_{it} bestudeerd. Op n-type zonnecellen, die een p-type emitter hebben, resulteert een toename in Q_f en D_{it} in versterkte vermindering van de concentratie van ladingsdragers aan het grensvlak (depletie), wat leidt tot een verlaging van de openklemspanning, V_{OC}, van meer dan 20 mV. Op p-type zonnecellen, die een n-type emitter hebben, resulteert een toename in Q_f in toegenomen accumulatie van ladingsdragers, wat een verwaarloosbaar effect heeft op het rendement van zonnecellen.

Een gedetailleerd beeld van de opbouw van de overgang tussen a-SiN_x:H en Si is verkregen door deze te karakteriseren met Hoge Resolutie Transmissie Elektronen-Microscopie (HRTEM). Er is een geleidelijke overgang over 2 nm in compositie van Si naar de bulk van a-SiN_x:H gevonden. Dit komt overeen met de resultaten die zijn gevonden met force field Molecular Dynamics (MD) modellering en *ab initio* Density Functional Theory (DFT) modellering. Daarnaast wordt er met HRTEM een zeer vervormde laag (ongeveer 1-3 nm) gevonden in het Si rooster, veroorzaakt door de incorporatie van N en/of H. Analyse van de HRTEM resultaten toont aan dat door de nitridatie te variëren door de temperatuur van de NH_3 voorbehandeling te veranderen, de hoeveelheid en penetratiediepte van N in de eerste paar nm's van het Si substraat worden veranderd. Gebruikmakend van MD modellering is aangetoond dat dit proces het aantal K-centra in de overgangslaag verandert, wat de experimentele verandering in Q_f en D_{it} verklaart. *Ab initio* DFT studies laten zien dat in a-SiN_x:H (x = 1.17) de K-centra en Si atomen in een vervormde structuur de belangrijkste defecten zijn die resulteren in een hogere D_{it}. Voor een lagere x (x = 1) is gevonden dat de D_{it} toeneemt door een verhoging in K-centra. Beide resultaten zijn experimenteel bevestigd.

Curriculum Vitae

Machteld Willemijn Petronel Elisabeth Lamers was born on March 21, 1979 in Lienden, the Netherlands. In 1996 she graduated from the Christelijk Lyceum in Veenendaal, the Netherlands. In 1996 she started medical school at the Maastricht University in Maastricht, the Netherlands and she completed the first two years. In 1998 she started at the Eindhoven University of Technology, where she has obtained her masters degree in Applied Physics at the department of Applied Physics in 2006. From 2006 till 2009 she worked at ECN Solar Energy as junior researcher in photovoltaics, focusing on p-type mc-Si cells and more specifically the emitter diffusion process. In 2009 she started her PhD work there. During her PhD she supervised the work of Le Thanh Nam to obtain his master thesis "Determine charge and its location in a-SiN_x:H layers used in Silicon Solar Cells with Kelvin Probe and CV-MIS Methods" (2011) and Bart Teussink for his internship (BSc) "Optimaliseren van SiO_2, SiO_x en SiN_xO_y lagen voor zonnecel via het PECVD proces" (2012). Her work on Metal-wrap-through cells resulted in 2009 and 2010 in world record module efficiencies on p-type mc-Si. Her article submission for the 25th European Photovoltaic Solar Energy Conference and exhibition named "17.9% Back-Contacted mc-Si Cells Resulting in Module Efficiency of 17.0%" was considered one of the highlights of that conference. Her abstract for the Silicon PV Conference in 2012 named "Interface properties of a-SiN_x:H/Si to improve surface passivation" belonged to the best ten submitted and she received an award for this. Her abstract for the Silicon PV Conference in 2013 named "The Interface of a-SiN_x:H and Si: Linking the nano-scale structure to passivation quality" was ranked among the best submitted and she received an award for this.

List of publications

Publications derived from this work

Journals, first author

1. M.W.P.E. Lamers, C. Tjendrawira, M. Koppes, I.J. Bennett, E.E. Bende, T.P. Visser, E. Kossen, B. Brockholz, A.A. Mewe, I.G. Romijn, E. Sauar, L. Carnel, S. Julsrud, T. Naas, P.C. de Jong, A.W. Weeber, "17.9% Metal-wrap-through mc-Si cells resulting in module efficiency of 17.0%", *Progress in Photovoltaics: Research and Applications* **20**, 62–73 (2012).
2. M.W.P.E. Lamers, K.T. Butler, J.H. Harding, A.W. Weeber, "Interface properties of a-SiNx:H/Si to improve surface passivation", *Solar Energy Materials & Solar Cells* **106**, 17–21 (2012).
3. M.W.P.E. Lamers, K.T. Butler, P.E. Vullum, J.H. Harding, A.W. Weeber, "Characterization of a-SiN_x:H layer: Bulk properties, interface with Si and solar cell efficiency", *Physica Status Solidi A* **210**, 658-668 (2013).
4. M.W.P.E. Lamers, L.E. Hintzsche, K.T. Butler, P.E. Vullum, C-M. Fang, M. Marsman, G. Jordan, J.H. Harding, G. Kresse. A.W. Weeber, "The Interface of a-SiN_x:H and Si: Linking the nano-scale structure to passivation quality", *Solar Energy Materials & Solar Cells*, **120**, 311–316 (2014).

Journals, co-author

1. K.T. Butler, M.W.P.E. Lamers, A.W. Weeber, J.H. Harding, "Molecular dynamics studies of the bonding properties of amorphous silicon nitride coatings on crystalline silicon", *Journal of Applied Physics* **110**, 124905 (2011).
2. K.T. Butler, J.H. Harding, M.W.P.E. Lamers, A.W. Weeber, "Stoichiometrically graded SiN_x for improved surface passivation in high performance solar cells", *Journal of Applied Physics* **112**, 094303 (2012).
3. L.E. Hintzsche, C.M. Fang, T. Watts, M. Marsman, G. Jordan, M.W.P.E. Lamers, A.W. Weeber, G. Kresse, "Density functional theory study of the structural and electronic properties of amorphous silicon nitrides: Si_3N_{4-x}:H, *Physical Review B* **86**, 235204 (2012).

4. L.E. Hintzsche, C.M. Fang, M. Marsman, G. Jordan, M.W.P.E. Lamers, A.W. Weeber, G. Kresse, "Defects and defect healing in amorphous $Si_3N_{4\text{-}x}$:H_y: An *ab initio* density functional theory study", *Physical Review B* **88**, 155204 (2013).

Conferences, first author

1. M.W.P.E. Lamers, A.A. Mewe, I.J. Bennett, M. Koppes, I.G. Romijn, P.C. de Jong, A.W. Weeber, "17+% Back-contacted Cells Resulting in New World Record Module Efficiency of 16.4%", in *Proceedings of the 19th Photovoltaic Science and Engineering Conference and Exhibition*, Jeju Island, South-Korea, 32 (2009), (oral presentation).

2. M.W.P.E. Lamers, C. Tjengdrawira, M. Koppes, I. Bennett, E.E. Bende, T.P. Visser, E. Kossen, B. Brockholz, A.A. Mewe, I.G. Romijn, E. Sauar, L. Carnel, S. Julsrud, T. Naas, P.C. de Jong, A.W. Weeber, "17.9% Back-Contacted mc-Si Cells Resulting in Module Efficiency of 17.0%", in *Proceedings of the 25th European Photovoltaic Solar Energy Conference and Exhibition*, Valencia, Spain, 1417–1421 (2010), (oral presentation).

3. M.W.P.E. Lamers, A.A. Mewe, I.G. Romijn, E.E. Bende, Y. Komatsu, M. Koppes, D. Morecroft, M. Cascant, F.J. Castaño, A.W. Weeber, I. Cesar, "Towards 21% Efficient N-Cz IBC Based on Screenprinting", in *Proceedings of the 26th European Photovoltaic Solar Energy Conference and Exhibition*, Hamburg, Germany, 2239-2242 (2011).

4. M.W.P.E. Lamers, K.T. Butler, I.G. Romijn, J.H. Harding, A.W. Weeber, "Examination of the properties of the interface of a-SiN_x:H/Si in crystalline silicon solar cells and its effect on cell efficiency", in *Proceedings of the Material Research Society Fall Meeting*, Boston, USA (2011), (oral presentation).

5. M.W.P.E. Lamers, K.T. Butler, J.H. Harding, A.W. Weeber, "Interface properties of a-SiN_x:H/Si to improve surface passivation", *Silicon PV Conference*, Leuven, Belgium (2012), (extended oral presentation).

6. M.W.P.E. Lamers, K.T. Butler, P.E. Vullum, J.H. Harding, A.W. Weeber, "Characterization of a-SiN_x:H layer: bulk properties and interface with Si", *Advanced Concepts for Silicon Based Photovoltaics*, Oslo, Norway (2012), (oral presentation).

7. M.W.P.E. Lamers, L.E. Hintzsche, K.T. Butler, P.E. Vullum, C-M. Fang, M. Marsman, G. Jordan, J.H. Harding, G. Kresse, A.W. Weeber, "The Interface of a-SiN_x:H and Si: Linking the nano-scale structure to passivation quality", *Silicon PV Conference*, Hamelin, Germany (2013), (extended oral presentation).

Conferences, co-author

1. A.A. Mewe, M.W.P.E. Lamers, I.J. Bennett, M. Koppes, I.G. Romijn, A.W. Weeber, "Reaching 16.4% module efficiency with back-contacted mc-Si solar cells", in *Proceedings of the 24th European Photovoltaic Solar Energy Conference and Exhibition*, 946–949 (2009).

2. I.J. Bennett, C. Tjengdrawira, A.A. Mewe, M.W.P.E. Lamers, P.C. de Jong, A.W. Weeber, "World Record Module Efficiency for Large and Thin mc-Si MWT Cells", in *Proceedings of the 24th European Photovoltaic Solar Energy Conference and Exhibition*, 3268–3261 (2009).

3. A.W. Weeber, I.J. Bennett, C. Tjengdrawira, M.W.P.E. Lamers, A.A. Mewe, I.G. Romijn, P.C. de Jong, "17.0% Aperture Area Module Efficiency using Large mc-Si Metal-Wrap-Through Cells", in *Proceedings of the 12th International Conference on Modern Materials and Technologies*, Montecatini Terme, Italy (2010).

4. C. Tjengdrawira, M.W.P.E. Lamers, I.J. Bennett, P.C. de Jong, "World first 17% efficient multi-crystalline silicon module", in *Proceedings of the 35th IEEE Photovoltaic Specialist Conference*, Honolulu, USA (2010).

5. K.T. Butler, M.W.P.E. Lamers, A.W. Weeber, J.H. Harding, "Studying the effect of interface structure on the electronic and optical properties of silicon/silicon nitride interfaces in solar cells using molecular dynamics simulations", at *Material Research Society Fall Meeting*, Boston, USA (2011), (oral presentation).

6. L.E. Hintzsche, C.M. Fang, T. Watts, M. Marsman, G. Jordan, M.W.P.E. Lamers, A.W. Weeber, G. Kresse, "Defect states in amorphous silicon nitrides: a-$Si_3N_xH_y$", in *Poster at Hermes Summer School*, London, United Kingdom, July (2012).

Other publications

Journals, co-author

1. I.G. Romijn, A.A. Mewe, I. Cesar, M.W.P.E. Lamers, Y. Komatsu, E.E. Bende, A.W. Weeber, D. Morecroft, H. Yuste, F.J. Castaño, "Back-contacted cells for pilot line processing with >19% efficiency", in *Future Photovoltaics* **5**, (2011).

2. N. Satoh, I. Cesar, M.W.P.E. Lamers, I.G. Romijn, K. Bakker, C. Olson, F. Verbakel, M. Wiggers, "Energy Band Diagram near the Interface

of Aluminium Oxide on p-Si Fabricated by Atomic Layer Deposition without and with Rapid Thermal Cycle Annealing Determined by Capacitance–Voltage Measurements", *e-Journal of Surface Science and Nanotechnology* **10**, 22–28 (2012).

3. B.B van Aken, E.E. Bende, M.W.P.E. Lamers, M.J.A.A. Goris, I.J. Bennett, "Cost, efficiency and material optimisation of back-contact cell and module design", *Energy Procedia* **55**, 374–379 (2014).

4. L.E. Hintzsche, C.M. Fang, M. Marsman, M.W.P.E. Lamers, A.W. Weeber, G. Kresse, "The formation of the positive, fixed charge at c-Si(111)/a-$Si_3N_{3.5}$:H interfaces", submitted (2015).

Conferences, first author

1. M.W.P.E. Lamers, I.G. Romijn, M. Gagliardo, M.N. van den Donker, C.J.J. Tool, A.W. Weeber, "Going to a Finite Source Emitter: Improved Emitter Technology by Reduction of the Dead P-layer for High-Efficiency Crystalline Silicon Solar Cells", in *Proceedings of the 23rd European Photovoltaic Solar Energy Conference and Exhibition*, 1708–1712 (2008).

Conferences, co-author

1. I.G. Romijn, M.W.P.E. Lamers, A.F. Stassen, A.A. Mewe, M. Koppes, E.J. Kossen, A.W. Weeber, "Aspire: A new Industrial MWT Cell technology enabling high efficiencies on thin and large mc-Si wafers", in *Proceedings of the 22nd European Photovoltaic Solar Energy Conference and Exhibition*, Milan, Italy (2007).

2. J. Hoornstra, W.J. van Strien, M.W.P.E. Lamers, C.J.J. Tool, A.W. Weeber, "High throughput in-line diffusion: emitter and cell results", in *Proceedings of the 22nd European Photovoltaic Solar Energy Conference and Exhibition*, Milan, Italy (2007).

3. M.N. van den Donker, P. Wijnen, S. Krantz, V. Siarheyeve, L. Janßen, M. Fleuster, I.G. Romijn, A.A. Mewe, M.W.P.E. Lamers, A.F. Stassen, E.E. Bende, A.W. Weeber, P. van Eijk, H. Kerp, K. Albertsen, "The Starfire Project: Towards In-Line Mass Production of Thin High Efficiency Back-Contacted Multicrystalline Silicon Solar Cells", in *Proceedings of the 23rd European Photovoltaic Solar Energy Conference and Exhibition*, 1048–1050 (2008).

4. I.G. Romijn, A.A. Mewe, M.W.P.E. Lamers, E. Kossen, E.E. Bende, A.W. Weeber, "An Overview of MWT cells and Evolution to the

ASPIRe Concept: A New Integrated mc-Si Cell and Module Design for High-Efficiencies", in *Proceedings of the 23rd European Photovoltaic Solar Energy Conference and Exhibition*, 1000–1005 (2008).

5. J. John, G. Beaucarne, P. Choulat, Y. Ma, R. Russell, I.G. Romijn, M.W.P.E. Lamers, A.A. Mewe, A.W. Weeber, M. Hofmann, R. Preu, L. Gautero, A. Slaoui, N. Le Quang, O. Nichiporuk, C. del Cañizo, A. Pan, H. Solheim, J. Evju, H. Nagel, B. Bitnar, M. Heemeier, T. Weber, M. Kaes, B. Raabe, H. Haverkamp, C. Strümpel, G. Hahn, "A Review of 5 Years Cell Development within the European Integrated Project Crystal Clear", in *Proceedings of the 24th European Photovoltaic Solar Energy Conference and Exhibition*, 1162-1166 (2009).

6. Y. Komatsu, G. Galbiati, M.W.P.E. Lamers, P. Venema, M. Harris, A.F. Stassen, C. Meyer, M. van den Donker, A.W. Weeber, "Innovative Diffusion Processes for Improved Efficiency on Industrial Solar Cells by Doping Profile Manipulation", in *Proceedings of the 24th European Photovoltaic Solar Energy Conference and Exhibition*, 1063–1067 (2009).

7. J. Löffler, L.A. Wipliez, W.J. Soppe, M.A. de Keijzer, J. Bosman, M.W.P.E. Lamers, A.A. Mewe, A.W. Weeber, I.J. Bennett, P.C. de Jong, "Laser processing for advanced solar cells", in *Proceedings of the 11th International Symposium on Laser Precision Microfabrication*, Stuttgart, Germany (2010).

8. O.M. Løvvik, E. Flage–Larsen, E. Sagvolden, P.E. Vullum, G. Kresse, M.W.P.E. Lamers, J. Friis, "Solid state hydrogen storage and interfaces in PV solar cells: Different meeting points between modelling and experiments", at *1st TYC-Workshop on Energy Materials*, London, United Kingdom (2010), (invited oral).

9. F.J. Castaño, D. Morecroft, M. Cascant, H. Yuste, M.W.P.E. Lamers, A.A. Mewe, I.G. Romijn, E.E. Bende, Y. Komatsu, A.W. Weeber, I. Cesar, "Industrially feasible >19% efficiency IBC cells for pilot line processing", in *Proceedings of the 37th IEEE Photovoltaic Specialists Conference*, Seattle, USA (2011).

10. M. Cascant, D. Morecroft, H. Yuste, M.W.P.E. Lamers, A.A. Mewe, I.G. Romijn, E.E. Bende, Y. Komatsu, A.W. Weeber, I. Cesar, F.J. Castaño, "Development Towards Pilot Line Efficiency Improvements of >19% Industrially Viable IBC Solar Cells", in *Proceedings of the 26th European Photovoltaic Solar Energy Conference and Exhibition*, Hamburg, Germany, 2223–2226 (2011).

11. I.G. Romijn, B.B. van Aken, J. Anker, A.R. Burgers, A. Gutjahr, B. Heurtault, M. Koppes, E. Kossen, M.W.P.E. Lamers, D.S. Saynova, C.J.J. Tool, F. Lang, J. Xiong, G. Li, Z. Xu, H. Wang, Z. Hu, P.R. Venema, A.H.G. Vlooswijk, "Industrial Implementation of

Efficiency Improvements in n-type Solar Cells and Modules", in *Proceedings of the 27th European Photovoltaic Solar Energy Conference and Exhibition*, Frankfurt, Germany, 533–537 (2012).

12. I.G. Romijn, B.B. van Aken, J. Anker, A.R. Burgers, A. Gutjahr, B. Heurtault, M. Koppes, E.J. Kossen, M.W.P.E. Lamers, D.S. Saynova-Oosterling, C.J.J. Tool, F. Lang, J. Xiong, G. Li, Z. Xu, H. Wang, Z. Hu, P. Venema, A.H.G. Vlooswijk, "Industrial implementation of efficiency improvements in n-type solar cells and modules", in *Proceedings of the 22nd Photovoltaic Science and Engineering Conference*, Hangzhou, China, (2012).

Acknowledgments (Dankwoord)

After a few years of working at ECN Solar Energy, I was kindly offered a PhD position by prof.dr. Wim Sinke, dr.drs. Arthur Weeber and dr. Jan Bultman. I gladly accepted their offer and am grateful for the opportunity, thank you!
In this final part of my thesis, I would like to thank everyone who contributed in any way to the realization of this work. Some, I will name personally.

Prof. dr. W.C. Sinke, Dear Wim, thank you for your guidance and inspirational discussions.
Dr. drs. A.W. Weeber, Dear Arthur, thank you for your time and clear views on issues and for your support throughout the PhD work. Your always positive attitude and kindliness gave me each time new energy.

I would like to thank my co-authors for the interesting discussions and their very much appreciated contribution to the work. Special thanks go to my colleagues with whom I cooperated, discussed and interacted during my work, especially Ingrid Romijn, Agnes Mewe and Mark Sillissen. I would also like to thank students Le Thanh Nam and Bart Teussink for their contribution to the research.
Many thanks go to my co-authors for the *ab initio* Density Functional Theory modeling work done at the University of Vienna: Leif Eric Hintzsche, Chang-ming Fang, Thomas Watts, Martijn Marsman, Gerald Jordan, Georg Kresse. Also much appreciated is the force field Molecular Dynamics modeling work on the interface of a-SiN_x:H/Si done at the University of Sheffield: Keith Butler, John Harding.

Ik wil ook graag dank uiten voor alle steun die ik buiten mijn werk heb gekregen van vrienden en familie.
Albert, Annet, Armelle, Dessie, Helen, Johan, Jurgen, Karen, Kim, Marcel, Martijn, Milla, Raaf, Roel, Wilma, bedankt!
Mijn lieve vriendinnetjes, Caat, Mo, Wen, Sam en Lie en natuurlijk ook jullie wederhelften Maarten, Jan-Martijn, Alexander en Maarten, het is altijd leuk om bij jullie te zijn en dagelijks even bij te chatten over ons wel en wee.
Ook gaat mijn dank uit naar mijn tantes, ooms, neven en nichten, in het speciaal Theo & Mariet, Theo & Clasien, Fer & Ton, Jan en Jessica.
En natuurlijk mijn schoonfamilie: Yvonne, Linda and Hans. Bedankt voor jullie interesse en jullie altijd warme welkom!
Ook mijn zus Liedewij, schoonbroer Jacco, mijn lieve nichtje Elyne en mijn enthousiaste neefje Ruben, het is altijd super om jullie te zien en de hele familie weer bij elkaar te hebben.
Mijn lieve moeder en vader, bedankt voor al hetgeen jullie mij geleerd hebben en jullie onvoorwaardelijke steun gedurende mijn hele leven.
Mijn allerliefste Michiel, bedankt dat je er altijd voor mij bent en dat er altijd een knuffeltje beschikbaar voor me is. Samen met Ysbrand, ons zoontje, ben jij de schildpad waarop mijn aarde rust.

Bibliography

[1] E. Becquerel. *Comptes Rendus*, 9:561, 1839.

[2] K.A. Tsokos. *Physics for the IB Diploma*. Cambridge University Press, 5th edition, 2008.

[3] G.F. Nemet. *Energy Policy*, 34:3218, 2006.

[4] International Renewable Energy Agency. *Renewable Power Generation Costs in 2012: An Overview*, November 2012.

[5] Mercom Capital Group. *Market Intelligence Report Solar*, June 2014.

[6] W. van Sark, G. Rutten, and J. Cace. Inventarisatie pv markt nederland: Status april 2014. *Stichting Monitoring Zonnestroom*, SMZ-2014-2, 2014.

[7] Navigant Consulting. *EUPD Module Price (since 2006)*, 2012.

[8] C. Olson, S. Luxembourg, W. Sark, and W. Sinke. In *Proceedings of the 28th European Solar Energy Conference and Exhibition*, page 4712, Paris, France, 2013.

[9] M.A. Green. *Silicon Solar Cells: Advanced Principles & Practice*. Centre for Photovoltaic Devices and Systems, University of New South Wales, Sydney, Australia, 1st edition, 1995.

[10] S.C. Baker-Finch and K.R. McIntosh. In *Proceedings of the 35th IEEE Photovoltaics Specialists Conference*, page 2184, Honolulu, USA, 2010.

[11] S.C. Baker-Finch and K.R. McIntosh. *Progress in Photovoltaics: Research and Applications*, 19:406, 2011.

[12] H. Tanaka, S. Yamashita, Y. Abe, M. Shikida, and K. Sato. *Sensors and Actuators A*, 114:516, 2004.

[13] I. Röver, G. Roewer, K. Bohmhammel, and K. Wambach. In *Proceedings of the 19th European Photovoltaic Solar Energy Conference and Exhibition*, page 895, Paris, France, 2004.

[14] M. Koppes. Pyramid texture: SEM pictures and reflections. Unpublished, april 2011.

[15] H.F.W. Dekkers. *Study and Optimization of Dry Process Technologies for Thin Crystalline Silicon Solar Cell Manufacturing*. PhD thesis, Katholieke Universiteit Leuven, Leuven, 2008.

[16] Jr. G.E. Jellison, F.A. Modine, P. Doshi, and A. Rohatgi. *Thin Solid Films*, 313-314:193, 1998.

[17] P. Grunow and K. Krauter. In *Proceedings of the 4th IEEE World Conference of Photovoltaic Energy Conversion*, page 2152, Hawaii, USA, 2006.

[18] M.H. Kang, K. Ryu, A. Upadhyaya, and A. Rohatgi. *Progress in Photovoltaics: Research and Applications*, 19:983, 2011.

[19] S.K. Ghandhi. *VLSI Fabrication Principles: Silicon and Gallium Arsenide*. John Wiley & Sons, Inc., 2nd edition, 1994.

[20] M. Uematsu. *Journal of Applied Physics*, 82:2228, 1997.

[21] R.B. Fair and J.C.C. Tsai. *Journal of the Electrochemical Society*, 124:1107, 1977.

[22] E. Kooi. *Journal of the Electrochemical Society*, 111:1383, 1964.

[23] A. Armigliato, D. Nobili, M. Servidori, and S. Solmi. *Journal of Applied Physics*, 47:5489, 1976.

[24] M.W.P.E. Lamers, I.G. Romijn, M. Gagliardo, M.N. van den Donker, C.J.J. Tool, and A.W. Weeber. In *Proceedings of the 23rd European Photovoltaic Solar Energy Conference and Exhibition*, page 1708, Valencia, Spain, 2008.

[25] G. Schubert. *Thick Film Metallisation of Crystalline Silicon Solar Cells: Mechanisms, Models and Applications*. PhD thesis, University of Konstanz, Konstanz, Germany, 2006.

[26] A. Bentzen and A. Holt. In *Proceedings of the 31st IEEE Photovoltaic Specialist Conference*, page 1153, Lake Buena Vista, USA, 2005.

[27] W. Soppe, H. Rieffe, and A. Weeber. *Progress in Photovoltaics: Research and Applications*, 13:551, 2005.

[28] W.J. Soppe, B.G. Duijvelaar, S.E.A. Schiermeier, A.W. Weeber, A. Steiner, and F.M. Schuurmans. In *Proceedings of the 16th European Photovoltaic Solar Energy Conference and Exhibition*, page 1420, Glasgow, Scotland, May 2000.

[29] B.F. Hanyaloglu and E.S. Aydil. *Journal of Vacuum Science & Technology A*, 16:2794, 1998.

[30] W.M.M. Kessels, F.J.H. van Assche, J. Hong, D.C. Schram, and M.C.M. van de Sanden. *Journal of Vacuum Science and Technology A*, 22:96, 2004.

[31] G. Kresse. Private communication. May 2011.

[32] Z.G. Li, L. Liang, A.S. Ionkin, B.M. Fish, M.E. Lewittes, L.K. Cheng, and L.R. Mikeska. *Journal of Applied Physics*, 110:074304, 2011.

[33] F. Huster. In *Proceedings of the 20th European Photovoltaic Solare Energy Conference and Exhibition*, page 1466, Barcelona, Spain, 2005.

[34] V.A. Popovich, M. Janssen, I.M. Richardson, T. van Amstel, and I.J. Bennett. In *Proceedings of the 24th European Solar Energy Conference and Exhibition*, page 1453, Hamburg, Germany.

[35] W. Shockley and W.T. Read. *Physical Review*, 87:835, 1952.

[36] R.N. Hall. *Physical Review*, 87:387, 1952.

[37] G. Dingemans. *Nanolayer surface passivation schemes for silicon solar cells.* PhD thesis, Eindhoven University of Technology, 2011.

[38] S. Dauwe. *Low Temperature Surface Passivation of Crystalline Silicon and its Application to the Rear Side of Solar Cells.* PhD thesis, University of Hannover, Hannover, Germany, 2004.

[39] A.G. Aberle. *Crystalline Silicon Solar Cells - Advanced Surface Passivation and Analysis.* Centre for Photovoltaic Engineering, University of New South Wales, 2000.

[40] M.J. Kerr and A. Cuevas. *Journal of Applied Physics*, 91:2473, 2002.

[41] J. Benick, A. Richter, M. Hermle, and S.W. Glunz. *Physica Status Solidi RRL*, 3:233, 2009.

[42] D.K. Schroder. *Semiconductor Material and Device Characterization.* John Wiley & Sons, Inc., Hoboken, New Jersey, United States, 3rd edition, 2006.

[43] F. Giorgis, F. Giulani, C.F. Pirri, E. Tresso, C. Summonte, R. Rizzolli, R. Galloni, A. Desalvo, and E. Rava. *Philosophical Magazine B*, 77:925, 1998.

[44] V. Verlaan. *Silicon nitride in high growth rate using hot wire chemical vapor deposition.* PhD thesis, Universiteit Utrecht, Utrecht, the Netherlands, 2008.

[45] H.G. Tompkins and W.A. McGahan. *Spectroscopic Ellipsometry and Reflectometry: A User's Guide.* John Wiley & Sons, Inc., New York, USA, 1999.

[46] F.K. Urban III. *Applied Optics*, 32:2339, 1993.

[47] E. Bustarret, M. Bensouda, M.C. Habrard, J.C. Bruyère, and S. Poulin adn S.C. Gujrathi. *Physical Review B*, 38:8171, 1988.

[48] A. Cuevas and D. Macdonald. *Solar Energy*, 76:255, 2004.

[49] Sinton Instruments. http://www.sintoninstruments.com/, Boulder, USA-CO, October 2012.

[50] R.A. Sinton. In *Proceedings of the 25th IEEE Photovoltaic Specialists Conference*, page 457, Washington D.C., USA, 1996.

[51] R.A. Sinton. In *Proceedings of the 23rd European Photovoltaic Solar Energy Conference and Exhibition*, page 1367, Valencia, Spain, 2008.

[52] N. Satoh, I. Cesar, M.W.P.E. Lamers, I.G. Romijn, K. Bakker, C. Olson, D. Saynova-Oosterling, Y. Komatsu, F. Verbakel, M. Wiggers, and A.W. Weeber. *e-Journal of Surface Science and Nanotechnology*, 10:22, 2012.

[53] E.H. Nicollian and J.R. Brews. *Metal Oxide Semiconductor Physics and Technology*. John Wiley & Sons, Inc., 2002.

[54] S.M. Sze and K.K. Ng. *Physics of Semiconductor Devices*. John Wiley and Sons, Inc., 2006.

[55] L.M. Terman. *Solid-State Electronics*, 5:285, 1962.

[56] University of Vienna VASP, Computational Materials Physics. http://www.vasp.at, Vienna, Austria, February 2013.

[57] J. Li. *Handbook of Materials Modeling: Basic Molecular Dynamics*. Springer, Dordrecht, the Netherlands, 2005.

[58] A.W. Weeber, R. Kinderman, P.C. de Jong, and C.J.J. Tool. In *Proceedings of the 21st European Photovoltaic Solar Energy Conference and Exhibition*, page 605, Dresden, Germany, 2006.

[59] J.H. Bultman, D.W.K. Eikelboom, R. Kinderman, A.C. Tip, C.J.J. Tool, M.A.C.J. van den Nieuwenhof, C. Schoofs, F.M. Schuurmans, and A.W. Weeber. In *Proceedings of the 3rd World Conference on Photovoltaic Energy Conversion*, pages 4O–D13–03, Osaka, Japan, 2003.

[60] P.C. de Jong, D.W.K. Eikelboom, R. Kinderman, A.C. Tip, J.H. Bultman, M.H.H. Meuwissen, and M.A.C.J. van den Nieuwenhof. In *Proceedings of the 19th European Photovoltaic Solar Energy Conference and Exhibition*, page 2145, Paris, France, 2004.

[61] Kyocera. http://www.kyocera.com/, Kyoto, Japan, June 2010.

[62] Photovoltech. http://www.photovoltech.be/, Tienen, Belgium, June 2010.

[63] F. Clement, M. Menkoe, T. Kubera, C. Harmel, R. Hoenig, W. Wolke, H. Wirth, D. Biro, and R. Preu. *Solar Energy Materials and Solar Cells*, 93:1051, 2009.

[64] I.J. Bennett, P.C. de Jong, M.J.H. Kloos, C.N.J. Stam, R.J. Gomez, P. Sanchez-Friera, B. Lalaguna, and H. Schmidt. In *Proceedings of the 22nd European Photovoltaic Solar Energy Conference and Exhibition*, pages 4A–V3, Milan, Italy, 2007.

[65] C. Tjengdrawira, M. Kloos, P. Manshanden, and J. Erlbaum. In *Proceedings of the 19th Photovoltaic Science and Engineering Conference and Exhibition*, page 71, Jeju Island, South-Korea, 2009.

[66] M.A. Green, K. Emery, Y. Hishikawa, and W. Warta. *Progress in Photovoltaics: Research and Applications*, 18:144, 2010.

[67] M.A. Green, K. Emery, Y. Hishikawa, and W. Warta. *Progress in Photovoltaics: Research and Applications*, 18:346, 2010.

[68] E. Schmich, Y. Gassenbauer, K. Ramspeck, K. Dressler, M. Fiedler, W. Hefner, M. Manole, B. Bethmann, E. Parr, E. Schlenker, P. Roth, B. Schum, J. Horzel, J. Moschner, A. Metz, and W. Schmidt. In *Proceedings of the 25th European Photovoltaic Solar Energy Conference and Exhibition*, page 1154, 2010.

[69] M.A. Green, K. Emery, Y. Hishikawa, W. Warta, and E.D. Dunlop. *Progress in Photovoltaics: Research and Applications*, 22:701, 2014.

[70] B.B van Aken, E.E. Bende, M.W.P.E. Lamers, M.J.A.A. Goris, and I.J. Bennett. *Energy Procedia*, 55:374, 2014.

[71] C. del Cañizo, G. del Coso, and W.C. Sinke. *Progress in Photovoltaics: Research and Applications*, 17:199, 2009.

[72] W. Eerenstein, I.J. Bennett, D. Veldman, T. Visser, B. Brockholz, P.C. de Jong, C.A. Copetti, and P. Wijnen. In *Proceedings of the 25th European Photovoltaic Solar Energy Conference and Exhibition*, page 4CO.19.5, Valencia, Spain, 2010.

[73] M. Späth, P.C. de Jong, I.J. Bennett, T.P. Visser, J. Bakker, and A.J. Verschoor. In *Proceedings of the 23rd European Photovoltaic Solar Energy Conference and Exhibition*, page 2917, Valencia, Spain, 2008.

[74] M.A. Green, K. Emery, Y. Hishikawa, and W. Warta. *Progress in Photovoltaics: Research and Applications*, 17:85, 2009.

[75] ASTM International. *ASTM Standard E948-09: Standard Test Method for Electrical Performance of Photovoltaic Cells Using Reference Cells under Simulated Sunlight.* http://www.astm.org/, West Conshohocken, USA-PA, June 2010.

[76] Sinton Instruments. http://www.sintoninstruments.com/, Boulder, USA-CO, June 2010.

[77] R.A. Sinton. *Testing Solar Cell Wafers after Phosphorus Diffusion: Application note developed under DOE subcontract ZDO-2-30628-08*. http://www.sintoninstruments.com/, Boulder, USA-CO, April 2004.

[78] C.J.J. Tool, G. Coletti, F.J. Franek, M. Koppes, E.J. Kossen, H.C. Rieffe, I.G. Romijn, and A.W. Weeber. In *Proceedings of the 20th European Photovoltaic Solar Energy Conference and Exhibition*, page 578, Barcelona, Spain, 2005.

[79] J. Dziewior and W. Schmid. *Applied Physics Letters*, 31:346, 1977.

[80] M.A. Green. *Solar Cells: Operating Principles, Technolog, and System Applications*. Prentice Hall: Englewood Cliffs, 1998.

[81] I.G. Romijn, W.J. Soppe, H.C. Rieffe, A.R. Burgers, and A.W. Weeber. In *Proceedings of the 20th European Photovoltaic Solar Energy Conference and Exhibition*, page 1352, Barcelona, Spain, 2005.

[82] H.F.W. Dekkers, L. Carnel, G. Beaucarne, and W. Beyer. In *Proceedings of the 20th European Photovoltaic Solar Energy Conference and Exhibition*, page 721, Barcelona, Spain, 2005.

[83] J. Hong, W.M.M. Kessels, W.J. Soppe, A.W. Weeber, W.M. Arnoldbik, and M.C.M. van de Sanden. *Journal of Vacuum Science and Technology*, 21:2123, 2003.

[84] G. Schubert, F. Huster, and P. Fath. In *Proceedings of the 20th European Photovoltaic Solar Energy Conference and Exhibition*, page 813, Barcelona, Spain, 2005.

[85] A.A. Mewe, I.G. Romijn, P. Wijnen, M.N. van den Donker, P. van Eijk, H. Kerp, A. Shaikh, and A.W. Weeber. In *Proceedings of the 23rd European Photovoltaic Solar Energy Conference and Exhibition*, page 1756, Valencia, Spain, 2008.

[86] H.C. Fang, C.P. Liu, H.S. Chung, and C.L. Huang. *Journal of the Electrochemical Society*, 157:H455, 2010.

[87] M.W.P.E. Lamers, A.A. Mewe, I.J. Bennett, M. Koppes, I.G. Romijn, P.C. de Jong, and A.W. Weeber. In *Proceedings of the 19th Photovoltaic Science and Engineering Conference and Exhibition*, page 32, Jeju Island, South-Korea, 2009.

[88] K.R. McIntosh, J.N. Cotsell, J.S. Cumpston, A.W. Norris, N.E. Powell, and B.M. Ketola. In *Proceedings of the 34th IEEE Photovoltaic Specialists Conference*, page 544, Philadelphia, USA, 2009.

[89] C.J.J. Tool, A.R. Burgers, P. Manshanden, and A.W. Weeber. In *Proceedings of the 17th European Photovoltaic Solar Energy Conference and Exhibition*, page 1551, Munich, Germany, 2001.

[90] J. Rentsch, O. Schultz, A. Grohe, D. Biro, R. Preu, and G.P. Willeke. In *Proceedings of the IEEE 4th World Conference on Photovoltaic Energy Conversion*, page 1008, Hawaii, USA, 2006.

[91] P. Choulat, G. Agostinelli, Y. Ma, F. Duerinckx, and G. Beaucarne. In *Proceedings of the 22nd European Photovoltaic Solar Energy Conference and Exhibition*, page 1011, Milan, Italy, 2007.

[92] I.G. Romijn, M.W.P.E. Lamers, A. Stassen, A.A. Mewe, M. Koppes, E. Kossen, and A.W. Weeber. In *Proceedings of the 22nd European Photovoltaic Solar Energy Conference and Exhibition*, page 1043, Milan, Italy, 2007.

[93] O. Schultz, S.W. Glunz, and G.P. Willeke. *Progress in Photovoltaics: Research and Applications*, 14:553, 2004.

[94] I.G. Romijn, A.A. Mewe, I. Cesar, M.W.P.E. Lamers, Y. Komatsu, E.E. Bende, A.W. Weeber, D. Morecroft, H. Yuste, and F.J. Castaño. *Future Photovoltaics*, 5, 2011.

[95] F.J. Castaño, D. Morecroft, M. Cascant, H. Yuste, M.W.P.E. Lamers, A.A. Mewe, I.G. Romijn, E.E. Bende, Y. Komatsu, A.W. Weeber, and I. Cesar. In *Proceedings of the 37th IEEE Photovoltaic Specialists Conference*, page 001038, Washington, USA, 2011.

[96] M. Cascant, D. Morecroft, H. Yuste, M.W.P.E. Lamers, A.A. Mewe, I.G. Romijn, E.E. Bende, Y. Komatsu, A.W. Weeber, I. Cesar, and F.J. Castaño. In *Proceedings of the 26th European Photovoltaic Solar Energy Conference and Exhibition*, page 2223, Hamburg, Germany, 2011.

[97] M. Hermle, F. Granek, O. Schultz-Wittmann, and S.W. Glunz. In *Proceedings of the 33rd IEEE Photovoltaic Specialists Conference*, page 1, St. Diego, USA, 2008.

[98] F. Granek. *High-Efficiency Back-Contact Back-Junction Silicon Solar Cells*. PhD thesis, Albert-Ludwigs-Universität Freiburg im Breisgau, Fraunhofer Institut für Solare Energiesysteme, Freiburg im Breisgau, 2009.

[99] F. Granek, M. Hermle, D.M. Huljić, O. Schultz-Wittmann, and S.W. Glunz. *Progress in Photovoltaics: Research and Applications*, 17:47, 2009.

[100] I. Cesar, N. Guillevin, A.R. Burgers, A.A. Mewe, E.E. Bende, V. Rosca, B. van Aken, M. Koppes, J. Anker, L.J. Geerligs, and A.W. Weeber. In *Proceedings of the 29th European Photovoltaic Solar Energy Conference and Exhibition*, page 681, Amsterdam, the Netherlands, 2014.

[101] D.S. Kim, V. Meemongkolkiat, A. Ebong, B. Rounsaville, V. Upadhyaya, A. Das, and A. Rohatgi. In *Proceedings of the 4th World Conference on Photovoltaic Energy Conversion*, page 1417, Hawaii, USA, 2006.

[102] J. Dicker, J.O. Schumacher, W. Warta, and S.W. Glunz. *Journal of Applied Physics*, 91:4335, 2002.

[103] X.M. Dai and Y.H. Tang. *Solar Energy Materials and Solar Cells*, 43:363, 1996.

[104] N. Guillevin, B.J.B. Heurtault, L.J. Geerligs, and A.W. Weeber. *Energy Procedia*, page 9, 2011.

[105] C. Reichel, F. Granek, M. Hermle, and S.W. Glunz. *Journal of Applied Physics*, 109:024507, 2011.

[106] J. Hong, W.M.M. Kessels, F.J.H. van Assche, H.C. Rieffe, W.J. Soppe, A.W. Weeber, and M.C.M. van de Sanden. *Progress in Photovoltaics: Research and Applications*, 11:125, 2001.

[107] C. Boehme and G. Lucovsky. *Journal of Vacuum Science & Technology A*, 19:2622, 2001.

[108] J.F. Lelièvre. *Elaboration de SiN_x:H par PECVD: optimisation des proprieties optiques, passivantes et structurales pour applications photovoltaïques*. PhD thesis, L'Institut National des Sciences Appliquées de Lyon, Lyon, 2007. pp. 80.

[109] Roth and Rau. *Hightech for Surfaces*. http://www.roth-rau.de/, Hohenstein-Ernstthal, Germany, October 2012.

[110] S. Garcia, D. Bravo, M. Fernandez, I. Martil, and F.J. López. *Applied Physics Letters*, 67:3263, 1995.

[111] J. Robertson. *Philosophical Magazine B*, 69:307, 1994.

[112] D.E. Aspnes. *American Journal of Physics*, 50:704, 1982.

[113] W.L. Warren, P.M. Lenahan, and J. Kanicki. *Journal of Applied Physics*, 70:2220, 1991.

[114] M.W.P.E. Lamers, K.T. Butler, I.G. Romijn, J.H. Harding, and A.W. Weeber. In *Proceedings of the Materials Research Society Fall Meeting*, page 1423, Boston, USA, 2011.

[115] F. de Brito Mota, J.F. Justo, and A. Fazzio. *Journal of Applied Physics*, 86:1843, 1999.

[116] J. Tersoff. *Physical Review Letters*, 56:632, 1986.

[117] A.F. Stassen, J. Anker, P. Danzl, Y. Komatsu, M. Koppes, and E. Kossen. In *Proceedings of the 25th European Photovoltaic Solar Energy Conference and Exhibition*, page 1939, Valencia, Spain, 2010.

[118] D. Macdonald, A. Cuevas, A. Kinomura, Y. Nakano, and L.J. Geerligs. *Journal of Applied Physics*, 97:033523, 2011.

[119] C. Boehme and G. Lucovsky. *Journal of Applied Physics*, 88:6055, 2000.

[120] A. Cuevas, P.A. Basore, G. GiroultMatlakowski, and C. Dubois. *Journal of Applied Physics*, 80:3370, 1996.

[121] P.A. Basore. In *Proceedings of the 25th IEEE Photovoltaic Specialists Conference*, page 377, Washington, USA-DC, 1996.

[122] M. Dai, Y. Wang, J. Kwon, M.D. Halls, and Y.J. Chabal. *Nature Materials*, 8:825, 2009.

[123] T. Takakura, R. Imai, Y. Okamoto, and H. Taniguchi. *Japanese Journal of Applied Physics*, 49:046502, 2010.

[124] F. Demichelis, F. Giorgis, and C.F. Pirri. *Philosophical Magazine B*, 74:155, 1996.

[125] S. Wolf. *Journal of Applied Physics*, 97:063303, 2005.

[126] A.W. Weeber, A.R. Burgers, N. Guillevin, A.J. Carr, P.C. Barton, X. Jingfeng, L. Gaofei, S. Weipeng, A. Haijlao, H. Zhiyan, P. Venema, A.H.G. Vlooswijk, and L.J. Geerligs. In *International Workshop on Science and Technology of Crystalline Silicon Solar Cells*, Taipei, Taiwan, 2010.

[127] B. Hoex, M.C.M. van de Sanden, J. Schmidt, R. Brendel, and W.M.M. Kessels. *Physica Status Solidi RRL*, 6:4, 2012.

[128] N. Tanaka, J. Yamasaki, K. Usuda, and N. Ikarashi. *Journal of Electron Microscopy*, 52:69, 2003.

[129] J. Park, S. Heo, J. Ghung, H. Kim, H. Lee, K. Kim, and G. Park. *Ultramicroscopy*, 109:1183, 2009.

[130] N. Ikarashi, K. Watanabe, and Y. Miyamoto. *Journal of Applied Physics*, 90:2683, 2001.

[131] R. Hezel and K. Jaeger. *Journal of the Electrochemical Society*, 136:518, 1989.

[132] R. Hezel and R. Schroner. *Journal of Applied Physics*, 52:3076, 1981.

[133] H. Ahn, C.L. Wu, S. Gwo, C.M. Wei, and Y.C. Chou. *Physical Review Letters*, 86:2818, 2001.

[134] G.L. Zhao and M.E. Bachlechner. *Physical Review B*, 58:1887, 1998.

[135] M.L. Colaianni, P.J. Chen, N. Nagashima, and J.J.T. Yates. *Journal of Applied Physics*, 73:4927, 1993.

[136] H.D. Goldbach, V. Verlaan, C.H.M. van der Werf, W.M. Arnoldbik, H.C. Rieffe, I.G. Romijn, A.W. Weeber, and R.E.I. Schropp. *Amorphous and Nanocrystalline Silicon Science and Technology*, 862:293, 2005.

[137] X.-S. Wang, G. Zhai, J. Wang, and N. Cue. *Physical Review B*, 60:R2146, 1999.

[138] G. Zhai, J. Yang, N. Cue, and X.S. Wang. *Thin Solid Films*, 366:121, 2000.

[139] P. Aubert, H.J. von Bardeleben, F. Delmotte, J.L. Cantin, and M.C. Hugon. *Physical Review B*, 59:10677, 1999.

[140] P. M. Lenahan and Sean E. Curry. *Applied Physics Letters*, 56:157, 1990.

[141] W.L. Warren, P. M. Lenahan, and Sean E. Curry. *Physical Review Letters*, 65:207, 1990.

[142] G. Pacchioni and D. Erbetta. *Physical Review B*, 60:12617, 1999.

[143] F. de Brito Mota, J.F. Justo, and A. Fazzio. *Physical Review B*, 58:8323, 1998.

[144] W. Smith and T.R. Forester. *Journal of Molecular Graphics*, 14:136, 1996.

[145] S.L. Roux and P. Jund. *Computational Materials Science*, 49:70, 2010.

[146] F. Alvarez and A.A. Valladares. *Physical Review B*, 68:205203, 2003.

[147] M.M. Guraya, H. Ascolani, G. Zampieri, J.I. Cisneros, J.H. Dias da Silv, and M.P. Cantõo. *Physical Review B*, 42:5677, 1990.

[148] F.L. Martínez, A. del Prado, I. Mártil, G. González-Díaz, B. Selle, and I. Sieber. *Journal of Applied Physics*, 86:2055, 1999.

[149] F.L. Martínez, A. del Prado, I. Mártil, D. Bravo, and F.J. López. *Journal of Applied Physics*, 88:2149, 2000.

[150] M.W.P.E. Lamers, K.T. Butler, J.H. Harding, and A.W. Weeber. *Solar Energy Materials & Solar Cells*, 106:17, 2012.

[151] D.R. Kim, C.H. Lee, P.M. Rao, I.S. Cho, and X. Zheng. *Nano Letters*, 11:2704, 2011.

[152] C.F. Chi, P. Chen, Y.L. Lee, I.P. Liu, S.C Chou, X.L. Zhang, and U. Bach. *Journal of Materials Chemistry*, 21:17534, 2011.

[153] Y. Dan, K. Seo, K. Takei, J.H. Meza, A. Javey, and K.B. Crozier. *Nano Letters*, 11:2527, 2011.

[154] H. Lee, T. Tachibana, N. Ikeno, H. Hashiguchi, K. Arafune, H. Yoshida, S. Ichi Satoh, T. Chikyow, and A. Ogura. *Applied Physics Letters*, 100:143901, 2012.

[155] A.G. Aberle. *Solar Energy Materials & Solar Cells*, 65:239, 2001.

[156] A.G. Aberle, S. Glunz, and W. Warta. *Journal of Applied Physics*, 71:4422, 1992.

[157] J. Schmidt, F.M. Schuurmans, W.C. Sinke, S.W. Glunz, and A.G. Aberle. *Applied Physics Letters*, 71:252, 1997.

[158] C. Gong, E. Simoen, N. Posthuma, E.V. Kerschaver, J. Poortmans, and R. Mertens. *Applied Physics Letters*, 96:103507, 2010.

[159] J. Schmidt and A.G. Aberle. *Journal of Applied Physics*, 85:3626, 1999.

[160] J.-F. Lelièvre, E. Fourmond, A. Kaminski, O. Palais, D. Ballutaud, and M. Lemiti. *Solar Energy Materials and Solar Cells*, 93:1281, 2009.

[161] H. Mackel and R. Ludemann. *Journal of Applied Physics*, 92:2602, 2002.

[162] M. Jaros. *Physics and Applications of Semiconductor Microstructures*. Oxford Science Publications, New York, 1989.

[163] V.A. Gritsenko, E.E. Meerson, and Y.N. Morokov. *Physical Review B*, 57:R2081, 1998.

[164] K. Nasyrov, V. Gritsenko, M. Kim, H. Chae, W. Ryu, J. Sok, J.-W. Lee, and B. Kim. *IEEE Electron Device Letters*, 23:336, 2002.

[165] Y. Shi, X. Wang, and T.-P. Ma. *IEEE Transactions on Electron Devices*, 46:362, 1999.

[166] J. Robertson. *Philosophical Magazine B*, 63:47, 1991.

[167] F. Duerinckx and J. Szlufcik. *Solar Energy Materials and Solar Cells*, 72:231, 2002.

[168] F. Giorgis, C. F. Pirri, and E. Tresso. *Thin Solid Films*, 307:298, 1997.

[169] C. J. Mogab and E. Lugujjo. *Journal of Applied Physics*, 47:1302, 1976.

[170] T. Aiyama, T. Fukunaga, K. Niihara, T. Hirai, and K. Suzuki. *Journal of Non-Crystalline Solids*, 33:131, 1979.

[171] M. Misawa, T. Fukunaga, K. Niihara, T. Hirai, and K. Suzuki. *Journal of Non-Crystalline Solids*, 34:313, 1979.

[172] J. Robertson and M. J. Powell. *Applied Physics Letters*, 44:415, 1984.

[173] J. Robertson, W.L. Warren, and J. Kanicki. *Journal of Non-Crystalline Solids*, 187:297, 1995.

[174] N. Umesaki, N. Hirosaki, and K. Hirao. *Journal of Non-Crystalline Solids*, 150:120, 1992.

[175] Lizhi Ouyang and W. Y. Ching. *Physical Review B*, 54:R15594, 1996.

[176] F. De Brito Mota, J. F. Justo, and A. Fazzio. *International Journal of Quantum Chemistry*, 70:973, 1998.

[177] J. F. Justo, F. de Brito Mota, and A. Fazzio. *Physical Review B*, 65:073202, 2002.

[178] S. Y. Lin. *Optical Materials*, 23:93, 2003.

[179] S. Zh. Karazhanov, P. Kroll, A. Holt, A. Bentzen, and A. Ulyashin. *Journal of Applied Physics*, 106(5):053717, sep 2009.

[180] L. Giacomazzi and P. Umari. *Physical Review B*, 80:144201, 2009.

[181] K. Jarolimek, R. A. de Groot, G. A. de Wijs, and M. Zeman. *Physical Review B*, 82:205201, 2010.

[182] M. Ippolito and S. Meloni. *Physical Review B*, 83:165209, 2011.

[183] S. Nekrashevich, A. Shaposhnikov, and V. Gritsenko. *JETP Letters*, 94:202, 2011.

[184] Eraldo C. Ferreira and C. E. T. Gonçalves da Silva. *Physical Review B*, 32:8332, 1985.

[185] P. Kroll. *Journal of Non-Crystalline Solids*, 293-295:238, 2001.

[186] R. P. Vedula, N. L. Anderson, and A. Strachan. *Physical Review B*, 85:205209, 2012.

[187] T. M. Searle. *Properties of amorphous silicon and its alloys*. Institution of Engineering and Technology, 1998.

[188] R. E. I. Schropp, S. Nishizaki, Z.S. Houweling, V. Verlaan, C.H.M. van der Werf, and H. Matsumura. *Solid-State Electronics*, 52:427, 2008.

[189] A. R. Denton and N. W. Ashcroft. *Physical Review A*, 43:3161, 1991.

[190] N. W. Ashcroft and N. D. Mermin. *Solid State Physics*. Brooks Cole, 1976.

[191] P. E. Blöchl. *Physical Review B*, 50:17953, 1994.

[192] J. Furthmüller, J. Hafner, and G. Kresse. *Physical Review B*, 50:15606, 1994.

[193] G. Kresse and J. Furthmüller. *Physical Review B*, 54:11169, 1996.

[194] G. Kresse and D. Joubert. *Physical Review B*, 59:1758, 1999.

[195] J.P. Perdew, A. Ruzsinszky, G.I. Csonka, O.A. Vydrov, G.E. Scuseria, L.A. Constantin, X. Zhou, and K. Burke. *Physical Review Letters*, 100:136406, 2008.

[196] R. Riedel and M. Seher. *Journal of the European Ceramic Society*, 7:21, 1991.

[197] Y. Cerenius. *Journal of the American Ceramic Society*, 82:380, 1999.

[198] K. Jarolimek, R. A. de Groot, G. A. de Wijs, and M. Zeman. *Physical Review B*, 79:155206, 2009.

[199] T. E. Faber and J. M. Ziman. *Philosophical Magazine*, 11:153, 1965.

[200] N. W. Ashcroft and D. C. Langreth. *Physical Review*, 156:685, 1967.

[201] P. Vashishta, R. K. Kalia, J. P. Rino, and I. Ebbsjö. *Physical Review B*, 41:12197, 1990.

[202] J. P. Hansen and I. R. McDonald. *Theory of simple liquids.* Number November. Elsevier, 3rd edition, 2005.

[203] G. Kresse, M. Marsman, L. E. Hintzsche, and E. Flage-Larsen. *Physical Review B*, 85:045205, 2012.

[204] E. D. Palik. *Handbook of optical constants of solids Vol. 3.* Academic Press, 1998.

[205] M. P. Prange, J. J. Rehr, G. Rivas, J. keJ. Kas, and John W. Lawson. *Physical Review B*, 80:155110, 2009.

[206] M. Gajdoš, K. Hummer, G. Kresse, J. Furthmüller, and F. Bechstedt. *Physical Review B*, 73:045112, 2006.

[207] J. Tauc. *Materials Research Bulletin*, 5:721, 1970.

[208] A. R. Zanatta and I. Chambouleyron. *Physical Review B*, 53:3833, 1996.

[209] L. Hedin. *Physical Review*, 139:A796, 1965.

[210] M.S. Hybertsen and S.G. Louie. *Physical Review B*, 34:5390, 1986.

[211] W. G. Aulbur, L. Jönsson, and J. W. Wilkins. *Solid State Physics*, 54:1, 1999.

[212] F. Aryasetiawan and O. Gunnarsson. *Reports on Progress in Physics*, 61:237, 1998.

[213] M. Shishkin and G. Kresse. *Physical Review B*, 74:035101, 2006.

[214] M. Shishkin and G. Kresse. *Physical Review B*, 75:235102, 2007.

[215] A. G. Aberle. *Progress in Photovoltaics: Research and Applications*, 8:473, 2000.

[216] J. Singh and K. Shimakawa. *Advances in amorphous semiconductors*. CRC Press, 2003.

[217] D.T. Krick, P.M. Lenahan, and J. Kanicki. *Journal of Applied Physics*, 64:3558, 1988.

[218] D.T. Krick, P.M. Lenahan, and J. Kanicki. *Physical Review B*, 38:8226, 1988.

[219] W.L. Warren and P.M. Lenahan. *Physical Review B*, 42:1773, 1990.

[220] W.L. Warren, F.C. Rong, E.H. Poindexter, G.J. Gerardi, and J. Kanicki. *Journal of Applied Physics*, 70:346, 1991.

[221] L. Zhong and F. Shimura. *Applied Physics Letters*, 62:615, 1993.

[222] D.Q. Chen, J.M. Viner, and P.C. Taylor. *Solid State Communications*, 98:745, 1996.

[223] V. Gritsenko, S. Nekrashevich, V. Vasilev, and A. Shaposhnikov. *Microelectronic Engineering*, 86:1866, 2009.

[224] A. Pasquarello, M.S. Hybertsen, and R. Car. *Nature*, 396:58, 1998.

[225] J. Sarnthein, A. Pasquarello, and R. Car. *Physical Review Letters*, 74:4682, 1995.

[226] A. Pasquarello and R. Car. *Physical Review Letters*, 5145:80, 1998.

[227] A. Pasquarello, M.S. Hybertsen, and R. Car. *Physical Review Letters*, 74:1024, 1995.

[228] M. Boero, A. Pasquarello, J. Sarnthein, and R. Car. *Physical Review Letters*, 78:887, 1997.

[229] S. Mukhopadhyay, P.V. Sushko, A.M. Stoneham, and A.L. Shluger. *Physical Review B*, 70:195203, 2004.

[230] L. Giordano, P.V. Sushko, A.M. Stoneham, and A.L. Shluger. *Physical Review Letters*, 99:136801, 2007.

[231] J. Furthmüller, J. Hafner, and G. Kresse. *Physical Review B*, 50:15606, 1994.

[232] P.A. Khomyakov, W. Andreoni, N.D. Afify, and A. Curioni. *Physical Review Letters*, 107:255502, 2011.